INELASTIC MULTIPLE SCATTERING OF INTERACTING BOSONS IN WEAK RANDOM POTENTIALS

DISSERTATION

zur Erlangung des Doktorgrades der
Fakultät für Mathematik und Physik der
Albert-Ludwigs Universität
Freiburg im Breisgau

vorgelegt von
Tobias Geiger
aus Radevormwald

2013

DEKAN:
Prof. Dr. Michael Růžička

BETREUER DER ARBEIT:
Prof. Dr. Andreas Buchleitner
IN ZUSAMMENARBEIT MIT:
PD Dr. Thomas Wellens

REFERENT:
Prof. Dr. Andreas Buchleitner
KOREFERENT:
Prof. Dr. Stefan Dittmaier

TAG DER MÜNDLICHEN PRÜFUNG:
23.07.2013

PRÜFER:
Prof. Dr. Andreas Buchleitner
Prof. Dr. Hanspeter Helm
apl. Prof. Dr. Thomas Filk

This document was typeset using the typographical look-and-feel `classicthesis` developed by André Miede.

Für meinen Opi.

… wie einst in Damp besprochen.

ABSTRACT

Within the present thesis we develop a diagrammatic scattering theory for interacting bosons in a three-dimensional, weakly disordered potential. Based on a microscopic N-body scattering theory, we identify the relevant diagrams including elastic and inelastic collision processes that are sufficient to describe quantum transport in the regime of weak disorder. By taking advantage of the statistical properties of the weak disorder potential, we demonstrate how the N-body dynamics can be reduced to a nonlinear integral equation of Boltzmann type for the single-particle diffusive flux. A presently available alternative description – based on the Gross-Pitaevskii equation – only includes elastic collisions. In contrast, we show that far from equilibrium the presence of inelastic collisions – even for weak interaction strength – must be accounted for and can induce the full thermalization of the single-particle current. In addition, we also determine the coherent corrections to the incoherent transport, leading to the effect of coherent backscattering. For the first time, we are able to analyze the influence of inelastic collisions on the coherent backscattering signal, which lead to an enhancement of the backscattered cone in a narrow spectral window, even for increasing non-linearity. With a short recollection of the presently available experimental techniques we furthermore show how an immediate implementation of our suggested setup with confined Bose-Einstein condensates can be accomplished. Thereby, the emergence of collective and/or thermodynamic behavior from fundamental, microscopic constituents can also be assessed experimentally.

In a second part of this thesis, we present first results for light scattering off strongly interacting Rydberg atoms trapped in a one-dimensional, chain-like configuration. In order to monitor the time-dependence of this interacting many-body system, we devise a weak measurement scenario for which we derive a master equation for the N-body density matrix of the atomic subspace. This allows us to study the influence of the weak laser fields onto the dynamics of the strongly interacting Rydberg chain, as a function of time. Whereas in the long time limit the N-body density matrix – due to the dephasing by the weak fields – relaxes to a fully mixed state, the dynamics for intermediate times reveals a strong influence of the Rydberg blockade mechanism, a signature of which can also be identified in the intensity scattered off the chain of Rydberg atoms.

ZUSAMMENFASSUNG

Die vorliegende Arbeit befasst sich mit der Entwicklung einer diagrammatischen Streutheorie für wechselwirkende Bosonen in dreidimensionalen, ungeordneten Potentialen. Ausgehend von einer mikroskopischen Vielteilchenstreutheorie berücksichtigen wir alle diagrammatischen Beiträge, die für die Beschreibung von quantenmechanischen Transportprozessen in schwachen Unordnungspotentialen relevant sind – insbesondere auch jene, die von elastischen oder inelastischen Stößen herrühren. Unter Ausnutzung der statistischen Eigenschaften des schwachen Unordnungspotentials reduziert sich die Vielteilchendynamik auf eine nicht-lineare Integralgleichung, die den diffusiven Einteilchenfluss beschreibt und einer nicht-linearen Boltzmann-Gleichung entspricht. Im Gegensatz zu bisher existierenden Modellen, die auf der Gross-Pitaevskij Gleichung basieren und nur elastische Stoßprozesse berücksichtigen, können wir im Rahmen dieser Arbeit zeigen, dass inelastische Kollisionen in Nichtgleichgewichtssituationen auch für schwache Wechselwirkungsstärken eine wichtige Rolle spielen und zu einer Thermalisierung des Einteilchenflusses führen. Darüberhinaus berücksichtigen wir den Einfluss von Kohärenzen auf den Transport, die sich als kohärente Rückstreuung außerhalb des Mediums manifestieren. Erstmals sind wir damit in der Lage, den Einfluss inelastischer Streuprozesse auf die kohärente Rückstreuung zu beschreiben, die mit anwachsender Nichtlinearität zu einer Verstärkung des Rückstreukegels innerhalb eines schmalen Frequenzfensters führt. Gleichzeitig deuten wir die experimentelle Realisierbarkeit dieser Vorhersage an, indem wir auf moderne Technologien zur Erzeugung von eingeschlossenen Bose-Einstein Kondensaten, insbesondere den Atomlaser, eingehen. Somit eröffnet sich die Möglichkeit, sowohl kollektive als auch thermodynamische Effekte, die als Konsequenz von fundamentaler, mikroskopischer Dynamik entstehen, experimentell zu untersuchen.

Im zweiten Teil dieser Arbeit präsentieren wir erste Ergebnisse zur Lichtstreuung an stark wechselwirkenden Rydberg-Atomen, die in einer eindimensionalen Gitterkonfiguration vorliegen. Mit dem Ziel, die Zeitabhängigkeit dieses wechselwirkenden Vielteilchensystems durch Streuung schwacher, externer Laserfelder zu beobachten, leiten wir eine Mastergleichung für die Vielkörperdichtematrix des atomaren Unterraums her, die gleichzeitig auch die Untersuchung des Einflusses der streuenden Felder auf die atomare Dynamik ermöglicht. Wir beobachten, dass die atomare Dichtematrix auf Grund der Dephasierung durch das gestreute, schwache Feld im Limes langer Zeiten in einen vollständig gemischten Zustand übergeht. Dagegen ist die Dynamik für intermediäre Zeiten stark von der Rydbergblockade benachbarter Atome und deren Korrelationen bestimmt. Dieser Unterschied in der Dynamik lässt sich ebenso an der Intensität der gestreuten, schwachen Felder festmachen und eröffnet somit die Möglichkeit einer experimentellen Klassifizierung der atomaren Dynamik.

PUBLICATIONS

List of publications that are based on the present thesis:

- *Inelastic Multiple Scattering of Interacting Bosons in Weak Random Potentials*
  Tobias Geiger, Thomas Wellens, and Andreas Buchleitner
  Physical Review Letters **109**, 030601 (2012)
- *Microscopic Scattering Theory for Interacting Bosons in Weak Random Potentials*
  Tobias Geiger, Thomas Wellens, and Andreas Buchleitner
  to be submitted (2013)

CONTENTS

Part I

INELASTIC MULTIPLE SCATTERING OF INTERACTING BOSONS IN WEAK RANDOM POTENTIALS

1 INTRODUCTION

Transport is of universal relevance. Its implications reach from astronomical questions, e. g. how photons propagate through interstellar clouds [1], over condensed matter systems, where e. g. the movement of charges is of everyday relevance [2, 3], to biology, where e. g. quantum properties of excitonic transport in light harvesting complexes in photosynthesis are currently debated, see e. g. [4].

Besides the interdisciplinary character of transport, transport also poses a problem of scales [5]. Whereas, on the microscopic level, transport is governed by quantum mechanics, and its *reversible* dynamics is predicted by the Schrödinger equation, the dynamics on mesoscopic scales is properly described by the *irreversible* kinetic theory of Boltzmann type. On macroscopic scales, the Boltzmann equation turns into a classical diffusion equation. Hence, naturally the question arises what is the trigger of these transitions and how does the limit of quantum and classical (statistical) mechanics come about?

Over the last two centuries, even without knowledge of the microscopic fundament, many generations of scientists have uncovered the foundations of transport processes from microscopic to macroscopic scales. The work of Ohm around 1827 [6] led to the insight of how a current in a metal is proportional to the applied voltage via the conductance – a scenario, which, on large scales, is today properly described by diffusion of electrons within an array of atoms. Actually, this simple model is also known as the *Drude model*, that Drude introduced in 1900 shortly after the discovery of the electron [7, 8].

Another relevant discovery in this context is the observation of errant motion of a flower pollen suspended in water by Brown in 1828 [9]. Due to the collisions with the water molecules, the pollen undergoes a random walk today known as *Brownian motion*. Einstein [10] and Smoluchowski [11] derived a diffusion equation, which predicted the mean squared displacement of the pollen to be proportional to the elapsed time, i. e. $\langle x^2 \rangle \propto Dt$. The predicted proportionality factor, i. e. the *diffusion constant* D, was experimentally verified shortly after [12] and gave strong evidence for the atomic nature of matter. This same experiment, albeit shortly after Boltzmann's death in 1906, also gave an uprise to the phenomenologically derived Boltzmann equation, which – despite its continuous formulation for phase-space densities – strongly relied on a microscopic collision kernel for two particles, as discussed in [13] and Section 2.2.

Nowadays, many urgent and (partially) unsolved questions are reconsidered in the context of ultracold atom experiments. With the help of the available experimental apparatus, one aims at simulating in great detail the transition from microscopic to macroscopic scales while accurately adjusting the interaction between the particles, the effect of external (disorder) potentials and/or sources of noise, cf. [14, 15] and Section 2.1. Additionally, as the transition towards macroscopic scales involves irreversibility, i. e. an increase of entropy, the question arises under which condition and how a certain system reaches (thermal) equilibrium [16].

1.1 ANDERSON LOCALIZATION – DISORDER VS. INTERACTION

An upheaval was created after Anderson [17] published his famous paper on "Absence of diffusion in certain random lattices". He predicted a threshold of disorder strength beyond which the diffusion comes to a halt and eigenstates remain exponentially localized, a situation now called *strong* or *Anderson localization*. To understand this phenomenon one strongly has to rely on the wave nature of the propagating particle. Then, transport of a particle in a certain direction exceeding the localization length is inhibited by totally destructive interference of all amplitudes that determine the propagation. Anderson localization will always occur for one- and two-dimensional infinite disordered systems, but will exhibit a mobility edge in three dimensions [18]. For waves with wave number k, the onset of Anderson localization – as determined by the *Ioffe-Regel criterion* [19] – will occur if $k\ell_{\mathrm{dis}} \leqslant 1$, where ℓ_{dis} is the disorder mean free path, i. e. the average distance between two consecutive scattering events off the disorder potential. Since localization only depends on the wave nature of the particle, it will occur for all types of waves and has experimentally been demonstrated, on the one side, for electromagnetic [20], acoustic [21], and matter waves, in 1D [22, 23] and 3D, for bosons [24] and fermions [25], in real space, and, on the other side, as dynamical localization in energy space, for light-matter interaction [26, 27]. All the real space experiments were explicitly done for non-interacting particles and, for 3D, in the regime of a very strong disorder potential and/or for very low single-particle energies (in agreement with $k\ell_{\mathrm{dis}} \leqslant 1$). The inclusion of inter-particle interaction rather leads to a suppression of Anderson localization [28–30] and, as demonstrated recently, to sub-diffusive behavior in 1D [31]. In 2D and 3D, however, the understanding is still far from complete, see [32–34] and references therein.

1.2 DIFFUSION AND THE WEAK LOCALIZATION CORRECTION

As the Anderson localization regime constitutes a relevant but only small part of the total parameter range, the opposite regime in 3D,[1] i. e. $k\ell_{\mathrm{dis}} \gg 1$, where diffusion essentially dominates over localization, will be in our focus within this thesis. Whereas all previous experimental proofs of diffusion relied on indirect measurements, e. g. conduction measurements in metals, a recent experiment with cold fermions allowed for a direct measurement of the characteristic linear decay of the fermionic density with distance in a disordered channel [36] (as well as the ballistic transport once the disorder potential is switched off).

1 Note that the localization length in 2D can become infinitely long such that diffusion can be studied on finite spatial and short time scales [35].

One has to distinguish two different experimental techniques for measuring diffusive transport. Whereas the fermionic experiment [36] was conducted in a stationary scenario (cf. our setup in Section 3.1), which is mathematically equivalent to a scattering setup (for a sufficiently large reservoir) and leads to a stationary flow of particles through the scattering region, most of the remaining experiments are conducted with initially trapped particles which, upon release from the trap, expand into the pre-set potential landscape as a function of time. Hence, initially high densities (corresponding to stronger interaction) become depleted as the initially confined particle cloud expands from the source, and (presumably) only single-particle dynamics remains [24, 37].

For the latter (time-dependent) scenario *not too far* from thermal equilibrium, different theoretical studies have extended the early results on

the "dirty boson problem" [38, 39] using either classical equations of motion [35] or taking the Hartree-Fock and/or Bogoliubov corrections to the Gross-Pitaevskii equation into account [40, 41], see also the discussion in Section 2.2.

Conversely, the stationary scattering scenario has been extensively studied also on the basis of the Gross-Pitaevskii equation [42–45] by neglecting the non-condensate fraction. Recently, matter wave scattering based on the Hartree-Fock Bogoliubov theory has been suggested [46, 47]. The analysis in [47] revealed that for increasing interaction strength a strong depletion of the condensate sets in, which, in turn, outreaches the regime of validity of this model. Hence, the development of a proper theoretical description far from equilibrium and capable of describing the full transition from a condensate to a non-condensate is in order.

For weak disorder potentials, i. e. $k\ell_{dis} \gg 1$, where the eigenstates are fully extended over the entire potential and Anderson localization is thus prohibited, *weak localization* – a precursor effect of Anderson localization – can occur in time-reversal symmetric media [48]. Despite being only a small correction within this diffusion dominated regime, weak localization induces an important correction due to the wave and/or quantum nature of the propagating quantity. It emerges due to counter-propagating wave amplitudes, whose constructive interference upon ensemble averaging leads • to an enhanced return probability to the origin within the medium, e. g. observed as unexpected magneto-resistance in quasi 2D metal films [49, 50], and • to the prominent effect of coherent backscattering, i. e. an enhancement of the backscattered intensity, outside the medium. This enhancement, first observed for sunlight scattered back from the rings of Saturn [51], has since then been measured for acoustic waves [52], laser light scattered off polystyrene spheres [53] and cold atomic gases [54], and recently also for bosonic matter waves [55, 56].

The maximal backscattering enhancement is only obtained for perfect phase coherence. Multiple dephasing mechanisms due to, e. g. , the random motion of scatterers [57], the internal structure of the scatterers [58], or the nonlinear response of strongly laser driven atoms [59–61] have been considered, theoretically and experimentally, and shown to lead to a suppression of the coherent backscattering interference. Furthermore, the presence of a nonlinearity may also produce an inversion of the backscattering cone [62], e. g. for matter waves in disordered potentials using the Gross-Pitaevskii equation [44]. As the experimental realization with matter waves [55, 56] was just able to confirm the effect for non-interacting (or very weakly interacting) particles [63], an experimental confirmation of the – debatable (as we will see) – Gross-Pitaevskii result for stronger interaction [44] is still missing.

1.3 EQUILIBRATION AND THERMALIZATION

From the early Bose-Einstein condensation experiments one knows that a condensate trapped in the ground state of a harmonic potential is very robust against perturbations and hence well described by the Gross-Pitaevskii equation [64]. This situation dramatically changes for non-equilibrium situations of propagating matter waves, as discussed in Section 2.2 in more detail, and quenched trapping potentials, where the change of the confining potential is very rapid in comparison to all other relevant system time scales. Whereas the latter scenario gave rise to a recent and renewed substantial interest in the underlying physics of how a quenched system adjusts to the

modified environment [16], a comparable transition occurs when a coherent matter wave state, i. e. a condensate, develops a non-condensate (thermal) fraction in a strictly unitary manner fostered by collisions. Whether a certain state equilibrates towards a thermal state remains a question of universal relevance within (quantum) statistical mechanics [65, 66]. One attempt to explain thermalization for a quantum system relies on the concept of *eigenstate thermalization* introduced by Deutsch [67] and Srednicki [68]. For a certain class of systems, i. e. those that allow for a semi-classical description, Srednicki was able to show that a quantum system will thermalize if the classical counterpart is non-integrable and thus shows chaotic dynamics. In other words, the whole classical phase space has to be accessible such that a state of maximal entropy can be reached. Conversely, a quantum version of Newton's cradle constructed out of one-dimensional colliding Bose-Einstein condensates [69] showed no significant signs of thermalization, in partial contrast to a previous conjecture [70] and despite experimental noise, that is expected to foster the thermalization process. The amount of discussion [71–74] recently triggered by the observation of [69] leads to the conclusion that the understanding of the emergence of thermodynamic behavior in quantum systems is not yet fully understood – a point we will come back to within this thesis.

1.4 AIM OF THIS THESIS

As we have demonstrated, transport in disordered environments has been a very relevant topic in many fields of physics for more than two centuries. Many important contributions have been developed in the field of condensed matter theory [2], which now – upon the emergence of ultracold atomic experiments – can be precisely analyzed and verified. However, along with the new experimental possibilities, novel theoretical concepts need to be devised which capture the whole realm of present-day technologies [75] and, more importantly, foster a fundamental understanding of multi-scale transport phenomena.

Within this thesis we aim to contribute to this honorable goal and to develop a diagrammatic theory for the weak localization regime, which, on the one hand, will tackle the relevant questions of thermalization and condensate depletion as introduced above, and, on the other hand, combines the microscopic and macroscopic insights into a unified description. We will try to be as general as possible but, of course, need to make certain assumptions and approximations. For clarity, a full list of all assumptions is included in Appendix A.

In the following *second chapter* we will comment on the presently available technologies in ultracold atomic physics, from which we infer the experimental scattering setup with atomic matter waves that we have in mind. Consequently, we focus on the creation of atomic matter waves and their adjustable parameters first. In a second step, we introduce the full N-body Hamiltonian and summarize existing theoretical models – based on this Hamiltonian – which make contact at different stages with our theory to be developed. We furthermore develop a general N-body diagrammatic scattering theory at the end of the second chapter, as a foundation for our further description of the dynamics within disordered potentials.

The *third chapter* is concerned with the application of the previously developed (and properly ensemble averaged) N-body scattering theory to a weak disorder potential with Gaussian statistics. We here identify all scattering diagrams relevant for diffusive transport of an interacting matter wave in the scattering setup. The diagrams then give rise to an analytically derived, closed integral equation that we solve numerically by iteration. As a final result, we predict how the diffusive flux of particles within the slab – in contrast to existing theories – leads to elastic and inelastic scattering contributions. The inelastic particle flux, which corresponds to a depletion of the population of the single-particle atomic matter wave state, is then monitored while it thermalizes as a function of the collision strength, a process in agreement with the thermalization dynamics touched upon in the introduction.

Within the weak disorder potential, the subtle but important contribution of coherent backscattering will be the focus of the *fourth chapter*. We here identify all leading crossed diagrams that give rise to the coherent correction of the diffusive ladder diagrams discussed in Chapter 3. In a similar manner as before, we can state a closed integral equation that, upon iteration, predicts how the coherent backscattering cone changes under elastic and inelastic collisions, as a function of the interaction strength. It is precisely the inelastic scattering that, in contrast to the result of the Gross-Pitaevskii approach, prevents an inversion of the coherent backscattering cone in the parameter regime under investigation.

A summary of the obtained results is given within the *fifth chapter*. Here, we also discuss how the assumptions and approximations introduced in the previous chapters were, on the one hand, crucial for the present formulation of the theory, but, on the other hand, can be overcome using presently available methods in a future extension of this work.

2 PHYSICS FAR FROM EQUILIBRIUM

In this chapter, we wish to pave the way to our diagrammatic scattering theory to be introduced in the subsequent chapters. Whereas in the previous chapter we tried to motivate why it is insightful to study transport phenomena, we here want to focus on the tools and present-day technologies required to theoretically describe and experimentally verify this out-of-equilibrium problem par excellence.

We start by describing how an atomic matter wave – the entity to be transported – can nowadays be extracted from a Bose-Einstein condensate (BEC) at equilibrium. In consecutive steps we collect all relevant ingredients for our theory, starting from the interaction between the particles and with the random disorder potential, until we spell out the general N-particle Hamiltonian and introduce the N-particle diagrammatic scattering theory.

2.1 FROM A BOSE-EINSTEIN CONDENSATE TO A MATTER WAVE

Upon the theoretical prediction of Bose-Einstein condensation by the groundbreaking work of Bose [76] and Einstein [77] almost 90 years ago, the proof-of-principal of the experimental realizability of Bose-Einstein condensation in dilute gases (closest to the ideal scenario anticipated by Bose and Einstein) was successfully conducted in 1995 [78, 79] and awarded the Nobel Prize in 2001. Prior to this observation, a large tool-box of novel experimental techniques had to devised that nowadays allows for precise and highly controllable setups with ultracold atomic gases up to the point where quantum simulators [80] may be employed to investigate fundamental questions of condensed matter physics [14].

2.1.1 *The Gross-Pitaevskii Equation*

From a mathematical point of view, a Bose-Einstein condensate, i. e. the macroscopic occupation of one single state,[1] corresponds to one macroscopic eigenvalue of order one (compared to all the others of order $1/N$; with N being the total number of particles) of the single-particle density matrix, obtained by integrating over the degrees of freedom of all but one particle, and known as the *Penrose-Onsager criterion* for condensation [82]. For the case of a single occupied mode at zero temperature, and in the thermodynamic limit ($N \to \infty$ with Na_s fixed and a_s being the s-wave scattering length), the condensate can be exactly described by a single-particle state $\psi(\mathbf{r}, t)$, where $\psi(\mathbf{r}, t)$ fulfills the Gross-Pitaevskii equation [83]:

$$i\hbar \frac{\partial}{\partial t}\psi(\mathbf{r}, t) = \left[-\nabla^2 + V(\mathbf{r}, t) + g|\psi(\mathbf{r}, t)|^2\right] \psi(\mathbf{r}, t)\,. \tag{1}$$

$g = 8\pi a_s$ is the two-particle interaction strength in the low energy limit, and $V(\mathbf{r}, t)$ the external (trapping) potential which we treat as a weak disorder potential, later-on in this thesis. Here (for the definition of g) and throughout this thesis, we will use units in which $\hbar^2/2m \equiv 1$. We will further assume the scattering length a_s to be positive hereafter (a positive or a negative value corresponds to repulsive or attractive interaction, re-

1 For the concept of generalized Bose-Einstein condensation we refer the reader to [81].

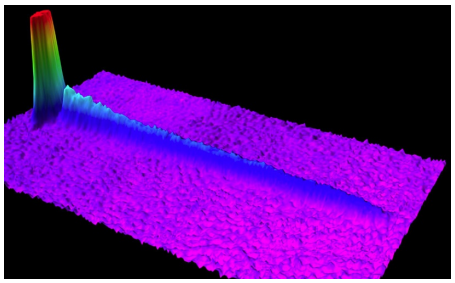

Figure 1: Three dimensional rendering of an Atom Laser beam emitted from a Bose-Einstein condensate. Text and image taken from [91].

spectively [84]). Eq. (1) is essentially a nonlinear Schrödinger equation [85] and $\psi(\mathbf{r}, t)$ is the quantum-mechanical probability amplitude. While this equation has been successfully applied to describe ultracold atom experiments close to equilibrium, see e. g. [64, 86, 87], it is not (or only partially) adequate for systems of finite temperature, stronger interaction and/or far from equilibrium, where many different modes can be occupied with rather large probability.

2.1.2 *The Atom Laser*

Once a coherent state of matter is produced by Bose-Einstein condensation, the availability of a coherent matter wave source opens exciting possibilities, e. g. the generation of coherent beams of matter similar to optical lasers. To this end, let us introduce how an atomic matter wave is extracted from a confined condensate, see Fig. 1. Once a condensate in the ground state of the trapping potential has been produced, one needs to uncouple the atoms from the binding force, e.g., as was done initially [88–90], release them directly to free space, where, however, a rapid change of the particle's de-Broglie wavelength occurs due to acceleration by gravity.

The general aim, however, is to produce a mono-mode atom laser via an isentropic process in a very elongated wave guide, e. g. by using focused, far-detuned, horizontally aligned laser beams as a guide, where possibly only the lowest transverse mode is populated. Furthermore, one wishes to adjust the density and the velocity of the outcoupled atoms as well as to realize a continuous steady state emission by constantly refilling the condensate. This goal, i. e. the transition from the proof-of-principle experiments to the creation of a high-quality, guided and continuos atom laser, has partially been accomplished recently [92–97].

Different possibilities exist to continuously extract condensate atoms. One can either use a weak resonant radio frequency field that transforms the magnetic state of a fraction of the atoms from a trapped to an untrapped state [89, 90] and then confine the untrapped atoms to an additional wave-guide [92]. Another possibility consists in using a so-called *crossed beam optical dipole trap*, essentially two intersecting, focused laser beams, where at the intersection point of the two beams a trapped condensate can be generated. In a next step, the trapping potential of one of the two beams is reduced, either magnetically or optically, in order to allow the atoms to enter the wave-guide defined by the second beam. This method has been reported to allow for a population of 85% of the atoms within the transverse ground state of the second laser beam [94].

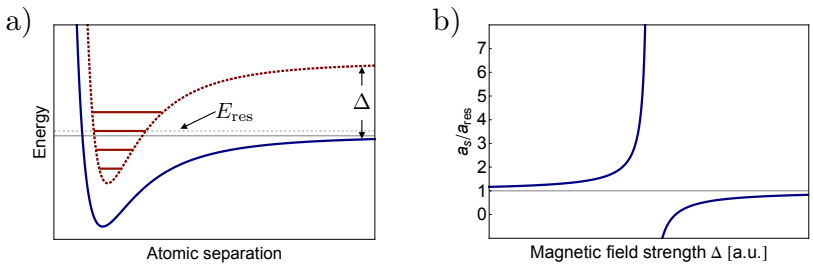

Figure 2: (a) Schematic plot to illustrate how the discrete energy levels E_{res} of the molecular binding potential (red dashed line) can be shifted, via change of the external magnetic field strength Δ, to match a resonance condition with the unbound fragment of atoms ($E \geqslant 0$) scattered into the open channel (blue solid line). Adopted from [110]. (b) Schematic plot of the s-wave scattering length (normalized to the asymptotic scattering length a_{res} far off resonance) in the vicinity of a resonance as depicted in a). The value of a_s can be changed by an order of magnitude when scaling the magnetic field strength properly [103].

Although experimental difficulties remain, cf. [97], recent applications of matter waves as quantum probes [98] open the horizon for matter wave applications in metrology and also for transport studies, as proposed in the present thesis. Microtrap geometries, also known as *atom chips* offer another intriguing possibility of creating and controlling matter waves in a precise manner [99].

2.1.3 *Tuning the Interaction Strength Between the Atoms*

As mentioned before, by adjusting the density of atoms within a matter wave, one certainly has some control over the interaction strength between the particles. As atomic condensates, and consequently matter waves, are very dilute objects, usually characterized by the smallness of the ratio of the s-wave scattering length to the mean particle spacing (defined by the negative third root of the initial particle density), i. e. $\rho_0^{1/3} a_s \ll 1$ [87], it is sufficient to take only pairwise interaction between the atoms into account. Under the assumption of a point-like or contact interaction, the real interaction potential is usually approximated by a properly scaled δ-function, where the scaling parameter g is given in the low-energy limit $k a_s \ll 1$ (tantamount to the s-wave scattering approximation) by $g = 8\pi a_s$, and independent of the particle energy, see eq. (1) above, or the discussion in Appendix B.1, and [100]. This result corresponds to the *Born approximation* and it is obvious that a truncation of the *Born series* after the first term might not be sufficient to describe the relevant physics, cf. Appendix B.1.[2]

Besides an adjustment of the particle density, the powerful tool of *Feshbach resonances* can be used to tune the interaction strength almost at will – from attractive to repulsive [102–105]. Here, the initial objective to produce ideal condensates with vanishing interaction in order to e. g. observe localization effects, see the discussion later in this section and [106], or create condensates out of elements whose interaction is usually attractive [107], gave way to studies involving explicitly (strong) interactions, e. g. to understand the so-called *BEC-BCS-crossover* [108].[3]

The underlying physics of a Feshbach resonance is based on *Zeeman* hyperfine level splitting, where the energy difference of levels with different magnetic moments can be adjusted via an external magnetic field. The res-

2 For example, the second term of the Born series is required to ensure energy conservation via the optical theorem [101].

3 The BCS (Bardeen, Cooper, Schrieffer) side [109] of this theory is given by almost non-interacting fermions forming a superfluid. With increasing interaction the crossover is reached upon which the fermions form bosonic molecules, leading to the formation of a molecular Bose-Einstein condensate.

onance occurs at that point where the total energies ($E \geqslant 0$) of a scattering state (open channel) and a quasi-bound molecular state (closed channel) of the two participating atoms become degenerate, i. e. the two channels become energetically indistinguishable. Although the coupling between these two channels, i. e. the possibility of the two scattering atoms to form a quasi-bound molecular state, is forbidden in a first order expansion in the coupling strength, a second order expansion yields a non-vanishing probability for a metastable bound state of the two atoms to form. This corresponds to an enhancement of the interaction strength between the atoms and the scattering length then exhibits the following resonance-like energy dependence [110]:

$$a_s \sim \frac{C}{E - E_{res}}, \tag{2}$$

where E and E_{res} are the respective total energies of the scattering particles and of the quasi-bound state, see Fig. 2a). And indeed, as depicted in Fig. 2b), over a small range of magnetic field strength the atomic interaction strength can be tuned from barely repulsive to barely attractive, with a strong interaction of closed and open channel in between.

Within this thesis, we make use of this precise adjustability, to propose a scattering scenario where, by precise Feshbach tuning, the matter waves become asymptotically non-interacting and thus the inter-particle interaction is restricted to a finite region in space, which we will model by a slab geometry.

2.1.4 *Atoms in Disordered Potentials*

Disorder is ubiquitous and the hidden origin for diffusive transport on macroscopic scales. It naturally occurs as a random distribution of defects in all sorts of conductors or due to the random positions of atoms in a gas. Whereas ultracold atom experiments were initially motivated by the advertised ability to screen out all sorts of disorder and noise, it nowadays becomes more and more important to introduce well-controlled disorder potentials into experiments [111]. In order to reproduce statistically relevant scenarios for many realizations of a single disorder potential, the potential strength as well as its correlations must be well controllable [112].

Currently, random disorder is created optically by two different means:[4] either by superposition of lattice potentials with incommensurate frequencies, or by random speckle potentials.[5]

The former case is easily implemented by two superimposed standing waves with different intensities and incommensurate frequencies and yields a quasi-random disorder potential with a correlation length approximately given by the wavelength of the strong laser field. The effect of the weak laser field is thus to introduce an inhomogeneous and non-periodic shift of the potential energy at the bottom of the wells [111]. As long as the system size is smaller than the periodicity related to the, of course, experimentally imperfect incommensurability, the assumption of true disorder is fulfilled.

The case of a speckle potential [115, 116] is achieved either by reflection (from a rough surface) or by transmission of a laser beam through a diffusing plate (typically ground glass) which imprints a random phase pattern onto the scattered light, that in turn leads to a random intensity distribution, due to the interference of different scattering paths. The thus obtained

4 A third possibility with strong correspondence to condensed matter physics has been introduced [113] and studied experimentally [114]. Here, atoms of another species trapped at the nodes of an optical lattice with less than unit filling are used as impurities.

5 The former [23] and the latter case [22, 24] have been successfully used to study e. g. Anderson localization.

random pattern of bright (constructive interference) and dark spots (destructive interference) constitutes a single static realization of a disorder potential, and can be characterized by an average grain size with transverse and longitudinal extension (in the far-field) proportional to $\Delta_\perp \sim \lambda_L z/D$ and $\Delta_\parallel \sim \lambda_L (z/D)^2$, respectively [75]. Here, λ_L, D, and z are the corresponding wavelength of the laser field, the diameter of, and the distance perpendicular to the diffusing plate. Upon rotation of e. g. the diffusing plate, a different realization of the disorder potential can be obtained.

Whereas the field amplitudes obey Gaussian statistics, i. e. are fully characterized by their respective mean value and second-order correlation function, the potential (proportional to the light intensity, i. e. to the modulus squared of the field) does not [117]. Using, however, the Gaussian statistics of the field amplitudes, i. e. $\langle \psi(\mathbf{r}) \rangle = 0$ and the dimensionless second-order correlation

$$\gamma(\mathbf{r}) = \frac{\langle \psi^*(\mathbf{r}+\mathbf{r}')\psi(\mathbf{r}') \rangle}{\langle |\psi(\mathbf{r})|^2 \rangle}\,, \tag{3}$$

where $\langle \cdots \rangle$ denotes the ensemble average, one can express all correlations of the disorder potential by products of the field correlation function, eq. (3) [117]. E. g. , the potential pair correlation function is given by:

$$\langle V(\mathbf{r}')V(\mathbf{r}'+\mathbf{r}) \rangle = V_0^2 \left(1 + |\gamma(\mathbf{r})|^2\right)\,. \tag{4}$$

One can rewrite the potential $V(\mathbf{r}) = V_0(1 + \delta V(\mathbf{r}))$, now characterized by its mean value V_0 and its fluctuations $\delta V(\mathbf{r})$, such that the fluctuations, with a vanishing mean $\langle \delta V(\mathbf{r}) \rangle = 0$, obey the following reduced two-point correlation function [117]:

$$\langle \delta V(\mathbf{r}')\delta V(\mathbf{r}'+\mathbf{r}) \rangle = |\gamma(\mathbf{r})|^2\,. \tag{5}$$

$\gamma(\mathbf{r})$, eq. (3), differs for different dimensions and geometries and decays over a characteristic length scale ξ, – the correlation length of the speckle potential – to zero. As we have mentioned above, ξ is usually larger than the laser wavelength, but can be reduced to $\sim \lambda_L$ with the help of sophisticated focusing techniques [118].

In the regime, where the de-Broglie wavelength of the atoms is larger than ξ, the correlations of the speckle potential cannot be resolved and it is justified to replace the speckle statistics by *Gaussian white noise* statistics, i. e.

$$\langle V(\mathbf{r}) \rangle = 0\,, \qquad \langle V(\mathbf{r})V(\mathbf{r}') \rangle = b\delta(\mathbf{r}-\mathbf{r}')\,, \tag{6}$$

where $b = 4\pi/\ell_{dis}$, as we will demonstrate later. To be more precise, the assumption of Gaussian statistics for the (disorder) potential itself explicitly requires the presence of a weak disorder potential [75], where all higher order correlation functions than stated in (6) can be neglected. Note that for the white noise disorder potential scattering is isotropic, i. e. rotationally invariant, and, furthermore, the mean free path ℓ_{dis} is independent of E [48], see eq. (92).

2.2 BEYOND THE GROSS-PITAEVSKII EQUATION

Depending on the field of study, there exist different techniques to accurately describe the physics beyond the validity of the Gross-Pitaevskii equation.

2.2.1 *The Hamiltonian Under Consideration*

Starting point for all these different techniques – and also for the Gross-Pitaevskii equation – is the same N-particle Hamiltonian:

$$\hat{H} = \sum_{n=1}^{N} \left[\hat{H}_0^{(1)}(\mathbf{r}_n) + \hat{V}^{(1)}(\mathbf{r}_n) \right] + \frac{1}{2} \sum_{n,m=1}^{N} \hat{U}^{(2)}(\mathbf{r}_n, \mathbf{r}_m) \,. \tag{7}$$

$\hat{H}_0^{(1)}(\mathbf{r}) = -\Delta$, the kinetic term, and $\hat{V}^{(1)}(\mathbf{r})$, the initially unspecified potential, are single-particle operators. Later in Chapter 3, $\hat{V}^{(1)}(\mathbf{r})$ will be replaced by the random disorder potential, specified in Section 2.1.4, but for now it may as well be an external trapping potential for an atomic gas. As described previously, we consider pairwise interaction between the particles such that $\hat{U}^{(2)}(\mathbf{r}_n, \mathbf{r}_m)$ is a two-particle operator. The factor $1/2$ takes the indistinguishability of bosonic particles into account and thus avoids double-counting. Calculations are most conveniently done in the formulation of *second quantization*:[6]

6 We here follow the discussion in [119].

$$\begin{aligned} \hat{H} &= \int d\mathbf{r}\, \hat{\Psi}^\dagger(\mathbf{r}) \left[\hat{H}_0(\mathbf{r}) + V(\mathbf{r}) \right] \hat{\Psi}(\mathbf{r}) \\ &\quad + \frac{1}{2} \iint d\mathbf{r}\, d\mathbf{r}'\, \hat{\Psi}^\dagger(\mathbf{r}) \hat{\Psi}^\dagger(\mathbf{r}') U(\mathbf{r} - \mathbf{r}') \hat{\Psi}(\mathbf{r}') \hat{\Psi}(\mathbf{r}) \\ &= \hat{H}_0 + \hat{V} + \hat{U} \,, \end{aligned} \tag{8}$$

where we abbreviated the three contributions in the first and second line by the corresponding expressions in the last line, and used the following replacements from (7) to (8):

$$\begin{aligned} \sum_{n=1}^{N} \hat{H}_0^{(1)}(\mathbf{r}_n) &\to \int d\mathbf{r}\, \hat{\Psi}^\dagger(\mathbf{r}) \hat{H}_0(\mathbf{r}) \hat{\Psi}(\mathbf{r}) \,, \\ \sum_{n=1}^{N} \hat{V}^{(1)}(\mathbf{r}_n) &\to \int d\mathbf{r}\, \hat{\Psi}^\dagger(\mathbf{r}) V(\mathbf{r}) \hat{\Psi}(\mathbf{r}) \,, \\ \frac{1}{2} \sum_{n,m=1}^{N} \hat{U}^{(2)}(\mathbf{r}_n, \mathbf{r}_m) &\to \frac{1}{2} \iint d\mathbf{r}\, d\mathbf{r}'\, \hat{\Psi}^\dagger(\mathbf{r}) \hat{\Psi}^\dagger(\mathbf{r}') U(\mathbf{r} - \mathbf{r}') \hat{\Psi}(\mathbf{r}') \hat{\Psi}(\mathbf{r}) \,. \end{aligned} \tag{9}$$

The corresponding single-particle field operators can be expressed in terms of plane waves as

$$\hat{\Psi}^\dagger(\mathbf{r}) = \frac{1}{(2\pi)^3} \int d\mathbf{k}\, e^{-i\mathbf{k}\mathbf{r}} \hat{a}_\mathbf{k}^\dagger \,, \qquad \hat{\Psi}(\mathbf{r}) = \frac{1}{(2\pi)^3} \int d\mathbf{k}\, e^{i\mathbf{k}\mathbf{r}} \hat{a}_\mathbf{k} \,. \tag{10}$$

$\hat{a}_\mathbf{k}^\dagger$ and $\hat{a}_\mathbf{k}$ create and annihilate a single particle with wave vector $\mathbf{k}$ and, according to our units, energy $E = |\mathbf{k}|^2 = k^2$, respectively. In Section 2.3, where the N-particle scattering theory is introduced, the individual contributions of the Hamiltonian (8) will be discussed in more detail.

2.2.2 *The Bogoliubov Approximation to the Underlying Hamiltonian*

The Hamiltonian (8) is the starting point of our analysis of different approaches that can overcome the limitations of the Gross-Pitaevskii equation as discussed in Section 2.1. For further considerations, we conduct the *contact interaction approximation*, as mentioned in the beginning of this

chapter, and replace $U(\mathbf{r}-\mathbf{r}') \to g\delta(\mathbf{r}-\mathbf{r}')$, which thus defines $g = 8\pi a_s$.[7] Eq. (8) thus simplifies to

$$\hat{H} = \int d\mathbf{r}\, \hat{\Psi}^\dagger(\mathbf{r}) \left[\hat{H}_0(\mathbf{r}) + V(\mathbf{r})\right] \hat{\Psi}(\mathbf{r}) + \frac{g}{2} \int d\mathbf{r}\, \hat{\Psi}^\dagger(\mathbf{r})\hat{\Psi}^\dagger(\mathbf{r})\hat{\Psi}(\mathbf{r})\hat{\Psi}(\mathbf{r})\,. \quad (11)$$

7 For a thorough discussion of the validity of this replacement we refer to Appendix B.1 and the literature cited there.

One of the possibilities to account for contributions of other modes beside the condensate mode leads to a separation of the field mode operator (10) into two parts [87],

$$\hat{\Psi}(\mathbf{r}) = \hat{\phi}(\mathbf{r}) + \hat{\delta}(\mathbf{r})\,, \quad (12)$$

where $\hat{\phi}(\mathbf{r})$ and $\hat{\delta}(\mathbf{r})$ describe the condensate and non-condensate mode, respectively.[8] So far, the step (12) merely changes the way we interpret the field operator because the chosen notation hints at the fact that we would like to treat the fraction of non-condensate atoms as a small correction. If this is the case and the number of atoms in the condensate N_0 is much larger than the number of atoms in the non-condensate, i. e. $N_0 \gg N - N_0$, the coherent quantum state of the condensate can be described by a coherent (quasi-classical) state $|\alpha\rangle$, with $\alpha = \sqrt{N_0}e^{i\varphi}$, and a (fixed) classical phase φ. Then, $\hat{\phi}(\mathbf{r}) \to \phi(\mathbf{r})$ can be approximated by a complex function, since the contribution of the commutator $[\hat{a}_0, \hat{a}_0^\dagger]\,|\alpha\rangle = N_0 + 1 - N_0\,|\alpha\rangle = |\alpha\rangle$ can be neglected for $N_0 \gg 1$. The nowadays called *Bogoliubov approximation* [87] thus amounts to replacing $\hat{a}_0 \simeq \sqrt{N_0} \simeq \hat{a}_0^\dagger$ by complex numbers, with the consequence, however, that the total particle number is *not* conserved (under the time evolution generated by the Hamiltonian (11)), see [119] for further details. Hence, eq. (12) can be written as

8 Consequently, the expansion of the field mode operator (10) in terms of plane waves separates into two parts, a single condensate mode, usually $\mathbf{k} = 0$, and the remaining other modes with the condensate mode excluded.

$$\hat{\Psi}(\mathbf{r}) = \phi(\mathbf{r}) + \hat{\delta}(\mathbf{r})\,. \quad (13)$$

The corresponding condensate density then simply reads $\rho_c(\mathbf{r}) = |\phi(\mathbf{r})|^2$ and all the operator dependence is now contained within $\hat{\delta}(\mathbf{r})$, giving rise to the density of the quantum fluctuations of the non-condensate atoms $\rho_{nc}(\mathbf{r}) = \langle\hat{\delta}^\dagger(\mathbf{r})\hat{\delta}(\mathbf{r})\rangle$. The substitution of (13) and its complex conjugate in the Hamiltonian (11) leads to a hierarchy of different Hamiltonians, which – depending on the occurrence of $\phi(\mathbf{r})$ and $\hat{\delta}(\mathbf{r})$ – solely describe the dynamics of the condensate and non-condensate alone as well as all levels of interaction between these two components. The Hamiltonian containing only contributions of the classical field $\phi(\mathbf{r})$

$$H_{GP} = \int d\mathbf{r} \left[\phi^*(\mathbf{r}) \left(\hat{H}_0(\mathbf{r}) + V(\mathbf{r})\right) \phi(\mathbf{r}) + \frac{g}{2}|\phi(\mathbf{r})|^4\right]\,, \quad (14)$$

gives rise to the Gross-Pitaevskii equation via Heisenberg's equation of motion [87], cf. (1).[9]

9 Note that we here assume stationary solutions of the form $\phi(\mathbf{r}, t) = \phi(\mathbf{r})e^{-i\mu t/\hbar}$, with the chemical potential μ.

The remaining Hamiltonians, where one by one the classical field $\phi(\mathbf{r})$ is replaced by the operators $\hat{\delta}(\mathbf{r})$, give rise to well-known corrections of the Gross-Pitaevskii mean-field behavior. For instance does the inclusion of up to two operators $\hat{\delta}(\mathbf{r})$ allow to describe density-density interactions between the condensate and non-condensate, which leads to the so-called Bogoliubov theory and the introduction of *Bogoliubov quasi-particles* [119, 120]. Including all Hamiltonian contributions but replacing – in a mean-field approximation – four-point, i. e. density-density, (and higher order) correlations by products of two-point correlations gives rise to the so-called *Hartree-Fock Bogoliubov* theory [119], which is capable of describing condensate physics close to equilibrium and/or for small finite temperatures $T > 0$, i. e. the separation

and interaction of a condensate and a thermal cloud, as observed in experiments [121, 122], see also references in [64]. The simplest case corresponds to the generalized finite-temperature Gross-Pitaevskii equation, where, in addition to the condensate density, the density of the thermal cloud is taken into account:[10]

$$i\hbar\frac{\partial}{\partial t}\phi(\mathbf{r},t) = \left[-\nabla^2 + V(\mathbf{r}) + g\left(|\phi(\mathbf{r},t)|^2 + 2\rho_{nc}(\mathbf{r},t)\right)\right]\phi(\mathbf{r},t)\,. \tag{15}$$

10 Note the factor of 2 in front of ρ_{nc}, which arises from the contribution of the Hartree and the Fock-term, respectively [119]. We will encounter this factor of 2 in a different context in eq. (110).

In addition to (15), an evolution equation for the non-condensate density $\rho_{nc}(\mathbf{r},t)$ has to be stated in order to solve the coupled equations simultaneously. We will consider such an equation further down.

However, due to the very structure of (15), the number of particles $N_0(t) = \int d\mathbf{r}\,|\phi(\mathbf{r},t)|^2$ inside the condensate remains fixed. (Dynamical) scenarios, where the condensate can grow or shrink as a consequence of collisions, require a treatment beyond the Hartree-Fock approximation and the explicit inclusion of contributions that mimic particle exchange – a situation that is also covered within the next section.

2.2.3 *Quantum Kinetic Gas Theory and the Quantum Boltzmann Equation*

The proper formulation of the dynamics within the thermal cloud is a problem of kinetic gas theory. Many decades ago, Uehling and Uhlenbeck [123] derived a nonlinear quantum Boltzmann equation (today also known as the *Uehling-Uhlenbeck equation*) that describes the evolution of a single particle in time and space due to the presence of potentials, on the one hand, and due to binary collisions with further particles, on the other hand.

Let us mention that the mathematically rigorous derivation of such an equation is of notorious difficulty and has only partially been successful in recent years [124–127], although the general existence of the following equation of Uehling-Uhlenbeck type is generally expected and accepted [5, 13]:

$$\left(\frac{\partial}{\partial t} + \frac{\hbar\mathbf{k}}{m}\cdot\nabla_{\mathbf{r}} - \nabla_{\mathbf{r}}V(\mathbf{r})\cdot\frac{\nabla_{\mathbf{k}}}{\hbar}\right)f(\mathbf{r},\mathbf{k},t) = \left(\frac{\partial f(\mathbf{r},\mathbf{k},t)}{\partial t}\right)_{\text{coll}}, \tag{16}$$

where $f(\mathbf{r},\mathbf{k},t)$ is the single-particle phase space density, i. e. the probability to find a particle with mass m and velocity $\hbar\mathbf{k}/m$[11] at point $\mathbf{r}$ at the time t, and can be determined as the expectation value $f(\mathbf{r},\mathbf{k},t) = \langle\hat{f}(\mathbf{r},\mathbf{k},t)\rangle_{qm}$[12] of the *Wigner operator* [128]

$$\hat{f}(\mathbf{r},\mathbf{k},t) = \int d\mathbf{s}\,\hat{\Psi}^\dagger(\mathbf{r}+\mathbf{s}/2,t)\hat{\Psi}(\mathbf{r}-\mathbf{s}/2,t)e^{i\mathbf{k}\mathbf{s}}\,. \tag{17}$$

11 Remember that in our units $\hbar^2/2m \equiv 1$. The units of $[\hbar] = \sqrt{kg}$, time $[t] = \sqrt{kg}\times\text{meter}^2$, and energy $[E] = \text{meter}^{-2}$ change accordingly.

12 As the notation $\langle\cdots\rangle$ is reserved for ensemble averages, we denote quantum mechanical expectation values by $\langle\cdots\rangle_{qm}$.

Upon integration of $f(\mathbf{r},\mathbf{k},t)$ over $\mathbf{k}$ the particle density (or the density of non-condensate particles $\rho_{nc}(\mathbf{r},t)$ by using $\hat{\delta}(\mathbf{r},t)$ in eq. (17) instead of $\hat{\Psi}(\mathbf{r},t)$, see (12)) is obtained:

$$\int\frac{d\mathbf{k}}{(2\pi)^3}f(\mathbf{r},\mathbf{k},t) = \rho(\mathbf{r},t)\,. \tag{18}$$

Under the assumption of a slowly varying external force $\mathbf{F} = -\nabla_{\mathbf{r}}V(\mathbf{r})$ for which a gradient expansion is applicable [119], the full derivative of $f(\mathbf{r},\mathbf{k},t)$, i. e.

$$\frac{df(\mathbf{r},\mathbf{k},t)}{dt} = \frac{\partial f(\mathbf{r},\mathbf{k},t)}{\partial t} + \frac{\hbar\mathbf{k}}{m}\cdot\nabla_{\mathbf{r}}f(\mathbf{r},\mathbf{k},t) - \nabla_{\mathbf{r}}V(\mathbf{r})\cdot\left(\frac{\nabla_{\mathbf{k}}}{\hbar}f(\mathbf{r},\mathbf{k},t)\right), \tag{19}$$

transforms to the left-hand side of (16). The right-hand side of (16) contains the two-particle interaction, in the here assumed limit of a dilute gas, where the colliding particles are assumed to be uncorrelated, a restriction also known as *molecular chaos* [13],

$$\left(\frac{\partial f(\mathbf{r},\mathbf{k},t)}{\partial t}\right)_{\text{coll}} = \frac{1}{\hbar}\iiint \frac{d\mathbf{k}'\,d\mathbf{k}_1\,d\mathbf{k}_2}{(2\pi)^9}\,\delta(\mathbf{K}_f-\mathbf{K}_i)\,\delta(E_f-E_i)|T_{fi}|^2 \times\left[f(\mathbf{r},\mathbf{k}_2,t)f(\mathbf{r},\mathbf{k}_1,t)-f(\mathbf{r},\mathbf{k}',t)f(\mathbf{r},\mathbf{k},t)\right]. \tag{20}$$

The collision integral ensures momentum (with $\mathbf{K}_f = \mathbf{k}+\mathbf{k}'$ and $\mathbf{K}_i = \mathbf{k}_1+\mathbf{k}_2$) and energy (with $E_f = \mathbf{k}^2+\mathbf{k}'^2$ and $E_i = \mathbf{k}_1^2+\mathbf{k}_2^2$) conservation, and contains the scattering kernel of the microscopic quantum setup within the *T-matrix* T_{fi}. Since this is the only part where the *quantum* nature enters, a pragmatic way to introduce (16) is to derive the classical Boltzmann equation and subsequently replace the scattering kernel by the quantum one [123]. Another procedure of derivation, e. g. followed in [129], relies on an evolution equation for the Wigner transform (17) of the corresponding quantum state, which under certain assumptions (e. g. neglect of correlations) transforms to an equation of type (16).

Adopted to the case of ultracold atoms and building on the fundamental work of Kirkpatrick *et al.* [130, 131], Zaremba, Nikuni, and Griffin derived a set of coupled equations which, on the one hand, is a quantum Boltzmann equation for the evolution of the non-condensate and, on the other hand, a generalized Gross-Pitaevskii equation beyond the Hartree-Fock-Bogoliubov theory (applicable far from equilibrium) for the evolution of the condensate [128]. The evolution of the non-condensate is identical to (16), however, the collision integral now consists of two terms

$$\left(\frac{\partial f(\mathbf{r},\mathbf{k},t)}{\partial t}\right)_{\text{coll}} = C_{12}[f]+C_{22}[f], \tag{21}$$

where $C_{22}[f]$ describes the collision between thermal atoms and $C_{12}[f]$ the exchange of particles between the condensate and thermal cloud due to collisions. For an explicit formula of these two collision terms we refer to [128]. Consequently, the coupling term also appears in the evolution equation of the condensate [119]:

$$i\hbar\frac{\partial}{\partial t}\phi(\mathbf{r},t) = \left[-\nabla^2+V(\mathbf{r})+g\left(|\phi(\mathbf{r},t)|^2+2\rho_{nc}(\mathbf{r},t)\right)-iR(\mathbf{r},t)\right]\phi(\mathbf{r},t), \tag{22}$$

where the additional factor $R(\mathbf{r},t)$, with respect to (15), is defined as:

$$R(\mathbf{r},t) = \frac{\hbar}{|\phi(\mathbf{r},t)|^2}\int\frac{d\mathbf{k}}{(2\pi)^3}\,C_{12}[f(\mathbf{r},\mathbf{k},t)], \tag{23}$$

which ensures the conservation of the total particle number.

In contrast to the rather "bottom-up" approach of [128] in the sense that the starting point is a simple mean-field Hamiltonian, cf. (15), and corrections to the Hamiltonian are added sequentially, a general quantum kinetic theory has been developed which upon necessary approximations reproduces the results of [128] in a "top-down" approach. We will briefly introduce the main ideas of the quantum kinetic theory and also comment on the

method of *non-equilibrium Green's functions* (which is also able to reproduce [128]) before we state what path we decide to follow within this thesis.

In a series of papers by Gardiner and Zoller and co-workers, the concept of a quantum kinetic theory has been introduced [132–138], see also [139]. Whereas [132] generally introduces the main concept (without an external potential), the following papers focus on applications of the theory and simulations of relevant experimental scenarios. Starting point of the theory [132] is again the general Hamiltonian (11). Motivated by concepts from quantum optics, the authors separate the coherent dynamics (consisting of a certain momentum band and to be identified with the condensate dynamics, comparable to the laser mode in quantum optics) from the non-condensate dynamics (comparable to the weakly populated modes within a heat bath in quantum optics), which they model incoherently by a quantum stochastic process. The authors proceed by writing down a quantum kinetic master equation for a certain momentum band, e. g. the condensate component, of the N-particle density matrix by tracing out the remaining bands under the Born-Markov approximation. This very general equation can then – under further assumptions – be applied to different scenarios [132]:

If the initial, full N-body density matrix separates into a band of zero and nonzero momentum, the resulting kinetic master equation transforms into the *condensate master equation*, which – under the replacement (13) – reproduces the Hartree-Fock equation (15) plus additional terms that mimic the collisions and exchange of particles between condensate and non-condensate, equivalent to (22).

In another limit, i. e. for non-condensate dynamics where "molecular chaos" can be assumed and correlations between different particles factorize, the kinetic master equation reduces to the quantum Boltzmann equation (16).

A related quantum kinetic description [140, 141] involving a number-conserving master equation [142] has been developed and the equivalence of the former to the theory of [128], i. e. eqs. (21) and (22), has been established in [143].

The identical result [144] as obtained via the quantum kinetic theory can be more elegantly derived using the method of *non-equilibrium Green's functions* [145, 146], initially developed by Kadanoff and Baym [147] and first applied to Bose gases by Kane [148]. (Compare also [149] for the application of the related *Keldysh-formalism*.)

We hereby finish the brief overview of presently available theories without going into further details. This is due to the fact that all approaches discussed so far – of course motivated by experiments of their time – focus on the situation of a trapped Bose gas and thus allow to study in great detail how a condensate is created in the first place, and how it behaves for finite temperatures and non-equilibrium situations in a trap.

2.2.4 *Relation to Our Setup: Matter Wave Scattering off a Disordered Potential*

As mentioned before, we rather wish to study the case of matter wave transport in a random disorder potential. We hereby want to focus on a stationary scattering setup, far from equilibrium, where all transients have faded out. However, as we will see, the formalism introduced in the previous section lends itself very handy, especially eq. (16), after taking the stationary limit, and accounting for scattering off the random disorder potential on the right-hand side.

Let us motivate our modus operandi with the help of the recent paper by Ernst *et al.* [47]. Within this work, the authors treat an asymptotically non-interacting matter wave, see Section 2.1, which is guided by means of an optical potential towards, and then scattered off a one-dimensional disorder potential. For the theoretical description, they rely on the Hartree-Fock-Bogoliubov theory, which – as discussed above – is valid for a moderate non-condensate population. And in fact, for a small incoming particle current (corresponding to a weak interaction and thus to a rather stable condensate) the authors report a stationary scattering solution. However, for an increased incoming particle current the scattering solution turns permanently time-dependent, and the condensate and non-condensate densities rapidly fluctuate. As conjectured in [47], the lack of a stationary scattering solution is associated with a large fraction of non-condensed atoms, which, in turn, implies the breakdown of the Hartree-Fock-Bogoliubov theory. In other words, in order to describe this scattering behavior more thoroughly, a theoretical description is needed which overcomes the limitations of the Hartree-Fock-Bogoliubov theory, and in particular allows for a realistic description of large non-condensate fractions.

As we have seen, a proper description for the non-condensate part is given by the quantum Boltzmann equation (16) which has to be consistently coupled to an equation for the condensate of Hartree-Fock-Bogoliubov type, see eqs. (21) and (22). Adopted to the setup we have in mind, eqs. (16), (21), and (22) need to be stated in the stationary limit, and under the additional presence of a random disorder potential.

Within this thesis, we will therefore develop an *averaged* (diagrammatic) scattering theory[13] for particles within a disorder potential that goes beyond the description by the Gross-Pitaevskii equation. This theory, in particular, includes collisions that transfer particles out of the condensate.[14] As we will see in Chapter 3, the propagation of a condensate within the disorder potential finally is described by an integral equation, see eq. (123), which is the integral version of the quantum Boltzmann equation (16) for the stationary case, under consideration of an appropriate description of the *average* propagation within the disorder potential.

13 Based on an already available diagrammatic scattering theory for the Gross-Pitaevskii equation [62].

14 As we will see below, collisions that transfer particles back into the condensate can be excluded for the case of a weak (disorder) potential where all modes are continuously distributed and no bound states exist, see the discussion in Section 3.4.2.

However, considerable care needs to be taken when deriving an effective, nonlinear single-particle equation for a microscopic N-particle problem. In order to ensure that our scattering theory will produce a stationary result, we thus start out with the introduction of the – by definition – *linear* diagrammatic N-particle scattering theory, which, as we will show, can be reduced to a nonlinear single-particle theory for the case of a weak disorder potential.

2.3 SCATTERING THEORY FOR N PARTICLES

In the present chapter, we have so far discussed how an atomic matter wave can be used as a quasi-monochromatic particle source to feed a scattering setup. The underlying Hamiltonian was introduced in the previous section. In this section, we introduce the scattering formalism and a diagrammatic representation that allows, in principle, to calculate the N-particle scattering amplitudes.

The fundamental Hamiltonian has the following contributions, cf. (8):

$$\hat{H} = \hat{H}_0 + \hat{V} + \hat{U} \,. \tag{24}$$

The free Hamiltonian is diagonal in momentum space, and takes the following simple form

$$\hat{H}_0 = \frac{1}{(2\pi)^3} \int d\mathbf{k}\, E \hat{a}^\dagger_{\mathbf{k}} \hat{a}_{\mathbf{k}} \,, \tag{25}$$

where $E = k^2$. For the external potential $V(\mathbf{r})$ we obtain

$$\hat{V} = \frac{1}{(2\pi)^6} \iint d\mathbf{k}_1\, d\mathbf{k}_2\, \hat{a}^\dagger_{\mathbf{k}_2} \hat{a}_{\mathbf{k}_1} \langle \mathbf{k}_2 | \hat{V} | \mathbf{k}_1 \rangle \,, \tag{26}$$

with the corresponding matrix elements defined via the Fourier-transform of the disorder potential $V(\mathbf{r})$:

$$\langle \mathbf{k}_2 | \hat{V} | \mathbf{k}_1 \rangle = \int d\mathbf{r}\, V(\mathbf{r}) e^{i(\mathbf{k}_1 - \mathbf{k}_2)\mathbf{r}} \,. \tag{27}$$

As apparent from (25) and (26), those contributions to the Hamiltonian affect only a single particle at a time and allow for a single-particle formulation of the scattering theory.

This picture changes when collisions between particles are included. As discussed above, the large interatomic separation in the dilute medium allows to restrict the interaction to binary collisions. The representation of the interaction contribution in second quantized notation, cf. eqs. (9) and (10), reads:

$$\hat{U} = \frac{1}{2^2 (2\pi)^{12}} \iiiint d\mathbf{k}_1\, d\mathbf{k}_2\, d\mathbf{k}_3\, d\mathbf{k}_4\, \hat{a}^\dagger_{\mathbf{k}_3} \hat{a}^\dagger_{\mathbf{k}_4} \hat{a}_{\mathbf{k}_1} \hat{a}_{\mathbf{k}_2} \langle \mathbf{k}_3, \mathbf{k}_4 | \hat{U} | \mathbf{k}_1, \mathbf{k}_2 \rangle \,, \tag{28}$$

where the factor $1/2^2$ again suppresses double-counting by taking into account the indistinguishability of bosonic particles within the two-particle states, $|\mathbf{k}_1, \mathbf{k}_2\rangle = |\mathbf{k}_2, \mathbf{k}_1\rangle$, and $|\mathbf{k}_3, \mathbf{k}_4\rangle = |\mathbf{k}_4, \mathbf{k}_3\rangle$, respectively. As demonstrated in Appendix B.1, the matrix element of eq. (28) can be expressed in center-of-mass and relative coordinates:

$$\langle \mathbf{k}_3, \mathbf{k}_4 | \hat{U} | \mathbf{k}_1, \mathbf{k}_2 \rangle = (2\pi)^3 \delta(\mathbf{k}_1 + \mathbf{k}_2 - \mathbf{k}_3 - \mathbf{k}_4) \langle \mathbf{k}_{34} | \hat{U}^{(1)} | \mathbf{k}_{12} \rangle \,, \tag{29}$$

where the collision matrix $\hat{U}^{(1)}$ now depends only on the relative momenta, see eq. (280), and the symmetrized single-particle states are defined as:

$$\begin{aligned} |\mathbf{k}_{12}\rangle &= \frac{1}{\sqrt{2}} \left[\left| \frac{\mathbf{k}_1 - \mathbf{k}_2}{2} \right\rangle + \left| \frac{\mathbf{k}_2 - \mathbf{k}_1}{2} \right\rangle \right] , \\ |\mathbf{k}_{34}\rangle &= \frac{1}{\sqrt{2}} \left[\left| \frac{\mathbf{k}_3 - \mathbf{k}_4}{2} \right\rangle + \left| \frac{\mathbf{k}_4 - \mathbf{k}_3}{2} \right\rangle \right] . \end{aligned} \tag{30}$$

The separation (29) can be also obtained for the two-body T-matrix $\hat{T}^{(2)}_U$ with total energy $E_1 + E_2$ and the symmetrized single-particle states (30), upon the introduction of the total and reduced mass, $M = 2m$ and $\mu = m/2$, respectively, see Appendix B.1:

$$\begin{aligned} \langle \mathbf{k}_3, \mathbf{k}_4 | \hat{T}^{(2)}_U (E_1 + E_2) | \mathbf{k}_1, \mathbf{k}_2 \rangle = (2\pi)^3 \delta(\mathbf{k}_1 + \mathbf{k}_2 - \mathbf{k}_3 - \mathbf{k}_4) \\ \times \langle \mathbf{k}_{34} | \hat{T}^{(1)}_U (E_{12}) | \mathbf{k}_{12} \rangle \,. \end{aligned} \tag{31}$$

In contrast to eq. (29), the T-matrix describes the scattering by the atom-atom potential $U(\mathbf{r})$, see eq. (9), as a series of collisions $\hat{U}$ and free propagations $\hat{G}_0(E)$, and thereby includes the repeated effect of virtual collisions between the same pair of particles:

$$\begin{aligned}\langle \mathbf{k}_3, \mathbf{k}_4 | \hat{T}_U^{(2)}(E) | \mathbf{k}_1, \mathbf{k}_2 \rangle = \\ = \langle \mathbf{k}_3, \mathbf{k}_4 | \left[\hat{U} + \hat{U}\hat{G}_0(E)\hat{U} + \hat{U}\hat{G}_0(E)\hat{U}\hat{G}_0(E)\hat{U} + \ldots \right] | \mathbf{k}_1, \mathbf{k}_2 \rangle \, .\end{aligned} \tag{32}$$

Here, the free Green's operator is defined as

$$\hat{G}_0(E) = \frac{1}{E - \hat{H}_0 + i\varepsilon} \, , \tag{33}$$

with infinitesimally small $\varepsilon > 0$, compare to the discussion in Section 3.2. In eq. (31), $\hat{T}_U^{(1)}(E_{12})$ (for which an explicit expression, that will be used later in this thesis, is derived in eq. (287)) denotes the T-matrix for a single particle with mass μ at the energy $E_{12} = E_1 + E_2 - E_{\mathbf{k}_1+\mathbf{k}_2}/2$. The single-particle T-matrix, as a consequence of the unitarity of the scattering process, fulfills the optical theorem [84]:[15]

$$\left[\hat{T}_U^{(1)}(E)\right]^\dagger \left(\hat{G}^\dagger_{0,m/2}(E) - \hat{G}_{0,m/2}(E) \right) \hat{T}_U^{(1)}(E) = \left[\hat{T}_U^{(1)}(E)\right]^\dagger - \hat{T}_U^{(1)}(E) \, , \tag{34}$$

and thus ensures conservation of the particle and the energy flux.

The two-body T-matrix as stated in (32) describes the interaction of two particles in the vacuum. A complete formulation needs to include also the effect of the disorder potential in between collisions and a replacement of $\hat{G}_0(E)$ by the Green's operator $\hat{G}_V(E)$, eq. (55), or, for many realizations of the disorder potential as discussed in Chapter 3, the corresponding average Green's function $\langle G(k') \rangle$, see eq. (84). For our setup in mind though, the use of the vacuum T-matrix is very well justified when the disorder potential is very weak and the range of the interaction potential $U(\mathbf{r})$ is small compared to the disorder mean free path ℓ_{dis}.

For a properly defined scattering scenario one needs to distinguish an asymptotically free initial and final state, and a finite scattering region $\mathcal{V}$ – which will be given by the slab later on – within which the disorder potential and the particle-particle interaction do not vanish.[16] The initial state is formed by N bosons that are all described by the same single-particle wave packet $w(\mathbf{k})$

$$|i_N\rangle = \frac{1}{\sqrt{N!}} \int \frac{d\mathbf{k}_1 \ldots d\mathbf{k}_N}{(2\pi)^{3N}} \, w(\mathbf{k}_1) \ldots w(\mathbf{k}_N) |\mathbf{k}_1, \ldots, \mathbf{k}_N\rangle \, , \tag{35}$$

where the factor $1/\sqrt{N!}$ arises from the indistinguishability of the particles. Each wave packet is normalized such that

$$\int d\mathbf{k} \, |w(\mathbf{k})|^2 = (2\pi)^3 \, . \tag{36}$$

Furthermore, we assume an atom laser scenario where each wave packet is quasi-monochromatic and sharply peaked around the wave vector $\mathbf{k}_L$ with single particle energy $E_L = \mathbf{k}_L^2$. Therefore, the wave packet acquires a very broad spatial extension (around its center located at position $\mathbf{r}$ inside the scattering region), and the particle density

$$\rho_0 = \langle i_N | \hat{\Psi}^\dagger(\mathbf{r}) \hat{\Psi}(\mathbf{r}) \, | i_N \rangle \simeq N \left| \int \frac{d\mathbf{k}}{(2\pi)^3} w(\mathbf{k}) \right|^2 \tag{37}$$

15 Note that, in order for the optical theorem to be fulfilled, not only $\hat{T}_U^{(1)}$, but, accordingly, the free Green's operator $\hat{G}_{0,m/2}(E)$ (unlike the one in definition (33)) have to be stated for particles with mass $\mu = m/2$ and the corresponding dispersion relation $E = 2k^2$.

16 Note that the introduction of a finite interaction region in principle breaks translational invariance, and therefore momentum conservation as expressed by the δ-function in eq. (31) is only approximately true. Since, however, we assume the extension of the scattering region $\mathcal{V}$ in any spatial direction to be much larger than the disorder mean free path ℓ_{dis}, we can safely ignore the associated small width and work with the T-matrix as stated in eq. (31).

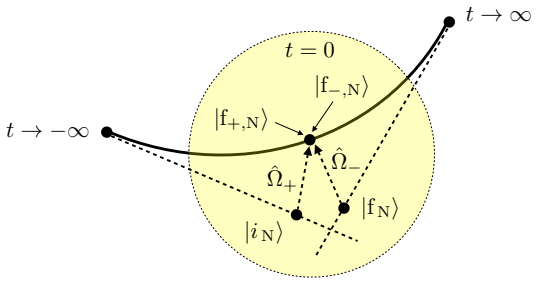

Figure 3: Illustration of the scattering formalism discussed in the main text. At $t \to -\infty$ ($t \to \infty$) the time evolution induced by the full Hamiltonian (solid line) coincides with the free evolution (dashed lines). This allows to define the asymptotically free initial and final states, $|i_N\rangle$ and $|f_N\rangle$, respectively, and the Møller operators $\hat{\Omega}_+$, eq. (39), and $\hat{\Omega}_-$, eq. (40). The state $|f_{+,N}\rangle = \hat{\Omega}_+ |i_N\rangle$ then defines the interacting scattering state reached under the full Hamiltonian evolution at time $t = 0$. As shown in eq. (43), the states $|f_{+,N}\rangle$ and $|f_{-,N}\rangle = \hat{\Omega}_- |f_N\rangle$ are equal for the case that the scattering potential contains no bound states.

turns approximately uniform within $\mathcal{V}$. Since, in this quasi-monochromatic limit, the single-particle density, i. e. ρ_0/N, approaches zero (as the wave packet is spread over an increasingly large region of space), the number of particles N must tend to infinity in order to obtain a finite single-particle density.

If the state $\exp(-i\hat{H}_0 t)\,|i_N\rangle$ is prepared at the asymptotic time $t \to -\infty$, where the action of $\hat{H}$ and $\hat{H}_0$ is indistinguishable (since we assume $\hat{V} = 0$ and $\hat{U} = 0$ outside of $\mathcal{V}$), the center of the wave packet arrives after a subsequent forward-propagation under the full Hamiltonian at the scattering region at time $t = 0$, and a quasi-stationary scattering state

$$|f_{+,N}\rangle = \hat{\Omega}_+ |i_N\rangle \tag{38}$$

at that time is defined via the *Møller operator* [84, 150]

$$\hat{\Omega}_+ = \lim_{t\to-\infty} \left[\hat{U}(t)\right]^\dagger \hat{U}_0(t) = \lim_{t\to-\infty} e^{i\hat{H}t} e^{-i\hat{H}_0 t}\,. \tag{39}$$

We observe that $\hat{\Omega}_+$ is time-independent for a time-independent Hamiltonian. Analogously,

$$\hat{\Omega}_- = \lim_{t\to\infty} \left[\hat{U}(t)\right]^\dagger \hat{U}_0(t) \tag{40}$$

is defined for times $t \to \infty$ such that

$$|f_{-,N}\rangle = \hat{\Omega}_- |f_N\rangle \tag{41}$$

is the corresponding backward propagation of the asymptotic final N-particle scattering state $|f_N\rangle$ – the state which can be detected in a scattering experiment, see also Fig. 3 for an illustration. The combined action of both Møller operators restores the unitarity of the scattering process fully described by the *S-operator*[17]

$$|f_N\rangle = \hat{\Omega}_-^\dagger \hat{\Omega}_+ |i_N\rangle = \hat{S}\,|i_N\rangle\,. \tag{42}$$

For the case that the scattering setup contains no bound states, i. e. that all asymptotically free initial states are transferred to asymptotically free final

17 Here, we defined the S-operator with respect to the eigenstates of the free Hamiltonian. In the literature [150] also the definition $\hat{S} = \hat{\Omega}_+ [\hat{\Omega}_-]^\dagger$ is found which is evaluated with respect to the eigenstates of the full Hamiltonian, that are identical asymptotically.

states, the Møller operators are unitary [84]. As a consequence, eq. (42) can be written as

$$|f_N\rangle = \hat{\Omega}_-^\dagger |f_{+,N}\rangle = \hat{\Omega}_-^\dagger |f_{-,N}\rangle \,, \tag{43}$$

such that $|f_{+,N}\rangle = |f_{-,N}\rangle$. As we will be interested in scattering potentials without bound states in the following, see Chapter 3, we can use the two states $|f_{+,N}\rangle$ and $|f_{-,N}\rangle$ interchangeably. In order to find eq. (43), we used eq. (38) in the first, and eq. (41) together with the unitarity condition $\hat{\Omega}_-^\dagger = \hat{\Omega}_-^{(-1)}$ in the second equality, respectively.

Eq. (42) furthermore demonstrates that the formulation of the scattering theory in terms of the Møller operators or the S-operator is fully equivalent. However, the S-matrix directly maps incoming onto outgoing asymptotically free states. On the contrary, all intermediate information about the scattering process *inside* the scattering region $\mathcal{V}$ is contained within the Møller operators. In the following, we are explicitly interested in the dynamics inside $\mathcal{V}$, e. g. in the stationary density or flux of particles inside the slab. Therefore, we choose to describe our scattering theory rather via the Møller operators than by the S-operator.

The time evolution operator (see eq. (39)) is related to its corresponding Green's operator via

$$\hat{U}(t) = \lim_{\varepsilon \to 0+} \int dE \exp(-iEt)\hat{G}(E)/(-2\pi i) \,, \tag{44}$$

where in analogy to the free Green's operator (33) the Green's operator in the presence of V and U is defined as [84]

$$\begin{aligned} \hat{G}(E) &= \frac{1}{E - \hat{H} + i\varepsilon} = \hat{G}_o(E) + \hat{G}(E)(\hat{V} + \hat{U})\hat{G}_o(E) \\ &= \hat{\Omega}_+(E)\hat{G}_o(E) \,. \end{aligned} \tag{45}$$

The second identity is the Lippmann-Schwinger equation for the Green's operator derived from the operator identity [84]

$$A^{-1} = B^{-1} + B^{-1}(B - A)A^{-1} \,, \tag{46}$$

with $A = E - \hat{H}_0 + i\varepsilon$ and $B = E - \hat{H} + i\varepsilon$. Using (46) with the inverse replacements, i. e. $A = E - \hat{H} + i\varepsilon$ and $B = E - \hat{H}_0 + i\varepsilon$, we obtain

$$\hat{G}(E) = \hat{G}_o(E) + \hat{G}_o(E)(\hat{V} + \hat{U})\hat{G}(E) \,, \tag{47}$$

which is therefore equivalent to the first line of (45). In the second line of (45), we introduced, what we here call, the *modified* Møller operator

$$\hat{\Omega}_+(E) = \mathbb{1} + \hat{G}(E)(\hat{V} + \hat{U}) \,. \tag{48}$$

Note that the modified Møller operator reduces to the Møller operator introduced above once applied to an eigen-state of the free Hamiltonian $|E_0\rangle$ with eigen-energy E_0, i. e.

$$\hat{\Omega}_+(E_0)\,|E_0\rangle = \hat{\Omega}_+ \,|E_0\rangle \,. \tag{49}$$

Since in the following $\hat{\Omega}_+(E_0)$ will only be applied to eigen-states (or the quasi-monochromatic eigen-states alike $|i_N\rangle$ defined in (35)) of $\hat{H}_0$, we will

use the compact terminology of Møller operator for both sides of eq. (49).

The introduction of the Møller operator (48) allows us to write down a Lippmann-Schwinger equation for $\hat{\Omega}_+(E)$[18] by inserting the relation (47) into (48)

18 The same reasoning is true for $\hat{\Omega}_-(E)$.

$$\hat{\Omega}_+(E) = \mathbb{1} + \hat{G}_o(E)\left(\hat{V} + \hat{U}\right)\hat{\Omega}_+(E)\,, \tag{50}$$

which can be iterated in powers of $\hat{V}$ and $\hat{U}$ to yield the following expansion:

$$\hat{\Omega}_+(E) = \hat{\Omega}_+^{(V)}(E) + \hat{G}_V(E)\hat{U}\hat{\Omega}_+^{(V)}(E) + \hat{G}_V(E)\hat{U}\hat{G}_V(E)\hat{U}\hat{\Omega}_+^{(V)}(E) + \dots\,. \tag{51}$$

Here, we summarized all scattering events off the disorder potential within $\hat{\Omega}_+^{(V)}(E)$ and $\hat{G}_V(E)$ that again fulfill a Lippmann-Schwinger equation in analogy to (50) and (47), respectively:

$$\hat{\Omega}_+^{(V)}(E) = \mathbb{1} + \hat{G}_o(E)\hat{V}\hat{\Omega}_+^{(V)}(E)\,, \tag{52}$$

$$\hat{G}_V(E) = \hat{G}_o(E) + \hat{G}_o(E)\hat{V}\hat{G}_V(E)\,, \tag{53}$$

if we define

$$\hat{\Omega}_+^{(V)}(E) = \mathbb{1} + \hat{G}_V(E)\hat{V}\,, \tag{54}$$

and

$$\hat{G}_V(E) = \frac{1}{E - \hat{H}_0 - \hat{V} + i\varepsilon}\,, \tag{55}$$

again with infinitesimally small $\varepsilon > 0$. In analogy to eqs. (45) and (47), the expression

$$\hat{G}_V(E) = \hat{G}_o(E) + \hat{G}_V(E)\hat{V}\hat{G}_o(E) \tag{56}$$

is equivalent to eq. (53). Remember that, according to eq. (28), each operator $\hat{U}$ annihilates and creates two particles. In contrast, the Green's operator $\hat{G}_V$ and the Møller operator $\hat{\Omega}_+^{(V)}(E)$ act now on all N particles. However, since these operators describe non-interacting particles, they can be factorized into single-particle operators. As an example, we give here the factorization formulas for the case $N = 2$:

$$\langle \mathbf{k}_3, \mathbf{k}_4|\hat{\Omega}_+^{(V)}(E_1 + E_2)|\mathbf{k}_1, \mathbf{k}_2\rangle = \tag{57}$$
$$\langle \mathbf{k}_3|\hat{\Omega}_+^{(V)}(E_1)|\mathbf{k}_1\rangle\langle \mathbf{k}_4|\hat{\Omega}_+^{(V)}(E_2)|\mathbf{k}_2\rangle + \langle \mathbf{k}_4|\hat{\Omega}_+^{(V)}(E_1)|\mathbf{k}_1\rangle\langle \mathbf{k}_3|\hat{\Omega}_+^{(V)}(E_2)|\mathbf{k}_2\rangle,$$

and[19]

19 As in (58), all subsequent integrals over energies E will range from $-\infty$ to $+\infty$. For the sake of compactness, we suppress the limits of integration if not stated otherwise.

$$\langle \mathbf{k}_3, \mathbf{k}_4|\hat{G}_V(E)|\mathbf{k}_1, \mathbf{k}_2\rangle = \frac{1}{(-2\pi i)}\int_{-\infty}^{\infty} dE'\,\Big[\langle \mathbf{k}_3|\hat{G}_V(E')|\mathbf{k}_1\rangle$$
$$\times\langle \mathbf{k}_4|\hat{G}_V(E - E')|\mathbf{k}_2\rangle + \langle \mathbf{k}_4|\hat{G}_V(E')|\mathbf{k}_1\rangle\langle \mathbf{k}_3|\hat{G}_V(E - E')|\mathbf{k}_2\rangle\Big]\,. \tag{58}$$

By an iterative application of the same argument, eqs. (52) and (53) are equally valid from N to single particles. As mentioned above, the energy argument of the Møller operator (49) is always fixed to the energy of the state it acts on. In contrast, Green's operators also act on states with different energies. Hence, the energy E of a two-particle Green's operator has to be distributed among two one-particle Green's operators according to

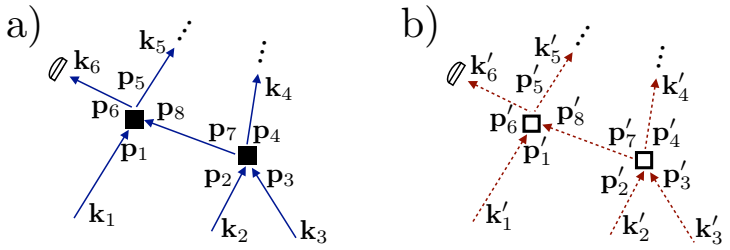

Figure 4: Example of a 3-particle scattering process for the scattering (a) and the complex conjugated scattering amplitude (b). In (a) the initial state $|\mathbf{k}_1, \mathbf{k}_2, \mathbf{k}_3\rangle$ is transferred to the final state $|\mathbf{k}_4, \mathbf{k}_5, \mathbf{k}_6\rangle$ via the intermediate states $\mathbf{p}_1 \cdots \mathbf{p}_8$. The three solid arrows associated with the initial state represent the Møller operator $\hat{\Omega}_+^{(V)}(E_L)$ of the disorder potential, see eq. (52), whereas the remaining solid arrows refer to the disorder Green's operator $\hat{G}_V$, eq. (53). Squares correspond to the two-body T-matrix of the particle-particle interaction, eq. (31). The transition amplitude corresponding to this scattering process is given in eq. (59). The complex conjugated scattering amplitude in (b) is diagrammatically obtained by replacing solid arrows by dashed arrows and solid squares with open squares, i. e. $\hat{G}_V \to [\hat{G}_V]^\dagger, \hat{\Omega}_+^{(V)} \to [\hat{\Omega}_+^{(V)}]^\dagger$, and $\hat{T}_U^{(2)} = [\hat{T}_U^{(2)}]^\dagger$. The primed wave-vectors are introduced to distinguish between both amplitudes. The detector symbol indicates the finally detected particle whereas the dots symbolize the undetected particles that will be traced out, see main text for details.

(58). Note that, due to the indistinguishability of particles, there exist two possibilities to associate the initial $(\mathbf{k}_1, \mathbf{k}_2)$ and final $(\mathbf{k}_3, \mathbf{k}_4)$ particles with each other, which have to be accounted for in eqs. (57) and (58). As it turns out for the case of two particles, however, these permutations are exactly counterbalanced by the factors 1/2 accounting for the indistinguishability in (28).

This factorization procedure can be generalized to $N > 2$ particles, as demonstrated in Appendix B.2, such that one obtains well-defined scattering paths for individual particles between the two-particle collisions $\hat{U}$. As pointed out in eq. (32), we replace two-particle matrix elements of $\hat{U}$ by matrix elements of $\hat{T}_U^{(2)}(E)$ (with appropriately defined two-particle energy E, see below) in (51), and thereby obtain a sequence of collision events between different pairs of particles, since the repeated interaction between the same pair of particles is already included in the T-matrix. As an example, we now treat a three-particle scattering process ($N = 3$), shown in Fig. 4a). In terms of eq. (51), see also Appendix B.2, it can be spelled out as:

$$\begin{aligned}
&\langle \mathbf{k}_4, \mathbf{k}_5, \mathbf{k}_6 | \, \hat{\Omega}_+(3E_L) \, |\mathbf{k}_1, \mathbf{k}_2, \mathbf{k}_3\rangle_{(\text{Fig. 4a})} = \int \frac{dE_4 dE_5}{(-2\pi i)^2} \int \frac{d\mathbf{p}_1 \ldots d\mathbf{p}_8}{(2\pi)^{24}} \\
&\times \langle \mathbf{k}_6 | \hat{G}_V(3E_L - E_4 - E_5) | \mathbf{p}_6 \rangle \langle \mathbf{k}_5 | \hat{G}_V(E_5) | \mathbf{p}_5 \rangle \langle \mathbf{k}_4 | \hat{G}_V(E_4) | \mathbf{p}_4 \rangle \\
&\times \langle \mathbf{p}_5, \mathbf{p}_6 | \hat{T}_U^{(2)}(3E_L - E_4) | \mathbf{p}_1, \mathbf{p}_8 \rangle \langle \mathbf{p}_8 | \hat{G}_V(2E_L - E_4) | \mathbf{p}_7 \rangle \langle \mathbf{p}_4, \mathbf{p}_7 | \hat{T}_U^{(2)}(2E_L) | \mathbf{p}_2, \mathbf{p}_3 \rangle \\
&\times \langle \mathbf{p}_1 | \hat{\Omega}_+^{(V)}(E_L) | \mathbf{k}_1 \rangle \langle \mathbf{p}_2 | \hat{\Omega}_+^{(V)}(E_L) | \mathbf{k}_2 \rangle \langle \mathbf{p}_3 | \hat{\Omega}_+^{(V)}(E_L) | \mathbf{k}_3 \rangle \, , \qquad (59)
\end{aligned}$$

with $E_1 \simeq E_2 \simeq E_3 \simeq E_L$, according to our above assumption of a quasi-monochromatic wave packet.

Eq. (59) must be read in the following way:

• The last line corresponds to all three initially injected particles, which have already been separated, by (57), into single-particle propagators.

• The third line of (59) contains both, collision events, and the single-particle propagation in between both collisions. The right and left collision event in Fig. 4a) correspond to the T-matrix elements $\hat{T}_U^{(2)}(2E_L)$ and $\hat{T}_U^{(2)}(3E_L - E_4)$, respectively. The respective energy arguments of the former and the latter arise because both incoming colliding particles originate directly from the source and because the energy of the incoming particle from the previous collision event is – by energy conservation – fixed to $2E_L - E_4$. Together with the other particle originating from the source, this sums up to $3E_L - E_4$.

• The second line of (59) correspondingly describes the single-particle propagation of the three particles after the collisions, equally factorized already with the help eq. (58).

As mentioned before, the multiplicity of terms arising through the application of eqs. (57) and (58) is compensated for by the prefactors for the collision events, i. e. eq. (28) upon substitution of eq. (31), due to the indistinguishability of the incoming particles. For an additional discussion see Appendix B.2.

From this exemplary calculation of the scattering amplitude we can determine general rules sufficient to construct an arbitrary N-particle scattering amplitude for a given diagram:

1. Apply the Møller operator $\hat{\Omega}_+^{(V)}(E_L)$ eq. (52) for the propagation within the disorder potential to each single-particle state $|\mathbf{k}_1\rangle, \cdots, |\mathbf{k}_N\rangle$. The energy associated with each injected particle is given by E_L.

2. Integrate over all intermediate particles – this corresponds to integrals over all $\mathbf{p}$ wave-vectors in Fig. 4.

3. Write down the corresponding two-body T-matrix element, see (31), for any collision between two particles (denoted by a solid and an empty square in Figs. 4a) and b), respectively). The energy argument of $\hat{T}_U^{(2)}(E)$ is given by the sum of the two incoming single-particle energies.

4. For each $\hat{T}_U^{(2)}(E)$, write down an integral $\int dE/(-2\pi i)$ which determines the energy arguments of the Green's operators $\hat{G}_V(E')$ and $\hat{G}_V(E - E')$, see eq. (58), for the two particles after the collision.

5. These two particles can now again collide with other particles...

The total transition amplitude is then obtained, in principle, by summing the contributions from all possible, different diagrams. How the above rules and the subsequent summation can be applied in practice is our subject in the following chapters.

In eq. (59) we stated the bare full three-particle transition amplitude. Once the complex conjugated diagram, Fig. 4b), which can be calculated identically to (59),

$$\langle \mathbf{k}_1, \mathbf{k}_2, \mathbf{k}_3 | \left[\hat{\Omega}_+(3E_L)\right]^\dagger |\mathbf{k}_4, \mathbf{k}_5, \mathbf{k}_6\rangle_{(\text{Fig. 4b})} = \left[\langle \mathbf{k}_4, \mathbf{k}_5, \mathbf{k}_6 | \hat{\Omega}_+(3E_L) |\mathbf{k}_1, \mathbf{k}_2, \mathbf{k}_3\rangle_{(\text{Fig. 4a})}\right]^*, \tag{60}$$

and a proper single-particle observable is defined, the two transition amplitudes, Fig. 4a) and b), can be joined together and all but one particle can be

traced out. This procedure, already indicated in Fig. 4, will be introduced in the following, where we start out with the detection process of a single particle and deal with the trace over the remaining particles in Section 2.3.1.

With the help of the Møller and the S-operator (eqs. (38), (41), and (42)) we can define a quasi-stationary (at $t = 0$) and an asymptotic ($t = \infty$) scattering state, $|f_{+,N}\rangle$ (or, equivalently, $|f_{-,N}\rangle$, see eq. (43)) and $|f_N\rangle$, respectively. The detector graphically depicted in Fig. 4a) for particle $\mathbf{k}_6$ annihilates one particle with given wave vector. Mathematically, this corresponds to the flux density operator:

$$\hat{\mathbf{J}}(\mathbf{r}) = 2\,\mathrm{Im}\left(\hat{\Psi}^\dagger(\mathbf{r})\nabla\hat{\Psi}(\mathbf{r})\right) = \int \frac{d\mathbf{k}d\mathbf{k}'}{(2\pi)^6}\left(\frac{\mathbf{k}+\mathbf{k}'}{2}\right) e^{-i(\mathbf{k}-\mathbf{k}')\cdot\mathbf{r}}\hat{a}^\dagger_{\mathbf{k}}\hat{a}_{\mathbf{k}'}\,. \quad (61)$$

Since $\hat{\mathbf{J}}(\mathbf{r})$ is a single-particle operator, this implies a partial trace of the density matrix $|f_N\rangle\langle f_N|$ (or equivalently $|f_{+,N}\rangle\langle f_{+,N}|$) over the $N-1$ undetected particles (denoted as dots for particles $\mathbf{k}_4$ and $\mathbf{k}_5$ in Fig. 4a)). The expectation value of the flux density operator thus reads:

$$\begin{aligned}\mathbf{J}(\mathbf{r}) &= \langle f_N|\hat{\mathbf{J}}(\mathbf{r})|f_N\rangle \\ &= \frac{N}{N!}\int \frac{d\mathbf{k}d\mathbf{k}'}{(2\pi)^6}\left(\frac{\mathbf{k}+\mathbf{k}'}{2}\right) e^{-i(\mathbf{k}-\mathbf{k}')\cdot\mathbf{r}} \\ &\times \int \frac{d\mathbf{k}_1\ldots d\mathbf{k}_{N-1}}{(2\pi)^{3(N-1)}}\langle \mathbf{k}_1,\ldots,\mathbf{k}_{N-1},\mathbf{k}'|f_N\rangle\langle f_N|\mathbf{k}_1,\ldots,\mathbf{k}_{N-1},\mathbf{k}\rangle\,.\end{aligned} \quad (62)$$

Again, the factor $1/N!$ arises from the indistinguishability of the bosonic particles. It turns out, however, that this factor – together with the factors $1/\sqrt{N!}$ in eq. (35) – is exactly counterbalanced once we sum the amplitudes of all processes where the initial and/or final particles are exchanged. In total, we get the same result as if the particles were distinguishable. This equivalence is generally valid if all particles are prepared in the same initial state, and if the Hamiltonian is symmetric under exchange of particles [151].

2.3.1 *Trace Over Undetected Particles*

As already stated in eq. (62), a trace over all but one particle is required to obtain the single-particle flux density. We will now deal with the general tracing procedure, mathematically and diagrammatically.

In order to conduct the trace, cf. (62), one has to join a diagram $|f_{+,N}\rangle$ and a complex conjugate diagram $\langle f_{+,N}|$ in such a way that the detected amplitudes and the traced-out amplitudes are grouped together, taking into account all different possibilities. For Fig. 4 this corresponds to joining either the arrows with final state $\mathbf{k}_4$ to $\mathbf{k}'_4$ and $\mathbf{k}_5$ to $\mathbf{k}'_5$ or $\mathbf{k}_4$ to $\mathbf{k}'_5$ and $\mathbf{k}_5$ to $\mathbf{k}'_4$ if we decide to detect particles $\mathbf{k}_6$ and $\mathbf{k}'_6$, as depicted in Fig. 4. However, we could as well choose to detect another combination leading to further combinatorics.

For the case of two particles, the tracing procedure becomes more evident and is thus depicted in Fig. 5. Two situations have to be distinguished for this purpose. For the first, depicted in Fig. 5a), both amplitudes have undergone a collision event resulting in a reshuffling of the single-particle energies according to eq. (58), a process that we call *inelastic*. In contrast, an *elastic* scattering contribution occurs if only one of the diagrams contains a collision event and thus – due to energy conservation – the single-particle energies must remain conserved, Fig. 5b).

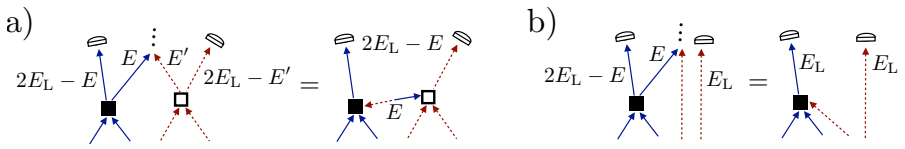

Figure 5: Illustration of the tracing formalism for the case of two particles introduced in the main text. (Blue) solid and (red) dashed arrows stand for $|f_{+,2}\rangle$ and $\langle f_{+,2}|$, respectively. The traced and detected particles are denoted by dots and a detector symbol as in Fig. 4, respectively. (a) For the case of inelastic scattering, the trace formula (63) can be used to transform the left diagram to the right diagram. The trace thus corresponds to a direct connection of the two collision events by the spectral function $\left[\hat{G}_V^\dagger(E) - \hat{G}_V(E)\right]/i$ (dashed-solid arrow pointing in different directions). The energy of the detected particle is, correspondingly, $2E_L - E$. (b) For the case of elastic scattering, the left and right diagram are connected via the trace formula (65). Since the (red) dashed arrows have not undergone a collision, the energy of the detected and traced-out particle must equal E_L, due to energy conservation. As we will see later in Chapter 3, this diagram equally occurs within a diagrammatic representation of the Gross-Pitaevskii equation.

The trace formula involving *inelastic collisions*, see Fig. 5a), can be summarized by the following expression:

$$\begin{aligned}\iint \frac{dE\,dE'}{|2\pi i|^2} \int \frac{d\mathbf{k}}{(2\pi)^3} (\dots)_{(-E')} \hat{G}_V^\dagger(E')|\mathbf{k}\rangle\langle\mathbf{k}|\hat{G}_V(E)(\dots)_{(-E)} \\ = \int \frac{dE}{2\pi i} (\dots)_{(-E)} \left(\hat{G}_V^\dagger(E) - \hat{G}_V(E)\right) (\dots)_{(-E)}\,, \end{aligned} \tag{63}$$

where we respectively summarized the remainder of the diagram and the conjugated diagram by $(\dots)_{(-E)}$ and $(\dots)_{(-E')}$, which themselves depend on the corresponding energies E and E', however, with a *negative* prefactor. The integrals over $\int dE/(-2\pi i)$ and $\int dE'/(2\pi i)$ come along with each collision event for each amplitude, according to the rules defined above, and respectively determine the energy of the undetected particle, E and E', as well as that of the detected particle, $2E_L - E$ and $2E_L - E'$, by energy conservation. Once the full expression for the left diagram in Fig. 5a) – given in Appendix B.3 – is factorized into single particle propagations and two-body collision events, see eqs. (57) and (58), the trace over the final single-particle state $\mathbf{k}$ with the corresponding single-particle propagators $\hat{G}_V^\dagger(E')$ and $\hat{G}_V(E)$ can be conducted independently. This is due to the fact that $(\dots)_{(-E)}$ and $(\dots)_{(-E')}$ are complex analytic functions with respective energy $2E_L - E$ and $2E_L - E'$, where the minus sign in front of E and E' shifts the corresponding poles of the respective constituents $\hat{G}_V(E)$ and $\hat{T}_U^{(2)}(E)$ as well as $\hat{G}_V^\dagger(E')$ and $[\hat{T}_U^{(2)}(E')]^\dagger$ to the opposite half space of the complex plane. One can thus choose the contour such that only the poles of $\hat{G}_V(E)$ and $\hat{G}_V^\dagger(E')$ in the respective *upper* half and *lower* half of the complex plane contribute.

By removing the identity

$$\int \frac{d\mathbf{k}}{(2\pi)^3} |\mathbf{k}\rangle\langle\mathbf{k}| = \mathbb{1}\,, \tag{64}$$

and after application of the identity $\hat{G}_V^\dagger(E')\hat{G}_V(E) = (\hat{G}_V^\dagger(E') - \hat{G}_V(E))/(E - E' + i\varepsilon)$, see eq. (304), one can integrate the term proportional to $\hat{G}_V^\dagger(E')$

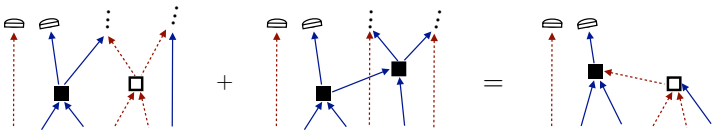

Figure 6: Extension of the diagram shown in Fig. 5b). Here, elastic scattering occurs with an undetected particle, which, however, originates from a previous elastic collision event. Addition of the diagrams on the left reproduces again a Gross-Pitaevskii equation diagram, i. e. described by an elastic non-linear equation for a single particle, cf. the discussion in Chapter 3.

and to $\hat{G}_V(E)$ over E and E', respectively. In both cases the two energies E and E' become equal (since only a single pole at $E = E' - i\varepsilon$ and $E' = E + i\varepsilon$ remains in the respective lower and upper half of the complex plane, see Appendix B.4) and we obtain the contribution $[\hat{G}_V^\dagger(E) - \hat{G}_V(E)]/i$ (also known as the *spectral function* since the imaginary part of the Green's function determines the density of states [48]). Diagrammatically, as depicted in Fig. 5a), this corresponds to a solid-dashed arrow directly connecting the collision events of each diagram.

The formula (63) does not only apply to the situation discussed but also to all inelastic scattering diagrams that we will encounter in the following. Its general validity is proven in Appendix B.4.

For an *elastic collision*, where one of the amplitudes has not undergone a previous collision, see Fig. 5b), we find, in a similar manner as in the previous discussion, the following trace formula:

$$\int \frac{dE}{2\pi i} \int \frac{d\mathbf{k}}{(2\pi)^3} \langle \mathbf{k}_L | \left[\hat{\Omega}_+^{(V)}(E_L)\right]^\dagger |\mathbf{k}\rangle\langle\mathbf{k}|\hat{G}_V(E)\big(\dots\big)_{(-E)}$$
$$= \langle \mathbf{k}_L | \left[\hat{\Omega}_+^{(V)}(E_L)\right]^\dagger \big(\dots\big)_{(-E_L)} . \tag{65}$$

The conjugate of relation (65) takes effect if the energy of the amplitude represented by solid arrows is fixed. The consequence of relation (65), which is also proven in Appendix B.4, is a direct connection of the dashed amplitude to the collision event, i. e. a contribution $\propto |\psi(\mathbf{r})|^2\psi(\mathbf{r})$ corresponding to the two solid and the single dashed arrow incident on the solid square in the rightmost diagram in Fig. 5. Hence, this two-particle amplitude is reduced to a scenario which can be described by a non-linear single-particle equation, which we will identity as the Gross-Pitaevskii equation, see eq. (1) and Chapter 3.

In expression (65) the dashed amplitude originates directly from the source state $\langle \mathbf{k}_L|$ and is propagated through the disorder potential by $[\hat{\Omega}_+^{(V)}(E_L)]^\dagger$. This expression, however, can be generalized to the case where the dashed amplitude originates from another collision event, an example of which is depicted in Fig. 6. Thereby, we again obtain an elastic non-linear diagrammatic contribution which can be equivalently obtained via the Gross-Pitaevskii equation, see Chapter 3 or [62].

In a similar manner, the inelastic diagrams can be generalized to the case where the undetected particle undergoes further collisions with other particles before the trace is performed. Here, it is however crucial that these collisions occur with particles that have not interacted with the detected particle before. Since this restriction, i. e. neglect of recurrent scattering, is

naturally realized in a weak disorder potential, we delay this discussion to Chapter 3. We note, however, that the neglect of recurrent scattering will allow us to trace out the undetected particle immediately after the collision with the detected particle, a tremendous simplification, as we will discuss further down.

2.4 SUMMARY

With this chapter we have laid the methodological foundation of this thesis, a scattering theory for a matter wave of interacting particles within a disorder potential. As we discussed, this requires asymptotically unperturbed states, which can be achieved by precise adjustment of the inter-particle interaction (via Feshbach resonances) and by spatially delimited disorder potentials (e. g. via focused speckle potentials). From the theoretical side, however, an insufficiency remained: an easily applicable technical tool that is able to treat far from equilibrium physics under inclusion of random disorder potentials. We therefore introduced a general, diagrammatic N-body scattering theory above, that we will adopt in the following chapter to describe the average interacting many-body transport in weak disorder potentials.

3 DIFFUSIVE TRANSPORT

Within the following chapter we will apply the N-particle scattering theory presented in Chapter 2 to the case of bosonic matter wave transport within a weakly disordered potential. To do so, we consider a three-dimensional slab geometry with the disorder potential confined to the region inside the slab. At first, we restrict our analysis to a linear transport theory that describes the propagation of non-interacting particles in a weakly disordered environment. Upon averaging the linear transport over many realizations of the disorder potential, we will be able to introduce the so-called *ladder diagrams* or *diffusons*, which, as their names state, describe classical diffusion within the slab geometry considered.

Equipped with this background, we introduce particle-particle collisions into our description that lead to more sophisticated diagrams. Nonetheless, we are able to efficiently reduce the many-body character of the underlying equations and to derive a nonlinear transport equation for the propagation of single particles in the slab. This equation accounts for inelastic scattering processes which lead to what is colloquially called *condensate depletion*. Our theory thus provides a microscopic description which goes beyond the celebrated Gross-Pitaevskii equation, in terms of the interaction-induced nonlinearity.

Finally, we link our theory to recent progress in the derivation of a nonlinear (quantum) Boltzmann equation. We show that the justification for certain assumptions of rigorous derivations of such an equation can be elegantly stated, due to the presence of the weak disorder potential.

3.1 THE SLAB GEOMETRY

The setup for which we develop our diagrammatic theory is given by a three-dimensional medium bounded by parallel planes, and graphically depicted in Fig. 7. Hence, the extension in the direction parallel to the planes, here called x and y, is infinite. The distance L between the two planes, usually expressed as the *optical thickness* $b = L/\ell_{\mathrm{dis}}$, i.e. L in units of the disorder mean free path ℓ_{dis}, see eq. (92) below, is measured along the normal component z. This geometry is rotationally-symmetric with respect to the z-axis, and allows us to separate the problem into solutions in the two-dimensional $x-y$-plane, and along the z-axis [48], respectively. We formulate our problem as that of a plane wave incident on and/or scattered back from the slab, which can be described using only two parameters, the position on the z-axis, i. e. the penetration depth into the slab, and the angle of incidence/emergence θ with respect to the z-axis.

We focus on the case of perpendicular incidence, and hence choose our coordinate system such that

$$\mathbf{k}_{\mathrm{in}} = \begin{pmatrix} 0 \\ 0 \\ k_L \end{pmatrix}, \quad \mathbf{k}_{\mathrm{out}} = \begin{pmatrix} k_D \sin\theta' \\ 0 \\ k_D \cos\theta' \end{pmatrix}, \quad \mathbf{q} = \mathbf{k}_{\mathrm{in}} + \mathbf{k}_{\mathrm{out}} = \begin{pmatrix} k_D \sin\theta \\ 0 \\ k_L - k_D \cos\theta \end{pmatrix},$$

with the backscattering angle $\theta = \pi - \theta'$. We further assume that the refractive index of the medium within the slab is comparable to the one in

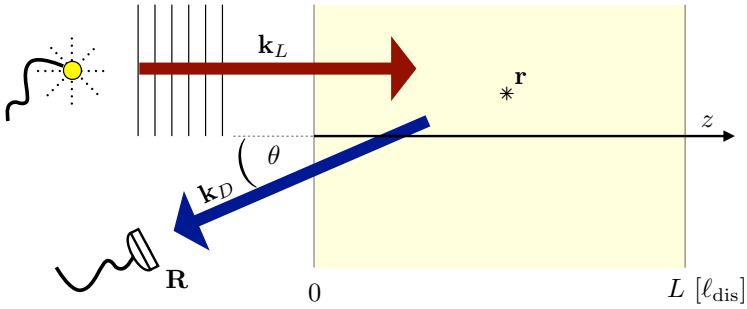

Figure 7: Schematic representation of the slab geometry considered within this thesis. We consider a plane wave with wave vector $\mathbf{k}_L$ and energy $E_L = k_L^2$ incident on a three-dimensional slab with thickness L. The emitted intensity with wave vector $\mathbf{k}_D$ and energy $E_D = k_D^2$ is detected under an angle θ in the far field of the slab, by a detector at position $\mathbf{R}$. As an ultimate goal of this thesis, we wish to quantitatively describe scattering phenomena which can occur for a bosonic matter beam incident on a weakly disordered potential within the slab, under inclusion of particle-particle interaction. The dynamics inside the slab and the detection in the far field of the slab is in the focus of Chapter 3 and Chapter 4, respectively.

the vacuum surrounding the slab, such that boundary effects of the in- and outgoing waves can be neglected.[1]

1 This again is in agreement with our all-underlying assumption of a weak disorder potential, where the total single-particle energy approximately equals its kinetic energy and the energy contribution of the disorder potential can be neglected.

3.2 LINEAR TRANSPORT THEORY

Within this section we wish to elucidate under which circumstances the Schrödinger equation for a single quantum particle is transformed to a classical equation which describes diffusive transport within a disordered sample, on macroscopic scales.[2] All coherent effects due to the wave nature of the quantum particle become small in a suitable limit which we define in the following. The foundation of our subsequent analysis is the time-independent general Hamiltonian eq. (7) reduced to contain only the single-particle contribution[3]

$$\hat{H} = -\Delta + \hat{V}(\mathbf{r})\,, \tag{66}$$

which generates the stationary Schrödinger equation,

$$-\Delta\psi(\mathbf{r}) + V(\mathbf{r})\psi(\mathbf{r}) = k^2\psi(\mathbf{r})\,, \tag{67}$$

with $k^2 = E$. For $V(\mathbf{r}) \to k^2 V(\mathbf{r})$ and $k = \omega/c$ instead of $k = \sqrt{E}$, this equation is known as the *stationary Helmholtz equation*, where $\psi(\mathbf{r})$ is now e. g. the amplitude of a scalar electromagnetic or acoustic field, instead of the quantum mechanical probability amplitude.
More generally, in the presence of an arbitrary distribution of sources $j_E(\mathbf{r})$ with energy E (cf. $j(\mathbf{r},t) = j_E(\mathbf{r})e^{iEt/\hbar}$), eq. (67) transforms to

$$\left(\Delta + k^2 - V(\mathbf{r})\right)\psi(\mathbf{r}) = j_E(\mathbf{r})\,, \tag{68}$$

for which a solution can be found via the Green's function[4] of the differential operator

$$\left(\Delta + k^2 - V(\mathbf{r})\right)G_E(\mathbf{r},\mathbf{r}') = \delta(\mathbf{r}-\mathbf{r}')\,. \tag{69}$$

2 For the derivation of the linear transport theory we follow the presentation in [48, 152, 153].

3 This entire section is concerned with linear transport theory, i. e. represented by single-particle operators.

4 Here, we spell out the full notation $G_E(\mathbf{k})$, the function with wave vector $\mathbf{k}$ at the energy E (or, accordingly, in real space $G_E(\mathbf{r})$). We will avoid the subscript indicating the energy in the following if not needed explicitly, e. g. for the case of linear transport where the energy remains fixed throughout the scattering process.

Remember that by virtue of eq. (58) all N-particle Green's functions can be decomposed into single-particle operators such that a single-particle expression can always be found.

A general solution for $\psi(\mathbf{r})$ in (68) for outgoing boundary conditions, i. e. $G(\mathbf{r}, \mathbf{r}')$ being the retarded Green's function, is obtained via

$$\psi(\mathbf{r}) = \int d\mathbf{r}' \, G(\mathbf{r}, \mathbf{r}') j(\mathbf{r}') \,. \tag{70}$$

3.2.1 *The Wave Equation and the Free Green's Function*

We first focus on the solution of (69) for the case of a particle in the vacuum without an additional potential, i. e. $V = 0$,

$$\left(\Delta + k^2\right) G_0(\mathbf{r} - \mathbf{r}') = \delta(\mathbf{r} - \mathbf{r}') \,, \tag{71}$$

which amounts to a wave created by a point source at point $\mathbf{r}'$ and propagated to point $\mathbf{r}$ by the *free Green's function* $G_0(\mathbf{r} - \mathbf{r}')$.

The solution of the free Green's function can be obtained by Fourier transformation to momentum space, such that eq. (71) reads:

$$G_0(\mathbf{k}') = \frac{1}{k^2 - k'^2 + i\varepsilon} \,, \tag{72}$$

where the infinitesimal $\varepsilon > 0$ is needed for convergence of the integrals. A subsequent back transformation to real space and integration using residual calculus leads to

$$G_0(\mathbf{r} - \mathbf{r}') = -\frac{e^{ik|\mathbf{r}-\mathbf{r}'|}}{4\pi|\mathbf{r} - \mathbf{r}'|} \,, \tag{73}$$

an outgoing spherical wave from the source at $\mathbf{r}'$.

3.2.2 *The Average Green's Function*

Reintroducing now the potential $V(\mathbf{r})$ into our calculations, we rewrite (69) in the integral form of a Lippmann-Schwinger equation:

$$G(\mathbf{r}, \mathbf{r}') = G_0(\mathbf{r} - \mathbf{r}') - \int d\mathbf{r}'' \, G_0(\mathbf{r} - \mathbf{r}'') V(\mathbf{r}'') G(\mathbf{r}'', \mathbf{r}') \,. \tag{74}$$

Application of the differential operator $\Delta + k^2$ to both sides of the above equation reproduces the original equation (69).
Equivalently, eq. (74) can be rewritten iteratively as a perturbative expansion in the disorder potential V, leading to the *Born series*

$$\begin{aligned} G(\mathbf{r}, \mathbf{r}') = {} & G_0(\mathbf{r} - \mathbf{r}') - \int d\mathbf{r}'' \, G_0(\mathbf{r} - \mathbf{r}'') V(\mathbf{r}'') G_0(\mathbf{r}'' - \mathbf{r}') \\ & + \iint d\mathbf{r}'' \, d\mathbf{r}''' \, G_0(\mathbf{r} - \mathbf{r}'') V(\mathbf{r}'') G_0(\mathbf{r}'' - \mathbf{r}''') V(\mathbf{r}''') G_0(\mathbf{r}''' - \mathbf{r}') \\ & + \cdots \,. \end{aligned} \tag{75}$$

The physical interpretation thereof is a superposition of waves which either do not scatter at all, scatter once, twice, $\cdots$, or n-times off the potential V on their way from $\mathbf{r}'$ to $\mathbf{r}$. In a next step, we replace the arbitrary potential

V by a disorder potential with Gaussian statistics as introduced earlier, cf. Section 2.1.4:

$$\langle V(\mathbf{r})\rangle = 0\,, \qquad \langle V(\mathbf{r})V(\mathbf{r}')\rangle = B(\mathbf{r}-\mathbf{r}')\,. \tag{76}$$

We can now integrate over all possible realizations of the disorder, to gain an understanding of how a wave propagates *on average* within this potential landscape. In other words, we obtain an equation for the average Green's function, the so-called *Dyson equation* [48]:

$$\langle G(\mathbf{r},\mathbf{r}')\rangle = G_0(\mathbf{r}-\mathbf{r}') - \iint \mathrm{d}\mathbf{r}''\,\mathrm{d}\mathbf{r}'''\, G_0(\mathbf{r}-\mathbf{r}'')\Sigma(\mathbf{r}'',\mathbf{r}''')\langle G(\mathbf{r}''',\mathbf{r}')\rangle\,. \tag{77}$$

The $\langle\cdots\rangle$ denotes the average over different realizations of the disorder potential, and $\Sigma(\mathbf{r},\mathbf{r}')$, whose importance is discussed in the following, is the *self-energy* which contains all the information about the scattering contributions after the disorder average. Under the assumption of an infinite medium (i. e. boundaries sufficiently far away),[5] the latter restores translational invariance and we obtain

$$\langle G(\mathbf{r},\mathbf{r}')\rangle = \langle G(\mathbf{r}-\mathbf{r}')\rangle\,, \qquad \Sigma(\mathbf{r},\mathbf{r}') = \Sigma(\mathbf{r}-\mathbf{r}')\,. \tag{78}$$

5 For points within the slab for which $zk \gg 1$ and $|L-z|k \gg 1$, respectively, the assumption of an infinite medium is approximately fulfilled [153, 154]. See also the discussion before eq. (35) regarding the assumption of translational invariance in our setup.

As translational invariance implies conservation of momentum, the Fourier transforms of the average Green's function and of the self-energy read

$$\langle G(\mathbf{k}',\mathbf{k}'')\rangle = (2\pi)^3\delta(\mathbf{k}'-\mathbf{k}'')\langle G(\mathbf{k}')\rangle\,, \quad \Sigma(\mathbf{k}',\mathbf{k}'') = (2\pi)^3\delta(\mathbf{k}'-\mathbf{k}'')\Sigma(\mathbf{k}')\,, \tag{79}$$

and Dyson's equation (77) in momentum space simply reads

$$\langle G(\mathbf{k}')\rangle = G_0(\mathbf{k}') + G_0(\mathbf{k}')\Sigma(\mathbf{k}')\langle G(\mathbf{k}')\rangle\,. \tag{80}$$

A solution for the average Green's function can now be expressed in terms of the vacuum Green's function (72) and of the self-energy,

$$\langle G(\mathbf{k}')\rangle = \frac{1}{k^2 - k'^2 - \Sigma(\mathbf{k}')}\,, \tag{81}$$

which simplifies, due to the rotational invariance[6] of our setup, to

$$\langle G(k')\rangle = \frac{1}{k^2 - k'^2 - \Sigma(k')}\,. \tag{82}$$

6 Remember that the rotational invariance results as a consequence of the Gaussian white noise statistics of the disorder potential, see Section 2.1.4.

The difference between (72) and (82) is the contribution of the self-energy that vanishes for a vanishing potential V. Hence, if we assume a sufficiently weak disorder potential, what, by virtue of (82), is characterized by $|\Sigma(k')| \ll k^2$, and only a weak dependence on momentum, we may replace $\Sigma(k') \to \Sigma(k)$ and define

$$\widetilde{k} = \sqrt{k^2 - \Sigma(k)} \approx k - \frac{\Sigma(k)}{2k}\,. \tag{83}$$

Hence, (82) simplifies to

$$\langle G(k')\rangle = \frac{1}{\widetilde{k}^2 - k'^2}\,. \tag{84}$$

In the scattering language the self-energy is the sum of all scattering paths (undergoing a certain sequence of disorder scattering events) which are *irreducible*. A path is called irreducible if all disorder scattering events for

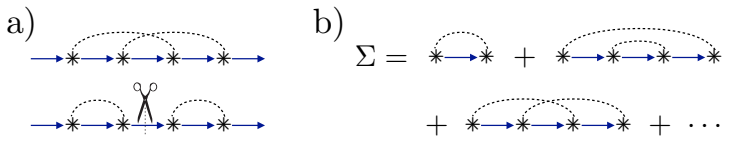

Figure 8: The disorder scattering events (✳) along a certain scattering path ((blue) solid arrows) are pairwise correlated with each other upon averaging over the random disorder potential (cf. (76)), leading, e. g. , in (a) to an irreducible (top), and to a reducible diagram (bottom). (b) The self-energy consists of all irreducible diagrams, where here all contributions of eq. (86) are indicated. Note that the free Green's functions ((blue) solid arrows) prior to the first and after the last disorder scattering event in (a) are not part of the self-energy. Parts of the graphics are taken from [155].

this scattering path are correlated with each other in such a way that the path cannot be cut into two pieces without cutting a correlation between two disorder scattering events, see Fig. 8a). By an iterative argument it can be shown that inserting the sum of all irreducible diagrams, i. e. the self-energy, into the Dyson equation (77) reproduces all possible scattering paths and thus the full averaged Born series [48].

In our case, due to the Gaussian statistics[7] of the disorder potential, only those scattering paths with pairwise correlations between the disorder scattering events contribute to the self-energy (odd orders vanish due to $\langle V(\mathbf{r})\rangle = 0$ and even n-point correlations reduce to pairwise correlations). E.g., a four-point correlation function thus simplifies to a sum of products of two-point correlations:

$$\begin{aligned}\langle V(\mathbf{r}_1)V(\mathbf{r}_2)V(\mathbf{r}_3)V(\mathbf{r}_4)\rangle = {}& \langle V(\mathbf{r}_1)V(\mathbf{r}_2)\rangle\langle V(\mathbf{r}_3)V(\mathbf{r}_4)\rangle \\ &+ \langle V(\mathbf{r}_1)V(\mathbf{r}_4)\rangle\langle V(\mathbf{r}_2)V(\mathbf{r}_3)\rangle \\ &+ \langle V(\mathbf{r}_1)V(\mathbf{r}_3)\rangle\langle V(\mathbf{r}_2)V(\mathbf{r}_4)\rangle\,. \end{aligned} \tag{85}$$

7 A distribution obeying Gaussian statistics is fully characterized by its first two moments, see eq. (76) and [156]. As a consequence, all higher moments can be expressed in terms of the first two.

The exemplary four-point correlation (85) can thus be represented by the first three terms of the series of irreducible diagrams for the self-energy, cf. Fig. 8b),

$$\begin{aligned}\Sigma(\mathbf{r}_1-\mathbf{r}_2) = {}& B(\mathbf{r}_1-\mathbf{r}_2)G_o(\mathbf{r}_1-\mathbf{r}_2) \\ &+ \iint d\mathbf{r}_3\, d\mathbf{r}_4\, B(\mathbf{r}_1-\mathbf{r}_4)B(\mathbf{r}_2-\mathbf{r}_3)G_o(\mathbf{r}_1-\mathbf{r}_2)G_o(\mathbf{r}_2-\mathbf{r}_3)G_o(\mathbf{r}_3-\mathbf{r}_4) \\ &+ \iint d\mathbf{r}_3\, d\mathbf{r}_4\, B(\mathbf{r}_1-\mathbf{r}_3)B(\mathbf{r}_2-\mathbf{r}_4)G_o(\mathbf{r}_1-\mathbf{r}_2)G_o(\mathbf{r}_2-\mathbf{r}_3)G_o(\mathbf{r}_3-\mathbf{r}_4) \\ &+ \cdots, \end{aligned} \tag{86}$$

where the definition of the second moment from eq. (76) was used. Of course, as the dots in the last line of (86) indicate, the self-energy consists, in principle, of an infinite number of terms. We will, however, only focus on the first contribution $\Sigma_1(\mathbf{r}_1-\mathbf{r}_2)$ of the self-energy, see first line of (86), since all higher orders are at least suppressed by a factor $(k\ell_{dis})^{-1} \ll 1$,[8] in the weak disorder potential limit (for a three-dimensional setup) [48]. The evaluation of $\Sigma_1(\mathbf{r}_1-\mathbf{r}_2)$ is most conveniently done in momentum space, i. e.

$$\Sigma_1(\mathbf{k}') = \int d\mathbf{r}\, e^{i\mathbf{k}'\mathbf{r}} B(\mathbf{r})G_o(\mathbf{r})\,, \tag{87}$$

8 The proportionality to $(k\ell_{dis})^{-1} \ll 1$ of the second and third line in eq. (86) can be seen upon evaluation of the spatial integrals (using the white noise statistics eq. (6)) and subsequent transformation of the self-energy to momentum space, see e. g. [157]. Physically, the rapidly varying phase of $G_o(\mathbf{r}) \propto e^{ikr}$, see eq. (73), leads to a small contribution ($\propto 1/k$) when integrating over r in an interval $\gg 1/k$. See also [5], for a rigorous proof of vanishing higher orders in the limit $k\ell_{dis} \to \infty$.

with $\mathbf{r} = \mathbf{r}_1 - \mathbf{r}_2$. Since $G_o(\mathbf{r})$, see eq. (73), and $B(\mathbf{r}) = B(r)$ (for the case of Gaussian white noise statistics of the disorder potential, see the discussion after eq. (6)) depend only on the modulus of $\mathbf{r}$, we can transform (87) to spherical coordinates and conduct the integration over the angular components:

$$\Sigma_1(\mathbf{k}') = -\frac{1}{k'} \int dr\, B(r) e^{ikr} \sin(k'r)\,. \tag{88}$$

Eq. (88) can be determined explicitly if we substitute for $B(r)$ the white noise correlation function eq. (6), which, however, leads to an ill-defined integral expression in (88) due to the δ-function. In order to overcome this inconsistency, we replace the δ-function by a properly normalized Gaussian function with a finite width σ, such that the correlation function reads:

$$B(r) = \frac{b}{(\pi\sigma^2)^{3/2}} e^{-(r/\sigma)^2}\,, \tag{89}$$

and expression (6) is retained in the limit for $\sigma \to 0$.[9] Using (89) in (88), we obtain, upon integration and in the subsequent limit of $\sigma \to 0$, for the imaginary and real part of Σ_1, respectively:

$$\lim_{\sigma\to 0} \left[\mathrm{Im}[\Sigma_1(k')]\right] = -\frac{bk}{4\pi}\,, \tag{90}$$

$$\lim_{\sigma\to 0} \left[\sigma\, \mathrm{Re}[\Sigma_1(k')]\right] = -\frac{b}{2\pi^{3/2}}\,. \tag{91}$$

Note that the imaginary part of Σ_1, see eq. (90), – which defines the mean free path ℓ_{dis}, see eq. (92) below – remains finite for $\sigma \to 0$. On the other hand, according to eq. (91), the real part diverges like $1/\sigma$ for $\sigma \to 0$. Physically, this divergence is just an artifact of the idealized scenario of a δ-correlated potential and – since $\mathrm{Re}[\Sigma_1(k')]$ is independent of k' – it just constitutes a constant shift of the zero-point energy. Therefore, it may, without loss of generality, be absorbed into the single-particle energy $E = k^2$ upon insertion of (91) into eq. (83).[10] The substitution of eq. (90) into eq. (83) results in a *positive* imaginary part of $\widetilde{k}$, i. e.

$$\mathrm{Im}[\widetilde{k}] = -\frac{\mathrm{Im}[\Sigma_1(k')]}{2k} = \frac{1}{2\,\ell_{dis}}\,, \quad \text{with} \quad \ell_{dis} = \frac{4\pi}{b}\,, \tag{92}$$

and in the definition of the disorder mean free path ℓ_{dis}, already commented on in Chapter 1 and after eq. (6). The physical significance of the imaginary part of $\widetilde{k} = k + i/(2\ell_{dis})$ becomes obvious after back transformation of (84) to real space,

$$\langle G(\mathbf{r} - \mathbf{r}')\rangle = -\frac{e^{i\widetilde{k}|\mathbf{r}-\mathbf{r}'|}}{4\pi|\mathbf{r}-\mathbf{r}'|}\,. \tag{93}$$

In addition to eq. (73), we here deal with a spherically emitted wave that is exponentially damped due to the presence of the disorder potential, i. e. the imaginary part of the self-energy. Thus, momentum eigenstates acquire a finite lifetime and a finite coherence length ℓ_{dis}, on which a particle is scattered, on average, off the disorder potential into a different momentum eigenstate.

In particular does now the former assumption $|\Sigma(k')| \ll k^2$ (see discussion before eq. (83)) imply $k\ell_{dis} \gg 1$, which again coincides with the weak disorder potential limit. Eq. (92) furthermore confirms our statement from Section 2.1.4 that ℓ_{dis} is independent of k for the case of Gaussian white noise statistics.

9 Note that the Gaussian representation of the δ-function in eq. (89), instead of eq. (6), is only used when mathematical rigor is required.

10 This divergence can be controlled rigorously by setting $\langle V(\mathbf{r})\rangle = -\mathrm{Re}[\Sigma_1(k')]$ in eqs. (76) and (6), in order to compensate for the shift.

3.2.3 *Transport Equation for the Average Intensity*

As demonstrated in the previous section, knowledge of the average Green's function allows to determine the average amplitude $\langle\psi(\mathbf{r})\rangle$, via (70), which upon averaging turns into

$$\langle\psi(\mathbf{r})\rangle = \int \mathrm{d}\mathbf{r}' \, \langle G(\mathbf{r},\mathbf{r}')\rangle j(\mathbf{r}') \,, \tag{94}$$

since the source term is assumed to be uncorrelated with the random potential $V(\mathbf{r})$, and thus unaffected by the disorder average. However, in most cases one is interested in the two-point correlation function $\langle\psi(\mathbf{r}_1)\psi^*(\mathbf{r}_2)\rangle$, and in particular in the average intensity $I(\mathbf{r}) = \langle|\psi(\mathbf{r})|^2\rangle$, which, in general, requires to calculate the average intensity propagator

$$\Phi(\mathbf{r}_1,\mathbf{r}_2,\mathbf{r}_3,\mathbf{r}_4) = \langle G(\mathbf{r}_1,\mathbf{r}_3)G^*(\mathbf{r}_2,\mathbf{r}_4)\rangle \tag{95}$$

in order to obtain

$$\begin{aligned}\langle\psi(\mathbf{r}_1)\psi^*(\mathbf{r}_2)\rangle &= \iint \mathrm{d}\mathbf{r}_3 \, \mathrm{d}\mathbf{r}_4 \, \langle G(\mathbf{r}_1,\mathbf{r}_3)G^*(\mathbf{r}_2,\mathbf{r}_4)j(\mathbf{r}_3)j(\mathbf{r}_4)\rangle \\ &= \iint \mathrm{d}\mathbf{r}_3 \, \mathrm{d}\mathbf{r}_4 \, \Phi(\mathbf{r}_1,\mathbf{r}_2,\mathbf{r}_3,\mathbf{r}_4)j(\mathbf{r}_3)j(\mathbf{r}_4) \,, \end{aligned} \tag{96}$$

again using the fact that the source terms are independent of the disorder potential and thus unaffected by the averages.

The role of Dyson's equation (77) for the average Green's function is taken by the *Bethe-Salpeter equation* for the two-point correlator:

$$\begin{aligned}&\langle\psi(\mathbf{r}_1)\psi^*(\mathbf{r}_2)\rangle = \langle\psi(\mathbf{r}_1)\rangle\langle\psi^*(\mathbf{r}_2)\rangle \\ &+ \int \mathrm{d}\mathbf{r}_3 \, \ldots \mathrm{d}\mathbf{r}_6 \, \langle G(\mathbf{r}_1,\mathbf{r}_3)\rangle\langle G^*(\mathbf{r}_2,\mathbf{r}_4)\rangle U(\mathbf{r}_3,\mathbf{r}_4;\mathbf{r}_5,\mathbf{r}_6)\langle\psi(\mathbf{r}_5)\psi^*(\mathbf{r}_6)\rangle \,. \end{aligned} \tag{97}$$

Here, we introduced the so-called *intensity operator* $U(\mathbf{r}_1,\mathbf{r}_2;\mathbf{r}_3,\mathbf{r}_4)$ which takes the role of the self-energy.[11] The intensity operator contains all irreducible scattering contributions of the average intensity between point $\mathbf{r}_1$ and $\mathbf{r}_3$ and between point $\mathbf{r}_2$ and $\mathbf{r}_4$ composed of the scattering amplitude and the complex-conjugated scattering amplitude, respectively. As for the self-energy, all intermediate points of the different scattering amplitudes are in such a way correlated with each other that the intensity operator cannot simply be reproduced by products of averaged scattering amplitudes. Consequently, the two-point correlation function at $\mathbf{r}_1$ and $\mathbf{r}_2$ in eq. (97) consists of two contributions: the uncorrelated contribution, given as the product of two averaged scattering amplitudes in the first line on the right-hand side of (97), and all the remaining correlated contributions in the second line of (97), which determine how an initial two-point correlation between two points $\mathbf{r}_5$ and $\mathbf{r}_6$ evolves under the intensity operator to $\mathbf{r}_3$ and $\mathbf{r}_4$, from where they propagate independently to $\mathbf{r}_1$ and $\mathbf{r}_2$. Thereby, integration over all intermediate points ensures that all possible scattering paths are taken into account.

[11] The connection between the self-energy and the intensity operator can be made rigorous involving a *Ward identity* which guarantees flux conservation for the solution of the Bethe-Salpeter equation [158, 159].

Since, in general, it is quite involved to obtain a solution of the Bethe-Salpeter equation as the intensity operator involves an infinite number of possible scattering contributions, we will dwell only on the case for which a significant simplification can be realized – the weak disorder potential limit.

In (86) we argued that only the first order of the self-energy needs to be taken into account once $k\ell_{\mathrm{dis}} \gg 1$. By virtue of a Ward identity [158, 159] this

corresponds to the first order contribution to the intensity operator which – for the case of the Gaussian correlated disorder – reads [48, 152]:

$$U(\mathbf{r}_1, \mathbf{r}_2; \mathbf{r}_3, \mathbf{r}_4) = \delta(\mathbf{r}_1 - \mathbf{r}_3)\delta(\mathbf{r}_2 - \mathbf{r}_4)B(\mathbf{r}_1 - \mathbf{r}_2)\,. \tag{98}$$

This is the simplest form of the intensity operator as it just contains the correlation between the points $\mathbf{r}_1$ and $\mathbf{r}_2$ and no additional propagation. As we will see later in Section 3.2.4, an iteration of eq. (97) under the approximation (98) corresponds to a ladder-like diagrammatic structure where correlated disorder events (the ladder rungs) are connected by independent propagation of the two conjugated scattering amplitudes (the ladder stringers), leading to an identical sequence of scattering events for both amplitudes in the same order.

For the case of the δ-correlated disorder potential, i. e. $B(\mathbf{r} - \mathbf{r}') = 4\pi\delta(\mathbf{r} - \mathbf{r}')/\ell_{\text{dis}}$ and the approximation eq. (98), eq. (97) simplifies to:

$$\begin{aligned}\langle\psi(\mathbf{r}_1)\psi^*(\mathbf{r}_2)\rangle &= \langle\psi(\mathbf{r}_1)\rangle\langle\psi^*(\mathbf{r}_2)\rangle \\ &\quad + \frac{4\pi}{\ell_{\text{dis}}}\int d\mathbf{r}_3\, \langle G(\mathbf{r}_1, \mathbf{r}_3)\rangle\langle G^*(\mathbf{r}_2, \mathbf{r}_3)\rangle\langle\psi(\mathbf{r}_3)\psi^*(\mathbf{r}_3)\rangle\,.\end{aligned} \tag{99}$$

The expression for the intensity $I(\mathbf{r}) = \langle|\psi(\mathbf{r})|^2\rangle$ simplifies under use of (93):

$$I(\mathbf{r}) = I_0(\mathbf{r}) + \int_{\mathcal{V}} d\mathbf{r}'\, P(\mathbf{r}, \mathbf{r}')I(\mathbf{r}')\,, \tag{100}$$

where we explicitly indicated that the integration only extends over the volume $\mathcal{V}$ of the slab, and we introduced the *linear average intensity propagator*[12]

12 This quantity is also known as a *Diffuson* in the literature [48].

$$P(\mathbf{r}, \mathbf{r}') = \frac{e^{-|\mathbf{r}-\mathbf{r}'|/\ell_{\text{dis}}}}{4\pi\ell_{\text{dis}}|\mathbf{r} - \mathbf{r}'|^2}\,, \tag{101}$$

and the *coherent intensity* $I_0(\mathbf{r}) = |\langle\psi(\mathbf{r})\rangle|^2$, i. e. the intensity stemming directly from the source, which – for a plane wave source, $\psi_0(\mathbf{r}) = \sqrt{\rho_0}e^{ikz}$, perpendicularly incident onto the slab at $z = 0$ and under neglect of boundary effects – can be approximated by

$$I_0(\mathbf{r}) = I_0(z) = I_0 e^{-z/\ell_{\text{dis}}}\,, \tag{102}$$

and $I_0 = \rho_0$. This corresponds to an exponential damping of the coherent intensity on the length scale of the disorder mean free path, in accordance with the *Lambert-Beer law*. The second term in eq. (100) is termed the *scattered intensity*, since the absolute value in the definition of $I(\mathbf{r})$ is independent of the phases of its amplitudes, and, consequently, describes an *incoherent* propagation of the average intensity across the disorder potential.

Eq. (100) is equivalent [48] to the *radiative transfer equation*, initially derived for the propagation of electromagnetic waves in random media [160]:

$$\hat{\mathbf{k}} \cdot \nabla I(\hat{\mathbf{k}}, \mathbf{r}) = -\frac{1}{\ell_{\text{dis}}} I(\hat{\mathbf{k}}, \mathbf{r}) + \frac{1}{\ell_{\text{dis}}}\langle I(\hat{\mathbf{k}}', \mathbf{r})p(\hat{\mathbf{k}} - \hat{\mathbf{k}}')\rangle_{\hat{\mathbf{k}}'} + \rho_0\delta(z)\,. \tag{103}$$

It describes how the *specific intensity* $I(\hat{\mathbf{k}}, \mathbf{r})$, whose angular average $I(\mathbf{r}) = \langle I(\hat{\mathbf{k}}, \mathbf{r})\rangle_{\hat{\mathbf{k}}}$ reproduces the intensity defined in eq. (100), with source $\rho_0\delta(z)$, varies under the influence of attenuation due to scattering from $\hat{\mathbf{k}}$ into a different direction $\hat{\mathbf{k}}'$ (first term on the right-hand side), and gain due to scattering from $\hat{\mathbf{k}}'$ into $\hat{\mathbf{k}}$ (weighted by $p(\hat{\mathbf{k}} - \hat{\mathbf{k}}')$, which is constant for isotropic scattering.) Eq. (103) corresponds to a stationary and disorder-averaged version of the Boltzmann equation (16) in the collision-free regime (i. e. the

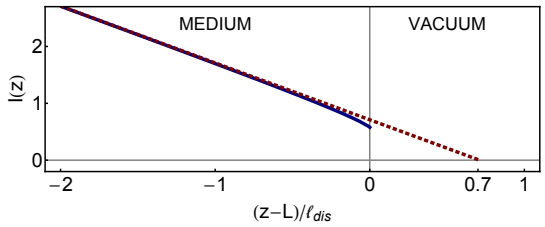

Figure 9: Incoherent intensity $I(z)$ as a function of the position $z - L$ in units of ℓ_{dis} at the border of a very long slab, i. e. $L \to \infty$, with the vacuum. The (blue) solid and the (red) dashed curve are given by the solution of the Milne problem, eq. (106), and $I(z) = \text{const.}(L - z + z_0)/\ell_{dis}$, respectively. The linear decay predicted by diffusion theory coincides with the solution of the Milne problem for $z_0 = 0.7104\ell_{dis}$. Only close to the border of the medium does eq. (106) deviate from the diffusive solution. See main text for details.

right-hand side of eq. (16) equals zero), where the term due to the force $\nabla_{\mathbf{r}} V(\mathbf{r})$ induced by the random potential on the left-hand side of eq. (16) is replaced – after averaging over many realizations of $V(\mathbf{r})$ – by the scattering terms on the right-hand side of eq. (103).

In Appendix D.1 we demonstrate how eq. (100) can be adopted to the slab geometry such that it only depends on the z-component, i. e. the propagation depth inside the slab,

$$I(z) = I_0(z) + \frac{1}{2\ell_{dis}} \int_0^L dz' \, P(z, z') I(z') \,, \tag{104}$$

where

$$P(z, z') = \mathcal{E}_1 \left(\frac{z - z'}{\ell_{dis}} \right) \tag{105}$$

equals the *exponential integral function* $\mathcal{E}_n(x)$ for $n = 1$ defined further down in eq. (318).
Towards the end of a very long slab (i. e. $L \to \infty$), where the influence of the exponentially decaying source term is negligible, the solution of (104) is known as *Milne's problem*, that Milne solved initially for the propagation of photons through surfaces of stars [161], and whose general relevance is in great detail discussed in [154]. We here only want to point out two aspects of the solution, the behavior of the solution towards the end of the slab and the very good approximation of Milne's exact solution by diffusion theory.

The intensity at the end of such a slab is, up to a constant, given by [154]

$$I(z) = \text{const.} \left[\frac{L - z}{\ell_{dis}} + 0.7104 \left[1 - 0.3429 \, \mathcal{E}_2 \left(\frac{L - z}{\ell_{dis}} \right) + 0.3159 \, \mathcal{E}_3 \left(\frac{L - z}{\ell_{dis}} \right) \right] \right] . \tag{106}$$

The contributions of the $\mathcal{E}_n$-functions, see eq. (318) for $n = 2$ and $n = 3$, vanish already for a few mean free path from the slab boundary and the intensity distribution inside the slab becomes linear (blue solid line in Fig. 9), an observation that suggests diffusive behavior and the applicability of diffusion theory. However, in order to capture the main features of the solution to the Milne problem by a linear extrapolation, one has to choose the boundary condition for the diffusive intensity, i. e. $I(z) = \text{const.}(L - z +$

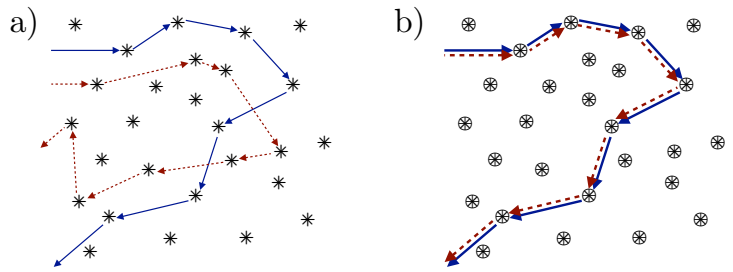

Figure 10: (a) Exemplary scattering paths for ψ and ψ^*, thin solid and dashed arrows, respectively, for a single realization of the disorder potential. (b) Exemplary scattering paths for the averaged intensity $\langle|\psi|^2\rangle$, thick solid and dashed arrows, respectively. In the case of a weak disorder potential only co-propagating ladder contributions survive the disorder average.

$z_0)/\ell_{\mathrm{dis}}$, such that it does not vanish at the end of the slab at $z = L$ but instead at $z = z_0 + L$, where $z_0 = 0.7104\ell_{\mathrm{dis}}$ is obtained from comparison with (106), see the red dashed line in Fig. 9. In other words, in order to gain a proper description of the transport in the slab by diffusion theory, one has to assume that the diffusion process extends, beyond the boundary of the slab, into the vacuum. Physically, although no diffusion takes place in the vacuum, this accounts for the non-vanishing transmission of the diffusive intensity across the slab.

For our purposes in the following, we will not apply the diffusion approximation, but rather solve the Bethe-Salpeter equation (100) exactly. Nevertheless, we want to emphasize the correspondence between both approaches and hence will speak about diffusive transport as the general transport mechanism within the slab, see Chapter 2.4 in [154] for further details concerning the derivation of a diffusion equation from eq. (100).

3.2.4 *Diagrammatic Representation of Transport in a Medium*

Within this chapter we have derived a transport equation for the average intensity, starting from the Schrödinger equation, and under the assumption of a Gaussian correlated, weak disorder potential with vanishing correlation length, i. e. white noise statistics. In other words, single scattering events are sufficiently far apart from each other, and the scatterers are assumed to be point-like. Hence, the wave function of the Schrödinger equation can be imagined as being composed of many different scattering amplitudes $\psi = \sum_n \psi_n$ which reproduce the Born series, eq. (75). Exemplary paths for ψ and ψ^*, which are independent of each other, are displayed in Fig. 10a) as thin solid and dashed lines, respectively. Each disorder potential scattering event is marked with a $\ast$.

A subsequent average over the disorder potential for each amplitude yields Dyson's equation, eq. (77). This accounts for the scattering path between a fixed starting and end point being in principle arbitrary, i. e. possibly consisting of all contributions to the self-energy in eq. (86). Averaged scattering amplitudes are now represented by thick solid and dashed arrows, respectively.

The step corresponding to eq. (97), which produces an average intensity, is depicted in Fig. 10b). As a matter of fact, we here show the diagrammatic representation of eq. (100) – better known as the diagrammatic *ladder*

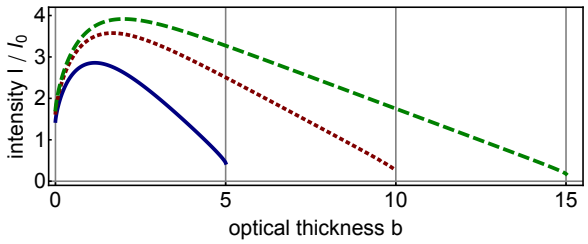

Figure 11: Solution of eq. (104) normalized to the incoming intensity I_0 injected from the left into a slab of optical thickness $b = 5$ ((blue) solid line), $b = 10$ ((red)dotted line), and $b = 15$ ((green) dashed line), respectively. The linear decay, characteristic of diffusion, can be observed within the slab, as well as the small deviation from linearity towards the end of the slab (compare Fig. 9).

contribution. In the weak disorder potential – the fundamental assumption employed to derive eq. (100) – only those scattering paths contribute to the average intensity where both amplitudes visit the same sequence of scattering events in the same order, i. e. $\langle|\psi|^2\rangle = \sum_{n=m}\langle\psi_n\psi_m^*\rangle$. All other contributions ($n \neq m$) acquire a large phase difference due to $k\ell_{dis} \gg 1$ and yield a zero contribution after averaging the exponential e^{ikr} over a full period. We denote the corresponding correlation function for averages over the disorder potential by $\circledast$, cf. (76).

The stationary intensity distribution[13] (or single-particle density) can be obtained by numerical iteration of eq. (104), i. e. by repeatedly re-inserting the obtained expression for the intensity into eq. (104) until convergence is reached. The thus obtained solution for a disordered slab of optical thickness $b = 5$, $b = 10$, and $b = 10$, respectively, is depicted in Fig. 11. Obviously – for this setup far from equilibrium – the distribution is not symmetric and the maximum density is reached at a certain position within the slab (and not at the surface) since particles constantly enter the slab from the left and are simultaneously scattered out of the former, also in direction of the source. The linear decay characteristic for diffusion can be observed within the slab, as well as the small deviation from linearity towards the end of the slab (compare Fig. 9).

13 In Chapter 2 as well as in the proceeding chapters, the relevant observable was and will be the flux density, see eq. (62). That we here call upon the intensity as our observable is, however, based on the fact that we so far developed the linear and *elastic* transport theory where simply $J(\mathbf{r}) = \sqrt{E_L}I(\mathbf{r})$ with fixed single-particle energy E_L.

3.3 NONLINEAR DIAGRAMMATIC TRANSPORT

In the preceding sections of this chapter we came to the conclusion that, upon averaging over the random disorder potential, only ladder diagrams have to be taken into account, see Fig. 10b), that can be interpreted as single particles undergoing a random walk across a potential resulting from an average over multiple realizations of disordered potential landscapes. How will this intuitive picture change once particles begin to *meet*? In other words, how will particle-particle interaction change the diagrammatic and physical picture?

In Chapter 2 we introduced and developed the mathematical and diagrammatic tools to describe two-particle interaction for a single realization of the disorder potential *and* in terms of scattering amplitudes.

In this chapter, we will show how to derive density contributions from amplitudes, and introduce all relevant interaction diagrams. Furthermore,

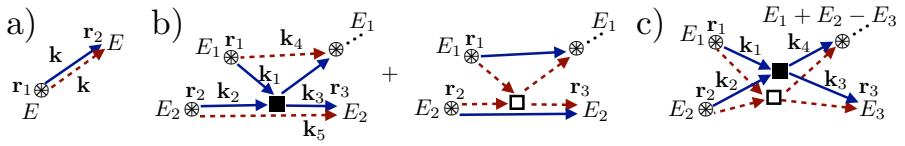

Figure 12: Diagrammatic building blocks for the description of average particle transport in the disorder potential. The single-particle transport $P_E(\mathbf{r}_1, \mathbf{r}_2)$, i. e. ladder transport, in (a) is now accompanied by two-particle interaction building blocks (b) and (c), where, respectively, only one amplitude or both amplitudes are affected by a collision event. The respective mathematical contributions are contained within $g^L_{E_1,E_2}(\mathbf{r}_1, \mathbf{r}_2, \mathbf{r}_3)$ and $f^L_{E_1,E_2,E_3}(\mathbf{r}_1, \mathbf{r}_2, \mathbf{r}_3)$, see (110) and (111). The dots in (b) and (c) again indicate a trace over this (undetected) particle, see main text for details.

we deduce under what conditions our representation either reproduces, or delivers a description *beyond* the celebrated Gross-Pitaevskii equation.

3.3.1 *The Building Blocks for the Ladder Contribution with Particle-Particle Interaction*

At first we adapt our previous notation to allow for the change of single-particle energies due to particle-particle interaction. The average Green's function for single-particle transport as expressed in eq. (84) (or in the real space representation eq. (93)) now reads

$$G_E(k) = \frac{1}{\widetilde{k}^2 - k^2}\,, \tag{107}$$

where again $\widetilde{k} = \sqrt{E} + i/(2\ell_{dis})$, cf. eqs. (83) and (92), with corresponding single-particle energy E (which, up to now, was fixed to E_L). We dropped the $\langle \ldots \rangle$-notation which indicated average propagation within the disorder potential since – from now on – we will deal with averaged quantities only, and the term *average Green's function* should be self-sufficient.

Accordingly, the linear average density propagator (eq. (101)) now takes following form

$$\begin{aligned} P_E(\mathbf{r}_1, \mathbf{r}_2) &= \frac{4\pi}{\ell_{dis}} \int \frac{d\mathbf{k}}{(2\pi)^3}\, e^{-i\mathbf{k}(\mathbf{r}_1-\mathbf{r}_2)} G_E(k) \int \frac{d\mathbf{k}'}{(2\pi)^3}\, e^{i\mathbf{k}'(\mathbf{r}_1-\mathbf{r}_2)} G_E(k') \\ &= \frac{4\pi}{\ell_{dis}} \left| \frac{e^{i\widetilde{k}(\mathbf{r}_1-\mathbf{r}_2)}}{4\pi|\mathbf{r}_1-\mathbf{r}_2|} \right|^2 = \frac{e^{-|\mathbf{r}_1-\mathbf{r}_2|/\ell_{dis}}}{4\pi\ell_{dis}|\mathbf{r}_1-\mathbf{r}_2|^2}\,, \end{aligned} \tag{108}$$

the diagrammatic form of which can be found in Fig. 12a). Since the product of both amplitudes corresponds to a propagating particle with energy E, the integrals reduce to the modulus squared of the average Green's function, see eq. (93), such that $P_E(\mathbf{r}_1, \mathbf{r}_2) = P(\mathbf{r}_1, \mathbf{r}_2)$ becomes independent of E, for our choice of a white noise disorder potential with energy-independent mean free path ℓ_{dis}.

Before we focus on the detailed derivation of the mathematical form of the two-particle interaction building blocks diagrammatically depicted in Figs. 12b) and c), we first – with the help of a showcase – try to develop some intuition of how to construct a many-particle ladder diagram, such as shown in Fig. 13.

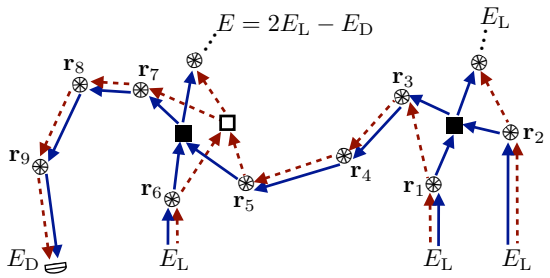

Figure 13: Exemplary 3-particle scattering diagram for the average ladder transport that involves interaction between the particles. The right collision event involves only the *solid* amplitude and the corresponding single-particle energies stay fixed as indicated by E_L for the undetected particle. The left collision event is inelastic, and leads to a redistribution of single-particle energies, i. e. of the undetected particle with energy $E = 2E_L - E_D$, and of the particle with energy E_D which is recorded by the detector.

The figure shows how a 3-particle ladder diagram – the same procedure is valid also for N particles – is obtained by combination of scattering amplitude $|f_3\rangle$ with its conjugate $\langle f_3|$, see Section 2.3 and Fig. 4, such as to construct a scattering diagram of co-propagating amplitudes. From Section 3.2 we know that the thus obtained scattering diagram corresponds to a ladder diagram for the average density if the free Green's functions are replaced by average Green's functions, i. e. replacing thin by thick arrows, and single disorder scattering by correlated disorder scattering events, i. e. replacing $\ast$ by $\circledast$. All other contributions were shown to vanish in the weak disorder potential limit.

As becomes obvious from Fig. 13, on average only co-propagating amplitudes propagate between two disorder scattering events here denoted by the $\mathbf{r}_i$'s. In order to keep the disregard of all but ladder diagrams valid we therefore further demand at least one disorder scattering event to take place between two collision events. This can be achieved if we assume $\ell_{\text{int}} \gg \ell_{\text{dis}}$, where

$$\ell_{\text{int}} = \frac{1}{8\pi a_s^2 \rho_0} \tag{109}$$

is the average distance between two (inelastic) collision events,[14] a_s is the s-wave scattering length introduced in eq. (1), see also Appendix B.1, and ρ_0 again denotes the initial density of the atomic cloud, see eq. (37). Physically, this corresponds to the limit where the effect of the disorder potential is *stronger* than the interaction strength between the particles.

In Fig. 13 we marked the energies of the incoming and detected particle, and of the particles which are traced over. Building on the insights of Section 2.3, we want to decompose such a many-particle ladder diagram, as e. g. Fig. 13, into the previously introduced linear single-particle propagation, cf. Fig. 12a), and the two-body collisions, cf. Figs. 12b) and c). Obviously, the collision process denoted in Fig. 12b) affects only one of the scattering amplitudes and we call this scattering process *elastic* because the single-particle energies remain unchanged. Process Fig. 12c), on the other hand, affects both scattering amplitudes in the same manner, and thus each particle involved in this collision can change its single-particle energy, as long as the energy of the two-particle process is conserved. Hence, this

14 As we will see below, the relevant interaction mean free path for the ladder contribution is $\ell_{\text{int}}^{\alpha} \equiv \ell_{\text{int}}$ as in (109). For the crossed diagrams to be dealt with in Chapter 4, we also have to introduce $\ell_{\text{int}}^{\beta} \neq \ell_{\text{int}}$, cf. eq. (181).

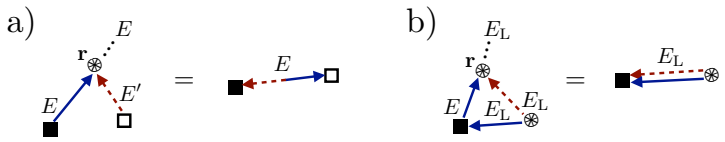

Figure 14: Illustration of the application of the trace formulas (63) and (65) derived in Section 2.3, to the present scenario of the propagation of the average intensity across the disorder potential. The trace formula for inelastic (63) and elastic (65) scattering yields the diagrammatic equivalence (a) and (b), respectively. The right diagram of (b) corresponds to the nonlinear term of the diagrammatic Gross-Pitaevskii equation, see the discussion further down in this section.

process is called *inelastic*, and will be responsible for a redistribution of the single-particle energies.

As already mentioned in Section 2.3, we can trace out the remaining particles as soon as they have interacted with the detected particle. This is justified if we can neglect all diagrams where two particles which have interacted once will interact again – an approximation which is equivalent to the neglect of *recurrent scattering* for a single particle [48, 162] and again, alike the neglect of non-ladder diagrams, valid for $k\ell_{\mathrm{dis}} \gg 1$.

To this end, we apply the trace formulas (63) and (65) derived in Section 2.3 for inelastic and elastic scattering processes. The trace over the inelastically scattered particle with energy E in Fig. 13 is given by the trace formula eq. (63), after replacing the Green's operators by their averages, i. e. $\hat{G}_V \to \hat{G}$. Interpreting this formula diagrammatically, it is equivalent to draw a last common disorder scattering event before the trace (as in Fig. 13), or to directly connect the two collision events by a solid-dashed arrow, cf. Fig. 14a). According to (63) and the above mentioned replacement of the Green's operators by their averages, this double-arrow is tantamount to $(G^*_E(k) - G_E(k))/2\pi i$.

For elastic collisions (as is the case for the undetected particle with energy E_L in Fig. 13) the trace formula (65) has to be applied. As depicted in Fig. 14b), the last common disorder scattering event of the undetected amplitudes can again be replaced by a direct connection of the corresponding (red dashed) amplitude to the collision event.[15]

15 The second possibility, i. e. the direct connection of the second blue solid amplitude to the collision event, can be shown to vanish since it is compensated for by other diagrams, see the discussion of the elastic trace formula (65) in Section 2.3 – and its equivalence to the Gross-Pitaevskii equation later in this section.

Under application of the trace formulas, we can write down the mathematical expressions for the elastic and inelastic diagrams in Figs. 12b) and c), respectively, following the set of rules formulated in Section 2.3. However, also these rules must be modified to account for average transport, i. e. we need to substitute $\hat{G}_V \to \hat{G}$, and $\langle V(\mathbf{r})V(\mathbf{r}')\rangle = 4\pi\,\delta(\mathbf{r}-\mathbf{r}')/\ell_{\mathrm{dis}}$.

The elastic building block, Fig. 12b), is then given as

$$g^{L}_{E_1,E_2}(\mathbf{r}_1,\mathbf{r}_2,\mathbf{r}_3) = 2\left(\frac{4\pi}{\ell_{\mathrm{dis}}}\right)^2 2\,\mathrm{Re}\left\{\frac{1}{2}\int \frac{d\mathbf{k}_1\ldots d\mathbf{k}_5}{(2\pi)^{15}} \times e^{-i[(\mathbf{k}_1-\mathbf{k}_4)\cdot\mathbf{r}_1+(\mathbf{k}_2-\mathbf{k}_5)\cdot\mathbf{r}_2+(\mathbf{k}_5-\mathbf{k}_3)\cdot\mathbf{r}_3]}\langle\mathbf{k}_3,\mathbf{k}_4|\hat{T}^{(2)}_U(E_1+E_2)|\mathbf{k}_1,\mathbf{k}_2\rangle \times G_{E_1}(k_1)G_{E_2}(k_2)G_{E_2}(k_3)G^*_{E_1}(k_4)G^*_{E_2}(k_5)\right\}. \tag{110}$$

As mentioned before, the trace over the undetected particle was performed according to Fig. 14b), and results in a contribution of the average Green's function $G^*_{E_1}(k_4)$. The first factor 2 in eq. (110) (and eq. (111)) originates from the fact that the solid and dashed incoming amplitudes can be grouped to-

gether in two different ways. In principle, one thus has to calculate the disorder average for the two incoming densities together, i. e. $\langle I^2 \rangle$. However, it can be shown – again relying on the weak disorder assumption – that this accounts for fluctuations of the atomic density inside the disordered slab such that $\langle I^2 \rangle = 2\langle I \rangle^2$ [163].[16] The factor $1/2$ in front of the integrals in eqs. (110) and eq. (111) regards the indistinguishability of the two particles and limits the integration to the symmetrized two-particle subspace. As we discussed previously in Section 2.3, the trace as conducted in Fig. 14b) exactly reproduces the nonlinear term in the diagrammatic representation of the Gross-Pitaevskii equation, see Fig. 16b).

16 The same factor 2 also appears in front of the non-condensate density in the Hartree-Fock equation (15).

The inelastic building block in Fig. 12c), where the energies of the two particles E_1 and E_2 change to E_3 and $E_4 = E_1 + E_2 - E_3$, reads in mathematical terms:

$$f^{L}_{E_1,E_2,E_3}(\mathbf{r}_1,\mathbf{r}_2,\mathbf{r}_3) = 2\left(\frac{4\pi}{\ell_{dis}}\right)^2 \int \frac{d\mathbf{k}_4}{(2\pi)^3} \frac{G^*_{E_1+E_2-E_3}(k_4) - G_{E_1+E_2-E_3}(k_4)}{2\pi i} \times \left| \frac{1}{2} \int \frac{d\mathbf{k}_1 d\mathbf{k}_2 d\mathbf{k}_3}{(2\pi)^9} e^{-i(\mathbf{k}_1\cdot\mathbf{r}_1 + \mathbf{k}_2\cdot\mathbf{r}_2 - \mathbf{k}_3\cdot\mathbf{r}_3)} \langle \mathbf{k}_3, \mathbf{k}_4 | \hat{T}^{(2)}_U(E_1+E_2) | \mathbf{k}_1, \mathbf{k}_2 \rangle \times G_{E_1}(k_1) G_{E_2}(k_2) G_{E_3}(k_3) \right|^2 . \quad (111)$$

The trace over the undetected particle has been conducted in accordance with Fig. 14a) and corresponds to the difference of the advanced and retarded Green's function, in the argument of the integral in the first line of (111). Note that the notation which has been used previously [164], i. e.

$$\frac{4\pi}{\ell_{dis}} \int \frac{d\mathbf{k}}{(2\pi)^3} \delta(k^2 - E) \iint \frac{d\mathbf{k}_1\, d\mathbf{k}'_1}{(2\pi)^6} G^*_E(k'_1) G_E(k_1) \int d\mathbf{r}\, e^{-i(\mathbf{k}_1 - \mathbf{k}'_1)\mathbf{r}} , \quad (112)$$

yields

$$\int \frac{d\mathbf{k}_1}{(2\pi)^3} \frac{G^*_E(k_1) - G_E(k_1)}{2\pi i} \quad (113)$$

as in (111), upon integration over $\mathbf{r}$, i. e. $(2\pi)^3\delta(\mathbf{k}_1 - \mathbf{k}'_1)$, and evaluation of the δ-functions. In order to see this, one uses

$$\sqrt{E}\,|G_E(k_1)|^2 = \frac{\ell_{dis}}{2i}\left(G^*_E(k_1) - G_E(k_1)\right) , \quad (114)$$

which follows from the operator identity

$$\hat{G}^\dagger(E')\hat{G}(E) = \frac{\hat{G}^\dagger(E') - \hat{G}(E)}{E - E' + 2i\varepsilon} , \quad (115)$$

as a consequence of the definition of the Green's operator (45), and the transformed operator identity (46), i. e.

$$\frac{1}{AB} = \left(\frac{1}{A} - \frac{1}{B}\right)\frac{1}{B-A} . \quad (116)$$

3.3.2 *The Nonlinear Transport Equation for the Ladder Contribution*

As shown in Fig. 13, the three building blocks of Fig. 12 (or equivalently eqs. (108), (110), and (111)) are sufficient to determine the transport mechanism of the ladder contribution (if one restricts the treatment to two-particle

collisions, and assumes that at least one scattering off the disorder potential takes place between two collision events).

If one attaches now the outgoing arrows of each building block to the incoming arrows of the next building block, and so on, one can construct an arbitrary N-particle ladder diagram. In accordance with eq. (100), a corresponding transport equation for the *spectral density* $I_E(\mathbf{r})$, i. e. a particle with energy E at position $\mathbf{r}$ within the slab, can be expressed as follows:

$$\begin{aligned} I_E(\mathbf{r}) = I_0(\mathbf{r})\delta(E-E_L) &+ \int_{\mathcal{V}} d\mathbf{r}' P_E(\mathbf{r},\mathbf{r}') I_E(\mathbf{r}') \\ &+ \int_0^\infty dE' \iint_{\mathcal{V}} d\mathbf{r}'\, d\mathbf{r}'' g^L_{E',E}(\mathbf{r}',\mathbf{r}'',\mathbf{r}) I_E(\mathbf{r}'') I_{E'}(\mathbf{r}') \\ &+ \iint_0^\infty dE'\, dE'' \iint_{\mathcal{V}} d\mathbf{r}'\, d\mathbf{r}'' f^L_{E',E'',E}(\mathbf{r}',\mathbf{r}'',\mathbf{r}) I_{E''}(\mathbf{r}'') I_{E'}(\mathbf{r}')\,, \end{aligned} \tag{117}$$

with $I_0(\mathbf{r})$ as in eq. (102), and P_E, g^L, and f^L as defined in eqs. (108), (110), and (111), respectively.

Note that, as mentioned before, all integrals over E formally need to be integrated from $-\infty$ to $+\infty$. However, integration over the poles of the Green's functions in (108) returns a fully real contribution proportional to $\exp[-2\sqrt{|E|}r - r/\ell_{dis}]$, such that negative contributions to the energy are rapidly damped out and – in the weak disorder potential limit, $\sqrt{E}\ell_{dis} \gg 1$ – their contribution to the total transport vanishes:

$$\int_{\mathcal{V}} d\mathbf{r}\, P_{(-|E|)}(\mathbf{r}) = \frac{1}{1+2\sqrt{|E|}\ell_{dis}} \quad \xrightarrow[\sqrt{E}\ell_{dis}\to\infty]{} \quad 0\,. \tag{118}$$

Therefore, we restrict the interval of integration, e. g. in eq. (117), to non-negative energies.

A numerical solution to (117), where the spectral intensities appear on both sides of the above equation, can be obtained by iteration. By plugging the result at position $\mathbf{r}$ with energy E again into the right-hand side of the equation, the solution is propagated to another point in space, with a possibly different energy, such that all possible diagrammatic contributions – constructed from the three building blocks in Fig. 12 – are included. A stationary scattering result is obtained once the iteration procedure converges, i. e. another iteration step does not differ from the previous iteration step.

The final figure of merit, however, as detected by a detector at position $\mathbf{R}$ in the far field of the slab, is the already mentioned flux density, integrated over all occurring single-particle energies, see (62):

$$\begin{aligned} \mathbf{J}(\mathbf{R}) &= \frac{4\pi}{\ell_{dis}} \int d\mathbf{r} \int dE \iint \frac{d\mathbf{k}\, d\mathbf{k}'}{(2\pi)^6} \frac{\mathbf{k}+\mathbf{k}'}{2} G^*_E(k') G_E(k) e^{i(\mathbf{k}-\mathbf{k}')(\mathbf{R}-\mathbf{r})} I_E(\mathbf{r}) \\ &= \frac{\mathbf{R}}{4\pi\ell_{dis}R^3} \int d\mathbf{r}\, e^{-\xi(\mathbf{R},\mathbf{r})/\ell_{dis}} \int dE\, \sqrt{E}\, I_E(\mathbf{r})\,, \end{aligned} \tag{119}$$

where (107) and the formal definition of the flux density [165], i. e.

$$(\mathbf{k}+\mathbf{k}')e^{i(\mathbf{k}-\mathbf{k}')(\mathbf{R}-\mathbf{r})} = i\left[e^{i\mathbf{k}(\mathbf{R}-\mathbf{r})}\nabla_{\mathbf{R}} e^{-i\mathbf{k}'(\mathbf{R}-\mathbf{r})} - e^{-i\mathbf{k}'(\mathbf{R}-\mathbf{r})}\nabla_{\mathbf{R}} e^{i\mathbf{k}(\mathbf{R}-\mathbf{r})}\right], \tag{120}$$

was used in order to evaluate the momentum integrals. The derivatives in (120) were truncated for all terms of order $\mathcal{O}(R^{-2})$ and higher, in accordance with the *Fraunhofer approximation* [156] for $|\mathbf{R}| \gg |\mathbf{r}|$. The function $\xi(\mathbf{R},\mathbf{r})$ denotes the distance the particle has to travel before leaving the slab. For

our slab geometry, $\xi(\mathbf{R},\mathbf{r}) = z/\cos\theta$, with backscattering angle $\cos\theta = -\mathbf{R}\cdot\mathbf{e}_z/R$.

The diagrammatic analogue to the expression (119) is a final disorder scattering event at $\mathbf{r}$ – the point where the spectral density scatters in the direction of the detector – and a respective average or vacuum propagation while being inside the slab or in the surrounding vacuum, where the detector is placed.

Eq. (119), i. e. the diffusive or ladder flux density that is detected outside the slab, will be of importance in Chapter 4, when we will compare the ladder to the crossed contribution that manifests itself only outside the slab. For now, we follow the line of thought for the linear ladder component and analyze eq. (117) – the contribution within the slab – in more detail.

Eq. (117) may be simplified in the weak interaction limit, i. e. if $\ell_{\text{int}} \gg \ell_{\text{dis}}$, cf. (109). Hence, mostly scattering off the disorder potential occurs, and the spatial transport of particles between $\mathbf{r}$ and $\mathbf{r}'$ is dominated by the single particle propagator $P_E(\mathbf{r},\mathbf{r}')$.[17] In a contact approximation for the collision contributions we may thus assume

$$\begin{aligned} g^L_{E',E}(\mathbf{r}',\mathbf{r}'',\mathbf{r}) &\simeq \delta(\mathbf{r}'-\mathbf{r})\delta(\mathbf{r}''-\mathbf{r})g^L_{E',E}\,,\\ f^L_{E',E'',E}(\mathbf{r}',\mathbf{r}'',\mathbf{r}) &\simeq \delta(\mathbf{r}'-\mathbf{r})\delta(\mathbf{r}''-\mathbf{r})f^L_{E',E'',E}\,, \end{aligned} \tag{121}$$

with

$$\begin{aligned} g^L_{E',E} &= \iint_{\mathcal{V}} d\mathbf{r}'\, d\mathbf{r}''\, g^L_{E',E}(\mathbf{r}',\mathbf{r}'',\mathbf{r})\,,\\ f^L_{E',E'',E} &= \iint_{\mathcal{V}} d\mathbf{r}'\, d\mathbf{r}''\, f^L_{E',E'',E}(\mathbf{r}',\mathbf{r}'',\mathbf{r})\,. \end{aligned} \tag{122}$$

Eq. (117) can thus be stated as

$$\begin{aligned} I_E(\mathbf{r}) = I_0(\mathbf{r})\delta(E-E_L) &+ \int_{\mathcal{V}} d\mathbf{r}'\, P_E(\mathbf{r},\mathbf{r}')I_E(\mathbf{r}')\\ &+ \int_0^\infty dE' \left[g^L_{E',E} I_E(\mathbf{r}) + \int_0^\infty dE'' f^L_{E',E'',E} I_{E''}(\mathbf{r}) \right] I_{E'}(\mathbf{r})\,. \end{aligned} \tag{123}$$

As mentioned above, contributions of the collisional processes to the transport arising, e.g., from repulsion between the particles are neglected for $\ell_{\text{int}} \gg \ell_{\text{dis}}$. Instead, the collisions lead to a re-distribution of single-particle energies in eq. (123).

Since only the linear propagation in eq. (123) is position-dependent, we can rewrite (123) with the help of Appendix D.1, as an equation that effectively becomes one-dimensional, and solely depends on the depth z in the slab, cf. (104). Our final result for the nonlinear integral equation describing ladder transport thus turns out to be:

$$\begin{aligned} I_E(z) = I_0(z)\delta(E-E_L) &+ \int_{\mathcal{V}} dz' P_E(z,z')I_E(z')\\ &+ \int_0^\infty dE' \left[g^L_{E',E} I_E(z) + \int_0^\infty dE'' f^L_{E',E'',E} I_{E''}(z) \right] I_{E'}(z)\,, \end{aligned} \tag{124}$$

where $I_0(z)$ and $P_E(z,z') = P(z,z')$ (since, as mentioned above, the mean free path is independent of E) are defined as in eq. (104).

17 As we will show in detail later in this chapter, the number of collision events in the weak interaction limit in a very large slab, e. g. for the collision strength $\alpha = 1/250$, see eq. (127), and optical thickness $b = 50$, will be of the order of 10, compared to the number of disorder scattering events on the order of 10^3.

Using (31), with the explicit form of the T-matrix derived in Appendix B.1,

$$\langle \mathbf{k}_{34}| \hat{T}_U^{(1)}(E_{12})\,|\mathbf{k}_{12}\rangle = 16\pi a_s \left(1 - i a_s \sqrt{\frac{E_{12}}{2}} + \dots\right), \tag{125}$$

the definition of the average Green's function (107), and the contact approximation, (110) simplifies, with some residual calculus, to

$$\begin{aligned} g^L_{E_1,E_2} &= \frac{2\mathrm{Re}}{\rho_0}\left\{ \frac{2\beta\sqrt{E_L}}{2i\sqrt{E_2} - 1/\ell_{dis}} - \frac{\alpha\left[\left(\sqrt{E_1}+\sqrt{E_2}\right)^3 - \left|\sqrt{E_1}-\sqrt{E_2}\right|^3\right]}{6\sqrt{E_1 E_2}(2\sqrt{E_2} + i/\ell_{dis})} \right\} \\ &\simeq -\frac{\alpha}{\rho_0} \times \begin{cases} 1 + \frac{E_1}{3E_2} & , E_1 \leqslant E_2\,. \\ \sqrt{\frac{E_1}{E_2}} + \frac{1}{3}\sqrt{\frac{E_2}{E_1}} & , E_1 > E_2\,. \end{cases} \end{aligned} \tag{126}$$

The terms proportional to β and α in the first line of (126) correspond to different orders in the s-wave scattering length a_s, cf. (125), with

$$\alpha = 8\pi a_s^2 \ell_{dis}\rho_0 = \frac{\ell_{dis}}{\ell_{int}}, \quad \text{and} \quad \beta = \frac{8\pi a_s \ell_{dis}^2 \rho_0}{k_L \ell_{dis}}, \tag{127}$$

where we used the definition of ℓ_{int}, see eq. (109), for the definition of α. From the s-wave scattering approximation we find that the dimensionless parameters α and β, which determine the collision strength, are related to each other as follows:

$$\alpha \ll \beta\,, \quad \text{since} \quad \frac{\alpha}{\beta} = k_L a_s \ll 1\,. \tag{128}$$

Note that the term ρ_0 in the denominator of (126) drops out once we normalize the spectral density I_E with respect to the initial density I_0 in eq. (124). The second line of expression (126) is obtained in the weak disorder potential limit $k\ell_{dis} \gg 1$, where we neglected the small but finite real contribution proportional to β, i. e. $-\beta E_L/\rho_0 E_2 k_L \ell_{dis}$. As this result becomes rigorous only in the limit $k\ell_{dis} \to \infty$, let us comment on it in more detail:[18] In Section 3.3.3 we will demonstrate, see eq. (131), that the integral equation (123) conserves the particle and energy flux for finite $k\ell_{dis}$ and for collision contributions proportional to α only, see eqs. (126) and (129). This in turn implies, however, that the small but finite contribution proportional to β in (126), i. e. of the order of $(k\ell_{dis})^{-1}$, must already be compensated for by another diagram, and thus does not affect the conservation laws (131). Indeed, as depicted in Fig. 15, a diagrammatic contribution can be identified which is equal in magnitude and opposite in sign, such that the contribution proportional to β in eq. (126) vanishes.

18 The same line of argument also holds for the nonlinear parameter g of the Gross-Pitaevskii equation in eq. (142).

The compensating diagram in Fig. 15 is in fact of non-ladder type and should not appear in our consideration here. However, in (125) we derived the *vacuum* T-matrix, in the weak disorder limit, which – in a more rigorous treatment – should be replaced by the T-matrix in the medium. Therefore, the compensating diagram in Fig. 15 must be seen rather as a first correction to the vacuum T-matrix. In order to be consistent, the disappearance of the term proportional to β in (126) must either occur in the limit $k\ell_{dis} \to \infty$ (vacuum), or by redoing our calculations with the full T-matrix for the disordered medium (a complicated procedure beyond the scope of this thesis). In the following, we will thus simply classify the different diagrams by their very small parameter $(k\ell_{dis})^{-n}$, with n being a positive integer, in order to identify the leading contributions.

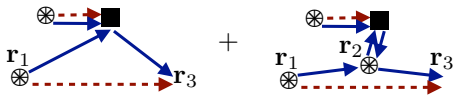

Figure 15: Illustration of how certain diagrammatic contributions can be compensated for by other diagrams. By virtue of Fig. 14b), the left diagram is identical to the left diagram of Fig. 12b); its mathematical form contains two terms proportional to α and β, see eqs. (126). By restricting the analysis to terms proportional to β, simple calculations with the help of Appendix E reveal that the left diagram contains a real contribution which is compensated for by the right diagram, thus leading to a fullly imaginary contribution up to order $\propto (k\ell_{dis})^{-2}$. Higher orders are compensated for by higher orders of the right diagram. Applying the same reasoning to the conjugated diagrams, and thus accounting for the right diagram in Fig. 12b), one concludes that the contribution proportional to β in eq. (126) vanishes identically, even for finite $k\ell_{dis} \gg 1$. See main text for further details.

Note that the contribution proportional to β in (126) is identical to the nonlinear contribution that appears within the stationary Gross-Pitaevskii equation [62]. Consequently, the nonlinearity of the ladder contribution for the Gross-Pitaevskii equation *vanishes* for the stationary scattering scenario – a result which we devote further attention to in Section 3.3.4, where we compare our model to the predictions of the Gross-Pitaevskii equation.

Along the same lines as the derivation of (126), eq. (111) can be equally determined in the weak disorder limit:

$$\begin{aligned} f^{L}_{E_1,E_2,E_3} &= \frac{-\alpha}{8\rho_0\sqrt{E_1E_2E_3}} \sum_{s_i\in\{0,1\}} (-)^{s_1+\cdots+s_4} \\ &\quad \times \left|(-)^{s_1}\sqrt{E_1}+(-)^{s_2}\sqrt{E_2}+(-)^{s_3}\sqrt{E_3}+(-)^{s_4}\sqrt{E_1+E_2-E_3}\right| \\ &= \frac{\alpha}{\rho_0\sqrt{E_1E_2E_3}} \times \min\left[\sqrt{E_1},\sqrt{E_2},\sqrt{E_3},\sqrt{E_1+E_2-E_3}\right] . \end{aligned} \tag{129}$$

The sum in the formula comprises arguments given in compact form, to display the different absolute value contributions with alternating signs, as long as the values of the single particle energies remain unspecified. Since the diagram Fig. 12c) involves one collision event for each amplitude, each at least proportional to a_s, see eq. (125), the corresponding density in (129) is already proportional to a_s^2, i. e. to α. All higher contributions in a_s are suppressed in the s-wave scattering limit, due to $ka_s \ll 1$, and will not be considered here.

3.3.3 *Particle and Energy Flux Conservation*

In order to verify that the three scattering building blocks in Fig. 12 are the only contributions one has to consider in the weak disorder limit $k\ell_{dis} \gg 1$, up to second order in a_s, one has to check eq. (123) for particle and energy flux conservation. Since the linear (collision-free) contribution (108) is itself probability-conserving, i. e.

$$\int_{\mathcal{V}} d\mathbf{r}\, P_E(\mathbf{r}) = 1\,, \tag{130}$$

the collision contributions have to compensate each other. And indeed, for our choice of building blocks one can show that eqs. (126) and (129) conserve

the particle and the energy flux as a consequence of the optical theorem, eq. (34):

$$\begin{aligned}\sqrt{E_2}\, g^L_{E_1,E_2} &= -\int_0^\infty dE_3\, \sqrt{E_3}\, f^L_{E_1,E_2,E_3}\,, && \text{(particle flux)}\\ (E_1+E_2)\sqrt{E_2}\, g^L_{E_1,E_2} &= -\int_0^\infty dE_3\, 2E_3\sqrt{E_3}\, f^L_{E_1,E_2,E_3}\,. && \text{(energy flux)}\end{aligned} \tag{131}$$

The proof of (131) is given in Appendix C. Consequently, it becomes obvious that (125) had to be expanded to second order in a_s, since otherwise the contribution (129), which is already proportional to a_s^2, could not be compensated for by (126).

Furthermore, the microscopic reversibility of the collision kernels (126) and (129) is worth noting:

$$\frac{g^L_{E_1,E_2}}{\sqrt{E_1}} = \frac{g^L_{E_2,E_1}}{\sqrt{E_2}}\,, \qquad \frac{f^L_{E_1,E_2,E_3}}{\sqrt{E_1+E_2-E_3}} = \frac{f^L_{E_3,E_1+E_2-E_3,E_1}}{\sqrt{E_2}}\,. \tag{132}$$

Up to the trace of the undetected particle (that leads to the square root in the denominators), our microscopic ansatz equally describes the collision process with reversed directionality of the arrows in Fig. 12b) and c). As a consequence of the terms in the denominator, we will see that the flux density rather than the density is invariant under reversal of the particle propagation direction, see the discussion in Section 3.4.

As a next step, we can now try to determine a stationary solution of eq. (123). For this purpose, let us define the respective total particle flux $J(\mathbf{r}) = \int dE\, J_E(\mathbf{r})$ and the total energy flux $K(\mathbf{r}) = \int dE\, K_E(\mathbf{r})$, where

$$J_E(\mathbf{r}) = \sqrt{E} I_E(\mathbf{r}) \quad \text{and} \quad K_E(\mathbf{r}) = E\sqrt{E} I_E(\mathbf{r})\,, \tag{133}$$

respectively. Due to the fact that $P_E(\mathbf{r},\mathbf{r}') = P(\mathbf{r},\mathbf{r}')$ is independent of E, together with (131), the total particle and energy flux fulfill the same linear transport equation (100):

$$\begin{aligned}J(\mathbf{r}) &= J_0(\mathbf{r}) + \int_{\mathcal{V}} d\mathbf{r}'\, P(\mathbf{r},\mathbf{r}') J(\mathbf{r}')\,,\\ K(\mathbf{r}) &= K_0(\mathbf{r}) + \int_{\mathcal{V}} d\mathbf{r}'\, P(\mathbf{r},\mathbf{r}') K(\mathbf{r}')\,,\end{aligned} \tag{134}$$

where the source terms $J_0(\mathbf{r}) = \sqrt{E_L} I_0(\mathbf{r})$ and $K_0(\mathbf{r}) = E_L\sqrt{E_L} I_0(\mathbf{r})$ are defined accordingly. Eq. (134) results from eq. (123) by multiplication with $\sqrt{E}$ (or $E\sqrt{E}$), and subsequent integration over E. The collision contributions drop out upon integration over the energy, because of relation (131). Hence, since the linear transport equation is flux conserving, cf. (130) and [48], also particle and energy flux are conserved. Furthermore, eqs. (134) are of identical linear form and related to each other via $K_0(\mathbf{r}) = E_L J_0(\mathbf{r})$, such that the total energy flux is fixed to

$$K(\mathbf{r}) = E_L J(\mathbf{r})\,. \tag{135}$$

We can now use the insights from above to determine a stationary solution far inside the medium, i. e. for $z \to \infty$, where the source term vanishes due to the exponential damping, and the constant solution of (123), here expressed for the particle flux $J_E = \sqrt{E} I_E$ must fulfill

$$\int_0^\infty dE'\, \frac{g^L_{E',E}}{\sqrt{E'}} J_E J_{E'} + \iint_0^\infty dE'\, dE''\, \sqrt{E}\, \frac{f^L_{E',E'',E}}{\sqrt{E'}\sqrt{E''}} J_{E'} J_{E''} = 0\,. \tag{136}$$

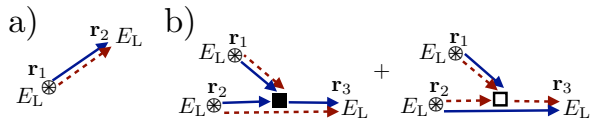

Figure 16: Diagrammatic representation of the fully elastic ladder contribution calculated via the Gross-Pitaevskii equation, eq. (142). (a) is the same building block as obtained in Fig. 12a), and (b) is equivalent to Fig. 12b), once the trace over the undetected particle is conducted according to (65), cf. Fig. 14b).

Eq. (131), together with the microscopic reversibility (132) ensures that the ansatz $J_E \propto E e^{-\gamma E}$ with $\gamma > 0$ satisfies eq. (136). Furthermore, γ can be determined via (135) as $\gamma = 2/E_L$. Therefore, a stationary solution of the integral equation (123) for the particle flux is found to be

$$\frac{J_E(\mathbf{r})}{J(\mathbf{r})} = \frac{4E}{E_L^2} e^{-2E/E_L} . \tag{137}$$

This is a Maxwell-Boltzmann distribution with a temperature T determined by the initial energy $E_L = k_B T/2$. As a consequence, we expect the particle flux incident on the slab to equilibrate towards the distribution (137), provided the slab is sufficiently long. However, before scrutinizing this prediction numerically, we come back to the diagrammatic Gross-Pitaevskii equation: In which limit does our result (123) reproduce the stable coherent state described by the Gross-Pitaevskii equation, rather than thermalization?

3.3.4 *Elastic Nonlinear Transport – the Gross-Pitaevskii Limit*

We come back to the Gross-Pitaevskii equation (1) introduced at the beginning of this thesis to demonstrate the relation of the former to our diagrammatic theory. For the case of stationary solutions of the form

$$\psi(\mathbf{r}, t) = \psi(\mathbf{r}) e^{-i\mu t/\hbar} , \tag{138}$$

the Gross-Pitaevskii equation, as e. g. derived in [87], reads

$$\left(-\nabla^2 + V(\mathbf{r}) + g|\psi(\mathbf{r})|^2\right) \psi(\mathbf{r}) = \mu\psi(\mathbf{r}) . \tag{139}$$

It describes, e.g., the ground state wave function of a dilute Bose gas of repulsively interacting particles at zero temperature [83]. As before, $V(\mathbf{r})$ denotes the external disorder potential, $\psi(\mathbf{r})$ is the single-particle wave function (associated with the wave function of the condensate), and $g = 8\pi a_s$ determines the interaction strength and accounts for one half the first term in (125). The factor 1/2 arises due to the indistinguishability of the two-particle scenario considered in detail in Appendix B.1. The value of the chemical potential μ is determined by the source term – an incident matter wave in a scattering setup – where $\psi(\mathbf{r})$ takes the role of the scattering amplitude, see e. g. [43, 44].

Consequently, a diagrammatic representation of the scattering process described by (139) can be developed [62], where now single particles propagate in a nonlinear medium. This scenario becomes more obvious if we rewrite (139) as an integral equation

$$\psi(\mathbf{r}) = \psi_0 e^{i\mathbf{k}_L\mathbf{r}} + \mu \int_{\mathcal{V}} d\mathbf{r}' G_0(\mathbf{r} - \mathbf{r}') \left(\widetilde{V}(\mathbf{r}') + \widetilde{g}|\psi(\mathbf{r}')|^2\right) \psi(\mathbf{r}') , \tag{140}$$

where we assumed as initial condition an incoming plane wave, in accordance with our slab scenario Fig. 7, and, again, the integration extends over the volume $\mathcal{V}$ of the slab. The free Green's function $G_0(\mathbf{r}-\mathbf{r}')$ is defined as in (73), $\widetilde{V} = V/\mu$, and

$$\widetilde{g} = g/\mu\,. \tag{141}$$

Despite the fact that we are dealing with a nonlinear equation which, for the stationary solution, however, only accounts for elastic collision events, one can repeat the average over the random disorder potential as explained in Section 3.2, to derive an expression for the average ladder density, in the weakly disordered medium, similar to (100) (for further details we refer the reader to [62]):

$$I^{(GP)}(\mathbf{r}) = I_0^{(GP)}(\mathbf{r}) + \int_{\mathcal{V}} d\mathbf{r}' P(\mathbf{r},\mathbf{r}') I^{(GP)}(\mathbf{r}') \left[1 - ik_L \ell_{dis}(\widetilde{g} - \widetilde{g}^*) I^{(GP)}(\mathbf{r}')\right]\,. \tag{142}$$

The linear propagator $P(\mathbf{r},\mathbf{r}')$ is given by (101). In accordance with the diagrams developed so far in this chapter, see Fig. 12, we depict the linear and nonlinear ladder building blocks of eq. (142) in Figs. 16a) and b), respectively. It turns out that the diagrammatic building blocks in Figs. 16a) and b) are identical to the building blocks in Figs. 12a) and b), respectively, if one conducts the trace over the undetected particle in Fig. 12b) according to (65) (diagrammatically depicted in Fig. 14b) and – for the case of a single realization of the disorder potential – already mentioned in Fig. 6).

This also follows from comparison of eqs. (123) and (142), where the case of elastic transport – as predicted by (142) – can be achieved by neglect of the contribution $f^L_{E',E'',E}$ in (123), i. e. by setting $\alpha = 0$. For the case of a scattering setup, where the initial and final states are asymptotically free, the chemical potential corresponds to the single-particle energy, i. e. $\mu = k_L^2$. Therefore, the remaining collision contribution proportional to β in (123) is related to (141) via $\beta = \rho_0 k_L \ell_{dis} \widetilde{g}$, which, expressed in terms of g, equals

$$g = \frac{\beta k_L}{\ell_{dis}\rho_0} = g^L_{E_L,E_L}(\alpha = 0)\,. \tag{143}$$

The last equality is due to eq. (126). Hence, eq. (143) exactly corresponds to the contribution proportional to β which we demonstrated to be negligible in eq. (126) and in Fig. 15. The same reasoning thus also applies for eq. (142): Since $\widetilde{g} \in \mathbb{R}$, we have $\widetilde{g} - \widetilde{g}^* = 0$, and the nonlinear contribution of the Gross-Pitaevskii equation vanishes identically for the case of ladder transport.

In conclusion, we have shown that our diagrammatic theory for the ladder component reproduces the corresponding stationary Gross-Pitaevskii equation for the collision strength $\alpha = 0$. In this limit, both approaches result in a *linear* elastic scattering process, where an initial particle (plane wave) with energy E_L will keep its energy throughout this transport process, and the influence of particle-particle collisions vanishes. Hence, eq. (142) and eq. (100) coincide.

However, switching on the collision parameter α will lead to a dramatic effect of the inter-particle collisions – a situation which we examine next when presenting the solution to eq. (124).

3.4 RESULTS

In Fig. 11 we show the particle density as obtained for linear ladder transport processes within the slab. Within this section we go beyond the linear scenario and solve the nonlinear eq. (124). In general, a solution to (124) can be found via (numerical) iteration until a stationary density profile within the slab is achieved. Two density profiles are of interest. First, the one corresponding to the integrated flux density of particles (also named particle flux before), and, second, the spectral flux density. Both will be analyzed in the following two subsections.

3.4.1 *Total Flux Density Inside the Slab*

In accordance with eqs. (119) and (133), we define the total flux inside the slab $J(\mathbf{r})$ as the flux of particles entering (and leaving) a small volume element around $\mathbf{r}$:

$$J(\mathbf{r}) = \int dE\, J_E(\mathbf{r})\,, \qquad \text{with} \quad J_E(\mathbf{r}) = \sqrt{E}\, I_E(\mathbf{r})\,. \tag{144}$$

In the following, we will determine $J(z)$ by numerical iteration of (124), as a function of the position z in the slab, and parametrized by α which controls the collision strength.[19] Furthermore, $J_E(z)$ can be divided into an *elastic* and an *inelastic* component that do and do not conserve the respective *single-particle* energy[20]

$$J_E(z) = J_E^{(el)}(z)\,\delta(E - E_L) + J_E^{(inel)}(z)\,. \tag{145}$$

This in turn allows to define the elastic and the inelastic components $J^{(el)}(z) = \sqrt{E_L} I^{(el)}(z)$ and $J^{(inel)}(z) = \int dE\, \sqrt{E} I_E^{(inel)}(z)$ of the total flux density $J(z) = \int dE\, J_E(z) = J^{(el)}(z) + J^{(inel)}(z)$, which we will compare to the solution of the flux density $J^{(lin)}(z) = \sqrt{E_L} I(z)$ of the linear integral equation (100). As shown in (134), the latter is identical to the total flux density, i. e. $J^{(lin)}(z) = J(z)$.

19 A certain choice of parameters ($b = 40$ and $\alpha = 1/250$) has already been investigated in [164].

20 Due to the particle and energy flux conservation (131), the total energy is conserved.

Due to our prior assumptions,

- weak disorder potential ($k\ell_{dis} \gg 1$),
- collisions less frequent than scattering events off the disorder potential ($\ell_{int} \gg \ell_{dis}$),
- s-wave scattering approximation ($ka_s \ll 1$),
- dilute gas limit ($a_s \rho_0^{1/3} \ll 1$),

we infer $\alpha = \ell_{dis}/\ell_{int} \ll 1$ (see (127)), and the following chain of inequalities:

$$a_s \ll \left[k^{-1}\,,\, \rho_0^{-1/3}\right] \ll \ell_{dis} \ll \ell_{int}\,. \tag{146}$$

Typical experimental parameters for ultracold bosonic gases are within the range $\rho_0 \simeq (10^{18} - 10^{21})\mathrm{m}^{-3}$ and $a_s \simeq (10^{-8} - 10^{-9})\mathrm{m}$ [110], respectively, what allows $\ell_{int} \simeq (4\mathrm{x}10^{-2} - 4\mathrm{x}10^{-7})\mathrm{m}$ to vary over five orders of magnitude, see (109). Monte-Carlo simulations reveal [166] that the number of scattering events off the disorder potential scales with the squared optical

thickness b^2, whereas the corresponding number of collision events is suppressed by α, i. e. scales approximately as $b^2 \ell_{dis}/\ell_{int}$.

In accordance with the range of validity of our theory, we now plot in the left columns of Figs. 17 and 18 the elastic, inelastic, the combined total, and – for comparison – the linear flux density $J^{(el)}(z)$, $J^{(inel)}(z)$, $J(z)$, and $J^{(lin)}(z)$, respectively, for different slab sizes b and nonlinear parameter α.

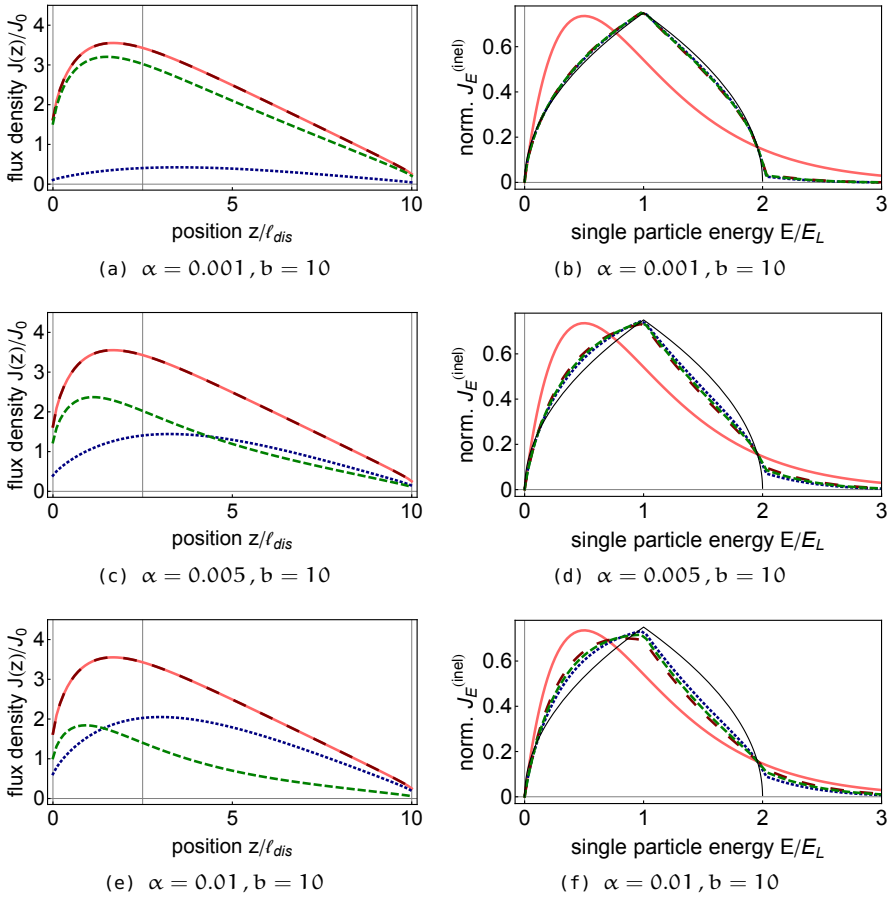

Figure 17: *Left column:* Different components of the total flux density normalized to the incoming flux density $J_0(z)$ for a slab of thickness $b = 10$ and increasing nonlinear collision strength $\alpha = 0.001$ (a), $\alpha = 0.005$ (c), $\alpha = 0.01$ (e). The (salmon) solid line and the (red) long-dashed line, i. e. $J^{(lin)}(z)$ and $J(z)$, are identical, a consequence of (134). Observe, how the inelastic flux density $J^{(inel)}(z)$ ((blue) dotted line) starts to dominate over the elastic flux density $J^{(el)}(z)$ ((green) dashed line) with increasing α. *Right column:* Normalized inelastic spectral flux density as a function of the single particle energy E/E_L (same parameters as on the left side). Here, the (blue) dotted line, the (green) dashed line, and the (red) long-dashed line correspond to different positions $z = 0$, $z = b/4$, and $z = b$ of $J^{(inel)}(z)$ within the slab (marked by vertical (gray) lines in the plots to the left), respectively. Here, the emergence of an inelastic flux density goes along with a collision-induced thermalization of the atomic cloud. With increasing slab depth, the inelastic particle current slightly moves from the thin (black) solid line, i. e. the normalized inelastic flux density of a *single* inelastic collision $\sqrt{E} f^L_{E_L,E_L,E}/(-\sqrt{E_L} g^L_{E_L,E_L})$, cf. (129) and (131) for the normalization, towards the (salmon) solid line representing the Maxwell-Boltzmann distribution $J^{(MB)}_E = 4E \exp[-2E/E_L]/E_L^2$, cf. (137).

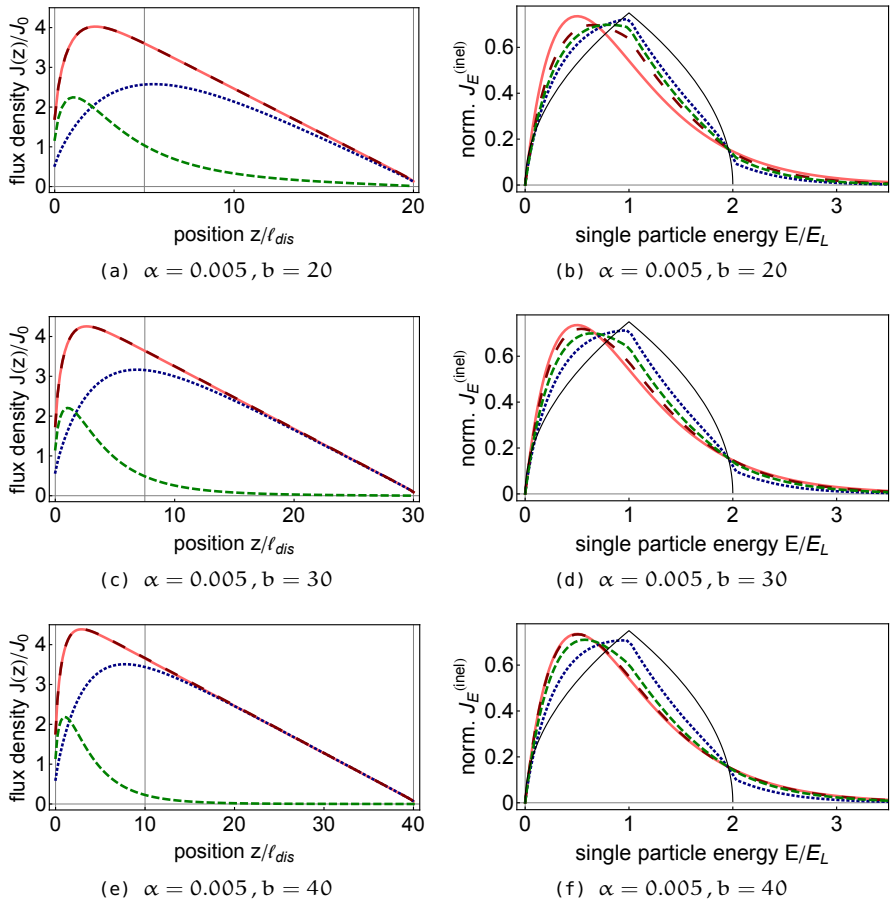

Figure 18: Same as in Fig. 17 but for increasing optical thickness and fixed $\alpha = 0.005$. *Left column:* Here, the dominance of the inelastic flux density $J^{(inel)}(z)$ ((blue) dotted line) over the elastic flux density $J^{(el)}(z)$ ((green) dashed line) is is emphasized in dependence of increasing slab length, $b = 20$ (a), $b = 30$ (c), and $b = 40$ (e). *Right column:* Consequently, also the equilibration of the normalized inelastic spectral flux density is more pronounced. The distribution at the end of the slab in (f), i. e. the (red) long-dashed line, cannot be distinguished from the thermal distribution, i. e. the (salmon) solid line, cf. also Fig. 19.

The equivalence of the linear flux density and of the total flux density, as mentioned at the beginning of this section, is reflected in our data, and can be checked by comparison of the (salmon) solid and of the (red) long-dashed lines in the left columns of Figs. 17 and 18. Both contributions show an initial rapid increase of the density in the slab which then decreases linearly towards the end of the slab – a behavior that has already been observed in Fig. 11. Remember that those curves are the same as predicted by the solution of the Gross-Pitaevskii equation, see (142), where the nonlinear terms cancel each other due to $\tilde{g} \in \mathbb{R}$.

Beyond the realm of the Gross-Pitaevskii equation lies the separation of the total flux density into elastic and inelastic contributions. We observe that for very small nonlinear parameter α and/or small optical thickness b, cf. Fig. 17a), the elastic component dominates the transport within the slab, and the impact of the collisions on the ladder component, i. e. the contribution described by the inelastic contribution, is very small. However,

if we increase α and/or the optical thickness b, but ensure $\alpha \ll 1$, the elastic component still dominates at the beginning of the slab, where only few collisions have occurred so far, but is rapidly overtaken by the inelastic component after only a few disorder events (i. e. for z of the order of few ℓ_{dis}) within the slab, see Figs. 17e) and 18).

3.4.2 *Spectral Flux Density Inside the Slab and the Creation of a Thermal Cloud*

We focus now on the inelastic component of the flux density and, in particular, on its normalized spectral decomposition, i. e. $J_E^{(\mathrm{inel})}(z)$ in (145), depicted for different depths z in the slab in the right columns of Figs. 17 and 18.

This continuous emergence of the inelastic component of the flux, and the simultaneous disappearance of the elastic component, are tantamount to the formation of what is colloquially called a *non-condensed fraction* or *thermal cloud*, see also the discussion in Section 2.2.2 and 2.2.3. The corresponding *depletion* of the condensate can be understood as follows: In the initial (non-interacting) state, see (35), all N particles are described by the same single-particle state, that – via the formal definition of a condensate via the one-particle density matrix, i. e. the *Penrose-Onsager criterion* [83] and references therein, – corresponds to a pure state, i. e. a pure condensate. Hence, the initial N-particle state factorizes and can be expressed as an N-fold product of a single-particle state where fixed total energy implies fixed energies also for the individual particles. The evolution of this single-particle state is described by the Gross-Pitaevskii equation, which – as we saw – is identical to the elastic contribution of the integral equation (124). This in turn means that scattering off the disorder potential – despite the population of modes with different momenta – amounts to a coherent process which can still be described by a single superposition state of these momenta. Thereby the condensate adapts to the presence of the disorder potential. The inelastic scattering process, however, involves two distinct particles that interact with each other and change their single-particle energies to eventually form a "thermal" cloud. The interplay of the nonlinear collision strength α and the optical thickness b hereby strongly determines this process. The opposite process where two particles of the "thermal" cloud collide and re-enter the condensate mode has a negligible probability for the case of a weak (disorder) potential. This is due to the infinite number of continuously distributed and infinitely extended modes into which the particles can scatter, i. e. the absence of a bound state (as found e. g. for setups including a trap) in which a condensate could form.

In Fig. 17b) we observe that, for small α and b, the spectral inelastic flux density only slightly differs from the spectral distribution to the flux density of a *single* inelastic two-particle collision event $\sqrt{E} f^L_{E_L,E_L,E}/(-\sqrt{E_L} g^L_{E_L,E_L})$ (thin (black) solid line), cf. eqs. (129) and (131) for the normalization. Hence, the probability for a given particle to take part in more than a *single* inelastic collision is very low for the chosen set of parameters. However, by increasing α and/or b, the spectral distribution evolves, while the particles propagate deeper into the slab, towards a thermal distribution, cf. the (salmon) solid lines in the right columns of Figs. 17 and 18 and eq. (137).

Since the integrated flux density (after reaching its maximum at the beginning of the slab) decreases linearly as a function of the depth in the slab, collisions become very unlikely towards the end of the slab, and the spectral distributions of the inelastic flux density are only slightly altered between $z = L/4$ and $z = L$. This also manifests in Fig. 19, where we see that the

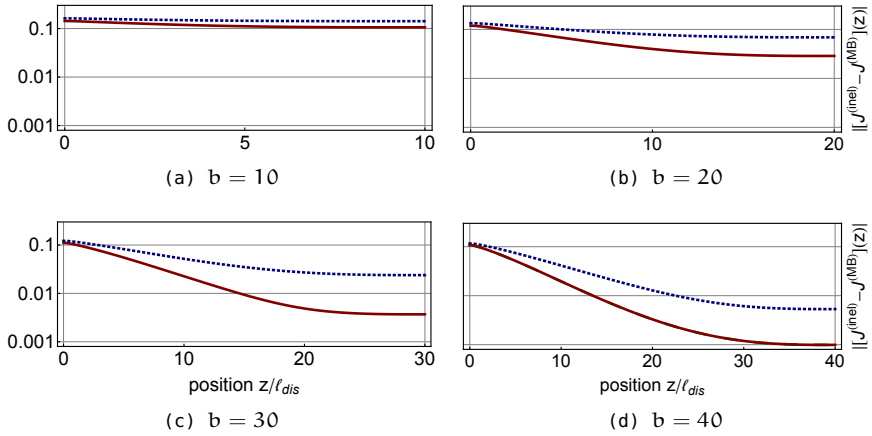

(a) b = 10 (b) b = 20

(c) b = 30 (d) b = 40

Figure 19: Absolute difference between the Maxwell-Boltzmann distribution and the inelastic spectral flux density as a function of the depth in the slab z, see (137) and (147). In all plots, the (blue) dashed and the (red) solid line correspond to $\alpha = 0.005$ and $\alpha = 0.01$, respectively. For the purpose of comparing the influence of the slab length on the thermalization dynamics, we choose the same logarithmic scale for all vertical axes. The discussion before (137) showed that exact agreement with the Maxwell-Boltzmann distribution is only achieved for $z \to \infty$, whereas the contribution to thermalization is most pronounced where the particle density is highest, i. e. in the first half of the slab.

difference between the (normalized) inelastic and the Maxwell-Boltzmann flux density,

$$\left|\left| J_E^{(\mathrm{inel})}(z) - J_E^{(\mathrm{MB})}(z) \right|\right| = \sqrt{E_L \int \mathrm{d}E \, \left[J_E^{(\mathrm{inel})}(z) - J_E^{(\mathrm{MB})}(z) \right]^2}, \tag{147}$$

saturates as a function of the position in the slab. Whereas full thermalization, of course, requires an infinite slab, it is nonetheless possible to roughly determine the number of collision processes which are sufficient to reach the degree of thermalization we observe in our simulation. From the width of a single inelastic two-particle collision ($\sim 0.5 E_L$) we can estimate that $\mathcal{O}(10)$ collision events lead to a sufficient energy spread for the distribution to become quasi-thermal. This is in accord with our observation of roughly $\alpha b^2 \sim 10$ collision events leading to a quasi-thermal distribution in Fig. 18f).

3.4.3 *Comments Regarding Our Results*

It is instructive to go back to Section 1.3, in order to gain some understanding for the mechanisms at work which lead to "thermalization" in a closed and unitary setup like ours. Within the proposed mechanism of eigenstate thermalization [67, 68, 167] it can be proven that a quantum system will equilibrate towards a Maxwell-Boltzmann distribution if the classical analogue of the quantum system shows chaotic behavior. Srednicki [68] considers a gas of N particles with mass m, radius a, and hard-core interaction in the semiclassical limit, $k^{-1} \leqslant a \ll \rho_0^{-1/3}$, as the classical counterpart of a cold quantum gas, where the eigenstates can be expressed as random superposition of plane waves. Precisely this condition – also known as *Berry's conjecture* [168] – breaks the integrability of the underlying system and allows the

eigenstates to mediate diffusive transport in phase space. As a consequence, the quantum system mimics "thermalization" by purely unitary dynamics.

Although we apply a different restriction $a_s \ll \left[k^{-1}, \rho_0^{-1/3}\right] \ll \ell_{dis}$, see (146), we find ourselves in the semiclassical, i. e. the weak disorder potential, limit, where it can be shown that the amplitudes, from which the ladder density is formed, coincide with a stationary Gaussian stochastic process [163, 169]. Hence, from the eigenstate thermalization hypothesis, "thermalization" is also expected for our setup, where the role of the disorder potential is precisely to randomize the individual particle's momenta, as a necessary prerequisite for seeding inelastic collision events [164].

Let us also mention again that our theory is limited to a certain parameter regime, in particular $k\ell_{dis} \gg 1$ and the inequalities (146). Strictly speaking, our theory fails to properly predict the behavior of particles with energy $E \to 0$ when we switch from the regime of weak to strong disorder $\sqrt{E}\ell_{dis} \leqslant 1$.[21] The formerly – over the whole disorder potential – extended eigenstates become now exponentially localized and particles below a certain energy become trapped. If our initial single-particle energy lies below the corresponding critical temperature for condensation – which is not excluded by (146) – we expect that fragmented condensates can form in the minima of the strong disorder potential [170] provided that the finite lifetime of the localized state is larger than the time needed to form a condensate [142, 171]. For a critical disorder strength one even expects to observe a quantum phase transition to the *Bose-glass phase* [40, 75, 172, 173]. These effects, however, require a different theoretical treatment and thus lie beyond the scope of this thesis.

21 Note, however, that for $\ell_{dis} \to \infty$, i. e. very weak disorder potentials, the fraction of particles with energy $\sqrt{E} < \ell_{dis}^{-1}$ becomes smaller and smaller.

In Section 2.2 we discussed the relevance of the quantum Boltzmann equation for our description, a discussion we like to prolong here. For the stationary case, we found that the Maxwell-Boltzmann distribution (137) solves the integral equation (123) as a consequence of the conserved particle and energy flux for the collision contributions, see (131) and (136). The same reasoning holds for the quantum Boltzmann equation (16) where – in the stationary limit and for vanishing external potential[22] – the linear propagation vanishes and the *H-theorem* [13] applied to the collision integral (20) leads to a Maxwell-Boltzmann distribution.

22 In our case, the disorder potential is already included within the average Green's functions, i. e. within the single-particle density (100).

Similarly, we already discussed in Section 3.2 that the linear transport of the quantum Boltzmann equation, in our case, involves averages over the random disorder potential and is thus given by the radiative transfer equation (103), the differential version of the integral equation (100). Our treatment thus combines the two general cases treated in the literature [5], where either a scenario of *one* particle within a random bath (Lorentz gas) or a dilute gas of N interacting particles without random disorder is discussed, and the validity of the derived equations strongly relies on scaling arguments. As it turns out in our stationary case, averaged over many realizations of the disorder potential, it is precisely the combination of *both* effects which allowed us to exactly quantify the regime of validity of our final integral equation (123) in terms of the parameters k, ℓ_{dis}, and ℓ_{int}.

Further support for our treatment and the immense simplification comes from a recent work by Benedetto et al. [129]. In their work, they treat the N interacting particle case in terms of a resummation of collision diagrams. They subdivide the full collision process of all particles into subcollision events which are connected by free flights of single particles. In our

language, the sub-collision events and the free single-particle flights correspond to single collision events g^L and f^L (and the subsequent trace over the undetected particle), and a required intermediate scattering off the disorder potential due to the condition $\ell_{\text{int}} \gg \ell_{\text{dis}}$, respectively. However, due to the presence of the weak disorder potential we can neglect recurrent collisions of two particles, what drastically simplifies the complicated resummation of the scattering series for the sub-collision events as encountered in [129].

3.5 SUMMARY

In this chapter, we started from the textbook derivation of linear diffusive transport of the average flux density in weak random disorder potentials, and expanded the former by taking into account binary collisions in a dilute gas of cold bosons.

The main result is the derivation of an integral equation which, upon iteration, predicts the stationary flux density of particles, injected with a certain energy, inside the slab. We demonstrated how this equation improves on the description by the Gross-Pitaevskii equation, and predicts – as a function of experimentally tunable parameters – the dynamical transition of an initial equilibrium condensate state to a thermalized single particle spectral density of the atoms as they travel across the slab. This elucidates the colloquial "formation of a thermal cloud" through fully unitary, non-equilibrium many-particle dynamics.

Finally, we extended our point of view and showed how our theoretical description is reflected in recent efforts of deriving a nonlinear quantum Boltzmann equation. Due to the presence of the weak disorder potential, we are able to explicitly quantify the regime of validity of our theory, which we demonstrated to take the form of a Boltzmann equation.

4 COHERENT TRANSPORT IN A SLAB GEOMETRY

In Section 3.2 we introduced the diagrammatic representation of incoherent transport in a weakly disordered slab, i. e. the so-called ladder diagrams. They were shown to be the only relevant diagrammatic component after averaging over the weak disorder potential. All other contributions are at least suppressed by the very small factor $1/(k\ell_{dis}) \ll 1$ (since $k\ell_{dis} \gg 1$). However, in addition to this contribution, which we identified as (classically) diffusive, hence phase-independent transport, there exists a small correction for the case of time-reversal symmetric media: The effect of coherent backscattering (CBS) – a phase-sensitive effect which, as the name states, only yields a relevant contribution in the direction opposite to the incoming source field.[1]

In this chapter we want to unravel to what extent the coherent transport dynamics, i. e. the height and width of the coherent backscattering cone, is affected by elastic and inelastic collisions. First of all, we review the effect of *linear* coherent backscattering, i. e. a single particle effect in the presence of the weak disorder potential only.

As a next step, we introduce particle collisions and, as in the previous chapter, identify elastic contributions that correspond to the solution of the Gross-Pitaevskii equation, as well as inelastic contributions that exceed the former. It will be instructive to see how the inelastic contribution, to some extent, counteracts the dephasing which arises due to the nonlinear term of the Gross-Pitaevskii equation. For larger nonlinearities, however, the overall dephasing outweighs this effect, and the coherent backscattering effect vanishes as the width of the inelastic cone goes to zero for $k\ell_{dis} \to \infty$.

1 Note that CBS only occurs for the average (flux) density. For a single realization of the disorder potential, the major scattering contribution results from random and different scattering paths for ψ and ψ^* that give rise to a rapidly fluctuating signal commonly known as *speckle pattern* [174], cf. Section 2.1.

4.1 LINEAR COHERENT BACKSCATTERING

Fig. 20 illustrates how to obtain the diagrammatic correction to the ladder density, namely by inverting one of the scattering amplitudes and hence producing a counter-propagating pair of amplitudes that visits the same sequence of scatterers in opposite order. For time-reversal symmetric media, this phase-sensitive *crossed* component (also called *Cooperon* in the literature [48]) contributes to the averaged scattering signal if the requirement for constructive interference is fulfilled, i. e. if the two scattering paths are exactly equal in length. On average, this is the case only in backscattering direction, $\theta = 0$, as depicted in Fig. 20c). For the ideal case of a stationary disorder potential and neglecting single scattering contributions, the backscattered density can be enhanced by a factor of two. The width of the cone is proportional to $1/(k\ell_{dis})$, whereas its height, characterized via the interference contrast or enhancement factor, i. e.

$$\text{enhancement factor} = 1 + \frac{\text{crossed density}(\theta = 0)}{\text{ladder density}(\theta = 0)}\,, \tag{148}$$

will depend on various dephasing mechanisms, which will be in the focus of the following sections.

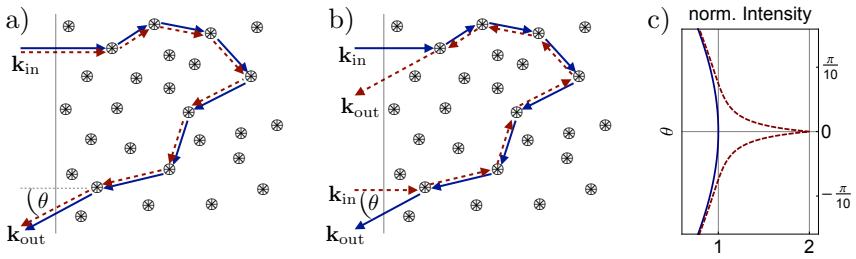

Figure 20: Exemplary scattering paths at the slab interface (thin vertical line) for the averaged ladder (a) and crossed (b) density as a function of their angle of emission θ from the slab, respectively. For the case of linear scattering we have $|\mathbf{k}_{in}| = |\mathbf{k}_{out}|$. The density of the phase-independent ladder contribution (solid line in (c), normalized to unity for $\theta = 0$) is only weakly θ-dependent, in contrast to the phase-sensitive crossed contribution (dashed line in (c)) that has maximal contrast for identical path-length of $\langle\psi|$ and $|\psi^*\rangle$, i. e. $\theta = 0$. The functional dependence of (c) for a semi-infinite medium, which includes the diffusion approximation and the neglect of single scattering, can be found in eqs. (8.16) (ladder) and (8.28) (crossed) in [48], and is here evaluated for $k_L \ell_{dis} = 10$.

4.1.1 *Integral Equation for the Average Density*

In contrast to the average ladder density (100) within the slab, where all phase factors cancel, the average crossed density depends on the sum of the incoming and outgoing wave vectors $\mathbf{q} = \mathbf{k}_{in} + \mathbf{k}_{out}$, however with $|\mathbf{k}_{in}| = k_{in} = k_{out} = |\mathbf{k}_{out}|$ for the linear case. Inspection of Fig. 20 tells us that the only difference between (a) and (b) occurs prior to the first and after the last scattering event within the slab, where due to the different path lengths the exponential attenuation factors for each path have to be adjusted and a difference of phase $e^{i\mathbf{q}\mathbf{r}}$ is acquired. In accordance with these observations, the average crossed density $C(\mathbf{r}, \mathbf{q})$ inside the medium can be obtained by modification of eq. (100) [48] as

$$C(\mathbf{r}, \mathbf{q}) = C_0(\mathbf{r}, \mathbf{q}) + \int d\mathbf{r}' \, \frac{e^{-|\mathbf{r}-\mathbf{r}'|/\ell_{dis}}}{4\pi\ell_{dis}|\mathbf{r}-\mathbf{r}'|^2} C(\mathbf{r}', \mathbf{q}) \,, \tag{149}$$

with

$$C_0(\mathbf{r}, \mathbf{q}) = C_0 e^{-z/(2\ell_{dis})} e^{-z/(2\ell_{dis}\cos\theta)} e^{i\mathbf{q}\mathbf{r}} \,, \tag{150}$$

and $C_0 = \rho_0$. In addition to the average ladder density eq. (100), the source term (150) now contains the additional phase factor $e^{i\mathbf{q}\mathbf{r}}$, as motivated above, and two different attenuation factors $e^{-z/(2\ell_{dis})}$ and $e^{-z/(2\ell_{dis}\cos\theta)}$ which account for the absorption of the perpendicularly incident source amplitude inside the slab and the – under the angle θ – emitted amplitude in the direction of the detector, respectively. For the exact backscattering direction, i. e. $\theta = 0$ and $\mathbf{q} = 0$, (149) reproduces the average ladder density, eq. (100), where again

$$\mathbf{q} = \mathbf{k}_{in} + \mathbf{k}_{out} = \begin{pmatrix} k_D \sin\theta \\ 0 \\ k_L - k_D \cos\theta \end{pmatrix} ,$$

with $k_L = k_{in}$ and $k_D = k_{out}$. Adaptation of eq. (149) to the slab geometry yields an equation for the transverse Fourier transform $\widetilde{C}(z, \mathbf{q})$ of $C(\mathbf{r}, \mathbf{q})$, see

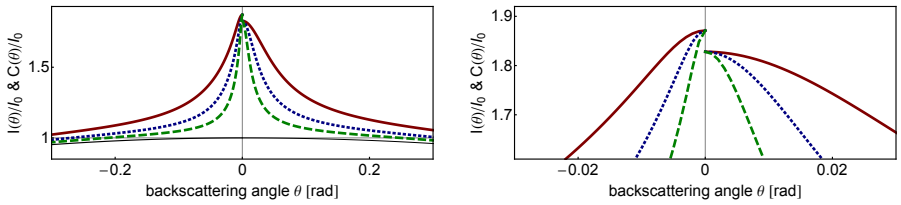

Figure 21: Normalized density for the ladder and the crossed component expressed here as $\gamma^{L}_{(lin)}(\theta)/\gamma^{L}_{(lin)}(0)$ and $[\gamma^{L}_{(lin)}(\theta)+\gamma^{C}_{(lin)}(\theta)]/\gamma^{L}_{(lin)}(0)$, respectively, see (151), as a function of the backscattering angle θ. Negative and positive θ correspond to an optical thickness of $b = 25$ and $b = 5$, respectively. The thin (black) solid line corresponds to the weakly angle-dependent ladder contribution (equally for different values of b and $k_L\ell_{dis}$), whereas the (red) solid line, the (blue) dotted line, and the (green) dashed line correspond to $k_L\ell_{dis} = 10$, 20, and 40, respectively. The right plot is a magnification of the left one and demonstrates how the cone slowly develops a cusp with increasing optical thickness. Note the enhancement factor $(1 + \text{crossed/ladder}) < 2$, due to the presence of the single-scattering contribution in $\gamma^{L}_{(lin)}(\theta)$.

eq. (329), which only depends on z and $\mathbf{q}$. This equation – the pendant of eq. (104) – can be found in eq. (341) in Appendix D.2 where we also give its detailed derivation.

However, as the effects of the crossed component become apparent only in the far-field of the slab, we introduce the *bistatic coefficient* (also known as *albedo* in different fields of physics) [160]. The bistatic coefficient describes the normalized density with respect to the incoming density at a detector located at point $\mathbf{R}$ in the far field of the slab. The respective coefficients for the ladder and crossed component are simply obtained by integrating over all points within the slab from which a scattering signal (weighted with the depth z) can reach the detector (the corresponding derivation can also be found in Appendix D.1 and D.2):

$$\gamma^{L}_{(lin)}(\theta) = \frac{1}{\ell_{dis}\, I_0}\int_0^L dz\, I(z) e^{-z/(\ell_{dis}\cos\theta)}\,, \tag{151}$$

$$\gamma^{C}_{(lin)}(\theta) = \frac{1}{\ell_{dis}\, C_0}\int_0^L dz\, \Big[\widetilde{C}(z,\mathbf{q}) e^{-z(1+1/\cos\theta)/(2\ell_{dis})} e^{-iq_z z} - \widetilde{C}_0(z,\mathbf{q}) e^{-z(1+1/\cos\theta)/(2\ell_{dis})} e^{-iq_z z}\Big]\,,$$

with $\widetilde{C}_0(z,\mathbf{q})$ and $\widetilde{C}(z,\mathbf{q})$ being the transverse Fourier transforms of $C_0(\mathbf{r},\mathbf{q})$ and $C(\mathbf{r},\mathbf{q})$, respectively, see eq. (329). We subtracted the single scattering contribution (in the second line) from $\gamma^{C}_{(lin)}(\theta)$ as this term appears identically[2] in $\gamma^{L}_{(lin)}(\theta)$ and would otherwise be double-counted. This is due to the fact that a singly scattered amplitude exhibits no distinct reversed counterpart; at least two disorder scattering events are required to obtain a distinct reversed path.

Exemplary normalized ladder and crossed intensities as detected in the far-field of the slab are plotted for $k_L\ell_{dis} = 10$ in Fig. 20c), where we neglect the contribution of single scattering such as to obtain the maximal enhancement by a factor of two in backscattering direction. It becomes obvious that the crossed component is strongly dependent on the backscattering angle whereas the ladder component is not. The backscattering cone develops a cusp for a semi-infinite medium, cf. Fig. 20c), where the scattering paths can become arbitrarily long [48]. Since the longest scattering paths, by definition,

2 The equivalence can be seen upon inserting the source ladder density $I_0(z) = \rho_0 e^{-z/\ell_{dis}}$, eq. (102), for $I(z)$ in $\gamma^{L}_{(lin)}(\theta)$, and after the corresponding replacement of $\widetilde{C}_0(z,\mathbf{q}) = \rho_0 e^{-z(1+1/\cos\theta)/(2\ell_{dis})} e^{iq_z z}$, cf. eq. (150) and the discussion in Appendix D.2, in the second line of $\gamma^{C}_{(lin)}(\theta)$.

are those which are most phase-sensitive, they will mostly contribute to the backscattering signal for very small angles $\theta \ll 1$ (whereas the contrary is true for short scattering paths). As observable in Fig. 21, for a finite medium the longest paths are limited by the size of the slab, and as a result the cone appears rather rounded. Fig. 21 furthermore illustrates that the cone width is inversely proportional to $k_L \ell_{dis}$, whereas the ladder contribution is independent of the parameter $k_L \ell_{dis}$.[3]

3 By construction, the ladder component only depends on the slab thickness b whose effect remains hidden, here due to the normalization $\gamma^L_{(lin)}(0) = 1$ in Figs. 20c) and Fig. 21.

Although the crossed contribution constitutes an important effect around backscattering direction $\theta = 0$, it decays quickly as a function of θ, and therefore yields only a very small correction with respect to the total ladder contribution integrated over all angles. This allows us to introduce the crossed effect in addition to the ladder contribution under neglect of mutual coupling effects due to flux conservation. Obviously, the total ladder contribution has to be reduced in order to allow for an enhanced backscattering signal without violating flux conservation. Since we neglect this effect here, we note that this reduction of the ladder contribution has been carefully measured [175], and recently the diagrams have been identified which allow one to predict these small corrections within a diagrammatic theory [176].

4.2 NONLINEAR COHERENT BACKSCATTERING

As discussed in the last section, linear coherent backscattering in the absence of single scattering, although a phase-sensitive effect, always leads to an enhancement of the backscattered density by a factor of two in exact backscattering direction, since the phase factors completely cancel each other for $\theta = 0$.

However, this pictures changes dramatically if one allows for dephasing mechanisms to be present along the path of a crossed diagram. Then, a decrease of the enhancement factor is observed. Physically, dephasing could originate from thermal effects or effects of polarization within the scattering medium, as e. g. observed when scattering laser light from a cold atomic gas [177, 178]. An equivalent scenario is given by the nonlinear Gross-Pitaevskii equation for Bose-Einstein condensates, eq. (142), where the atom-atom interaction serves as a source of dephasing, see Section 4.3. Although predicted theoretically e. g. by [44, 62, 63], an experimental observation – as a proof of principle – has only been conducted for the case of non-interacting atoms [55, 56].[4] In addition to the dephasing induced by elastic collisions as described by the Gross-Pitaevskii equation, we will focus in this thesis on the influence of inelastic collisions, which lead to another dephasing mechanism for matter waves. Again, a similar situation[5] has been investigated for strong laser light fields scattering off cold atomic gases, where the saturation of the atomic dipole transition leads to inelastic scattering [61, 169, 179–182]. A corresponding reduction of the coherent backscattering enhancement was measured [59], but a clarifying answer whether the reduction is based on elastic or inelastic scattering is still missing. For atoms, we give the answer below.

4 The resolution of the experiments [55, 56] only allows to identify the presence of a coherent backscattering cone. Dephasing effects that are experimentally present in addition to the very small residual atom-atom interaction have not been quantified yet.

5 Here, the disorder potential is realized by the randomly located atoms in the gas, the photons correspond to the atoms of the matter wave in our setup, and the elastic and inelastic particle-particle interaction is taken into account by the absorption and emission of the photons by the atoms.

4.2.1 *Diagrammatic Crossed Building Blocks*

In this section, we determine the elementary building blocks in order to describe nonlinear crossed transport processes. In Fig. 13 in Chapter 3, we

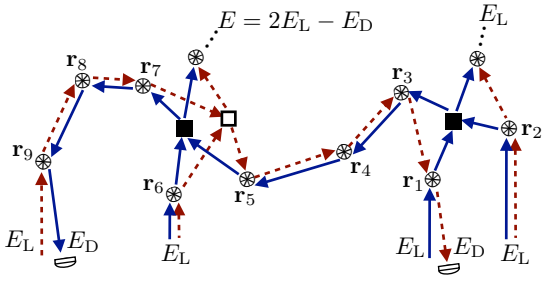

Figure 22: Exemplary nonlinear crossed diagram obtained by inversion of one of the (red) dashed amplitudes from the corresponding ladder diagram in Fig. 13.

depicted an exemplary ladder diagram for three particles. A corresponding three-particle crossed diagram is shown in Fig. 22. It consists of fundamental crossed building blocks, which are summarized in Fig. 23. As explained in Section 4.1, crossed diagrams are obtained by reversing the direction of one of the scattering amplitudes of the building blocks defined in Fig. 12. Additionally, the energies of counter-propagating scattering amplitudes can be, in principle, different from each other, according to the possibility $|\mathbf{k}_{in}| \neq |\mathbf{k}_{out}|$ in Fig. 20. However, energy has to be conserved for each scattering amplitude, which in turn enforces the following relation for the conjugate single-particle energies E and $\overline{E}$:

$$\overline{E} = E_L + E_D - E\,, \tag{152}$$

with $E_L = k_{in}^2$ and $E_D = k_{out}^2$. The limit of linear crossed transport is, of course, reestablished for $E = E_D = E_L$, and thus $\overline{E} = E_L$.

The linear crossed building block, Fig. 23a), is related to the linear ladder component (108) as follows:

$$\begin{aligned} P_E^C(\mathbf{r}_1, \mathbf{r}_2) &= \frac{4\pi}{\ell_{dis}} \iint \frac{d\mathbf{k}_1\, d\mathbf{k}_2}{(2\pi)^6}\, e^{-i(\mathbf{k}_1 - \mathbf{k}_2)(\mathbf{r}_1 - \mathbf{r}_2)} G_E(k_1) G_{\overline{E}}^*(k_2) \\ &= P_E(\mathbf{r}_1, \mathbf{r}_2) e^{i|\mathbf{r}_1 - \mathbf{r}_2|(k - \overline{k})}\,, \end{aligned} \tag{153}$$

where $\overline{k} = \sqrt{\overline{E}}$ as usual, and it is implicitly understood that $P_E^C(\mathbf{r}) = P_{E,\overline{E}}^C(\mathbf{r})$ via relation (152). The only difference to (108) lies in the crossed-specific phase factors which arise due to the two different average Green's functions at energies E and $\overline{E}$, respectively, in (153).

In contrast to Fig. 23a), we have two possibilities to reverse one of the arrows for g^L, depicted in Fig. 12b). The first contribution amounts to the elastic contribution, Fig. 23b),

$$\begin{aligned} g_{E_1,E_2}^C(\mathbf{r}_1, \mathbf{r}_2, \mathbf{r}_3) = \left(\frac{4\pi}{\ell_{dis}}\right)^2 \int \frac{d\mathbf{k}_1 \ldots d\mathbf{k}_5}{(2\pi)^{15}} \langle \mathbf{k}_3, \mathbf{k}_4 | \hat{T}_U^{(2)}(E_1 + E_2) | \mathbf{k}_1, \mathbf{k}_2 \rangle \\ \times e^{-i[(\mathbf{k}_1 - \mathbf{k}_4)\cdot\mathbf{r}_1 + (\mathbf{k}_2 + \mathbf{k}_5)\cdot\mathbf{r}_2 - (\mathbf{k}_5 + \mathbf{k}_3)\cdot\mathbf{r}_3]} \\ \times G_{E_1}(k_1) G_{E_2}(k_2) G_{E_2}(k_3) G_{E_1}^*(k_4) G_{\overline{E}_2}^*(k_5)\,, \end{aligned} \tag{154}$$

where we kept – in order not to overload Fig. 23b) – the notation for the wave vectors used in Fig. 12b). The trace over the undetected particle for the crossed contribution (154) is conducted as for the corresponding ladder component and yields again $G_{E_1}^*(k_4)$, see Section 2.3 for further details.

In Fig. 12b) we included the complex conjugate diagram into the definition of g^L. For the crossed case, we treat the complex conjugate diagram

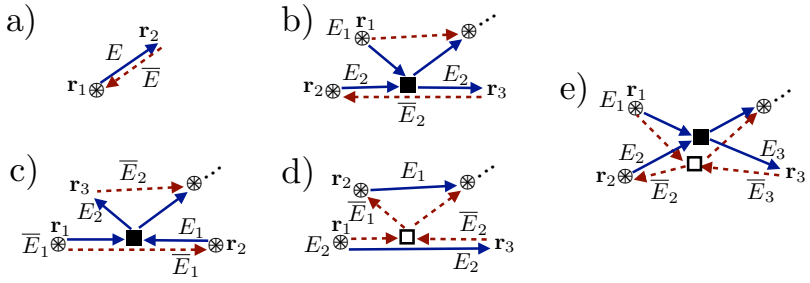

Figure 23: Collection of all diagrammatic crossed building blocks which are obtained by inversion of one of the corresponding arrows from Fig. 12, and under consideration of energy conservation, see eq. (152). The propagation direction of the crossed density is defined by the (blue) solid arrow. The linear propagation $P^{C}_{E}(\mathbf{r}_1,\mathbf{r}_2)$ (a), see (153), and the inelastic collision process $f^{C}_{E_1,E_2,E_3}(\mathbf{r}_1,\mathbf{r}_2,\mathbf{r}_3)$ (e), see (158), are uniquely defined with respect to their ladder counterparts. An ambiguity exists for the crossed counterpart of the elastic ladder collision process. Depending on which arrow is inverted, we obtain an elastic contribution $g^{C}_{E_1,E_2}(\mathbf{r}_1,\mathbf{r}_2,\mathbf{r}_3)$ (b) and its complex conjugate (not shown), see (154) and (155), respectively, and the two inelastic contributions $h^{C}_{E_1,E_2}(\mathbf{r}_1,\mathbf{r}_2,\mathbf{r}_3)$ (c) and $\left[h^{C}_{E_2,\overline{E}_1}(\mathbf{r}_1,\mathbf{r}_2,\mathbf{r}_3)\right]^*$ (d), see (156) and (157), respectively. Note that for reasons of clarity the amplitudes are not labelled by wave vectors. We, however, use the same notation as in Fig. 12 for our calculations.

of Fig. 23b) (not shown in Fig. 23) separately as it requires an additional replacement $E_2 \to \overline{E}_2$:

$$\tilde{g}^{C}_{E_1,E_2}(\mathbf{r}_1,\mathbf{r}_2,\mathbf{r}_3) = \left[g^{C}_{E_1,\overline{E}_2}(\mathbf{r}_1,\mathbf{r}_2,\mathbf{r}_3)\right]^* . \tag{155}$$

This relation can be easily checked by looking at the diagrams in Fig. 23b) (keeping in mind that the solid arrow defines the direction of propagation, and that complex conjugation amounts to turning solid into dashed arrows, and vice versa).

The second contribution, where the other arrow of Fig. 12b) is reversed, is depicted in Fig. 23c) and d), respectively. As we will see, once an inelastic diagram of type Fig. 23e) or Fig. 12c) has taken place, the diagrams of type Fig. 23c) and d) can reshuffle the single-particle energies and therefore also contribute to the inelastic flux. Fig. 23c) is calculated as follows:

$$\begin{aligned} h^{C}_{E_1,E_2}(\mathbf{r}_1,\mathbf{r}_2,\mathbf{r}_3) = \left(\frac{4\pi}{\ell_{dis}}\right)^2 \int \frac{d\mathbf{k}_1 \ldots d\mathbf{k}_5}{(2\pi)^{15}} \langle \mathbf{k}_1,\mathbf{k}_4|\hat{T}^{(2)}_{U}(E_1+\overline{E}_1)|\mathbf{k}_2,\mathbf{k}_3\rangle \\ \times e^{-i[(\mathbf{k}_2-\mathbf{k}_5)\cdot\mathbf{r}_1+(\mathbf{k}_5+\mathbf{k}_3)\cdot\mathbf{r}_2-(\mathbf{k}_1+\mathbf{k}_4)\cdot\mathbf{r}_3]} \\ \times G_{E_2}(k_1)G_{\overline{E}_1}(k_2)G_{E_1}(k_3)G^*_{\overline{E}_2}(k_4)G^*_{\overline{E}_1}(k_5), \end{aligned} \tag{156}$$

where we again kept the notation for the wave vectors used in Fig. 12b), and the trace over the undetected particle is summarized within the contribution $G^*_{\overline{E}_2}(k_4)$. The diagram depicted in Fig. 23d) is related to Fig. 23c) by the transformation

$$\tilde{h}^{C}_{E_1,E_2}(\mathbf{r}_1,\mathbf{r}_2,\mathbf{r}_3) = \left[h^{C}_{\overline{E}_2,\overline{E}_1}(\mathbf{r}_1,\mathbf{r}_2,\mathbf{r}_3)\right]^* . \tag{157}$$

This relation can also be verified by looking at the diagrams in Fig. 23c) and d).

Finally, we present the calculation for the inelastic crossed diagram involving a collision for each amplitude, as depicted in Fig. 23e):

$$\begin{aligned} f^{C}_{E_1,E_2,E_3}(\mathbf{r}_1,\mathbf{r}_2,\mathbf{r}_3) = 4 \left(\frac{4\pi}{\ell_{dis}}\right)^2 \int \frac{d\mathbf{k}_4}{(2\pi)^3} \frac{G^*_{E_1+E_2-E_3}(k_4) - G_{E_1+E_2-E_3}(k_4)}{2\pi i} \\ \times \left\{ \frac{1}{2} \int \frac{d\mathbf{k}_1 d\mathbf{k}_2 d\mathbf{k}_3}{(2\pi)^9} e^{-i(\mathbf{k}_1\cdot\mathbf{r}_1+\mathbf{k}_2\cdot\mathbf{r}_2-\mathbf{k}_3\cdot\mathbf{r}_3)} \langle \mathbf{k}_3,\mathbf{k}_4|\hat{T}^{(2)}_U(E_1+E_2)|\mathbf{k}_1,\mathbf{k}_2\rangle \right. \\ \left. \times G_{E_1}(k_1) G_{E_2}(k_2) G_{E_3}(k_3) \right\} \\ \times \left\{ (\mathbf{k}_2 \leftrightarrow \mathbf{k}_3),\, (E_2 \leftrightarrow \overline{E}_3),\, (E_3 \leftrightarrow \overline{E}_2) \right\}^* \end{aligned} \tag{158}$$

Also here we retained the notation from Fig. 12c). Note, however, an additional factor of two for the crossed in comparison to the ladder component, which arises due to two possibilities to obtain a crossed diagram by reversing the arrows of the corresponding ladder diagram. The term in curly brackets in the second and third line appears twice, however with the replacements indicated in the last line. Note that the term which results from the trace over the undetected particle (the argument of the integral still in the first line of (158)) remains unchanged in comparison to eq. (111), since $E_1 + \overline{E}_3 - \overline{E}_2 = E_1 + E_2 - E_3$. The second and third, as well as the last line correspond to the contribution of the solid and dashed amplitudes (that connect the points $\mathbf{r}_1$, $\mathbf{r}_2$, and $\mathbf{r}_3$ with the collision events) in Fig. 23e), respectively.

4.2.2 *The Nonlinear Transport Equation for the Crossed Contribution*

Following the line of thought of Section 3.3, knowledge of the microscopic building blocks is sufficient to construct arbitrary scattering contributions for N interacting particles simply by connecting the outgoing arrows of each building block with the incoming arrows of another building block. For the ladder case, we thereby produced the integral equation (117).

For the crossed case, however, one discovers a relevant issue that was already brought up in a diagrammatic approach for the Gross-Pitaevskii equation [62], when the combination of certain diagrams leads to closed loops, i. e. dead ends within the diagrammatic theory. It turns out, however, that these *forbidden diagrams* cannot be reproduced by an iterative solution of the underlying nonlinear single-particle equation and, hence, must be excluded from the diagrammatic expansion of the theory [62, 163]. For our, a priori, many particle description, the forbidden diagram consists of a certain combination of the building blocks in Figs. 23c) and d) and is depicted in Fig. 24a). By inspecting this diagram in more detail, one discovers that the detected amplitudes are unaffected by the collisions of their respective conjugated amplitudes. In other words, the diagram in Fig. 24a) is *redundant* as is does not affect the propagation of the detected amplitudes.[6] This is in contrast to Fig. 24b), where the collisions really affect the detected amplitudes.

Thus, in order to formulate an applicable theory, we have to split the desired integral equation into two parts such that Fig. 24b) is allowed, but Fig. 24a) is suppressed. Consequently, we write down an integral equation for the nonlinear crossed component involving the contribution in Figs. 23a),

6 In general, we can disregard the evolution of all undetected atoms which are not connected to the detected atom by a sequence of collision events. Therefore, Fig. 24a) must either give a vanishing contribution, or be compensated by other diagrams.

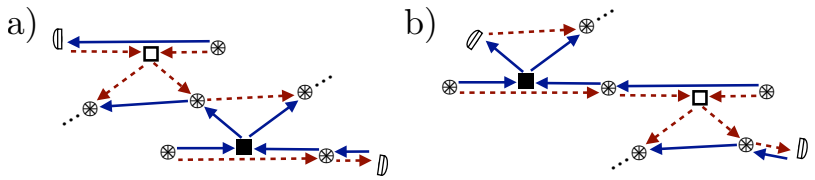

Figure 24: Exemplary forbidden (a) and allowed (b) diagrams. (a) results as a combination of diagram Fig. 23c) and then Fig. 23d), whereas (b) corresponds to the inverse ordering. The respective, finally detected amplitudes are marked with a detector symbol, such as to stress that the detected amplitudes in (a) (in contrast to (b)) are unaffected by the collisions of their respective conjugated amplitudes.

b), d), and e) (thus prohibiting that a contribution of the diagram in Fig. 23c) can occur prior to that):

$$\begin{aligned} C_E^{(1)}(\mathbf{r},\mathbf{q}) &= C_0(\mathbf{r},\mathbf{q})\delta(E-E_L) + \int_{\mathcal{V}} d\mathbf{r}' P_E^C(\mathbf{r},\mathbf{r}') C_E^{(1)}(\mathbf{r}',\mathbf{q}) \\ &+ \int_0^\infty dE' \iint_{\mathcal{V}} d\mathbf{r}'\, d\mathbf{r}'' \left(g^C_{E',E}(\mathbf{r}',\mathbf{r}'',\mathbf{r}) + \left[g^C_{E',\overline{E}}(\mathbf{r}',\mathbf{r}'',\mathbf{r}) \right]^* \right) C_E^{(1)}(\mathbf{r}'',\mathbf{q}) I_{E'}(\mathbf{r}') \\ &+ \int_0^{E_q} dE' \iint_{\mathcal{V}} d\mathbf{r}'\, d\mathbf{r}'' \left[h^C_{\overline{E},\overline{E'}}(\mathbf{r}',\mathbf{r}'',\mathbf{r}) \right]^* C_{E'}^{(1)}(\mathbf{r}'',\mathbf{q}) I_E(\mathbf{r}') \\ &+ \int_0^\infty dE' \int_0^{E_q} dE'' \iint_{\mathcal{V}} d\mathbf{r}'\, d\mathbf{r}'' f^C_{E',E'',E}(\mathbf{r}',\mathbf{r}'',\mathbf{r}) C_{E''}^{(1)}(\mathbf{r}'',\mathbf{q}) I_{E'}(\mathbf{r}')\,, \end{aligned} \tag{159}$$

where we introduced the integral limit $E_q = E_L + E_D$. As for the ladder case, the crossed density $C_E^{(1)}(\mathbf{r},\mathbf{q})$ within the slab decomposes into linear transport (first line) and nonlinear contributions due to particle-particle interaction (second to fourth line). The source density $C_0(\mathbf{r},\mathbf{q})$ is defined as in (150).

So far, we have neglected the diagram Fig. 23c) in our considerations, for which we now state a second nonlinear integral equation:

$$\begin{aligned} C_E^{(2)}(\mathbf{r},\mathbf{q}) &= \int_{\mathcal{V}} d\mathbf{r}' P_E^C(\mathbf{r},\mathbf{r}') C_E^{(2)}(\mathbf{r}',\mathbf{q}) \\ &+ \int_0^\infty dE' \iint_{\mathcal{V}} d\mathbf{r}'\, d\mathbf{r}'' \left(g^C_{E',E}(\mathbf{r}',\mathbf{r}'',\mathbf{r}) + \left[g^C_{E',\overline{E}}(\mathbf{r}',\mathbf{r}'',\mathbf{r}) \right]^* \right) C_E^{(2)}(\mathbf{r}'',\mathbf{q}) I_{E'}(\mathbf{r}') \\ &+ \int_0^{E_q} dE' \iint_{\mathcal{V}} d\mathbf{r}'\, d\mathbf{r}'' h^C_{E',E}(\mathbf{r}',\mathbf{r}'',\mathbf{r}) \left(C_{E'}^{(1)}(\mathbf{r}'',\mathbf{q}) + C_{E'}^{(2)}(\mathbf{r}'',\mathbf{q}) \right) I_{\overline{E'}}(\mathbf{r}') \\ &+ \int_0^\infty dE' \int_0^{E_q} dE'' \iint_{\mathcal{V}} d\mathbf{r}'\, d\mathbf{r}'' f^C_{E',E'',E}(\mathbf{r}',\mathbf{r}'',\mathbf{r}) C_{E''}^{(2)}(\mathbf{r}'',\mathbf{q}) I_{E'}(\mathbf{r}')\,. \end{aligned} \tag{160}$$

In order to ensure that the diagram depicted in Fig. 24b) is taken into account, $C_E^{(1)}(\mathbf{r},\mathbf{q})$ enters into $C_E^{(2)}(\mathbf{r},\mathbf{q})$ – however *not* the other way around, in order to prohibit the forbidden diagram Fig. 24a). Likewise, also those diagrams are excluded where an arbitrary sequence of processes as in Figs. 23a), b), and e) occurs between Figs. 23c) and d), which are forbidden for the same reason as Fig. 24a). Note that the source term enters only once in $C_E^{(1)}(\mathbf{r},\mathbf{q})$, but is included in $C_E^{(2)}(\mathbf{r},\mathbf{q})$, via the coupling of both integral equations. Further note that the two crossed components $C_E^{(1)}(\mathbf{r},\mathbf{q})$ and $C_E^{(2)}(\mathbf{r},\mathbf{q})$ are not only dependent on the position but – as mentioned for the linear crossed case – depend on the sum $\mathbf{q} = \mathbf{k}_{in} + \mathbf{k}_{out}$ of the initial and final wave vector.

Once we now conduct the contact interaction approximation as we did for the ladder component, cf. (121), the equations (159) and (160) simplify appreciably. Remember that within the contact interaction approximation the contribution of the collision processes to the transport (due to predominant disorder scattering for $k\ell_{\mathrm{dis}} \gg 1$) can be neglected, and one can thus approximate the occurrence of a collision by a single point in space:

$$\begin{aligned} g^{C}_{E',E} &= \iint \mathrm{d}\mathbf{r}'\,\mathrm{d}\mathbf{r}''\, g^{C}_{E',E}(\mathbf{r}',\mathbf{r}'',\mathbf{r})\,, \\ h^{C}_{E',E} &= \iint \mathrm{d}\mathbf{r}'\,\mathrm{d}\mathbf{r}''\, g^{C}_{E',E}(\mathbf{r}',\mathbf{r}'',\mathbf{r})\,, \\ f^{C}_{E',E'',E} &= \iint \mathrm{d}\mathbf{r}'\,\mathrm{d}\mathbf{r}''\, f^{C}_{E',E'',E}(\mathbf{r}',\mathbf{r}'',\mathbf{r})\,. \end{aligned} \tag{161}$$

Using (161), eqs. (159) and (160) simplify, respectively:

$$\begin{aligned} C^{(1)}_{E}(\mathbf{r},\mathbf{q}) &= C_0(\mathbf{r},\mathbf{q})\delta(E-E_L) + \int_{\mathcal{V}} \mathrm{d}\mathbf{r}' P^{C}_{E}(\mathbf{r},\mathbf{r}') C^{(1)}_{E}(\mathbf{r}',\mathbf{q}) \\ &+ \int_0^{\infty} \mathrm{d}E' \left[\left(g^{C}_{E',E} + \left[g^{C}_{E',\overline{E}} \right]^{*} \right) C^{(1)}_{E}(\mathbf{r},\mathbf{q}) + \int_0^{E_q} \mathrm{d}E''\, f^{C}_{E',E'',E} C^{(1)}_{E''}(\mathbf{r},\mathbf{q}) \right] I_{E'}(\mathbf{r}) \\ &+ \int_0^{E_q} \mathrm{d}E' \left[h^{C}_{\overline{E},\overline{E'}} \right]^{*} C^{(1)}_{E'}(\mathbf{r},\mathbf{q}) I_{E}(\mathbf{r})\,, \end{aligned} \tag{162}$$

$$\begin{aligned} C^{(2)}_{E}(\mathbf{r},\mathbf{q}) &= \int_{\mathcal{V}} \mathrm{d}\mathbf{r}' P^{C}_{E}(\mathbf{r},\mathbf{r}') C^{(2)}_{E}(\mathbf{r}',\mathbf{q}) \\ &+ \int_0^{\infty} \mathrm{d}E' \left[\left(g^{C}_{E',E} + \left[g^{C}_{E',\overline{E}} \right]^{*} \right) C^{(2)}_{E}(\mathbf{r},\mathbf{q}) + \int_0^{E_q} \mathrm{d}E'' f^{C}_{E',E'',E} C^{(2)}_{E''}(\mathbf{r},\mathbf{q}) \right] I_{E'}(\mathbf{r}) \\ &+ \int_0^{E_q} \mathrm{d}E' h^{C}_{E',E} \left(C^{(1)}_{E'}(\mathbf{r},\mathbf{q}) + C^{(2)}_{E'}(\mathbf{r},\mathbf{q}) \right) I_{\overline{E'}}(\mathbf{r})\,. \end{aligned} \tag{163}$$

Let us stress that these equations can again be adopted to the slab geometry, where all quantities only depend on the spatial variable z and the components of $\mathbf{q}$. The expressions obtained in this case are quite lengthy and rather obscure the view for the fundamental physics. We thus refer the reader to Appendix D.2, and especially to eq. (339).

With the approximation (161), the momentum integrals for the collision diagrams can be evaluated. Taking into account the explicit collision matrix element (125) for s-wave scattering (see also Appendix B.1), we evaluate (154) in the limit of large $k\ell_{\mathrm{dis}} \gg 1$,[7]

$$\begin{aligned} g^{C}_{E_1,E_2} = &\frac{i\beta\sqrt{E_L}}{\rho_0\sqrt{E_2}\left[i + \ell_{\mathrm{dis}}\left(\sqrt{E_2} - \sqrt{\overline{E}_2} \right) \right]^2} \\ &+ \frac{\alpha\left[\left(\sqrt{E_1} + \sqrt{E_2} \right)^3 - \left| \sqrt{E_1} - \sqrt{E_2} \right|^3 \right]}{12\rho_0 E_2 \sqrt{E_1}\left[i + \ell_{\mathrm{dis}}\left(\sqrt{E_2} - \sqrt{\overline{E}_2} \right) \right]^2}\,. \end{aligned} \tag{164}$$

Accordingly, the contribution $\left[g^{C}_{E_1,\overline{E}_2} \right]^{*}$ can be read off (164) under consideration of (155). As it should be, we recover the ladder contribution, eq. (126), in the limit $\overline{E}_2 \to E_2$.

7 We follow the same procedure as for the ladder contribution. See the discussion before eq. (126) for further details.

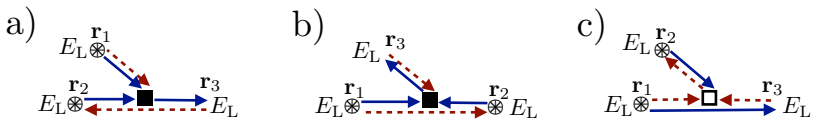

Figure 25: Nonlinear crossed diagrams contributing to the diagrammatic expansion of the Gross-Pitaevskii equation. The diagrams (a), (b), and (c) are equivalent to the respective collision diagrams in Fig. 23b), c), and d), in the limit $\alpha \to 0$ and under the replacement of all single-particle energies by E_L.

The same assumptions we implied to calculate eq. (164) also apply for (156), and we obtain, accordingly

$$h^{C}_{E_1,E_2} = \frac{2\left[i\beta\sqrt{E_L} + \alpha\sqrt{(E_L+E_D)/2}\right]}{\rho_0\left[i+\ell_{dis}\left(\sqrt{\overline{E}_1}-\sqrt{E_1}\right)\right]\left[i+\ell_{dis}\left(\sqrt{\overline{E}_2}-\sqrt{E_2}\right)\right]\left(\sqrt{\overline{E}_1}+\sqrt{E_1}\right)}\,. \tag{165}$$

The expression corresponding to the diagram Fig. 23d) is obtained from (165) with the help of expression (157). After interchanging $E_1 \leftrightarrow E_2$ – as becomes obvious by comparison of Figs. 23c) and d) with Fig. 12b) – the term proportional to β in (165) coincides with the ladder component, eq. (126), in the limit $\overline{E}_2 \to E_2$ and $\overline{E}_1 \to E_1$.[8]

8 It is expected that the α-term does not coincide with the corresponding ladder component, since $\mathbf{k}_{12} \neq \mathbf{k}_{23}$ after reversing the arrows to obtain the crossed component.

At last, we explicitly state the final form of (158), as needed to determine solutions to the integral equations (162) and (163),

$$\begin{aligned} f^{C}_{E_1,E_2,E_3} = \frac{\alpha}{\rho_0}\sum_{s_i\in\{0,1\}}(-)^{s_1+\cdots+s_4}\left[|\mathcal{E}| + \frac{2i\mathcal{E}}{\pi}\log|\mathcal{E}|\right] \\ \times\left(\sqrt{E_1}\left[i\left(\sqrt{\overline{E}_2}+\sqrt{E_2}\right)-\ell_{dis}\left(\overline{E}_2-E_2\right)\right]\right. \\ \left.\times\left[i\left(\sqrt{\overline{E}_3}+\sqrt{E_3}\right)-\ell_{dis}\left(\overline{E}_3-E_3\right)\right]\right)^{-1}, \end{aligned} \tag{166}$$

where

$$\begin{aligned} \mathcal{E} = (-)^{s_1}\sqrt{E_1} + (-)^{s_2}\left[s_2\sqrt{\overline{E}_2} + (1-s_2)\sqrt{E_2}\right] \\ + (-)^{s_3}\left[s_3\sqrt{\overline{E}_3} + (1-s_3)\sqrt{E_3}\right] + (-)^{s_4}\sqrt{E_1+E_2-E_3}\,. \end{aligned} \tag{167}$$

The sum formula (166) as a function of (167) is similar to the one defined for the ladder contribution, eq. (129), with the additional complication that also the energies $\overline{E}_2$ and $\overline{E}_3$ occur. In the ladder limit $\overline{E}_2 \to E_2$ and $\overline{E}_3 \to E_3$, the term proportional to $|\mathcal{E}|$ equals the corresponding ladder contribution (up to the previously discussed factor of two), eq. (129), and the term proportional to $2i\mathcal{E}\log|\mathcal{E}|/\pi$ vanishes.

4.2.3 *The Nonlinear Crossed Contribution – the Gross-Pitaevskii Limit*

For the ladder contribution we observed that the nonlinear contributions of the Gross-Pitaevskii equation vanish, and that eq. (142) reproduces the linear transport equation (100). This was due to the fact that the nonlinear

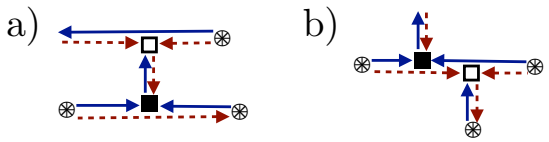

Figure 26: Gross-Pitaevskii analogue of Fig. 24. (a) All diagrams which exhibit a closed loop, after attaching the diagram in Fig. 25c) to the tail of Fig. 25b), must be excluded, whereas the inverse construction of the diagrams is allowed (b). See main text and [62] for details.

coupling constant is purely real such that the nonlinear contribution in (142) exactly cancels.

Let us recall – as we showed in the previous chapter – that the Gross-Pitaevskii limit of our theory is given for $\alpha \to 0$ and $\beta = \rho_0 k_L \ell_{dis} \tilde{g} = \rho_0 \ell_{dis} g / k_L$ in the weak interaction limit, and g is again the nonlinear coupling constant known from Gross-Pitaevskii theory [87]. Since the collision contributions proportional to β do not vanish for our theory, cf. (164) and (165), we expect that also a nonlinear contribution of the Gross-Pitaevskii equation contributes to the crossed component. This expectation is due to the trace formula (65) with the help of which we were able to show that the elastic two-particle diagrams coincide with the ones obtained from the diagrammatic representation of the Gross-Pitaevskii equation, see Figs. 14 and 16.

Consequently, we can immediately draw the corresponding collision diagrams for the crossed contribution, see Fig. 25. As mentioned previously, the same reasoning as concerns their combination, i. e. the existence of forbidden and allowed diagrams, is recovered within the Gross-Pitaevskii picture, see Fig. 26. The corresponding integral equation will thus also split into two contributions. Neglecting the collision contributions proportional to α, we find for eqs. (164) and (165)

$$g^C_{E_L,E_L} = h^C_{E_L,E_L} = -i\frac{\beta}{\rho_0} = -ik_L \ell_{dis} \tilde{g} \,. \tag{168}$$

The integral equations (162) and (163) hence simplify considerably, and we obtain the integral version of the Gross-Pitaevskii equation for the crossed contribution,

$$C^{(1)}(\mathbf{r},\mathbf{q}) = C_0(\mathbf{r},\mathbf{q}) + \int_{\mathcal{V}} d\mathbf{r}'\, P^C(\mathbf{r},\mathbf{r}') C^{(1)}(\mathbf{r}',\mathbf{q}) \left[1 + ik_L \ell_{dis} \tilde{g}\, I(\mathbf{r}')\right] , \tag{169}$$

$$C^{(2)}(\mathbf{r},\mathbf{q}) = \int_{\mathcal{V}} d\mathbf{r}'\, P^C(\mathbf{r},\mathbf{r}') \times \left[C^{(2)}(\mathbf{r}',\mathbf{q}) \left(1 - ik_L \ell_{dis} \tilde{g}\, I(\mathbf{r}')\right) - ik_L \ell_{dis} \tilde{g}\, C^{(1)}(\mathbf{r}',\mathbf{q})\right] , \tag{170}$$

which were also derived in [62]. Note that, for reasons of comparison with [62], we substituted $\mathbf{r} \to \mathbf{r}'$ in the collision contributions, such that now each collision event takes place at $\mathbf{r}'$ and is subsequently, linearly propagated to $\mathbf{r}$ (in contrast to eqs. (162) and (163) where the linear propagation from $\mathbf{r}'$ to $\mathbf{r}$ occurs prior to the collisions at $\mathbf{r}$).

Note that all quantities in eqs. (169) and (170) are purely elastic, i. e. they are associated with a δ-function $\delta(E - E_L)$ in eqs. (162) and (163). At first sight, it might seem that the terms $[h^C_{E,E'}]^*$ in (162) and $h^C_{E',E}$ in (163) could induce inelastic scattering also for $\alpha = 0$. A closer inspection reveals that

this is not the case: inserting elastic quantities ($C^{(1,2)}_{E'} \propto \delta(E' - E_L)$, $I_E \propto \delta(E - E_L)$) on the right-hand side of eqs. (162) and (163) yields δ-functions $\delta(E - E_L)$ or $\delta(E_D - E_L)$ on the corresponding left-hand side. Therefore, h^C and $[h^C]^*$ induce inelastic scattering only after seeding with a previous inelastic event (f^L or f^C) at $\alpha > 0$.

Having established the connection of our theory with the Gross-Pitaevskii equation, we now turn our attention to the detection of the crossed density, which manifests itself only outside the slab, around backscattering direction.

4.3 RESULTS

This section is devoted to the analysis of the coherent backscattering cone detected in the far field of the slab around backscattering direction. Its properties as a consequence of linear transport processes have been discussed at the beginning of this chapter, but also exhaustively in the literature, see [48] and references therein. The consequences of weak nonlinearities, as described, e.g., by the Gross-Pitaevskii equation, which lead to a dephasing of counter-propagating paths, have been analyzed previously for clouds of cold atoms, but have attracted further attention, in the context of ultracold atom experiments. Here, a decrease of the enhancement factor with increasing nonlinearity is expected, and numerical experiments even predict an inversion of the cone, i. e. an enhancement factor smaller than one [44].

However, these theories apply to the weakly interacting regime and predict elastic scattering contributions. The question remains how coherent backscattering will change if inelastic scattering processes are included. Will the enhancement factor decrease more rapidly due to an additional source of dephasing? Can the predicted inversion of the cone be confirmed? What can the spectral decomposition of the cone tell us about the underlying processes?

But before addressing these questions, we define the figure of merit, the flux density and the bistatic coefficient outside of the slab.

4.3.1 *Coherent Backscattering – the Figure of Merit*

Equivalently to the ladder scenario, where particles acquire different single-particle energies and, hence, propagate with different momenta, the final figure of merit is not anymore given by the density, but rather by the flux density. In contrast to the detected ladder flux density, additional phase factors have to be considered for the crossed flux density, as already discussed for the case of linear coherent backscattering.

According to (119), the crossed flux density for the energy E_D detected in the far-field of the slab reads:

$$\mathbf{J}^C(\mathbf{R}) = \frac{\mathbf{R}}{4\pi\ell_{dis}R^3}\int d\mathbf{r}\int dE_D\, e^{-z(1+1/\cos\theta)/(2\ell_{dis})}e^{-i\mathbf{qr}}\,J^C_{E_D}(\mathbf{r},\mathbf{q})\,, \quad (171)$$

with the spectral flux density within the slab given as

$$J^C_{E_D}(\mathbf{r},\mathbf{q}) = \sqrt{E_D}\left[C^{(1)}_{E_D}(\mathbf{r},\mathbf{q}) + C^{(2)}_{E_D}(\mathbf{r},\mathbf{q})\right] - \sqrt{E_L}C_0(\mathbf{r},\mathbf{q})\,. \quad (172)$$

In order to avoid double-counting, we again subtracted the single scattering contribution $C_0(\mathbf{r},\mathbf{q})$, eq. (150). As before, the spectral flux density separates into an elastic and an inelastic component,

$$J^C_{E_D}(\mathbf{r},\mathbf{q}) = J^{(el)}_{E_D}(\mathbf{r},\mathbf{q})\,\delta(E_D - E_L) + J^{(inel)}_{E_D}(\mathbf{r},\mathbf{q})\,, \quad (173)$$

from which the total flux density within the slab is once again obtained by integration over all energies

$$J^C(\mathbf{r},\mathbf{q}) = \int dE_D\, J^C_{E_D}(\mathbf{r},\mathbf{q})\,. \tag{174}$$

However, as noted before, we rather want to quantify the detected flux density by the bistatic coefficient – the flux density detected in direction $\mathbf{R}$, and normalized with respect to the incoming flux density and the distance to the detector:

$$\gamma^C_{E_D}(\theta) = \frac{1}{J^C_0 \ell_{dis} A} \int d\mathbf{r}\, J^C_{E_D}(\mathbf{r},\mathbf{q}) e^{-z(1+1/\cos\theta)/(2\ell_{dis})} e^{-i\mathbf{qr}}\,, \tag{175}$$

with $J^C_0 = \sqrt{E_L} C_0$, and A the illuminated surface area transverse to the incoming field (required to normalize the integration over the x- and y-components). Note that, with the help of (173), we can also define

$$\gamma^C_{E_D}(\theta) = \gamma^{C,(el)}_{E_D}(\theta) + \gamma^{C,(inel)}_{E_D}(\theta)\,, \tag{176}$$

and, in accordance with (174),

$$\gamma^C(\theta) = \int dE_D\, \gamma^C_{E_D}(\theta)\,. \tag{177}$$

Note that $\gamma^C_{E_D}(\theta)$ must be a real number (since it represents a flux). As we have checked, our numerically determined solutions of eqs. (162) and (163) (see below) indeed fulfill this condition. Since other general conditions like the conservation of the particle and energy flux, as proven for the ladder contribution, see eq. (131), do not hold for the crossed component, the vanishing imaginary part of the crossed flux density resembles a valuable check of consistency of our theory (and its correct numerical implementation).

In addition, the bistatic coefficient for nonlinear crossed transport adapted to the slab geometry is derived in Appendix D.2, as well as the corresponding ladder result, see Appendix D.1, which we state here for comparison:

$$\gamma^L_{E_D}(\theta) = \frac{1}{J_0 \ell_{dis} A} \int d\mathbf{r}\, J_{E_D}(\mathbf{r}) e^{-z/(\ell_{dis}\cos\theta)}\,, \tag{178}$$

with, as above,

$$\gamma^L_{E_D}(\theta) = \gamma^{L,(el)}_{E_D}(\theta) + \gamma^{L,(inel)}_{E_D}(\theta)\,, \tag{179}$$

and

$$\gamma^L(\theta) = \int dE_D\, \gamma^L_{E_D}(\theta)\,. \tag{180}$$

While calculating the ladder contribution in Chapter 3 we found that the contribution proportional to the collision parameter β vanishes, and only α determines the collision strength. We defined $\alpha = 8\pi a_s^2 \ell_{dis} \rho_0 \ll 1$, what is tantamount to the requirement $\ell_{int} \gg \ell_{dis}$, cf. eqs. (109) and (127), and limits the validity of our theory to the regime where collisions are less frequent than scattering events off the disorder potential. However, as we demonstrated within this chapter, the crossed contribution proportional to the collision parameter β does not vanish, and we henceforth also have to

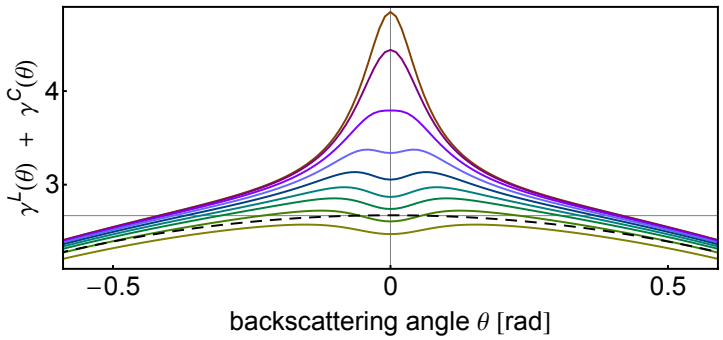

Figure 27: Sum of elastic ladder and elastic crossed bistatic coefficients, cf. eqs. (180) and (177), as a function of the backscattering angle θ, for the optical thickness $b = 10$, $k_L \ell_{dis} = 10$, and different values of the collision strength β ($\beta = 0$, 0.02, 0.04, 0.06, 0.08, 0.1, 0.12, 0.15, 0.2 from top to bottom), and for the collision strength $\alpha = 0$. For comparison, the (black) dashed curve shows the ladder bistatic coefficient only, whose maximal value is marked with a horizontal (gray) thin line. Observe how constructive changes to destructive interference, as a consequence of elastic collisions which induce dephasing for increasing values of β.

assume $\beta \ll 1$. Furthermore, since $\beta \gg \alpha$ (see (128)), we, nonetheless, have to ensure that $\ell_{int}^{\alpha} \gg \ell_{int}^{\beta} \gg \ell_{dis}$, where $\ell_{int}^{\alpha} \equiv \ell_{int}$ and

$$\ell_{int}^{\beta} = \frac{k_L}{8\pi a_s \rho_o}, \tag{181}$$

i. e. collisions proportional to β must as well be less frequent than scattering events off the disorder potential.

4.3.2 *Coherent Backscattering – the Gross-Pitaevskii Limit*

We now consider the elastic component, see (173), of the crossed bistatic coefficient (177), specifically in the Gross-Pitaevskii limit, i. e. with eqs. (169) and (170) instead of eqs. (162) and (163). As we showed earlier in this chapter, this corresponds to $\alpha = 0$.[9]

9 Similar results have been obtained before [62]. We therefore restrict ourselves to a brief discussion of the results in the Gross-Pitaevskii limit.

Numerically, we proceed by iteratively solving the two coupled integral equations (169) and (170). Upon convergence, the crossed intensities are then propagated out of the slab, and detected in the far field, as a function of the angle θ.

In Fig. 27 the total backscattered bistatic coefficient (ladder plus crossed) is plotted as a function of the backscattering angle θ for different values of $\beta \in [0, 0.2]$, and $\alpha = 0$. For comparison, the total ladder bistatic coefficient is plotted as a dashed line. Obviously, the effect of increasing β leads to a decreasing enhancement factor, and for $\beta \geqslant 0.15$ to an inversion of the cone below the value predicted by ladder transport only. This effect can be understood in terms of dephasing processes for counter-propagating scattering amplitudes, which change the constructive into destructive interference in exact backscattering direction. It is worth noting that long scattering paths are most affected by dephasing, leading to a rapid fall-off of the peak around $\theta = 0$, and the development of a central dip, which – with increasing β – also affects larger values of θ. As a consequence, the inverted peak acquires a larger width, with contributions mostly from short scattering paths.

The lowest curve in Fig. 27 corresponds to the value $\beta = 0.2$, in accordance with the requirement $\beta \ll 1$. We note that simulations for larger values of

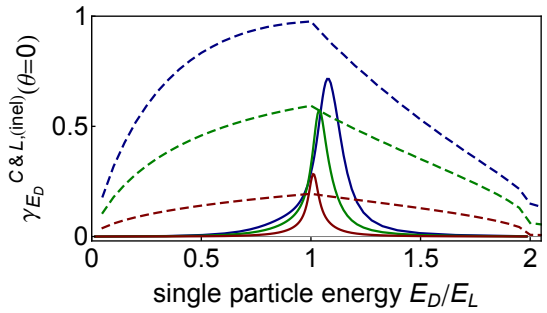

Figure 28: Inelastic crossed (solid lines) and ladder (dashed lines) bistatic coefficients for $\theta = 0$, optical thickness $b = 4$, $k_L \ell_{dis} = 10$, and fixed $k_L a_s = 0.2$, corresponding to values $\beta = 0.02$ (red curves), 0.08 (green curves), and 0.2 (blue curves), as a function of the single-particle energy. Note that in the very weakly interacting regime, i. e. small β and α, the crossed component around $E_D = E_L$ is enhanced by a factor > 2 (i. e. larger than the corresponding ladder contribution) [183], which only becomes < 2 for stronger nonlinearities. Also note that the position of the maxima of the crossed component is shifted towards higher single-particle energies with increasing β, see main text for details.

β show a further decrease of the backscattered flux density. However, as these predictions extend beyond the regime of validity of our theory, we restrict our further analysis to $\beta \leqslant 0.2$ and refer the reader to Chapter 5 for a discussion of a possible extension of our present theory.

4.3.3 *Coherent Backscattering – Beyond the Gross-Pitaevskii Limit*

We now go beyond the *elastic* results of the Gross-Pitaevskii equation and focus on inelastic scattering processes. Since a variety of parameters will become crucial for the analysis, we will restrict most of the discussion to the exact backscattering direction $\theta = 0$. Furthermore, as discussed for the linear case of coherent backscattering, the width of the coherent backscattering cone is inversely proportional to $k\ell_{dis}$. Besides this effect, as we have checked, no qualitative change of our results is observed as long as we guarantee that $k\ell_{dis} \gg 1$, i. e. that we remain in the regime of weak disorder (see the discussion in Chapter 3). Hence, our results presented here are all obtained for the case $k_L \ell_{dis} = 10$.

A similar reasoning applies for the thickness of the slab. Since coherent backscattering including particle-particle collisions is even more phase-dependent than the linear case, very long paths are damped out. Checking carefully for a minimal slab thickness (corresponding to shorter computing time in our numerical simulations) without altering the underlying physics, we chose a slab of thickness $L = 4\ell_{dis}$ throughout our simulations.

The remaining parameters α, β, and their ratio $\alpha/\beta = k_L a_s \ll 1$ will be in the focus of our subsequent analysis. With $k_L a_s \in \{0.05\,, 0.1\,, 0.2\}$, we acquire possible values for $\alpha \in \{0.0005 - 0.04\}$ and $\beta \in \{0.01 - 0.2\}$, where we set the minimal value to $\beta = 0.01$, and note that the limit $\beta \to 0$ implies also $\alpha \to 0$.

In Fig. 28 we show an exemplary spectrum of the inelastic ladder (dashed lines) and crossed (solid lines) bistatic coefficients, for $k_L a_s = 0.2$ and $\beta = 0.02$, 0.08, and 0.2.

First of all, we focus on the ladder contribution (dashed lines) in Fig. 28. One observes, as expected from our findings in Chapter 3, that the contribution of the inelastic flux density (i. e. of the dashed lines in Fig. 28

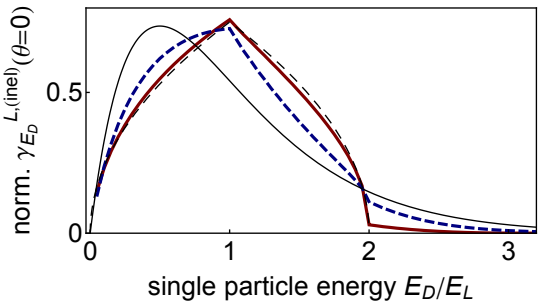

Figure 29: Comparison of the inelastic ladder bistatic coefficient (normalized to $\gamma^{L,(inel)}(\theta = 0) = 1$) taken from Fig. 28 for $\beta = 0.02$ ((red) solid line) and $\beta = 0.2$ ((blue) dashed line) with the spectrum of a single inelastic collision event f^L (thin (black) dashed line) and the Maxwell-Boltzmann distribution (thin (black) line), see eqs. (129) and (137). Note that since the contribution of short scattering paths to the backscattered signal dominates, thermalization of the ladder flux density, that requires long scattering paths for a sufficient number of collisions to occur, as discussed in Chapter 3, is not observed here.

integrated over the single-particle energy) grows with increasing collision strength. From the discussion in the preceding chapter we furthermore know that for increasing slab length and/or collision strength, the single particle flux density thermalizes towards a Maxwell-Boltzmann distribution. Here, only scattering paths with a limited length will contribute to the signal in backscattering direction and, hence, the thermalization will rather depend on the collision strength. As for the case inside the slab, we plot in Fig. 29 the spectral bistatic coefficient $\gamma_{E_D}^{L,(inel)}(\theta = 0)$ (normalized to $\gamma^{L,(inel)}(\theta = 0) = 1$) for $\beta = 0.02$ (lowest dashed curve in Fig. 28) and $\beta = 0.2$ (upmost dashed curve in Fig. 28), versus the contribution of a single inelastic collision event f^L and the Maxwell-Boltzmann distribution, see (129) and (137), respectively. We observe that the ladder spectrum spreads under an increasing influence of collisions within the single-particle energy landscape, but remains far from thermalized, a strong indicator of the contribution of rather short scattering paths, as expected.

Focusing now on the crossed component, we see in Fig. 28 how the amount as well as the position of the maxima of the inelastic bistatic coefficient (solid lines) changes with increasing β. For small nonlinearities, i. e. small β and α, we observe that the enhancement around $E_D = E_L$ of the inelastic crossed flux density can exceed the predicted value of 2, i. e. the crossed exceeds the corresponding ladder contribution. This is indeed expected also diagrammatically [183]. Remember that an enhancement of 2 arises solely due the appearance of the linear crossed component which becomes indistinguishable from the linear ladder component for $\theta = 0$, see Section 4.1 and Appendix D.2. If, additionally, nonlinear contributions are included into the theory, further combinations of diagrams exist which equally contribute to the backscattered flux density. In Fig. 22, e.g., this additional diagram immediately arises if one replaces the detected dashed amplitude emitted from point $\mathbf{r}_1$ by a corresponding source amplitude and the source amplitude at point $\mathbf{r}_6$ by a detected dashed amplitude. This thereby obtained diagram interferes constructively with the one depicted in Fig. 22 and, thus, an enhancement factor of up to 3 can occur. For larger nonlinearities, even more different combinations exist, which are, however, largely overcompensated for by dephasing that reduces the amount of in-

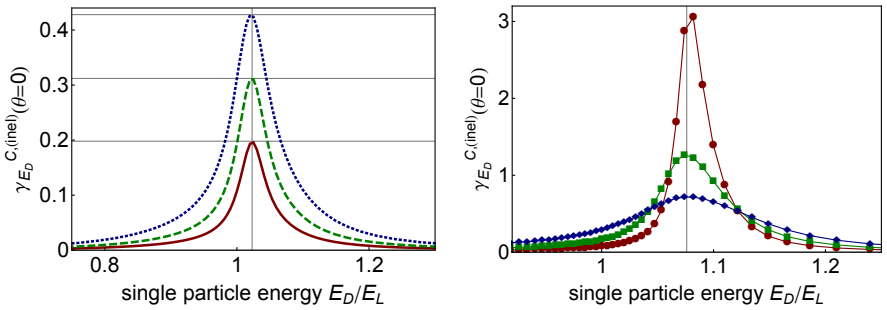

(a) $\beta = 0.04$ (b) $\beta = 0.2$

Figure 30: Spectral crossed flux densities for $\theta = 0$, optical thickness $b = 4$, $k_L \ell_{dis} = 10$, fixed β and variable α. In (a), the (red) solid line, the (green) dashed line, and the (blue) dotted line respectively correspond to $\alpha = 0.002, 0.004, 0.008$. In (b), the (red) circles, the (green) squares, and the (blue) diamonds, respectively, correspond to $\alpha = 0.01, 0.02, 0.04$. The colored lines in (b) are to guide the eye. The (gray) thin lines roughly mark the maxima of all curves. Whereas for small α and β, a doubling of α leads to an equal increase of the corresponding bistatic coefficient in (a), this effect is overwhelmed by inelastic scattering processes proportional to β, which lead to a *decrease* of the inelastic crossed density for increasing α, see (b). Further note that fixed β leads to a fixed (but different) position of the maxima (in (a) and (b)), what in turn identifies β as responsible for the shift observed in Fig. 28.

terference as compared to the ladder component, see the solid and dashed lines for larger values of β in Fig. 28. Nonetheless, in comparison to the Gross-Pitaevskii equation, they give rise to a significant contribution, as we will see below.

Despite the general observation of a decreasing total crossed flux density with increasing collision strength, as e. g. depicted in Fig. 27 for the purely elastic case, does the inelastic crossed flux density in Fig. 28 increase alongside with the collision strength, such that the importance of the inelastic component grows. Let us try to resolve to what extent the different collision parameters, α and β, are responsible for an increase of the inelastic contribution. In Figs. 30a) and b) we therefore fix β to $\beta = 0.04$ and 0.2, respectively, and vary the ratio $\alpha/\beta = k_L a_s \in \{0.05, 0.1, 0.2\}$ in order to determine the role of α.

In accordance with our expectation from the previous chapter (where β was absent and α gave rise to inelastic collisions), the amount of inelasticity is determined by α if β is small, see Fig. 30a): As indicated by the horizontal gray lines, a doubling of α yields an approximately equal increase in the inelastic enhancement factor. In this regime, the elastic contribution is dominant, and only collisions proportional to α lead to inelastic processes. (Remember that the collisions proportional to β can only contribute to the inelastic flux density if inelastic collisions proportional to α have occurred previously, see also the following discussion.) This picture dramatically changes once β is increased to the fixed value $\beta = 0.2$, see Fig. 30b). Not only does the overall inelastic flux density increase, but also the order of α-contributions is reversed. The largest value of inelastic enhancement is now given by $\alpha = 0.01$, whereas the largest value of $\alpha = 0.04$ corresponds to the lowest curve. This observation – as mentioned above – can be explained by the fact that the collision building block h^C proportional to β, see (165), can lead to inelastic scattering processes provided inelastic events of the type f^L and f^C (proportional to α) have occurred before. However, once

the inelasticity is sufficiently seeded (what is the case for Fig. 30b)) α and β start to work in different directions: α rather promotes a spectral broadening whereas β (once a critical value of α is exceeded) leads to a rapid growth of the inelastic contribution in a narrow spectral window. In terms of the underlying microscopic particle picture, β and α respectively promote scattering processes where the two particles either retain their approximate single-particle energies, or experience a reshuffling of their single-particle energies due to isotropic collisions.

As was already visible in Fig. 28 and more pronounced in Fig. 30, an increase of β goes in hand with a shift of the maximum of the inelastic flux density towards higher single-particle energies. The position of the maxima for identical values of β and variable values of α, as indicated by the respective thin (gray) vertical lines in Fig. 30a) and b), remains fixed and only shifts if β is changed. Thus β is responsible for the underlying dynamics for which a plausible explanation is still missing. This effect might, however, be related to the asymmetric ladder spectrum, see Fig. 28, which constantly feeds the crossed building blocks.

So far, we considered the spectral density of the *inelastic* bistatic coefficients, not accounted for by the Gross-Pitaevskii equation, and discussed the role of the different collision parameters α and β. However, we did not compare the inelastic contributions to the total (i. e. inelastic plus elastic) backscattered flux densities. This is of crucial importance in order to judge whether the inelastic contributions play a relevant role as compared to the elastic component.

We will do so by looking at the bistatic coefficient integrated over all energies, i. e. $\gamma^C(\theta)$, and its elastic and inelastic constituents, see eqs. (177) and (176). In Fig. 31 we compare the total crossed bistatic coefficient (the sum of the elastic and integrated inelastic bistatic coefficient), in backscattering direction $\theta = 0$, with the crossed bistatic coefficient predicted by the Gross-Pitaevskii equation, as a function of β and for two different fixed values of $k_L a_s = 0.05$ and $k_L a_s = 0.2$ in (a) and (b), respectively. As expected, both total crossed contributions decrease for increasing β. Initially, for small values of β, the crossed contribution predicted by our theory decreases faster than the crossed result obtained by the solution of the Gross-Pitaevskii equation. However, this fact changes for larger β, when the Gross-Pitaevskii equation predicts an inversion of the cone, whereas our theory (in the chosen regime) does not. The additional source of dephasing in our theory due to the presence of the collision parameter α results in a larger loss of coherence initially but, in turn, also dephases the destructive interference contributions which lead to an inversion of the coherent backscattering cone in the Gross-Pitaevskii picture. Consequently, the crossed curves for the Gross-Pitaevskii equation and our theory must cross in Fig. 31. However, the fact that this crossing occurs for $\beta \simeq 0.4$ for $\gamma^C(\theta) > 0$ shows that the inelastic enhancement factor decreases slower than the elastic one – a consequence of many-particle interferences discussed in Fig. 28 and in [183]. In fact, in Fig. 31a), around $\beta \simeq 0.2$, where the total crossed contribution (blue solid line) almost vanishes, it is precisely the role of the *positive* contribution of the inelastic flux density (dotted blue line) that balances the *negative* elastic component (not shown here, but deducible from Fig. 31, as the difference of the total and the inelastic component). Thus, although the inelastic crossed density flux remains small over the full range of β, it plays an important role when it becomes comparable in size with the total crossed flux density.

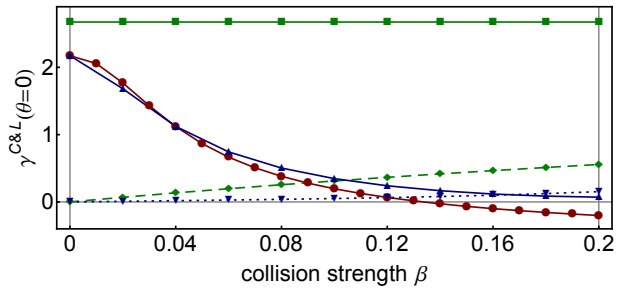

(a) $k_L a_s = 0.05$

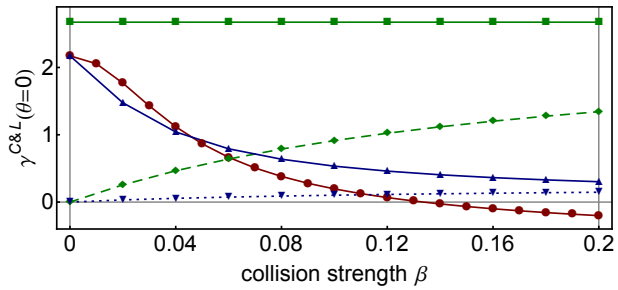

(b) $k_L a_s = 0.2$

Figure 31: Integrated crossed and ladder bistatic coefficients for $\theta = 0$, optical thickness $b = 4$, $k_L \ell_{dis} = 10$, as a function of β and fixed $k_L a_s = 0.05$ and $k_L a_s = 0.2$ in (a) and (b), respectively. The (green) squares and (green) diamonds (connected by a solid and a dashed line, respectively) denote the total $\gamma^L(\theta = 0)$ and the inelastic ladder bistatic coefficient $\gamma^{L,(inel)}(\theta = 0)$, respectively, whereas the (blue) pyramids and (blue) triangles (connected by a solid and dotted line, respectively) denote the respective total $\gamma^C(\theta = 0)$ and inelastic crossed bistatic coefficient $\gamma^{C,(inel)}(\theta = 0)$. For comparison, the crossed bistatic coefficient as predicted by the Gross-Pitaevskii equation is marked with red circles (and connected by a red solid line). The dots (data points) are connected by lines in order to guide the eye. It becomes obvious that the inelasticity is more dominant for the ladder (approximately one half of the total component, for $\beta = 0.2$ in (b)) than for the crossed contribution. However, for large β (and almost vanishing crossed component) it is precisely the latter that inhibits an inversion of the coherent backscattering cone as observed for the Gross-Pitaevskii equation (see also Fig. 27). This absence of an inversion is due to additional dephasing (that reduces constructive as well as destructive interference), as a consequence of inelastic collisions, and due to the occurrence of many-particle contributions that can enlarge the enhancement factor beyond 2 (when interfering constructively), cf. Fig. 28 and [183]. In total, a net surplus remains, that leads to a slower decrease of the inelastic enhancement factor compared to the elastic one.

In addition to the crossed contribution, we also depict the total ladder bistatic coefficient in Fig. 31, i. e. $\gamma^L(\theta)$, and its inelastic component, see (180) and (179), respectively. Conversely to the crossed case, the total ladder contribution remains constant with increasing nonlinear parameters (green solid line). Here, the role of the inelastic ladder bistatic coefficient (green dashed line) is also more pronounced and can make up more than one half of the total ladder contribution, cf. Fig. 31b). This is precisely the situation discussed in Fig. 29, where one would expect a fully thermalized ladder density flux for the backscattered signal once the inelastic ladder component converges to the total ladder contribution.

The results presented above were all obtained in the exact backscattering direction $\theta = 0$, where the major contribution of the crossed flux density

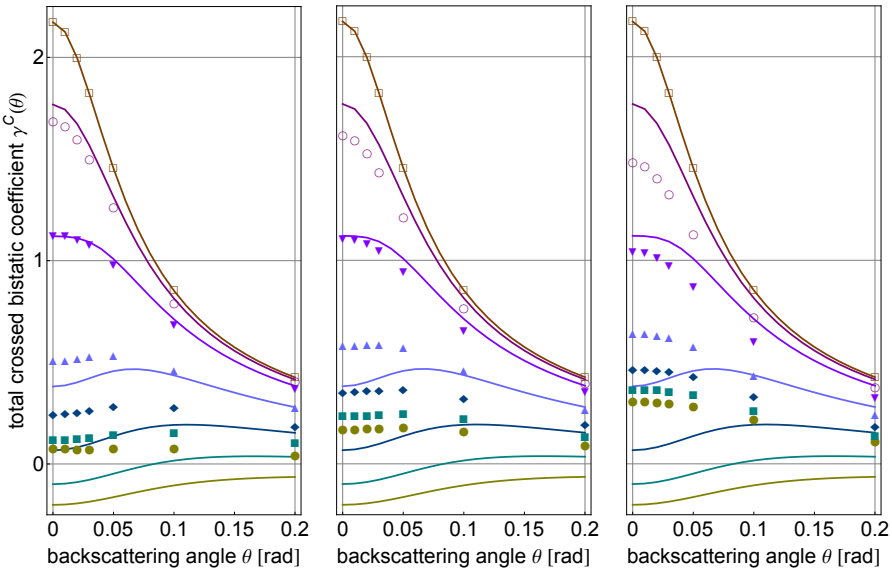

(a) $k_L a_s = 0.05$ (b) $k_L a_s = 0.1$ (c) $k_L a_s = 0.2$

Figure 32: Integrated total crossed bistatic coefficient, as a function of the detection angle θ in backscattering direction. The lines correspond to the solution of the Gross-Pitaevskii equation for different collision strengths β ($\beta = 0, 0.02, 0.04, 0.08, 0.12, 0.16, 0.2$, from top to bottom), identical in all figures. The symbols with the same color code represent data points obtained with our theory (open squares: $\beta = 0$, open circles: $\beta = 0.02$, triangles: $\beta = 0.04$, pyramids: $\beta = 0.08$, diamonds: $\beta = 0.12$, solid squares: $\beta = 0.16$, solid circles: $\beta = 0.2$). The different figures now correspond to different but fixed values of $k_L a_s = 0.05$, $k_L a_s = 0.1$, and $k_L a_s = 0.2$, in (a), (b), and (c), respectively. Observe that our findings from Fig. 31 remain valid also for angles $\theta \neq 0$. Whereas the largest correction to the Gross-Pitaevskii equation due to our theory is visible for small angles (since the dip within the central peak of the cone predicted by the Gross-Pitaevskii equation shows up in our theory only for small $k_L a_s$), our theory does not result in an inversion (and not even in a vanishing contribution) of the cone for the full range of parameters depicted here.

is observed. However, our observations remain valid also for a backscattering angle $\theta \neq 0$. This is emphasized by Fig. 32 where we show the integrated total crossed bistatic coefficient as a function of the backscattering angle θ – again in comparison to the crossed contribution obtained from the Gross-Pitaevskii equation. We here only show one half of the symmetric backscattering cone, for positive θ. Note that the lines corresponding to the solution of the Gross-Pitaevskii equation are identical in all three plots. The topmost (brown) line is the linear crossed contribution (151) for $\beta = 0$. For increasing β from top to bottom, we recover the scenario discussed in Fig. 27, leading to an inversion of the coherent backscattering cone. Most interesting is the comparison with the crossed solution of our theory, i. e. eq. (177), here marked by different symbols for increasing β. Whereas the results are identical for $\beta = 0$, the discrepancy between both solutions becomes again evident for large β, where an inversion of the cone is contrasted with an enhancement factor > 1, for all plots in Fig. 32.

Both solutions show an increasing width of the cone, indicating major contributions of short scattering paths, with increasing β. However, the suppression of very long scattering paths leading to a dip within the cen-

tral peak around $\theta \simeq 0$ for the crossed contribution obtained by the Gross-Pitaevskii theory, is barely visible for $k_L a_s = 0.05$, and even disappears for $k_L a_s \geqslant 0.1$, within our theory.

4.4 SUMMARY

In summary, we gave a detailed derivation of the diagrammatic theory leading to linear and nonlinear coherent backscattering, and applied this theory to a slab geometry. We extended the recently developed diagrammatic theory for nonlinear elastic transport [62] to the case of nonlinear and inelastic coherent backscattering, and could verify that our theory reproduces the predictions of the Gross-Pitaevskii equation in a certain limit. For the first time, we were thus able to predict interference corrections for a bosonic, interacting many-particle system within the weak disorder limit.

Explicitly, we could show that the properties of the coherent backscattering cone differ from the results predicted by the Gross-Pitaevskii equation not only for large nonlinearity, where our simulations do *not* predict an inversion of the cone, but also for small nonlinearity, where we predict a more rapid decrease of the cone height. Our analysis of the coherent backscattering cone's properties in more detail allowed for an understanding of the underlying physical processes, in terms of constructive interference of many-particle diagrams, as well as of the identification of an additional dephasing mechanism due to inelastic collisions.

We also addressed the relevant limitations of our present theory, i. e. the assumption that collisions are less frequent than scattering off the disorder potential, which in turn limits the validity of our simulations to small nonlinearities.

However, the present state of our theory allows for an experimental validation in contemporary ultracold atom experiments, where the required matter waves can be nowadays created [94–96], and the strength of the disorder potential [35, 112] together with the interatomic interaction strength – by means of Feshbach resonances [184, 185] – can be chosen at will.

5 SUMMARY AND OUTLOOK

Within this first part of the present thesis we derived a microscopic N-body scattering theory for interacting particles in a weak disorder potential in three dimensions. We applied this diagrammatic theory to a stationary scattering scenario for an asymptotically non-interacting, quasi-plane matter wave incident on a three-dimensional slab, with the disorder potential and inter-particle collisions confined to the slab region, and hereby certified the viability of our theory to address, on the one hand, very fundamental but, on the other hand, very timely questions of quantum transport for interacting particles in random environments. In a clear and precise manner we demonstrated how one – in a strictly unitary treatment – can bridge the gap between a general many-body microscopic theory and its implications on the mesoscopic level governed, e.g., by a nonlinear quantum Boltzmann equation. As precisely the stationary version of the latter equation represents our final result, we are able to fully capture the emergence of thermodynamic behavior from microscopic laws.

Furthermore, and in addition to the results on diffusive transport, we have determined the coherent corrections due to the wave-nature of the particles, i. e. the effect of coherent backscattering. For the first time, we were able to analyze the contributions of inelastic scattering to the backscattering cone, and to demonstrate their importance with increasing non-linearity.

Let us briefly summarize under what circumstances we were able to reduce the rather intractable interacting N-body problem to a nonlinear equation of Boltzmann type. Of fundamental importance as well as of great relevance in realistic transport scenarios is the presence of a random and weak disorder potential. We here restricted ourselves to the case of averages over a Gaussian and δ-correlated disorder potential, which – as we discussed – is a special case of a speckle potential for low single-particle energies and weak potential strength. The weakness of the disorder potential is represented by the very small ratio of the particle's wavelength with the disorder mean free path, i. e. $k\ell_{\mathrm{dis}} \gg 1$, where ℓ_{dis} can be, in principle, chosen arbitrarily large (also experimentally, by adjusting the potential strength). All other relevant length scales can be expressed as a function of ℓ_{dis}, and thus scale accordingly. The presence of the weak disorder potential implies a series of immediate consequences: (Note that these consequences are rather simplifications than restrictions of our theory, see below.)

- For the case of Gaussian white noise in three dimensions, ℓ_{dis} is independent of the single-particle energy and the scattering off the disorder potential is isotropic, thus ℓ_{dis} also constitutes the only relevant linear transport length scale in our system.
- The only transport contributions that survive an average over many realizations of the disorder potential (up to higher orders in $\mathcal{O}[(k\ell_{\mathrm{dis}})^{-1} \ll 1]$) are the so-called diffusive ladder and coherent crossed diagrams of co- and counter-propagating scattering amplitudes, respectively.
- It is well known that the amplitudes, from which the ladder intensity is formed, coincide with a stationary Gaussian stochastic process.

Thereby, scattering off the disorder potential randomizes the individual particle's momenta, a prerequisite, also known as molecular chaos, for the derivation of the Boltzmann transport theory.

- The presence of the disorder potential inhibits recurrent scattering for colliding particles. As a consequence, we can trace out the undetected particle immediately after its collision with the detected particle and thus obtain a non-linear equation for the propagation of a single particle.
- Conversely, the effects of the interaction between the particles approximately decouple from the presence of the disorder potential. In other words, the particles interact as if they were in the vacuum. (As discussed in Section 3.3, a "dressing" of the vacuum T-matrix to first order in the disorder potential strength occurs, which, however, is again well controlled by the small parameter $(k\ell_{dis})^{-1}$.)

In addition to these consequences solely following from the presence of the weak (white noise) disorder potential, we need to quantify the requirements for the collisions between the particles. We assumed a dilute and low energy Bose gas, i. e. a mean particle spacing much larger than the s-wave scattering length, $a_s\rho_0^{1/3} \ll 1$ and $ka_s \ll 1$, such that the inclusion of binary collisions and s-wave scattering is sufficient, where the latter assumption was chosen for computational convenience only. In order for the restriction to ladder and crossed diagrams to be valid, we further assumed that the average mean path ℓ_{int} between successive collisions must be so large that at least *one* scattering off the disorder potential occurs in between, i. e. $\ell_{int} \gg \ell_{dis}$.

As indicated above, these assumptions were sufficient to derive a non-linear integral equation that is equivalent to the stationary quantum Boltzmann equation. Guided by the experimental realizability with present-day technologies, we conducted a numerical experiment for a stationary scattering scenario that involves a three-dimensional slab.

At first, we focused on numerical simulations of our theory within the slab. In addition to the expected diffusive transport of the total particle current we observed a separation of the initial mono-energetic current into elastic and inelastic contributions, where the latter emerges due to inelastic collisions and increases with increasing interaction strength and/or slab length. Whereas the initial matter wave corresponds to a condensate state (which is retained under the influence of disorder scattering and elastic collisions), the inelastic collisions deplete the former and create a thermal cloud that follows a Maxwell-Boltzmann distribution. We were able to monitor this process by snapshots of the particle current inside the slab, and to quantify its occurrence by the parameters k, ℓ_{dis}, and ℓ_{int}.

In a second step, we also included the coherent corrections due to the wave nature of the particles, i. e. the crossed component. As this contribution emerges only outside the slab, due to constructive interference of time-reversal symmetric scattering paths, i. e. coherent backscattering, we numerically determined the normalized backscattered currents for the ladder and crossed component. Recent treatments based e. g. on the Gross-Pitaevskii equation have revealed the dephasing character of the nonlinearity (due to elastic scattering) that can turn constructive into destructive interference, and thus predicted an inversion of the cone. For the first time, we were able to determine the role of additional inelastic collisions on the height

of the coherent backscattering cone. Interestingly, this additional source of dephasing speeds up the gradual reduction of the cone height with increasing collision strength initially, but also inhibits the emergence of destructive interference. This in turn corresponds to a slowing down of the decrease of the coherent backscattering interference signal with increasing interaction strength, and the absence of an inversion of the cone for the parameter regime considered within this thesis. In the inelastic coherent backscattering contribution, the importance of constructive many-particle interference, that is known to give rise to an enhancement factor larger than two for weak nonlinearities, was shown to persist in a narrow spectral window close to the initial energy.

As we await an experimental verification of our results, it is worthwhile to widen the applicability of our theory. The application to a stationary scattering setup with matter waves constitutes, on the one hand, a very timely scenario, as e. g. the developments of atom lasers and matter wave interferometers on atom chips, see Section 2.1, rapidly progress. On the other hand, many years of expertise have been gathered within the field of wave-packet spreading upon releasing the condensate from a trap into a new environment, where e. g. the first experiments on coherent backscattering of (non-interacting) matter waves have been reported recently [55, 56]. Consequently, an extension of our theory to time-dependent scenarios based on recent progress in this field [186, 187] presents a significant and feasible task.

Another regime, which so far has been excluded, would involve the possibility of stronger interactions between the particles, i. e. the relaxation of the requirement $\ell_{\mathrm{int}} \gg \ell_{\mathrm{dis}}$. There, the repulsion or attraction between the particles is expected to affect the spatial density profile inside the slab. A first step towards this scenario corresponds to an inclusion of collision processes to the overall transport, i. e. removing the contact approximation for the collisions, see eq. (121). In subsequent steps, one has to analyze how the disregard of all but ladder and crossed diagrams is affected by stronger interactions.

Let us also comment on our present choice of the disorder potential and the dimensionality of the setup. Although a very weak speckle potential has an approximately Gaussian white noise statistics for low single-particle energies, see Section 2.1, it would be more realistic to include finite (non δ-like) correlations which are then, of course, also energy dependent. A worthwhile intermediate step towards this goal could correspond to a reduction of this present theory to the two-dimensional case. There, the Gaussian white noise disorder mean free path is energy-dependent [48] and allows for an investigation of energy-dependent transport processes. Note that, albeit the simplified choice of the statistics of the disorder potential presented here, we expect the main findings of the work to remain valid also in more realistic disorder potentials, which, however, elude a simple calculation.

In conclusion, we are confident that our present theory and the rather straightforward extensions discussed above will substantially foster a more complete understanding of quantum transport under the interplay of disorder and inter-particle interaction, and can contribute to a unifying picture from microscopic to macroscopic scales.

Part II

INTERACTING RYDBERG ATOMS IN A DEPHASING ENVIRONMENT

6

LIGHT SCATTERING OFF STRONGLY INTERACTING RYDBERG ATOMS IN A 1D CHAIN

6.1 INTRODUCTION AND MOTIVATION

Atoms with valence electrons excited to high principal quantum numbers as large as $n \simeq 100$ are called *Rydberg atoms*. Due to this large quantum number they exhibit exaggerated properties (see below) and have therefore constituted an intense field of research over the last decades, as e. g. summarized in [188, 189]. The proposed possible application of Rydberg physics to realize quantum information processing [190, 191], together with the experimental ability to control center of mass and electronic degrees of freedom simultaneously, has revived the field. This allows, on the one side, to investigate novel collective dynamics of interacting Rydberg gases [188, 192, 193], and to explore the potential of Rydberg physics for robust and fault-tolerant quantum control [194, 195] and engineering [196].

An atom can be excited to a Rydberg state using e. g. a dipole-allowed two-photon transition via an intermediate p-orbital. As the radii of such Rydberg atoms scale as n^2, they are huge on atomic scales and can be as large as several thousand Bohr radii a_0 corresponding to $0.1 - 1\mu m$ [188]. The large distance between the highly excited valence electron and a, possibly, multi-electron core causes a hydrogen-like behavior and large polarizabilities which can scale as n^7 [188]. The radiative lifetime of the Rydberg state which scales as n^α, with $\alpha = 3, 4, 5$ (depending on the angular momentum) [194] is much longer than any other time scale in the system such that spontaneous decay – especially for s-orbitals – can be neglected most of the times [197, 198].

Another intriguing feature, which arises as a consequence of the large polarizability, is the strong interaction between different Rydberg atoms over distances of several μm [188]. Rydberg atoms excited to s-orbitals, which we will focus on in the following, interact repulsively via *van der Waals* interaction with the interaction potential given as

$$V(r) = -\frac{C_6}{r^6}\,, \tag{182}$$

where the dispersion coefficient C_6 scales as n^{11} [188, 199] giving rise to an interaction strength for e. g. $n \simeq 100$ which is *twelve* orders of magnitude stronger than the corresponding ground-state interaction [196]. A consequence of the large polarizability is the effective energy level shift of atoms in the neighborhood of a Rydberg atom leading to a vanishing probability to be excited (if the laser is tuned with respect to the energy levels of a single Rydberg atom). Within this so-called exclusion or blockade volume with radius ℓ_b only a *single* excitation is present [200] and can thus be shared among all N atoms leading e. g. to collective Rabi oscillations with enhanced frequency $\sqrt{N}\Omega$ [201]. An explicit expression for the blockade radius is obtained by determining the interaction energy of two Rydberg atoms at a distance ℓ_b and setting this equal to the collective laser coupling $\sqrt{N}\Omega$ for the N atoms inside the blockade radius, leading to $\ell_b = [C_6/(\Omega\sqrt{1/\ell})]^{2/13}$ [202], with ℓ being the average spacing between the atoms. Although the physical radius is not a sharp limit, it has been shown theoretically and

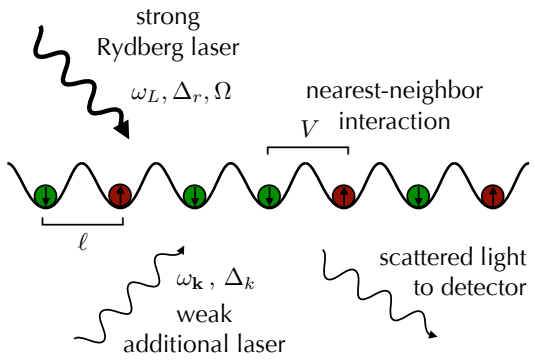

Figure 33: Chain of atoms trapped in the wells of a 1D-lattice potential (as e. g. suggested in [209]) with lattice spacing (between the lattice sites m and $m+1$ given by) ℓ. The ground state atoms (green spin-down symbols) are driven with a strong laser field (frequency ω_L, Rabi-frequency Ω, detuning Δ_r) to a highly-excited Rydberg state (red spin-up symbols) and interact via next-neighbor interaction V with each other, i. e. as given by eq. (183) expressed as a function of the lattice sites, and for $n = m+1$. An additional, far-detuned, weak laser field (frequency $\omega_{\mathbf{k}}$, detuning Δ_k) is scattered off another atomic dipole transition. The scattered intensity is detected by a detector in the far-field.

experimentally that this quantity captures nonetheless the relevant physics [203].

The atomic dynamics (including the blockade mechanism due to the interatomic interaction and the driving of the laser field) is generated by a simple spin Hamiltonian [204], with the interaction contribution between two atoms respectively located at positions $\mathbf{r}_m$ and $\mathbf{r}_n$ given as follows:

$$H_{m,n} = \hbar C_6 \frac{\sigma_m^r \sigma_n^r}{|\mathbf{r}_m - \mathbf{r}_n|^6}\,, \tag{183}$$

where $\sigma_m^r = |r\rangle\langle r|_m$ denotes the projector onto the Rydberg state (with fixed quantum numbers nlm) of the m^{th} atom. The rather simple blockade picture has nonetheless been shown to grasp important features of the collective excitation mechanism quite well [205, 206, 200]. Since interacting Rydberg gases do undeniably constitute slightly more complicated physical objects than what can reliably be mimicked by two interacting two level systems, non-resonantly coupled Rydberg states, autoionization [207] and other effects [193, 208] induce deviations from the simple blockade model's predictions.

6.1.1 *Our Setup*

Our setup is depicted in Fig. 33. We imagine a chain of ground state atoms where each atom is trapped at the bottom of a well of a one-dimensional optical lattice potential. The atoms are quasi-resonantly, strongly laser-driven to a Rydberg s-state, under inclusion of next-neighbor interactions, i. e. as given by eq. (183) expressed as a function of the lattice sites, and for $n = m+1$. Additionally, another weak laser is tuned far off-resonant with another atomic dipole transition. The off-resonance condition ensures that the occupation probability of the excited state is negligible and this state can

thus be adiabatically eliminated. As a result, the photons of the weak laser field can be described as effectively being scattered off the atomic ground state (without intermediate population of the excited state) into the modes of the free radiation field initially in the vacuum state (into which the atomic system is embedded). In fact, we will model the incident weak laser field by a macroscopically occupied mode of this radiation field, see below, that is the same for all atoms, and that is coupled to the atomic subsystem. In order to describe the atomic subsystem by itself, we derive a master equation – based on previous results in different fields [210, 211] – by tracing out the degrees of freedom of the surrounding radiation field (also called environment in the following).

As we will see, the coupling to the radiation field via photon scattering of the additional weak laser field within the master equation corresponds to a dephasing noise that equally occurs experimentally, e. g. by unwanted photon scattering from the light fields needed to produce optical lattices [212]. We, however, show that by detection of these photons scattered off the chain of interacting Rydberg atoms, one can monitor the atomic dynamics, and characterize the influence of the scattered light on the Rydberg atoms.

Furthermore, we introduce a simple dimer-model [213] that, on the one hand, reproduces the main features of the atomic dynamics and, on the other hand, can straight-forwardly be used to calculate the intensity scattered off the atomic chain. We demonstrate that the interatomic correlations present in the atomic chain alter the angular distribution of the detected light intensity.

6.2 A SINGLE RYDBERG ATOM IN AN EXTERNAL FIELD

Starting point of our considerations is a single atom at position $\mathbf{r}$, with three different electronic energy levels in a V-shaped arrangement, see Fig. 34. The ground state $|g\rangle$ is coupled by a classical laser field

$$\mathbf{E}_L(t,\mathbf{r}) = \hat{\varepsilon}_L \mathcal{E}_L \cos(\omega_L t - \mathbf{k}_L \mathbf{r}) \tag{184}$$

to the excited Rydberg-state $|r\rangle$, which is detuned from the laser frequency ω_L by $\Delta_r = \omega_r - \omega_L$. $\mathcal{E}_L$ is a real amplitude and $\hat{\varepsilon}_L$ denotes the unit polarization vector. The second transition is driven from $|g\rangle$ to the excited state $|e\rangle$, via coupling to the free radiation field with modes $\mathbf{k}$ and frequency $\omega_k = |\mathbf{k}|c$, which are detuned from the atomic transition by $\Delta_k = \omega_e - \omega_k$.

Within the rotating-wave and dipole approximation [214], the Hamiltonian in the Schrödinger picture is the following:[1]

$$\begin{aligned} H(t) = \hbar \sum_{\mathbf{k}} \omega_k a_{\mathbf{k}}^\dagger a_{\mathbf{k}} + \hbar\omega_e \sigma^e + \hbar\omega_r \sigma^r + \hbar \sum_{\mathbf{k}} \left(g_{\mathbf{k}}^* a_{\mathbf{k}} \sigma^{+,\mathrm{dip}} + g_{\mathbf{k}} a_{\mathbf{k}}^\dagger \sigma^{-,\mathrm{dip}} \right) \\ - \hbar \frac{\Omega}{2} \left(\sigma^+ e^{i(\mathbf{k}_L \mathbf{r} - \omega_L t)} + \sigma^- e^{-i(\mathbf{k}_L \mathbf{r} - \omega_L t)} \right) , \end{aligned} \tag{185}$$

1 To keep the notation as simple as possible, we suppress the "hat"-operator notation in this chapter.

where we set the ground-state energies of atomic and field degrees of freedom equal to zero, and introduced the operators

$$\begin{aligned} \sigma^e &= |e\rangle\langle e| , & \sigma^{+,\mathrm{dip}} &= |e\rangle\langle g| , \\ \sigma^r &= |r\rangle\langle r| , & \sigma^{-,\mathrm{dip}} &= |g\rangle\langle e| , \\ \sigma^g &= |g\rangle\langle g| , & \sigma^+ &= |r\rangle\langle g| , \\ & & \sigma^- &= |g\rangle\langle r| . \end{aligned} \tag{186}$$

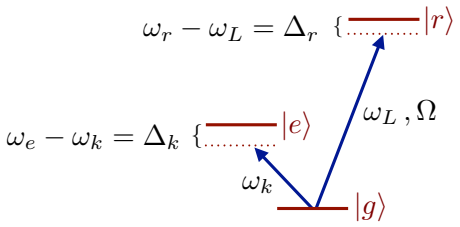

Figure 34: V-shaped three-level structure of a single atom under consideration. The transition $|g\rangle \leftrightarrow |r\rangle$ between the electronic ground and Rydberg states $|g\rangle$ and $|r\rangle$, respectively, is laser driven with frequency ω_L, Rabi-frequency Ω, and an adjustable detuning Δ_r. In addition, another dipole transition $|g\rangle \leftrightarrow |e\rangle$ is coupled to a macroscopically occupied mode of the surrounding radiation field with frequency ω_k and detuning Δ_k, e. g. realized by an additional laser field.

In addition, $\Omega = (\hat{\varepsilon}_L \cdot \hat{\varepsilon}_{d_r}) d_r \mathcal{E}_L/\hbar$ is the Rabi-frequency of the laser driven Rydberg transition with real dipole matrix element d_r, and the orientation of the dipole given by the unit-vector $\hat{\varepsilon}_{d_r}$.[2] $g_{\mathbf{k}} = -\hat{\varepsilon}_d \cdot \hat{\varepsilon}_k \mathcal{E}_k d\, e^{-i\mathbf{kr}}/\hbar$ is the coupling strength between the radiation field and the atom, with d the dipole moment corresponding to the transition driven by the field component with polarization $\hat{\varepsilon}_d$, $\hat{\varepsilon}_k$ the polarization of mode $\mathbf{k}$, and $\mathcal{E}_k = \sqrt{\hbar\omega_k \varepsilon_0 \mathcal{V}/2}$, with the electric constant ε_0 and the quantization volume $\mathcal{V}$.

Note that $H(t)$ becomes time-independent in the frame that co-rotates with the laser frequency ω_L. For further convenience, we transform eq. (185) to the interaction picture (identified by the superscript I):

$$H^I = U_F^\dagger U_A^\dagger H U_A U_F\,, \quad U_F = e^{-i\sum_k \omega_k a_k^\dagger a_k t}\,, \quad U_A = e^{-i(\omega_e \sigma^e + \omega_L \sigma^r)t}\,,$$

to finally obtain:

$$H^I(t) = \hbar\Delta_r \sigma^r + \hbar \sum_{\mathbf{k}} \left(g_{\mathbf{k}}^* a_{\mathbf{k}} \sigma^{+,\mathrm{dip}} e^{i\Delta_k t} + g_{\mathbf{k}} a_{\mathbf{k}}^\dagger \sigma^{-,\mathrm{dip}} e^{-i\Delta_k t} \right) - \hbar\frac{\Omega}{2}\left(\sigma^+ e^{i\mathbf{k}_L \mathbf{r}} + \sigma^- e^{-i\mathbf{k}_L \mathbf{r}} \right)\,. \tag{187}$$

Subsequently, we will assume that the transition $|g\rangle \leftrightarrow |e\rangle$ is only weakly driven by the free radiation field, due to a very large detuning Δ_k. Therefore, we can neglect the population of state $|e\rangle$, and thereby derive an effective two-level Hamiltonian for the transition $|g\rangle \leftrightarrow |r\rangle$ (upon adiabatic elimination of $|g\rangle \leftrightarrow |e\rangle$ [214, 215]).

6.2.1 *Derivation of an Effective Two-Level Hamiltonian for a Single Atom*

Effective Hamiltonians have been derived in different fields of physics, e. g. in condensed matter theory [216], in semiclassical treatments [217], and in the field of quantum optics [218, 219]. We will use here a formula derived by James and Jerke [220, 221] which allows to extract an effective Hamiltonian from an existing interaction picture Hamiltonian if the interaction is sufficiently weak and if the perturbation has a harmonic time dependence.

The general formula given in [220] reads:

$$H_{\mathrm{eff}}(t) = \sum_{m,n} \frac{1}{\hbar\overline{\omega}_{mn}} [h_m^\dagger, h_n] e^{i(\omega_m - \omega_n)t}\,, \tag{188}$$

2 We will not further specify the (relative) orientations of the atomic dipole moments. In an experiment, one has to specify the polarizations of the incoming fields, such as to distinguish the photons scattered off the two atomic transitions.

where $\overline{\omega}_{mn}$ is the harmonic average

$$\frac{1}{\overline{\omega}_{mn}} = \frac{1}{2}\left[\frac{1}{\omega_m} + \frac{1}{\omega_n}\right] \tag{189}$$

of the frequencies ω_m and ω_n, that will be associated with the respective frequencies Δ_k and Δ_q, see below, that determine the time-dependence of the interaction Hamiltonian (187). Furthermore, the h_m are the m interaction parts of the full Hamiltonian which one wants to describe effectively, i. e. for blue-detuned free field modes with $\Delta_k = \omega_e - \omega_k < 0$, we identify

$$\begin{aligned} H^I_{\text{int}}(t) &= \hbar \sum_{\mathbf{k}} \left(g^*_{\mathbf{k}} a_{\mathbf{k}} \sigma^{+,\text{dip}} e^{i\Delta_k t} + g_{\mathbf{k}} a^\dagger_{\mathbf{k}} \sigma^{-,\text{dip}} e^{-i\Delta_k t} \right) \\ &= \hbar \sum_{\mathbf{k}} \left(h^\dagger_{\mathbf{k}} e^{i\Delta_k t} + h_{\mathbf{k}} e^{-i\Delta_k t} \right) , \end{aligned} \tag{190}$$

with $h_{\mathbf{k}} = g_{\mathbf{k}} a^\dagger_{\mathbf{k}} \sigma^{-,\text{dip}}$ and the hermitian conjugate $h^\dagger_{\mathbf{k}}$. Note that (for the moment) we neglect all terms in the second line of eq. (187) that depend on the transition $|g\rangle \leftrightarrow |r\rangle$.

After evaluation of the commutator in eq. (188) with $h_{\mathbf{k}}$ ($h_{\mathbf{q}}$) and Δ_k (Δ_q) instead of h_m (h_n) and ω_m (ω_n), respectively, eq. (190) is replaced by the effective Hamiltonian:

$$H^I_{\text{int,eff}}(t) = \hbar \sum_{\mathbf{k},\mathbf{q}} \frac{1}{\overline{\omega}_{kq}} \left(R_{\mathbf{k}} R^\dagger_{\mathbf{q}} \sigma^e - R^\dagger_{\mathbf{q}} R_{\mathbf{k}} \sigma^g \right) e^{i(\omega_q - \omega_k)t} . \tag{191}$$

As we initially start out with all population in the atomic ground state, i. e. $\sigma^g = 1$, and the detuning Δ_k is very large, the population of the excited state ($\sigma^e \approx 0$) can be neglected and we obtain from (191)

$$H_{\text{int,eff}}(t) = -\hbar \sum_{\mathbf{k},\mathbf{q}} \frac{1}{\overline{\omega}_{kq}} R^\dagger_{\mathbf{q}} R_{\mathbf{k}} \sigma^g e^{i(\omega_q - \omega_k)t} , \tag{192}$$

where

$$R_{\mathbf{k}} := g^*_{\mathbf{k}} a_{\mathbf{k}} , \qquad R^\dagger_{\mathbf{k}} := g_{\mathbf{k}} a^\dagger_{\mathbf{k}} . \tag{193}$$

Note the self-adjointness

$$\begin{aligned} &\left[\sum_{\mathbf{k},\mathbf{q}} R_{\mathbf{k}} R^\dagger_{\mathbf{q}} \right]^\dagger = \left[\sum_{\mathbf{k},\mathbf{q}} g^*_{\mathbf{k}} g_{\mathbf{q}} a_{\mathbf{k}} a^\dagger_{\mathbf{q}} \right]^\dagger = \sum_{\mathbf{k},\mathbf{q}} g_{\mathbf{k}} g^*_{\mathbf{q}} a_{\mathbf{q}} a^\dagger_{\mathbf{k}} = \sum_{\mathbf{q},\mathbf{k}} g^*_{\mathbf{k}} g_{\mathbf{q}} a_{\mathbf{k}} a^\dagger_{\mathbf{q}} \\ &= \sum_{\mathbf{k},\mathbf{q}} R_{\mathbf{k}} R^\dagger_{\mathbf{q}} , \end{aligned} \tag{194}$$

and the commutation relation

$$\sum_{\mathbf{k},\mathbf{q}} [R_{\mathbf{k}}, R^\dagger_{\mathbf{q}}] = \sum_{\mathbf{k},\mathbf{q}} g^*_{\mathbf{k}} g_{\mathbf{q}} [a_{\mathbf{k}}, a^\dagger_{\mathbf{q}}] = \sum_{\mathbf{k},\mathbf{q}} g^*_{\mathbf{k}} g_{\mathbf{q}} \delta_{\mathbf{k},\mathbf{q}} = \sum_{\mathbf{k}} |g_{\mathbf{k}}|^2 . \tag{195}$$

As a consequence of eq. (189), $\overline{\omega}_{kq}$ in eq. (192) is given by

$$\overline{\omega}_{kq} = \frac{(\omega_e - \omega_k)(\omega_e - \omega_q)}{\omega_e - (\omega_k + \omega_q)/2} \quad \left(\text{and} \;\; \overline{\omega}_{kq} = \Delta_k \;\; \text{if} \;\; \omega_k = \omega_q \right) , \tag{196}$$

where we again note that $\Delta_k = \omega_e - \omega_k$ and $\Delta_q = \omega_e - \omega_q$ were replaced for ω_m and ω_n in eq. (190), respectively.

For the case of red-detuned free field modes, i. e. $\Delta_k > 0$, eq. (192) differs by a prefactor

$$H^I_{\text{int,eff}}(t) = \hbar \sum_{\mathbf{k},\mathbf{q}} \frac{1}{\overline{\omega}_{kq}} R^\dagger_{\mathbf{q}} R_{\mathbf{k}} \sigma^g e^{i(\omega_q - \omega_k)t} \,. \tag{197}$$

Thus, we observe that $\overline{\omega}_{kq} < 0$ if $\Delta_k < 0$ and $\Delta_q < 0$, i. e. for blue-detuning, and $\overline{\omega}_{kq} > 0$ for red-detuning. Therefore, $H_{\text{int,eff}}$ does not depend on the sign of the detuning, and can be written as

$$H^I_{\text{int,eff}}(t) = \hbar \sum_{\mathbf{k},\mathbf{q}} \frac{1}{|\overline{\omega}_{kq}|} R^\dagger_{\mathbf{q}} R_{\mathbf{k}} \sigma^g e^{i(\omega_q - \omega_k)t} \,. \tag{198}$$

The total Hamiltonian (187) in the interaction picture thus transforms to the effective Hamiltonian

$$\begin{aligned} H^I_{\text{eff}}(t) = {} & \hbar \Delta_r \sigma^r - \hbar \frac{\Omega}{2} \left(\sigma^+ e^{i\mathbf{k}_L \mathbf{r}} + \sigma^- e^{-i\mathbf{k}_L \mathbf{r}} \right) \\ & + \hbar \sum_{\mathbf{k},\mathbf{q}} \frac{1}{|\overline{\omega}_{kq}|} R^\dagger_{\mathbf{q}} R_{\mathbf{k}} \sigma^g e^{i(\omega_q - \omega_k)t} \,. \end{aligned} \tag{199}$$

In (199), the time-dependence stems from the explicit time-dependence of the creation and annihilation operators of the free field, which was introduced into the initial Hamiltonian (185) after transformation to the interaction picture, see eq. (187).

In the next section, we introduce the chain of Rydberg atoms, and – in addition to the dynamics of eq. (199) – explicitly account for the interaction between the atoms.

6.3 INTERACTING RYDBERG ATOMS IN AN EXTERNAL FIELD – A MASTER EQUATION APPROACH

As mentioned before, atoms excited to a Rydberg s-state strongly interact via van-der-Waals forces. As we showed in the beginning of this chapter, the interaction term can be mapped to a spin coupling and added to the effective Hamiltonian (199), which extends our treatment to the case of many interacting atoms. Each atom will be trapped at one well of a one-dimensional lattice, and we assume that only nearest neighbors interact, i. e. $n = m + 1$ in eq. (183). Such a situation is also experimentally feasible, due to the precise control of the lattice spacing and the rapid decay ($\propto r^{-6}$, see eq. (183)) of the interaction strength between the atoms with increasing distance.

6.3.1 *Derivation of a Master Equation for a 1D Chain of Interacting Rydberg Atoms*

The Hamiltonian in the interaction picture for a 1D chain of Rydberg atoms we start out with reads

$$H^I(t) = \sum_{m=1}^{L} \left(H^I_m + H^I_{m,m+1} + H^I_{\text{int},m}(t) \right) \,, \tag{200}$$

where m now denotes the m^{th} of L atoms in the chain. The Hamiltonian acting only on the site m is obtained from the effective Hamiltonian (199) as

$$H_m^I = \hbar\Delta_r \sigma_m^r - \hbar\left(\Omega_m \sigma_m^+ + \Omega_m^* \sigma_m^-\right) , \tag{201}$$

$$H_{\text{int},m}^I(t) = \hbar \sum_{\mathbf{k},\mathbf{q}} \frac{1}{|\overline{\omega}_{kq}|} R_{\mathbf{q},m}^\dagger R_{\mathbf{k},m} \sigma_m^g e^{i(\omega_q - \omega_k)t} , \tag{202}$$

where

$$\sigma_m^r = |r\rangle\langle r|_m , \qquad \sigma_m^g = |g\rangle\langle g|_m ,$$
$$\sigma_m^+ = |r\rangle\langle g|_m , \qquad \sigma_m^- = |g\rangle\langle r|_m ,$$

are now the respective projectors on the Rydberg and ground state of the m^{th} atom, and the respective m^{th} atom creation and annihilation operators. The Rabi-frequencies Ω also turn position-dependent and read

$$\Omega_m = \Omega e^{i\mathbf{k}_L \mathbf{r}_m}/2 \qquad \text{and} \qquad \Omega_m^* = \Omega e^{-i\mathbf{k}_L \mathbf{r}_m}/2 . \tag{203}$$

The interaction between neighboring atoms in (200) is described by adaption of eq. (183) to the 1D case, i. e.

$$H_{m,m+1}^I = \hbar V \sigma_m^r \sigma_{m+1}^r , \tag{204}$$

with $V = -C_6/\ell^6$ the interaction potential, cf. eq. (182), and ℓ the lattice spacing. As discussed in the beginning of this chapter, if V is sufficiently large, the excitation of two neighboring atoms into Rydberg states becomes energetically very costly and is effectively blocked.

We will now focus on the effective interaction Hamiltonian (202) and assume that one of the field modes (with the subscript 0) is initially in a macroscopically occupied coherent state, such that the corresponding field operators can be replaced by c-numbers ($a_0 \to \alpha_0$) [214], i. e.

$$\begin{aligned} H_{\text{int},m}^I(t) &= \hbar \sum_{\mathbf{k},\mathbf{q}} \frac{1}{|\overline{\omega}_{kq}|} g_{\mathbf{k},m} g_{\mathbf{q},m}^* a_{\mathbf{k}}^\dagger a_{\mathbf{q}} \sigma_m^g e^{i(\omega_q - \omega_k)t} \\ &\approx \hbar \sum_{\mathbf{k}} \frac{1}{|\overline{\omega}_{k0}|} g_{0,m} g_{\mathbf{k},m}^* \alpha_0^* a_{\mathbf{k}} \sigma_m^g e^{-i(\omega_0 - \omega_k)t} \\ &\quad + \hbar \sum_{\mathbf{k}} \frac{1}{|\overline{\omega}_{k0}|} g_{\mathbf{k},m} g_{0,m}^* a_{\mathbf{k}}^\dagger \alpha_0 \sigma_m^g e^{i(\omega_0 - \omega_k)t} . \end{aligned} \tag{205}$$

Following Lehmberg [222], we write down an equation of motion for an arbitrary atomic operator $Q(t)$ using eqs. (201), (204), and (205):

$$\begin{aligned} \dot{Q}(t) &= i \sum_m \left(\Delta_r [\sigma_m^r, Q]_t - \Omega_m [\sigma_m^+, Q]_t + \Omega_m^* [\sigma_m^-, Q]_t + V [\sigma_m^r \sigma_{m+1}^r, Q]_t\right) \\ &\quad + i \sum_{\mathbf{k},m} \frac{1}{|\overline{\omega}_{k0}|} g_{0,m} g_{\mathbf{k},m}^* \alpha_0^* a_{\mathbf{k}}(t) e^{-i(\omega_0 - \omega_k)t} [\sigma_m^g, Q]_t \\ &\quad + i \sum_{\mathbf{k},m} \frac{1}{|\overline{\omega}_{k0}|} g_{\mathbf{k},m} g_{0,m}^* \alpha_0 e^{i(\omega_0 - \omega_k)t} [Q, \sigma_m^g]_t \, a_{\mathbf{k}}^\dagger(t) , \end{aligned} \tag{206}$$

where $[A, B]_t = [A(t), B(t)]$.

We also spell out the equation of motion for the field mode $a_{\mathbf{k}}$, which we then formally integrate:

$$\begin{aligned} \dot{a}_{\mathbf{k}}(t) &= -i \sum_m \frac{1}{|\overline{\omega}_{k0}|} g_{\mathbf{k},m} g_{0,m}^* \alpha_0 e^{i(\omega_0 - \omega_k)t} \sigma_m^g(t) , \\ a_{\mathbf{k}}(t) &= a_{\mathbf{k}}(0) - i \sum_m \frac{1}{|\overline{\omega}_{k0}|} g_{\mathbf{k},m} g_{0,m}^* \alpha_0 \int_0^t dt' \, e^{i(\omega_0 - \omega_k)t'} \sigma_m^g(t') . \end{aligned} \tag{207}$$

Taking the hermitian adjoint of (207) and plugging it into the last term of eq. (206), we obtain:

$$i\sum_{\mathbf{k},m}\frac{\alpha_o}{|\overline{\omega}_{ko}|}g_{\mathbf{k},m}g^*_{o,m}e^{i(\omega_o-\omega_k)t}[Q,\sigma^g_m]_t\,a^\dagger_{\mathbf{k}}(0) \tag{208}$$

$$-\sum_{\mathbf{k},m,m'}\frac{|\alpha_o|^2}{\overline{\omega}^2_{ko}}g_{\mathbf{k},m}g^*_{o,m}g^*_{\mathbf{k},m'}g_{0,m'}\,[Q,\sigma^g_m]_t\int_0^t dt'\,e^{i(\omega_o-\omega_k)(t-t')}\,\sigma^g_{m'}(t')\,.$$

As a next step, we explicitly consider the coupling term $g_{\mathbf{k},m}$, in order to account for polarization effects in our calculations:

$$g_{\mathbf{k},m}=-\frac{\hat{\varepsilon}_d\cdot\hat{\varepsilon}^{(\lambda)}_k}{\hbar}\mathcal{E}_k d\,e^{-i\mathbf{k}\mathbf{r}_m}\,,\qquad\qquad \mathcal{E}_k=\sqrt{\frac{\hbar\omega_k}{2\varepsilon_o\mathcal{V}}}\,, \tag{209}$$

where λ now denotes the possible polarizations of the free field modes. It is convenient to take the continuum limit and transform the sum over the field modes $\mathbf{k}$ into an integral, and separate the summation over the field polarization indices, i. e.

$$\sum_{\mathbf{k}}\to\frac{\mathcal{V}}{(2\pi)^3}\sum_{\lambda=1}^{2}\int d^3k\,. \tag{210}$$

The sum over polarization unit-vectors appearing in the second term of expression (208) can be evaluated to give:

$$\begin{aligned}(\hat{\varepsilon}_d\cdot\hat{\varepsilon}_o)^2\sum_{\lambda=1}^{2}\left(\hat{\varepsilon}_d\cdot\hat{\varepsilon}^{(\lambda)}_k\right)^2&=(\hat{\varepsilon}_d\cdot\hat{\varepsilon}_o)^2\left(1-(\hat{\varepsilon}_d\cdot\hat{\mathbf{k}})^2\right)\\&=(\hat{\varepsilon}_d\cdot\hat{\varepsilon}_o)^2\,\hat{\varepsilon}_d\cdot\left(\mathbb{1}-\hat{\mathbf{k}}\hat{\mathbf{k}}\right)\cdot\hat{\varepsilon}_d\,,\end{aligned} \tag{211}$$

where we used that

$$\left(\hat{\varepsilon}_d\cdot\hat{\varepsilon}^{(1)}_k\right)^2+\left(\hat{\varepsilon}_d\cdot\hat{\varepsilon}^{(2)}_k\right)^2+\left(\hat{\varepsilon}_d\cdot\hat{\mathbf{k}}\right)^2=1\,, \tag{212}$$

and $\hat{\mathbf{k}}\hat{\mathbf{k}}$ denotes the dyadic product of the unit-vector $\hat{\mathbf{k}}$. Let us continue by evaluation of the integral in (208) (which appears due to the substitution (210)). To do so, we switch to spherical coordinates. The wave vectors $\mathbf{k}$ and $\mathbf{k}_o$ of the field and the orientation of the atomic dipole moment $\hat{\varepsilon}_d$, see Fig. 35, are given by

$$\mathbf{k}=k\begin{pmatrix}\sin\theta\cos\phi\\ \sin\theta\sin\phi\\ \cos\theta\end{pmatrix}\,,\quad \mathbf{k}_o=k_o\begin{pmatrix}\sin\theta_o\cos\phi_o\\ \sin\theta_o\sin\phi_o\\ \cos\theta_o\end{pmatrix}\,,\quad \hat{\varepsilon}_d=\begin{pmatrix}\sin\eta\cos\xi\\ \sin\eta\sin\xi\\ \cos\eta\end{pmatrix}\,. \tag{213}$$

We choose the 1D lattice to be oriented along the z-axis, such that $\mathbf{r}_m=m\ell\hat{z}$ defines the position of the m^{th} atom (and ℓ is again the lattice spacing between neighboring atoms). Consequently, $\mathbf{r}_{m'}-\mathbf{r}_m=\ell(m'-m)\hat{z}$.[3]

3 In the meantime we abbreviate $\ell(m'-m)\hat{z}=r\hat{z}$, and note that $r=r(m,m')$ is a function of two different lattice points m and m'.

In the following we will only focus on the second term of eq. (208) (as the first term will vanish since we assume later that the free radiation field, apart from the macroscopically occupied state, is initially in the vacuum state). Using $\omega_k=|\mathbf{k}|c=kc$ together with (209) and (211) we obtain:

$$\begin{aligned}-|\alpha_o|^2\frac{\omega_o c d^4(\hat{\varepsilon}_d\cdot\hat{\varepsilon}_o)^2}{4(2\pi)^3\hbar^2\varepsilon_o^2\mathcal{V}}\sum_{m,m'}e^{-ik_o r\cos\theta_o}\int_0^\infty\frac{dk k^3}{\overline{\omega}^2_{ko}}\int_0^{2\pi}d\phi\int_{-1}^{+1}d\cos\theta\,e^{ikr\cos\theta}\\ \times\,\hat{\varepsilon}_d\cdot\left(\mathbb{1}-\hat{\mathbf{k}}\hat{\mathbf{k}}\right)\cdot\hat{\varepsilon}_d\,[Q,\sigma^g_m]_t\int_0^t dt'\,e^{i(\omega_o-\omega_k)(t-t')}\,\sigma^g_{m'}(t')\,.\end{aligned} \tag{214}$$

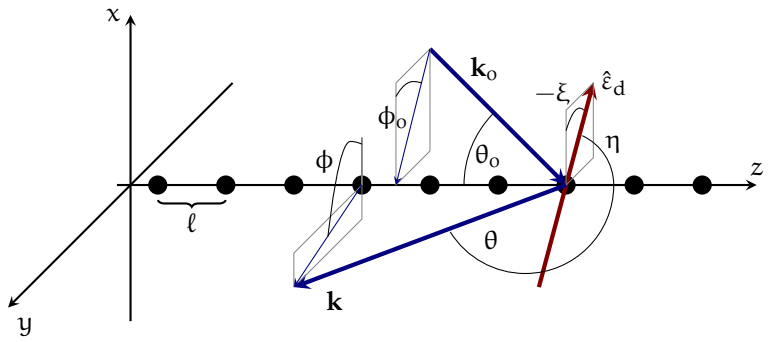

Figure 35: 1D chain of Rydberg atoms with lattice spacing ℓ, aligned in z-direction. The coherent mode $\mathbf{k}_o$, incident on the atoms under an angle of θ_o with the z-axis, and ϕ_o about the z-axis, is scattered into the free radiation field mode $\mathbf{k}$, defined by the angles θ and ϕ. Here only the orientation of the dipole $\hat{\varepsilon}_d$ with respect to the weak radiation field is depicted, which is characterized by the angles η and ξ.

First, we focus on the integrals over ϕ, $\cos\theta$, and k in (214). Integration over ϕ and $\cos\theta$ yields the following expression:

$$\frac{4\pi}{r^3}\int_0^\infty \frac{dk}{\overline{\omega}_{k_o}^2}\,\hat{\varepsilon}_d\cdot\begin{pmatrix}\mathcal{K}_{11} & 0 & 0\\ 0 & \mathcal{K}_{22} & 0\\ 0 & 0 & \mathcal{K}_{33}\end{pmatrix}\cdot\hat{\varepsilon}_d\,, \tag{215}$$

with

$$\mathcal{K}_{11}=\mathcal{K}_{22}=krcos(kr)+(k^2r^2-1)sin(kr)\,, \tag{216}$$

$$\mathcal{K}_{33}=2\,[sin(kr)-krcos(kr)]\,. \tag{217}$$

The different contributions in powers of $1/r$ in expression (215) (note the prefactor $1/r^3$) correspond, respectively, to far-field ($1/r$) and near-field ($1/r^2\,, 1/r^3$) contributions. The integration over k is conducted under the *Wigner-Weisskopf approximation* [223], i. e. contributions of k that do not appear as arguments of the trigonometric functions in eqs. (216) and (217) are replaced by $k\to k_o$, and the interval of integration is expanded to $-\infty$. The k-integral therefore yields for the different components in $1/r^n$:

$$n=1:\quad \frac{4\pi}{c^3\Delta_0^2}\frac{\omega_0^2}{r}\int_{-\infty}^{\infty}d\omega_k\sin(\omega_k r/c)\,e^{-i\omega_k(t-t')} \tag{218}$$

$$=-i\frac{(2\pi)^2}{c^3}\frac{\omega_0^2}{r}\left\{\delta\left(\frac{r}{c}-t+t'\right)-\delta\left(\frac{r}{c}+t-t'\right)\right\}\,,$$

$$n=2:\quad \frac{4\pi}{c^2\Delta_0^2}\frac{\omega_o}{r^2}\int_{-\infty}^{\infty}d\omega_k\cos(\omega_k r/c)\,e^{-i\omega_k(t-t')} \tag{219}$$

$$=\frac{(2\pi)^2}{c^2}\frac{\omega_o}{r^2}\left\{\delta\left(\frac{r}{c}-t+t'\right)+\delta\left(\frac{r}{c}+t-t'\right)\right\}\,,$$

$$n=3:\quad \frac{4\pi}{c\Delta_0^2}\frac{1}{r^3}\int_{-\infty}^{\infty}d\omega_k\sin(\omega_k r/c)\,e^{-i\omega_k(t-t')} \tag{220}$$

$$=-i\frac{(2\pi)^2}{c}\frac{1}{r^3}\left\{\delta\left(\frac{r}{c}-t+t'\right)-\delta\left(\frac{r}{c}+t-t'\right)\right\}\,.$$

Now the integral over t' in expression (214) can be conducted for the three contributions (218)–(220):

$$\int_0^t dt'\, e^{i\omega_o(t-t')}\, \sigma^g_{m'}(t') \left\{\delta\left(\frac{r}{c}-t+t'\right) \pm \delta\left(\frac{r}{c}+t-t'\right)\right\} = e^{i\omega_o r/c}\, \sigma^g_{m'}(t-r/c) \pm e^{-i\omega_o r/c}\, \sigma^g_{m'}(t+r/c)\,. \tag{221}$$

In order to ensure that the arguments of the δ-functions contained in the integral (221) fall within the limits of integration, i. e. the weight of the δ-functions outside the limits of integration is zero and the limits thus become insignificant, we had to assume for the evaluation of (221) that $t > |r/c| = |\ell(m'-m)/c|$. In other words, we thereby include only *physical* times t, that respect a finite propagation time between different lattice sites m and m'.

Before we can rewrite (214), we still need to take scalar products with $\hat{\varepsilon}_d$, see eq. (215). The corresponding contributions from (218)–(220) must be multiplied, respectively, with

$$(218) \times \sin^2\eta\,, \qquad (219) \times (3\sin^2\eta - 2)\,, \qquad (220) \times (2 - 3\sin^2\eta)\,. \tag{222}$$

Combination of eqs. (218)–(222) gives for (214):

$$\begin{aligned}
&\frac{g_o^2}{\Delta_o^2}\frac{3|\alpha_o|^2}{4}\,\Gamma_o(\hat{\varepsilon}_d\cdot\hat{\varepsilon}_o)^2 \sum_{m,m'} [Q,\sigma^g_m]_t \\
&\times\Bigg[\left\{\sigma^g_{m'}(t-r/c)e^{ik_o r(1-\cos\theta_o)} - \sigma^g_{m'}(t+r/c)e^{-ik_o r(1+\cos\theta_o)}\right\} \\
&\times\left\{\frac{i}{rk_o}\sin^2\eta + \frac{i}{r^3k_o^3}(2-3\sin^2\eta)\right\} \\
&-\left\{\sigma^g_{m'}(t-r/c)e^{ik_o r(1-\cos\theta_o)} + \sigma^g_{m'}(t+r/c)e^{-ik_o r(1+\cos\theta_o)}\right\} \\
&\times\frac{1}{r^2k_o^2}(3\sin^2\eta-2)\Bigg]\,,
\end{aligned} \tag{223}$$

where, under the Wigner-Weisskopf approximation, $\overline{\omega}_{ko} \to \overline{\omega}_{oo} = \Delta_o = \omega_e - \omega_o$, and the decay rate and coupling constant (see eq. (209)) are given by

$$\Gamma_o = \frac{1}{4\pi\varepsilon_o}\frac{4\omega_o^3 d^2}{3\hbar c^3}\,, \qquad g_o^2 = \frac{\omega_o d^2}{2\varepsilon_o\hbar\mathcal{V}}\,. \tag{224}$$

The expression (223) contains advanced and retarded contributions, i. e. with respective time dependence $(t + r/c)$ and $(t - r/c)$. We will first focus on the retarded contribution. Under usual experimental circumstances the propagation time between different sites m and m' is very small, such that this propagation time can be neglected within the operator $\sigma^g_{m'}(t - r/c) = \sigma^g_{m'}(t - \ell(m'-m)/c) \approx \sigma^g_{m'}(t)$ and the retarded contribution of expression (223) becomes local in time:

$$\begin{aligned}
&\gamma\sum_{m,m'}\left[\frac{i}{rk_o}\sin^2\eta + \frac{1}{r^2k_o^2}(2-3\sin^2\eta) + \frac{i}{r^3k_o^3}(2-3\sin^2\eta)\right] \\
&\qquad\times [Q,\sigma^g_m]_t\, \sigma^g_{m'}(t)e^{ik_o r(1-\cos\theta_o)}\,,
\end{aligned} \tag{225}$$

with

$$\gamma = \frac{g_o^2}{\Delta_o^2}\frac{3|\alpha_o|^2}{4}\,\Gamma_o(\hat{\varepsilon}_d\cdot\hat{\varepsilon}_o)^2\,. \tag{226}$$

The advanced contribution of (223), with $\sigma^g_{m'}(t + r/c) = \sigma^g_{m'}(t + \ell(m' - m)/c) \approx \sigma^g_{m'}(t)$, is given by the complex conjugate of (225),

$$\gamma \sum_{m,m'} \left[-\frac{i}{rk_o}\sin^2\eta + \frac{1}{r^2k_o^2}(2-3\sin^2\eta) - \frac{i}{r^3k_o^3}(2-3\sin^2\eta) \right] \times [Q, \sigma^g_m]_t \, \sigma^g_{m'}(t) e^{-ik_o r(1+\cos\theta_o)} \,. \tag{227}$$

Note that the expressions (225) and (227) only correspond to the last term of eq. (206). The term in the second line of eq. (206) is given by the respective hermitian adjoint of the expressions (225) and (227):

$$\gamma \sum_{m,m'} \left[-\frac{i}{rk_o}\sin^2\eta + \frac{1}{r^2k_o^2}(2-3\sin^2\eta) - \frac{i}{r^3k_o^3}(2-3\sin^2\eta) \right] \times \sigma^g_{m'}(t) \, [\sigma^g_m, Q]_t \, e^{-ik_o r(1-\cos\theta_o)} \,, \tag{228}$$

$$\gamma \sum_{m,m'} \left[\frac{i}{rk_o}\sin^2\eta + \frac{1}{r^2k_o^2}(2-3\sin^2\eta) + \frac{i}{r^3k_o^3}(2-3\sin^2\eta) \right] \times \sigma^g_{m'}(t) \, [\sigma^g_m, Q]_t \, e^{ik_o r(1+\cos\theta_o)} \,. \tag{229}$$

We will now combine the expressions (225), (227), (228), and (229). In order to obtain a more compact form, we will switch the indices $m \leftrightarrow m'$ in eqs. (228) and (229), taking into account that this results in the replacement $r \leftrightarrow -r$. Our line of conduct can be summarized as follows:

$$\big[(228) + (229)\big] + \big[(225) + (227)\big] = \big[(225) + (228)(m \leftrightarrow m')\big] + \big[(227) + (229)(m \leftrightarrow m')\big] \,, \tag{230}$$

The first term on the right-hand side of (230) thus reads:

$$-\gamma \sum_{m,m'} \left[\frac{i}{rk_o}\sin^2\eta + \frac{1}{r^2k_o^2}(2-3\sin^2\eta) + \frac{i}{r^3k_o^3}(2-3\sin^2\eta) \right] e^{ik_o r(1-\cos\theta_o)} \times \left\{ 2\sigma^g_m(t)Q(t)\sigma^g_{m'}(t) - \Big(Q(t)\sigma^g_m(t)\sigma^g_{m'}(t) + \sigma^g_m(t)\sigma^g_{m'}(t)Q(t) \Big) \right\} \,, \tag{231}$$

and the corresponding second term follows immediately:

$$\gamma \sum_{m,m'} \left[\frac{i}{rk_o}\sin^2\eta - \frac{1}{r^2k_o^2}(2-3\sin^2\eta) + \frac{i}{r^3k_o^3}(2-3\sin^2\eta) \right] e^{-ik_o r(1+\cos\theta_o)} \times \left\{ 2\sigma^g_m(t)Q(t)\sigma^g_{m'}(t) - \Big(Q(t)\sigma^g_m(t)\sigma^g_{m'}(t) + \sigma^g_m(t)\sigma^g_{m'}(t)Q(t) \Big) \right\} \,, \tag{232}$$

Finally, addition of (231) and (232) leads to the following contribution

$$2\gamma \sum_{m,m'} \mathcal{M}_{mm'} \times \left\{ 2\sigma^g_m(t)Q(t)\sigma^g_{m'}(t) - \Big(Q(t)\sigma^g_m(t)\sigma^g_{m'}(t) + \sigma^g_m(t)\sigma^g_{m'}(t)Q(t) \Big) \right\} \,, \tag{233}$$

where we introduced the matrix $\mathcal{M}_{mm'}$ under explicit consideration of $r = r(m, m') = \ell(m' - m)$ as

$$\mathcal{M}_{mm'} = \left[\sin\left[\ell(m'-m)k_o\right] \left(\frac{\sin^2\eta}{\ell(m'-m)k_o} + \frac{2-3\sin^2\eta}{\ell^3(m'-m)^3k_o^3} \right) - \cos\left[\ell(m'-m)k_o\right] \frac{2-3\sin^2\eta}{\ell^2(m'-m)^2k_o^2} \right] e^{-ik_o\ell(m'-m)\cos\theta_o} \,. \tag{234}$$

Note that the part of (234) in the brackets is real symmetric under exchange of $m \leftrightarrow m'$, and that $\mathcal{M}$ is thus hermitian. For $r \to 0$, i. e. $m = m'$, we obtain $\mathcal{M}_{mm} = 2/3$.

The expression (233) only contains the contribution of the second and third line in eq. (206). We will now state the full contribution of (206) under the assumption that the free radiation field ($k \neq k_0$) is initially, i. e. at $t = 0$, in the vacuum state. We can therefore take vacuum expectation values such that $\langle 0|Q(0)|0\rangle = \langle Q(0)\rangle_0$. As a consequence, the contribution in the first line of expression (208) (and its hermitian adjoint) vanish (since they involve single field creation and annihilation operators which vanish upon taking vacuum expectation values), and we obtain, for eq. (208):

$$\begin{aligned}\langle \dot{Q}(t)\rangle_0 = {} & i\Delta_r \sum_m \langle [\sigma_m^r, Q]_t\rangle_0 - i\sum_m \left(\Omega_m \langle [\sigma_m^+, Q]_t\rangle_0 + \Omega_m^* \langle [\sigma_m^-, Q]_t\rangle_0\right) \\ & + iV \sum_m \langle [\sigma_m^r \sigma_{m+1}^r, Q]_t\rangle_0 + 2\gamma \sum_{m,m'} \mathcal{M}_{mm'} \\ & \times \langle 2\sigma_m^g(t) Q(t) \sigma_{m'}^g(t) - \Big(Q(t)\sigma_m^g(t)\sigma_{m'}^g(t) + \sigma_m^g(t)\sigma_{m'}^g(t)Q(t)\Big)\rangle_0 .\end{aligned} \tag{235}$$

This is a master equation of Lehmberg-type, for an arbitrary atomic operator $Q(t)$. Since we so far are only interested in the atomic subspace, eq. (235) can also be expressed in terms of the atomic density matrix ρ_A if we assume that, initially, i. e. at $t = 0$, the density matrix of the entire system can be written as a product of the density matrices of both subsystems, i. e. for the free radiation field and the atomic part, $\rho = \rho_A \otimes \rho_F$ (together with the assumption that all modes, apart from the macroscopically occupied mode, are initially in the vacuum state). This is due the fact that all operators acting on the field degrees of freedom, see eq. (208), are evaluated at time $t = 0$. Since, again, at this time the free radiation field is in its vacuum state, the contribution of the corresponding field operators vanishes, and the decoupled equation for the density matrix ρ_A can be stated:

$$\begin{aligned}\dot{\rho}_A(t) = {} & -i\Delta_r \sum_m [\sigma_m^r, \rho_A]_t + i\sum_m \left(\Omega_m [\sigma_m^+, \rho_A]_t + \Omega_m^* [\sigma_m^-, \rho_A]_t\right) \\ & - iV \sum_m [\sigma_m^r \sigma_{m+1}^r, \rho_A]_t + 2\gamma \sum_{m,m'} \mathcal{M}_{mm'} \\ & \times \left[2\sigma_{m'}^g(t)\rho_A(t)\sigma_m^g(t) - \Big(\rho_A(t)\sigma_m^g(t)\sigma_{m'}^g(t) + \sigma_m^g(t)\sigma_{m'}^g(t)\rho_A(t)\Big)\right] .\end{aligned} \tag{236}$$

Note that eq. (235) is regained by exploiting $\langle Q(t)\rangle = \mathrm{Tr}[\rho_A(t)Q(t)]$, $\langle \dot{Q}(t)\rangle = \mathrm{Tr}[\dot{\rho}_A(t)Q(t)]$, and the fact that the trace is invariant under cyclic permutations.

Let us state the final version of our master equation such that it contains the population of the excited state only, i. e. after substitution $\sigma_m^g = \mathbb{1}_m - \sigma_m^r$ into eq. (236):

$$\begin{aligned}\dot{\rho}_A(t) = {} & -i\Delta_r \sum_m [\sigma_m^r, \rho_A]_t + i\sum_m \left(\Omega_m [\sigma_m^+, \rho_A]_t + \Omega_m^* [\sigma_m^-, \rho_A]_t\right) \\ & - iV \sum_m [\sigma_m^r \sigma_{m+1}^r, \rho_A]_t + 4i\gamma \sum_{m,m'} \mathrm{Im}\left[\mathcal{M}_{mm'}\right] [\sigma_m^r, \rho_A]_t \\ & + 2\gamma \sum_{m,m'} \mathcal{M}_{mm'} \\ & \times \left[2\sigma_{m'}^r(t)\rho_A(t)\sigma_m^r(t) - \left(\rho_A(t)\sigma_m^r(t)\sigma_{m'}^r(t) + \sigma_m^r(t)\sigma_{m'}^r(t)\rho_A(t)\right)\right] .\end{aligned} \tag{237}$$

By doing so, an additional detuning ($\propto \mathrm{Im}[\mathcal{M}_{mm'}] = \mathcal{M}_{mm'} - \mathcal{M}_{mm'}^*$) is encountered within the Hamiltonian dynamics of the master equation which –

since $\mathcal{M}$ is hermitian – will only appear for off-diagonal, i. e. $m \neq m'$, contributions and can be chosen to vanish for a specific atomic setup, e. g. $\cos\theta_o \equiv 0$, such that eq. (234) becomes real.

We also note that the damping term, i. e. the third and fourth line of eq. (237) can be (anti-)symmetrized, in order to clearly separate the damping from the Hamiltonian dynamics. With the real part of $\mathcal{M}$ defined as $\mathrm{Re}[\mathcal{M}_{mm'}] = \mathcal{M}_{mm'} + \mathcal{M}^*_{mm'}$, we obtain for the third and fourth line of eq. (237):

$$4\gamma \sum_{m \leqslant m'} \Big\{ \mathrm{Re}[\mathcal{M}_{mm'}] \Big[[\sigma^r_m, \rho_A]_t \, , \sigma^r_{m'} \Big]_t \\ -i\,\mathrm{Im}[\mathcal{M}_{mm'}] \left(\sigma^r_m(t)\rho_A(t)\sigma^r_{m'}(t) - \sigma^r_{m'}(t)\rho_A(t)\sigma^r_m(t) \right) \Big\} \, . \tag{238}$$

Note that the real part of $\mathcal{M}$ vanishes if $\cos[k_o \ell (m' - m)\cos\theta_o] = 0$, see eq. (234), such that the atomic dynamics becomes purely Hamiltonian. Further note that the Lindblad form of eq. (237) can be obtained by diagonalizing the matrix $\mathcal{M}_{mm'}$ [224].

We will not focus on the derivation of the master equation of Lindblad type here but rather – within the following sections – study the atomic dynamics of eq. (237) for an increasing number of atoms.

6.3.2 *Atomic Dynamics for a Single Atom*

Here the situation is the following: We look at a single atom which is driven by two laser fields. The first one is the weak laser field with frequency ω_o that is far-detuned from any atomic transition and thus results in effective photon scattering off the atomic ground state.[4] The second one is the Rydberg laser with frequency ω_L and Rabi-frequency $\Omega = \Omega_m$. Although the interaction with neighboring atoms is obviously absent, we can mimic the effect of strong interaction (corresponding to a neighboring atom being in the $|r\rangle$-state) by assuming that the corresponding laser field is weak and far-detuned from the Rydberg transition, i. e. $\Delta_r \gg \Omega \gg \gamma$. This corresponds to a large contribution V, which – for two or more atoms – effectively shifts the excited state of neighboring atoms out of resonance, see eq. (204).

4 Whether the photon is effectively scattered off the atomic ground state, as described by eq. (236), or off the excited Rydberg state, see eq. (237), is a matter of choice. As we will see in Fig. 38, the description based on effective scattering off the excited Rydberg state has an intuitive physical explanation and is thus preferably used later on.

For the case of a single atom only four equations of motion have to be considered in (237), corresponding to the following density matrix of the atomic subspace:

$$\dot\rho_A(t) = \begin{pmatrix} \dot\rho_{rr}(t) & \dot\rho_{rg}(t) \\ \dot\rho_{gr}(t) & \dot\rho_{gg}(t) \end{pmatrix} . \tag{239}$$

In Fig. 36 the numerically obtained solutions to the equations of motion (239) are depicted in the limit $\Delta_r \gg \Omega \gg \gamma$, with the atom initially in its ground state. Due to the dephasing rate γ with which photons are scattered off the atomic ground state, the coherences are damped out, and a steady state is reached where both, the ground and the excited state, are populated with equal probability 1/2. This corresponds to a totally mixed state. The rate with which this mixed state is reached can be determined by a rate equation that is derived by adiabatic elimination of the coherences from the equations of motion in (239). For this, it is useful to assume that the Rydberg state spontaneously decays with a very small but finite rate γ_r which we have – owing to its long lifetime – neglected so far in our considerations. If one assumes that γ_r also affects the coherences of the corresponding transition,

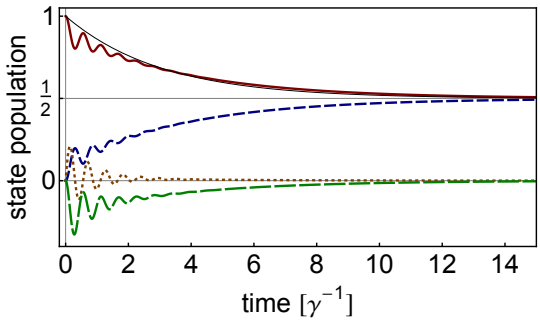

Figure 36: Single atom with laser driven Rydberg transition with Rabi-frequency $\Omega = 5\gamma$ and detuning $\Delta_r = 10\gamma$, where γ determines the scattering rate with which an additional weak laser is scattered off the ground state, see (237). The (red) solid and (blue) dashed line describe the time evolution of the population of the ground state and of the excited state, respectively. The (brown) dotted and (green) long-dashed lines correspond to the respective imaginary and real part of the coherence $\rho_{gr}(t)$. The thin (black) line is the decay rate of the population of the ground state, determined by the rate equation (240). For increasing times, the coherences are damped, due to the effective dephasing γ, and the fully mixed state is reached, see eq. (241).

one can derive – assuming that $\Delta_r \gg \Omega \gg \gamma \gg \gamma_r$ – the following relation for the respective populations of the excited and ground state [214]:

$$\rho_{rr(gg)}(t) = \frac{1}{2}\left(1 - (+)e^{-2\Gamma t}\right), \qquad \Gamma = \frac{\frac{4}{3}\gamma\Omega^2}{2\left[(\frac{4}{3}\gamma)^2 + \Delta_r^2\right]}. \tag{240}$$

This relation is plotted as a thin black line for the decay of the ground state population in Fig. 36, and is in very good agreement with the observed dynamics. Correspondingly, it is easy to see that the atomic density matrix for a single atom converges towards a fully mixed state in the steady state limit (indicated by the subscript ss),

$$\rho_A(t) = \begin{pmatrix} \rho_{rr}(t) & \rho_{rg}(t) \\ \rho_{gr}(t) & \rho_{gg}(t) \end{pmatrix} \longrightarrow \rho_{A,ss} = \begin{pmatrix} \frac{1}{2} & 0 \\ 0 & \frac{1}{2} \end{pmatrix}. \tag{241}$$

6.3.3 *Two-Atom Dynamics*

Let us now turn to the case of two interacting atoms by including eq. (204) and assuming strong interaction, i. e. $V \gg 0$. Henceforth (and in contrast to the single atom case), we can focus on the quasi-resonant case where the detuning Δ_r is weak in comparison to the Rabi frequency and overwhelmed by the large interaction contribution that governs the dynamics. Due to the large interaction strength, the Rydberg blockade sets in and one expects only one of the atoms to be in the Rydberg state at a time. In total, this corresponds to three possible states, i. e. $\rho_{gg\otimes gg}(t)$, $\rho_{gg\otimes rr}(t)$, and $\rho_{rr\otimes gg}(t)$, where both atoms are in the ground state or where either one is in the excited and ground state, respectively. The subscript indicates the state of the first and of the second atom to the left and to the right of the $\otimes$-symbol, respectively. As for the single atom case, identical letters (gg and rr) and different letters (gr and gr) in the subscript specify a population and a coherence with respect to the atom under consideration.

As a consequence – following the line of thought we had followed above in the single-atom case – the steady state, after damping out of all coherences, should contain equal populations of $1/3$ for all three states mentioned above. Indeed, in Fig. 37, where the time evolution for certain elements of the atomic density matrix, i. e.

$$\dot{\rho}_A(t) = \begin{pmatrix} \dot{\rho}_{rr\otimes rr}(t) & \dot{\rho}_{rr\otimes rg}(t) & \dot{\rho}_{rg\otimes rr}(t) & \dot{\rho}_{rg\otimes rg}(t) \\ \dot{\rho}_{rr\otimes gr}(t) & \dot{\rho}_{rr\otimes gg}(t) & \dot{\rho}_{rg\otimes gr}(t) & \dot{\rho}_{rg\otimes gg}(t) \\ \dot{\rho}_{gr\otimes rr}(t) & \dot{\rho}_{gr\otimes rg}(t) & \dot{\rho}_{gg\otimes rr}(t) & \dot{\rho}_{gg\otimes rg}(t) \\ \dot{\rho}_{gr\otimes gr}(t) & \dot{\rho}_{gr\otimes gg}(t) & \dot{\rho}_{gg\otimes gr}(t) & \dot{\rho}_{gg\otimes gg}(t) \end{pmatrix}, \tag{242}$$

is depicted, we find that on the time-scale $1/\gamma$ all coherences are damped out, and the three mentioned states are approximately equally populated. However, in Fig. 37, a slight but increasing contribution of the doubly-excited Rydberg state is already visible for short times that becomes more pronounced for longer times. The states with equal population $1/3$ thus represent only an intermediate and transient regime of the system, before it reaches a steady state, in the long time limit.

Let us try to determine rate equations for the population of the four atomic states via adiabatic elimination, which is, however, more involved than for the case of a single atom. Nonetheless, there exist two limits in which one can describe the dynamics in a simplified way.

In the short time limit, when the population of the doubly-excited state is suppressed, see Fig. 37, an adiabatic elimination of the coherences and a simultaneous expansion up to factors of order $1/V$ predicts a decay governed by the rate γ. For large Ω and vanishing detuning Δ_r, this rate is independent of V and, e. g. for the population of the joined ground state, given by:

$$\rho_{gg\otimes gg}(t) = \frac{1}{3} + \frac{2}{3} e^{-8\gamma t}. \tag{243}$$

In Fig. 37, eq. (243) is plotted as a thin black line.

In the long time limit, when the population of the doubly-excited state becomes important, the dynamics is well captured by rate equations where we first set the double coherences, i. e. the anti-diagonal terms of expression (242), to zero and then adiabatically eliminate all the other coherences. This procedure is suggested by the evolution equations of the populations which do not directly couple to the anti-diagonal entries of (242). The rate equations thereby obtained read:

$$\dot{\rho}_{rr\otimes rr}(t) = \frac{6\gamma\Omega^2}{16\gamma^2 + 9(V-\Delta_r)^2} \left[\rho_{rr\otimes gg}(t) + \rho_{gg\otimes rr}(t) - 2\rho_{rr\otimes rr}(t)\right], \tag{244}$$

$$\dot{\rho}_{gg\otimes gg}(t) = \frac{6\gamma\Omega^2}{16\gamma^2 + 9\Delta_r^2} \left[\rho_{rr\otimes gg}(t) + \rho_{gg\otimes rr}(t) - 2\rho_{gg\otimes gg}(t)\right], \tag{245}$$

$$\begin{aligned} \dot{\rho}_{rr\otimes gg}(t) = {} & \frac{6\gamma\Omega^2}{16\gamma^2 + 9(V-\Delta_r)^2} \rho_{rr\otimes rr}(t) + \frac{6\gamma\Omega^2}{16\gamma^2 + 9\Delta_r^2} \rho_{gg\otimes gg}(t) - \\ & - \frac{6\gamma\Omega^2(32\gamma^2 + 9\Delta_r^2 + 9(V-\Delta_r)^2)}{(16\gamma^2 + 9(V-\Delta_r)^2)(16\gamma^2 + 9\Delta_r^2)} \rho_{rr\otimes gg}(t). \end{aligned} \tag{246}$$

From these equations we can read off the relevant time scales of our system. In our case, when $V \gg \Omega \gg \gamma$, the rapid decay of the initial coherences

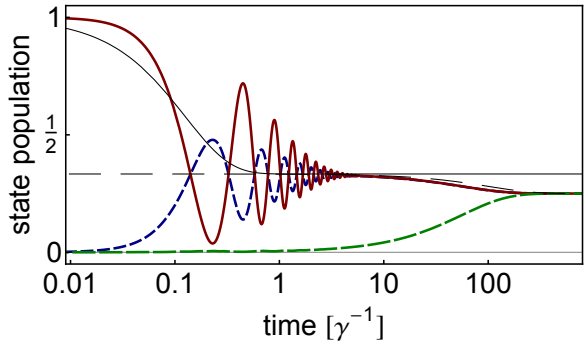

Figure 37: Time-evolution of the two-atom populations in the blockade regime $V \gg \Omega \gg \gamma$, with $\Omega = 10\gamma$, $\Delta_r = 0$, $V = 100\gamma$. We only include the diagonal contributions of $\mathcal{M}_{mm'}$, see eq. (234), and neglect the off-diagonal interferential contributions between the two atoms, as they are small (for sufficiently large lattice spacing ℓ) in comparison to the interaction strength V. The (red) solid, the (blue) dashed, and the (green) long-dashed line correspond to the abundances of two atoms being in the ground state, one being in the ground and the other in the excited state, and two atoms being excited, respectively. The thin (black) solid and dashed lines are the predictions of eqs. (243) and (247), respectively. Initially, the populations oscillate in time, until the coherences (not shown) are damped out, and a transient state with equal population of $1/3$ is reached after $5\gamma^{-1}$. At this point, the population of the doubly-excited Rydberg state is negligible. In the limit of long times, i. e. $\propto V^2/\Omega^2\gamma$, a fully mixed steady state is reached, with equal population of $1/4$ for all four states.

and populations of the ground and singly-excited states is given by the fastest time scale $1/\gamma$ in our system, see also (243). The slow decay of the transient regime towards the steady state is determined by the slowest time scale $V^2/\Omega^2\gamma$ in our system. Interpreted physically, Ω^2/V^2 determines the (small) probability to find two neighboring atoms in a Rydberg state which is yet multiplied with the (small) rate γ to scatter a photon off such a Rydberg state, see also Fig. 38. Consequently, the decay from the transient to the steady state regime is, e. g. for the population of the joined ground state, determined by

$$\rho_{gg\otimes gg}(t) = \frac{1}{4} + \frac{1}{12} e^{-\frac{\gamma\Omega^2}{V^2} t}, \tag{247}$$

indicated by the thin black dashed line in Fig. 37. The corresponding steady state – despite the Rydberg blockade mechanism – again corresponds to a totally mixed state with equal population

$$\rho_A(t) \longrightarrow \rho_{A,ss} = \begin{pmatrix} \frac{1}{4} & 0 & 0 & 0 \\ 0 & \frac{1}{4} & 0 & 0 \\ 0 & 0 & \frac{1}{4} & 0 \\ 0 & 0 & 0 & \frac{1}{4} \end{pmatrix}. \tag{248}$$

And indeed, for the master equation (237) the dephasing noise acts only on the populations (and not on the coherences) such that a totally mixed state is expected in the steady state limit [224].

In summary, already the two-atom scenario analyzed in the blockade regime, i. e. $V \gg \Omega \gg \gamma$, reveals interesting dynamics. First, the system relaxes to a quasi-steady state with no doubly-excited Rydberg states, as expected from the strong Rydberg-Rydberg interaction. Asymptotically in

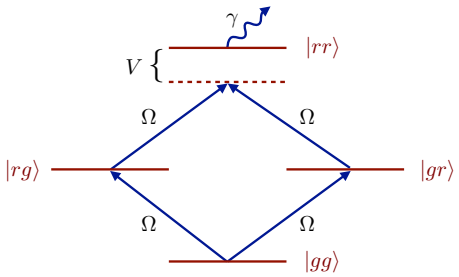

Figure 38: Excitation scheme for two atoms. Due to the Rydberg-blockade the probability to excite the doubly excited Rydberg state is suppressed by a factor Ω^2/V^2 multiplied by the small rate γ to scatter photons off the Rydberg state.

time, the dephasing caused by the additional scattering of photons off the Rydberg state finally leads to a fully mixed state.

6.3.4 *Three-Atom Dynamics*

Here, we analyze the dynamics for three atoms in a chain. In contrast to the two-atom case, now doubly-occupied Rydberg states of non-neighboring atoms are not blocked. In accordance with our observation for the two-atom case, the transient regime is reached with five non-blocked populations ($|ggg\rangle$, $|rgg\rangle$, $|grg\rangle$, $|ggr\rangle$, and $|rgr\rangle$) and equal occupations 1/5. Then, these populations decrease, as the populations first of the doubly- and then of the triply-excited Rydberg states increase until the totally mixed steady state is reached with equal populations of 1/8. Fig. 39 summarizes the results. Note that the derivation of a rate equation describing the underlying time scales is already very cumbersome for the case of three atoms. In Fig. 39 we therefore plot the decay rates of the joined ground state population (i. e. the probability for all three atoms to be in the ground state) found in eqs. (243) and (247), adopted to the case of three atoms, i. e.

$$\rho_{gg\otimes gg\otimes gg}(t) = \frac{1}{5} + \frac{4}{5}e^{-8\gamma t}, \tag{249}$$

for the short time limit, and

$$\rho_{gg\otimes gg\otimes gg}(t) = \frac{1}{8} + \frac{3}{40}e^{-\frac{\gamma\Omega^2}{V^2}t}, \tag{250}$$

for the decay to the steady state regime (i.e., $t \geqslant V^2/\gamma\Omega^2$).

6.3.5 *Summary*

Within this section, we extended the previously derived single-particle Hamiltonian to the case of N interacting atoms trapped in the wells of a 1D optical lattice. We derived a master equation for the atomic sub-system by tracing out the free radiation field's degrees of freedom. The coupling between the radiation field and the atoms is governed by the recycling term of the master equation (237), that mimics photon scattering off the atomic Rydberg state.

In the remainder of this section we analyzed the influence of this scattering process on the dynamics within the atomic subspace, in the blockade regime where $V \gg \Omega \gg \gamma$. Already for the case of two atoms, the evolution

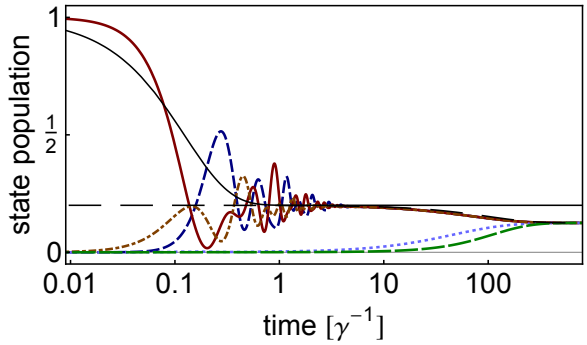

Figure 39: Time-evolution of the three-atom populations in the blockade regime $V \gg \Omega \gg \gamma$, with $\Omega = 10\gamma$, $\Delta_r = 0$, $V = 100\gamma$. As for the two-atom case, we only include the diagonal contributions of $\mathcal{M}_{mm'}$, see eq. (234). The (red) solid, (brown) dash-dotted, and (blue) dashed line correspond to selected populations with zero, one, and two non-neighboring atoms excited to the Rydberg state, respectively. These in total five states acquire an equal population of $1/5$ in the transient regime, after a relaxation time approximately equal to $5\gamma^{-1}$, once the coherences (not shown) are damped out. The (light-blue) dotted and the (green) long-dashed line are a selected doubly-excited Rydberg state of neighboring atoms, and the triply-excited Rydberg state, respectively. Their contribution increases successively for longer times, until the steady state with equal population of $1/8$ is reached. The thin (black) solid and dashed lines are the respective predictions of eqs. (249) and (250), and approximately determine the time-dependence of the observed dynamics.

of the atomic populations in time revealed the existence of three different regimes.

In the first regime, the populations oscillate in time as they would do in a closed quantum system. However, the dephasing due to the scattering of photons from the surrounding radiation field leads to a damping of these oscillations.

As soon as the coherences are damped out, a transient regime is reached where the interaction-based blockade mechanism between the atoms prohibits the excitation of neighboring Rydberg states, thus leading to correlations between the Rydberg-excited and ground state atoms, that encode the ordering of the atoms in the lattice.

In the long time limit, these correlations vanish and the density matrix of the atomic sub-system becomes diagonal. The steady state of the system is thus given by a fully mixed state.

Although this observation has been made only for a small number of atoms, we expect the same result to hold for an increasing number of atoms. As e. g. observed in Fig. 39, the three-body states with a different number of Rydberg excitations approach the fully mixed state at different times. Similarly, for a larger number of atoms, we expect the transition to the fully mixed state for many-body states with a different number of Rydberg excitations to occur at different times as well. Consequently, the N-body fully mixed state is expected to occur smoothly and *not* via a collective quantum jump for all many-body states at the same instance of time.

In the following, it will be interesting to see whether the transition between the transient and the steady state regime can be captured by detection of the photons scattered off the atoms.

6.4 LIGHT SCATTERED OFF A 1D CHAIN OF INTERACTING RYDBERG ATOMS

In the previous section the focus was on the dynamics of the atomic subspace. The question we would like to answer now concerns the (experimental) detectability of the dynamics observed in Section 6.3.

We will focus here on the transition from the transient regime to the steady state regime discussed above. Whereas in the transient regime the Rydberg blockade mechanism is still present, interaction with the free radiation field leads to a dephasing and ultimate breakdown of the blockade, and to an equal occupation of ground and excited Rydberg states. Experimentally, dephasing (noise) is always present and thus an increase of the number of excited Rydberg atoms beyond the limit predicted by the blockade mechanism was e. g. observed in [193, 208].

We will here use a simple model of atomic dimers [213] to characterize the correlations between the atoms in the transient regime, that will allow us to distinguish this regime from the (correlation-free) steady state regime by looking at the scattered intensity of the atomic chain.

6.4.1 *Intensity Detected in the Far-Field of the Atomic Chain*

The intensity scattered off the chain of Rydberg atoms is detected at time t at the position $\mathbf{R}$ in the far-field of the lattice, and is given as the expectation value of the product of negative and positive frequency components of the electric field [223]

$$I(\mathbf{R}, t) = \langle \mathbf{E}^{(-)}(\mathbf{R}, t)\mathbf{E}^{(+)}(\mathbf{R}, t)\rangle \,, \tag{251}$$

where $\mathbf{E}^{(+)}(\mathbf{R}, t) = \left[\mathbf{E}^{(-)}(\mathbf{R}, t)\right]^{\dagger}$ and

$$\mathbf{E}^{(+)}(\mathbf{R}, t) = \sum_{\mathbf{k},\lambda} \mathcal{E}_k \hat{\varepsilon}_k^{(\lambda)} a_{\mathbf{k}}(t) e^{i\omega_k t} e^{i\mathbf{k}\mathbf{R}} \,. \tag{252}$$

Here, the phase factor $\exp[i\omega_k t]$ accounts for the back-transformation of the field mode annihilation operator from the interaction picture to the Schrödinger picture, cf. eqs. (187) and (199), once we insert eq. (207) into (252). Assuming again that the radiation field is initially in the vacuum mode, we only need to plug the second term of eq. (207) into (252), to obtain

$$\begin{aligned}\mathbf{E}^{(+)}(\mathbf{R}, t) = &-\frac{i\alpha_0 d^2}{\hbar^2}(\hat{\varepsilon}_d \cdot \hat{\varepsilon}_0) \sum_{\mathbf{k},\lambda,m} \frac{\mathcal{E}_k^2 \mathcal{E}_0}{|\overline{\omega}_{k0}|} \hat{\varepsilon}_k^{(\lambda)} \hat{\varepsilon}_d \cdot \hat{\varepsilon}_k^{(\lambda)} e^{i\omega_0 t} e^{i\mathbf{k}(\mathbf{R}-\mathbf{r}_m)} e^{i\mathbf{k}_0 \mathbf{r}_m} \\ &\times \int_0^t dt' \, e^{i(\omega_0-\omega_k)(t'-t)} \sigma_m^g(t') \,.\end{aligned} \tag{253}$$

Using the relations (209), we apply the continuum limit and transform the sum into an integral over $\mathbf{k}$, conduct the sum over polarizations, and integrate over the angular components of $\mathbf{k}$:

$$\int \frac{d\Omega_{\hat{\mathbf{k}}}}{2\pi} (\mathbb{1} - \hat{\mathbf{k}}\hat{\mathbf{k}}) e^{i\mathbf{k}(\mathbf{R}-\mathbf{r}_m)} = \frac{e^{ik|\mathbf{R}-\mathbf{r}_m|} - e^{-ik|\mathbf{R}-\mathbf{r}_m|}}{ik|\mathbf{R}-\mathbf{r}_m|} \left[\mathbb{1} - \frac{(\mathbf{R}-\mathbf{r}_m)(\mathbf{R}-\mathbf{r}_m)}{|\mathbf{R}-\mathbf{r}_m|^2}\right] . \tag{254}$$

In (254) we just included the far-field contributions ($\propto 1/r$) of the general integral expression

$$\begin{aligned}\mathcal{F}_{m,m'}(\omega_k) &= \int \frac{d\Omega_{\hat{\mathbf{k}}}}{4\pi}\,(\mathbb{1}-\hat{\mathbf{k}}\hat{\mathbf{k}})e^{\pm\frac{i\omega_k}{c}\hat{\mathbf{k}}\mathbf{r}_{m,m'}} \\ &= \left[j_0\left(\frac{\omega_k r_{m,m'}}{c}\right) - \frac{j_1\left(\frac{\omega_k r_{m,m'}}{c}\right)}{\frac{\omega_k r_{m,m'}}{c}}\right]\mathbb{1} + j_2\left(\frac{\omega_k r_{m,m'}}{c}\right)\frac{\mathbf{r}_{m,m'}\mathbf{r}_{m,m'}}{r^2_{m,m'}}\,,\end{aligned} \tag{255}$$

where the product of the spatial vectors, i. e. the last term in (254) and (255), is again a dyadic product, and $j_n(x)$ represents the n-th order spherical Bessel function of the first kind [225]. Note that $\mathcal{F}_{m,m'}(\omega_k) = \mathcal{F}_{m',m}(\omega_k)$, and $\mathcal{F}_{m,m}(\omega_k) = \frac{2}{3}\cdot\mathbb{1}$.

The integral over the modulus of $\mathbf{k}$ is again evaluated in the Wigner-Weisskopf approximation, see (218):

$$\begin{aligned}&\frac{\mathcal{V}}{(2\pi)^2}\frac{\omega_0^2}{c^2|\Delta_0|}\left[e^{i\omega_0\frac{|\mathbf{R}-\mathbf{r}_m|}{c}}\int_{-\infty}^{\infty}d\omega_k e^{i(\omega_0-\omega_k)(t'-t-\frac{|\mathbf{R}-\mathbf{r}_m|}{c})}\right.\\ &\left.- e^{-i\omega_0\frac{|\mathbf{R}-\mathbf{r}_m|}{c}}\int_{-\infty}^{\infty}d\omega_k e^{i(\omega_0-\omega_k)(t'-t+\frac{|\mathbf{R}-\mathbf{r}_m|}{c})}\right]\\ &= \frac{\mathcal{V}}{2\pi}\frac{\omega_0^2}{c^2|\Delta_0|}\left[e^{i\omega_0\frac{|\mathbf{R}-\mathbf{r}_m|}{c}}\delta\left(t'-t-\frac{|\mathbf{R}-\mathbf{r}_m|}{c}\right)\right.\\ &\left.- e^{-i\omega_0\frac{|\mathbf{R}-\mathbf{r}_m|}{c}}\delta\left(t'-t+\frac{|\mathbf{R}-\mathbf{r}_m|}{c}\right)\right].\end{aligned} \tag{256}$$

The integral over t' is conducted by evaluation of the respective δ-functions, and eq. (253) transforms into

$$\begin{aligned}\mathbf{E}^{(+)}(\mathbf{R},t) &= -\mathcal{E}_0\Gamma_0\frac{3\alpha_0}{4|\Delta_0|k_0}(\hat{\varepsilon}_d\cdot\hat{\varepsilon}_0)\,e^{i\omega_0 t}\\ &\times\sum_m\left(\mathbb{1}-\frac{(\mathbf{R}-\mathbf{r}_m)(\mathbf{R}-\mathbf{r}_m)}{|\mathbf{R}-\mathbf{r}_m|^2}\right)\cdot\hat{\varepsilon}_d\,e^{i\mathbf{k}_0\mathbf{r}_m}\\ &\times\left[\frac{e^{i\omega_0\frac{|\mathbf{R}-\mathbf{r}_m|}{c}}}{|\mathbf{R}-\mathbf{r}_m|}\sigma^g_m\left(t+\frac{|\mathbf{R}-\mathbf{r}_m|}{c}\right)-\frac{e^{-i\omega_0\frac{|\mathbf{R}-\mathbf{r}_m|}{c}}}{|\mathbf{R}-\mathbf{r}_m|}\sigma^g_m\left(t-\frac{|\mathbf{R}-\mathbf{r}_m|}{c}\right)\right],\end{aligned} \tag{257}$$

with Γ_0 as in (224). In the far-field limit, i.e. $R \gg r_m$, the exponentials in (257) simplify to

$$\frac{e^{i\omega_0\frac{|\mathbf{R}-\mathbf{r}_m|}{c}}}{|\mathbf{R}-\mathbf{r}_m|} \approx \frac{e^{ik_0R}}{R}e^{-ik_0\hat{\mathbf{R}}\mathbf{r}_m}\,. \tag{258}$$

If we focus only on the retarded contribution, i.e. including only outgoing fields, eq. (257) can be transformed further using (258):

$$\begin{aligned}\mathbf{E}^{(+)}(\mathbf{R},t) &= \mathcal{E}_0\Gamma_0\frac{3\alpha_0}{4|\Delta_0|k_0}(\hat{\varepsilon}_d\cdot\hat{\varepsilon}_0)\left(\mathbb{1}-\hat{\mathbf{R}}\hat{\mathbf{R}}\right)\cdot\hat{\varepsilon}_d\,e^{i\omega_0 t}\frac{e^{-ik_0R}}{R}\\ &\times\sum_m e^{ik_0 m\ell(\cos\theta_0+\cos\theta_R)}\sigma^g_m\left(t-\frac{R}{c}\right),\end{aligned} \tag{259}$$

where we used that $\mathbf{r}_m = m\ell\hat{z}$ points along the z-axis, and $\mathbf{R}$ in spherical coordinates reads

$$\mathbf{R} = R\begin{pmatrix}\sin\theta_R\cos\phi_R\\ \sin\theta_R\sin\phi_R\\ \cos\theta_R\end{pmatrix}. \tag{260}$$

Accordingly, $E^{(-)}(\mathbf{R},t)$ is given by the hermitian adjoint of eq. (259),

$$\mathbf{E}^{(-)}(\mathbf{R},t) = \mathcal{E}_o\Gamma_o\frac{3\alpha_o^*}{4|\Delta_o|k_o}(\hat{\varepsilon}_d\cdot\hat{\varepsilon}_o)\,\hat{\varepsilon}_d\cdot\left(\mathbb{1}-\hat{\mathbf{R}}\hat{\mathbf{R}}\right)\,e^{-i\omega_o t}\frac{e^{ik_oR}}{R} \times\sum_m e^{-ik_o m\ell(\cos\theta_o+\cos\theta_R)}\sigma_m^g\left(t-\frac{R}{c}\right). \tag{261}$$

The intensity is defined as the expectation value of the product of eqs. (259) and (261), see (251),

$$I(\mathbf{R},t) = \frac{|\alpha_o|^2}{R^2}\left(\frac{3\mathcal{E}_o\Gamma_o}{4|\Delta_o|k_o}(\hat{\varepsilon}_d\cdot\hat{\varepsilon}_o)\right)^2\hat{\varepsilon}_d\cdot\left(\mathbb{1}-\hat{\mathbf{R}}\hat{\mathbf{R}}\right)^2\cdot\hat{\varepsilon}_d \times\sum_{m,m'}e^{-ik_o\ell(\cos\theta_o+\cos\theta_R)(m'-m)}\left\langle\sigma_{m'}^g\left(t-\frac{R}{c}\right)\sigma_m^g\left(t-\frac{R}{c}\right)\right\rangle. \tag{262}$$

Subtracting the uncorrelated contribution, i. e. the product of expectation values, we obtain for eq. (262):

$$I(\mathbf{R},t) = \frac{|\alpha_o|^2}{R^2}\left(\frac{3\mathcal{E}_o\Gamma_o}{4|\Delta_o|k_o}(\hat{\varepsilon}_d\cdot\hat{\varepsilon}_o)\right)^2\hat{\varepsilon}_d\cdot\left(\mathbb{1}-\hat{\mathbf{R}}\hat{\mathbf{R}}\right)^2\cdot\hat{\varepsilon}_d \times\sum_{m,m'}e^{-ik_o\ell(\cos\theta_o+\cos\theta_R)(m'-m)} \times\left[\left\langle\sigma_{m'}^g\left(t-\frac{R}{c}\right)\sigma_m^g\left(t-\frac{R}{c}\right)\right\rangle-\left\langle\sigma_{m'}^g\left(t-\frac{R}{c}\right)\right\rangle\left\langle\sigma_m^g\left(t-\frac{R}{c}\right)\right\rangle\right]. \tag{263}$$

The same relation holds if one expresses eq. (263) in terms of the the population of the excited Rydberg state, i. e.

$$I(\mathbf{R},t) = \frac{|\alpha_o|^2}{R^2}\left(\frac{3\mathcal{E}_o\Gamma_o}{4|\Delta_o|k_o}(\hat{\varepsilon}_d\cdot\hat{\varepsilon}_o)\right)^2\hat{\varepsilon}_d\cdot\left(\mathbb{1}-\hat{\mathbf{R}}\hat{\mathbf{R}}\right)^2\cdot\hat{\varepsilon}_d\times \times\sum_{m,m'}e^{-ik_o\ell(\cos\theta_o+\cos\theta_R)(m'-m)} \times\left[\left\langle\sigma_{m'}^r\left(t-\frac{R}{c}\right)\sigma_m^r\left(t-\frac{R}{c}\right)\right\rangle-\left\langle\sigma_{m'}^r\left(t-\frac{R}{c}\right)\right\rangle\left\langle\sigma_m^r\left(t-\frac{R}{c}\right)\right\rangle\right]. \tag{264}$$

In the steady state limit, where a single atom is uncorrelated with the surrounding atoms (i. e. only diagonal elements of the atomic density matrix are non-zero), the atomic ground and excited state are equally populated, i. e. $\langle\sigma_m^g(t)\rangle = \langle\sigma_m^r(t)\rangle = 1/2$. Thus, the correlation function in eq. (262) can be written as a product of single-atom expectation values, and we simply obtain

$$I(\mathbf{R},t) = \frac{|\alpha_o|^2}{R^2}\left(\frac{3\mathcal{E}_o\Gamma_o}{4|\Delta_o|k_o}(\hat{\varepsilon}_d\cdot\hat{\varepsilon}_o)\right)^2\hat{\varepsilon}_d\cdot\left(\mathbb{1}-\hat{\mathbf{R}}\hat{\mathbf{R}}\right)^2\cdot\hat{\varepsilon}_d \times\frac{1}{4}\sum_{m,m'}e^{-ik_o\ell(\cos\theta_o+\cos\theta_R)(m'-m)}. \tag{265}$$

The second line of (265) is nothing else but the relation known from *Bragg* scattering which leads in zeroth order to constructive interference of the outgoing wave if $\theta_R = \theta_o$, see Fig. 40.

Eqs. (263) or (264), however, are the final expressions for the intensity detected in the far-field of the chain of Rydberg atoms, including non-vanishing correlations. In order to obtain the corresponding atomic expectation values

one has to solve the master equation (237). The density-density correlations are equally obtained from (237), by use of the quantum regression theorem [226, 227]. However, as this is a very involved procedure, especially for an increasing number of atoms, we rather make use of our above analysis from which we know how the atoms evolve under the dynamics of the master equation. Remember that the dynamics in the transient and in the steady state regime is particularly simple and that, as argued above, we expect our observations to qualitatively hold for an increasing number of atoms in the chain. In the next section, we therefore introduce a simple model which reproduces the correlations observed within the transient regime, and thus allows for a straightforward calculation of the scattered intensity.

6.4.2 *Approximate Description of the Atomic Many-Body State*

In the discussion of the atomic dynamics above we encountered a many-body transient state for the case of two and three atoms that only depends on the ground and Rydberg-excited state populations of neighboring atoms. For a first analysis of the scattered intensity (and for computational convenience), it is therefore desirable to construct a (simple) many-body state of the atomic subspace that reproduces the features of the actual many-body transient state. We call this state $|\xi\rangle$ and construct it as the coherent superposition of all the states for which a strict next-neighbor blockade exists [213], i. e. it will only promote the m^{th}-atom initially in the ground state to the Rydberg state if both neighboring atoms are in the ground state:[5]

$$|\xi\rangle = \frac{1}{\sqrt{Z}} \prod_{m=1}^{L} (1 - \sigma^g_{m-1}\sigma^+_m\sigma^g_{m+1}) \, |\downarrow\downarrow \ldots \downarrow\rangle \; . \tag{266}$$

5 As all the terms in $|\xi\rangle$ have the same phase and the same correlated weights, this is by no means the most general state. However, as the actual many-body transient state depends only on the atomic populations and not on phase-related quantities, $|\xi\rangle$ at least gives a "correct sampling" of state space, cf. [202].

Here, Z is a normalization constant which counts the number of all possible states of the superposition in $|\xi\rangle$. Due to the strict nearest neighbor exclusion the normalization constant Z is equivalent to the partition function of a lattice gas of hard-core dimers, i.e. hard objects that occupy two neighboring lattice sites [213]. In order to calculate the partition sum for a chain of atoms of length L, we use the following model Hamiltonian:

$$H = \hbar V \sum_m \sigma^r_m \sigma^r_{m+1} - \mu \sum_m \sigma^r_m \, , \tag{267}$$

which includes the next-neighbor exclusion (for V very large) and the chemical potential μ, instead of the term proportional to the detuning $\hbar\Delta_r$, see eq. (200). The partition sum can then be determined as follows:

$$\begin{aligned} Z &= \sum_{\sigma^r_m=0,1} e^{-\beta H} \\ &= \sum_{\sigma^r_m=0,1} e^{\beta\frac{\mu}{2}\sigma^r_1} e^{-\beta\hbar V\sigma^r_1\sigma^r_2+\beta\frac{\mu}{2}(\sigma^r_1+\sigma^r_2)} \\ &\quad \times e^{-\beta\hbar V\sigma^r_2\sigma^r_3+\beta\frac{\mu}{2}(\sigma^r_2+\sigma^r_3)} \quad \ldots \quad e^{\beta\frac{\mu}{2}\sigma^r_L} \\ &= \mathrm{Tr}\left[\begin{pmatrix} e^{\beta\mu/2} \\ 1 \end{pmatrix} \begin{pmatrix} e^{-\beta\hbar V} & e^{\beta\mu/2} \\ e^{\beta\mu/2} & 1 \end{pmatrix} \begin{pmatrix} e^{-\beta\hbar V} & e^{\beta\mu/2} \\ e^{\beta\mu/2} & 1 \end{pmatrix} \cdots \begin{pmatrix} e^{\beta\mu/2} \\ 1 \end{pmatrix}\right] , \end{aligned} \tag{268}$$

where the sum extends over the possible states ($\sigma^r_m = 1$ ($\sigma^r_m = 0$): Rydberg state of the m^{th} atom (not) populated) of each of the m atoms in the atomic chain. Furthermore, we explicitly spelled out the sum of eq. (267) in the

second line of (268), and, as usual, β is proportional to the inverse temperature. The precise definition of the temperature is irrelevant for the model case considered here, except for the fact that it should be non-zero, finite, and fixed, see below.

In order for the partition sum to represent the blockade limit considered above (as well as the lattice gas of hard-core dimers), we need to assume a vanishing chemical potential μ, a very large V, and a fixed β, such that we may approximate $\exp[\beta\mu/2] \to 1$ and $\exp[-\beta\hbar V] \to 0$. Eq. (268) therefore turns into

$$Z \simeq \mathrm{Tr}\left[\begin{pmatrix}1\\1\end{pmatrix}\begin{pmatrix}0&1\\1&1\end{pmatrix}\begin{pmatrix}0&1\\1&1\end{pmatrix}\ \dots\ \begin{pmatrix}1\\1\end{pmatrix}\right] = \mathrm{Tr}\left[T_{\sigma_1^r} T^L T_{\sigma_L^r}\right], \tag{269}$$

where we, respectively, defined the transfer matrices at the beginning and at the end, as well as inside the atomic chain as:

$$T_{\sigma_1^r} = T_{\sigma_L^r} = \begin{pmatrix}1\\1\end{pmatrix}, \qquad T = \begin{pmatrix}0&1\\1&1\end{pmatrix}. \tag{270}$$

With the help of eqs. (266) and (269), we can now determine expectation values. The expectation value with respect to the state $|\xi\rangle$ for the m^{th}-atom to be in the Rydberg state thus reads:

$$\frac{\langle\sigma_m^r\rangle}{L} = \frac{1}{Z\,L}\mathrm{Tr}\left[\frac{\partial}{\partial\mu}e^{-\beta H}\Big|_{m,\mu=0}\right] = \frac{1}{Z\,L}\mathrm{Tr}\left[T_{\sigma_1^r} T^m \sigma_m^r T^{L-m} T_{\sigma_L^r}\right]. \tag{271}$$

The correlation between two excited atoms at position m and n is obtained accordingly:

$$\begin{aligned}\frac{\langle\sigma_n^r\sigma_m^r\rangle}{L} &= \frac{1}{Z\,L}\mathrm{Tr}\left[\frac{\partial}{\partial\mu}e^{-\beta H}\Big|_{n,\mu=0}\ \frac{\partial}{\partial\mu}e^{-\beta H}\Big|_{m,\mu=0}\right]\\ &= \frac{1}{Z\,L}\mathrm{Tr}\left[T_{\sigma_1^r} T^n \sigma_n^r T^{m-n} \sigma_m^r T^{L-m} T_{\sigma_L^r}\right].\end{aligned} \tag{272}$$

Eqs. (271) and (272) can be identically obtained for the ground state operators $\sigma_m^g = \mathbb{1}_m - \sigma_m^r$, i. e.

$$\frac{\langle\sigma_m^g\rangle}{L} = \frac{1}{Z\,L}\mathrm{Tr}\left[T_{\sigma_1^r} T^m \sigma_m^g T^{L-m} T_{\sigma_L^r}\right], \tag{273}$$

$$\frac{\langle\sigma_n^g\sigma_m^g\rangle}{L} = \frac{1}{Z\,L}\mathrm{Tr}\left[T_{\sigma_1^r} T^n \sigma_n^g T^{m-n} \sigma_m^g T^{L-m} T_{\sigma_L^r}\right]. \tag{274}$$

As mentioned above, we can now exploit the analogy with the case of Rydberg atoms in a 1D chain, making use of the fact that the state $|\xi\rangle$, see (266), approximately corresponds to the physical many-body transient state encountered for the case of two and three atoms above. However, the atomic expectation values which we need in order to obtain the scattered light intensity in eqs. (262) – (264) can now be obtained for a larger number of atoms, using eqs. (271) and (272). The scattered intensity can then be contrasted with Bragg scattering which one obtains for the case of uncorrelated atoms in the steady state regime, see (265).

In Fig. 40 we plot the intensity scattered off the ground state of 30 atoms, as a function of the observation angle θ_R in the $y-z$-plane, and for different realizations of the incoming field, of the inter-atomic distance, and of the orientations of the atomic dipoles, see Fig. 35 for details regarding the geometry. Although the Bragg peaks dominate the scattered intensity in both

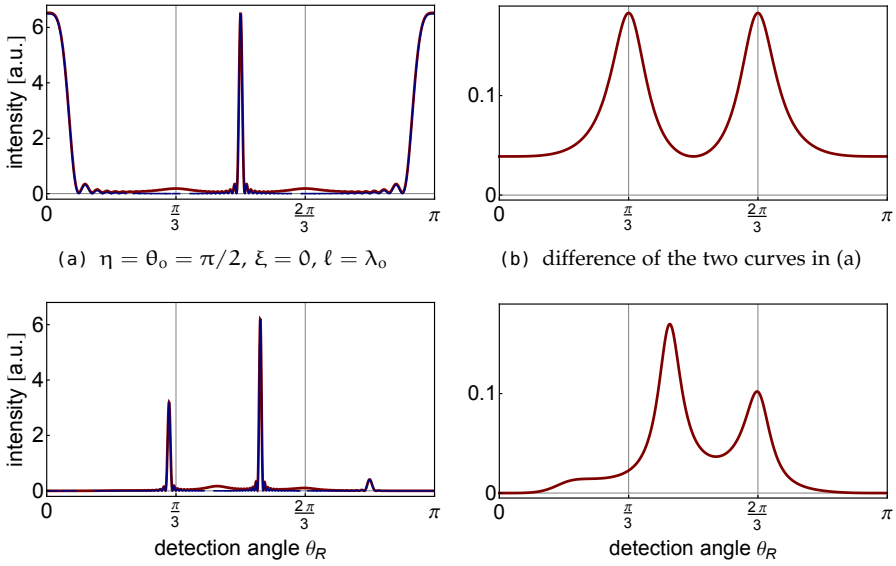

(a) $\eta = \theta_o = \pi/2$, $\xi = 0$, $\ell = \lambda_o$

(b) difference of the two curves in (a)

(c) $\eta = \xi = 0$, $\theta_o = \pi/6$, $\ell = \sqrt{2}\lambda_o$

(d) difference of the two curves in (c)

Figure 40: Intensity scattered off the ground state of 30 atoms, each at the well of a 1D optical lattice with lattice spacing ℓ, as a function of the angle θ_R in the $y-z$-plane, i. e. $\phi = \pi/2$, see Fig. 35 for details regarding the geometry. The thick (red) and the thin (blue) line in (a) and (c) are proportional, respectively, to eqs. (262) and (265). For the evaluation of the atomic ground state correlation function we have used eq. (274). In addition to the Bragg peaks, which correspond to the intensity scattered off a chain of uncorrelated atoms (that are in their ground state with probability 1/2), the residual correlations of the transient regime (where the probability for each atom to be in the ground state is $> 1/2$, due to the blockade mechanism) show up in the detected signal as the difference of the two curves in (a) (see (b)) and (c) (see (d)), respectively.

regimes, corrections due to the correlations between the atoms within the transient regime can be identified even within our simplified model. This is due to the blockade mechanism in the transient regime, where the probability for each atom to be in its respective ground state is $> 1/2$, in contrast to the uncorrelated steady state regime where each atom is in its ground state with probability 1/2. Consequently, the distribution of ground state populations in the transient regime depends on the position of the atom in the chain, and, thus, the angular distribution of the scattered intensity reveals a more complicated structure in addition to the Bragg peaks.

6.5 SUMMARY

Within this chapter, we gave a short introduction to Rydberg atoms, and especially focused on the strong interaction between neighboring atoms, predicted to induce the blockade mechanism. Our major goal was to exploit this mechanism and to investigate a detection scheme to monitor the underlying atomic dynamics. We envisaged a 1D optical lattice with single atoms excited to a Rydberg state sitting at the wells of each site. In addition to the strongly driven Rydberg transition, we laser-addressed another weakly and far-detuned dipole transition in the atom off which photons were scattered and detected to read out the atomic state. The thus achieved monitoring process leads to a dephasing of the atomic subsystem (which we accounted for

by derivation of a master equation) and a relaxation to a fully mixed state in the steady state limit. For intermediate times, however, a transient state is reached where the blockade mechanism persists and limits the maximal excitation present in the system. The duration of this intermediate regime, which is reached on timescales on the order of the inverse dephasing rate $1/\gamma$, strongly depends on the ratio of the interaction potential to the driving strength of the Rydberg transition, and, as we could show for the case of few atoms, scales as $V^2/\Omega^2\gamma$. We could furthermore show how the intermediate regime differs from the steady state regime with respect to the angular resolved intensity signal of scattered photons, thus allowing for an experimental verification and quantification of the stability of the Rydberg blockade mechanism vital for application, e.g., in quantum information processing.

So far we were only able to monitor the transition from the transient to the steady state regime by mimicking the correlations in the quantum system with a classical analogue, i. e. by replacing the Rydberg gas with a gas of hard-core dimers which occupy two lattice sites. Therefore, account of the detected intensity by solving the full master equation (237) is still missing. Of equal interest for future work is the further analysis of additional phenomena and time scales in the atomic system, which e. g. lead to autoionization processes that may modify the relaxation to the steady state. Additionally, the analysis of different geometries, e. g. ring lattices [228], or inclusion of disorder effects into our treatment as suggested in [229] offer possible challenges for future work.

Part III

APPENDIX

A

SUMMARY OF ASSUMPTIONS AND APPROXIMATIONS

Here we summarize all assumptions and approximations as well as additional information relevant to obtain the main results of this thesis.

- All our calculations are conducted in units where $\hbar/2m \equiv 1$, implying particularly $E = k^2$.
- Our theory is valid in the weak disorder potential limit, $\sqrt{E}\ell_{\mathrm{dis}} \equiv k\ell_{\mathrm{dis}} \gg 1$, which implies:
  - neglect of all non-ladder and non-crossed diagrams (see Chapter 3 and Chapter 4, respectively)
  - neglect of a second interaction of particles that interacted with each other before (Section 3.3) (known as recurrent scattering for single-particle transport)
- Due to collisional energy transfer, a very small number of particles can acquire energies $E = k^2$, such that $k\ell_{\mathrm{dis}} \gg 1$ is violated. Consequently, we must exclude the energy range $E \approx 0$ from the predictions of our theory.
- We assume Gaussian white noise statistics for averages over the disorder potential, i. e. a vanishing mean value and δ-like two-point correlations. This results in isotropic scattering off the disorder potential and energy-independence of the disorder mean free path ℓ_{dis}. As a consequence, our setup becomes rotationally invariant.
- Restricting our calculations to the dilute and low-energy Bose gas involves, to a very good approximation, only two-particle collisions ($a_s \rho_0^{1/3} \ll 1$) and s-wave scattering ($k a_s \ll 1$). We assume the interaction between the particles to be point-like.
- We consider our theory to be in the limit where the effect of the disorder potential is stronger than the interaction strength between the particles, i. e. $\ell_{\mathrm{int}} \gg \ell_{\mathrm{dis}}$. This implies a vanishing contribution of collisions to transport, that we neglect explicitly in a contact interaction approximation, cf. eq. (121).
- We treat the inter-particle interaction to occur in vacuum. This is approximately true for very weak disorder potentials, see discussion of Fig. 15. For the same reason, boundary effects at the beginning and end of the slab are also neglected.
- We assume the slab length to be very large in comparison to the wavelength of the particles, i. e. $L \gg \lambda$. As a consequence, the small width of the δ-function expressing momentum conservation of the two-body T-matrix, see eq. (31) and Appendix B.1, can be neglected (and translational invariance is restored).
- All energy integrals throughout this thesis must be evaluated from $-\infty \to +\infty$, if not stated otherwise. However, we most of the times

evaluate only positive energy integrals, since the contributions of negative energies provide a vanishingly small contribution in the weak disorder limit, see the discussion around eq. (118).

B

N-BODY SCATTERING THEORY

This appendix is devoted to rigorous statements about the N-body scattering theory introduced in Section 2.3.

B.1 THE TWO-BODY T-MATRIX

Here, we derive eq. (29), show its relation to eq. (31) indicated in Chapter 2, and finally apply the *contact interaction approximation* to eq. (31), that leads to an explicit expression for $\hat{T}_U^{(1)}(E_{12})$. We again employ units in which $\hbar/2m \equiv 1$.

Starting from the interaction Hamiltonian in second quantized notation

$$\frac{1}{2}\iint d\mathbf{r}\, d\mathbf{r}'\, \hat{\Psi}^\dagger(\mathbf{r})\hat{\Psi}^\dagger(\mathbf{r}')U(\mathbf{r}-\mathbf{r}')\hat{\Psi}(\mathbf{r}')\hat{\Psi}(\mathbf{r})\,, \tag{275}$$

and plugging in the corresponding field operators

$$\hat{\Psi}^\dagger(\mathbf{r}) = \frac{1}{(2\pi)^3}\int d\mathbf{k}\, e^{-i\mathbf{k}\mathbf{r}}\hat{a}_\mathbf{k}^\dagger\,, \qquad \hat{\Psi}(\mathbf{r}) = \frac{1}{(2\pi)^3}\int d\mathbf{k}\, e^{i\mathbf{k}\mathbf{r}}\hat{a}_\mathbf{k}\,, \tag{276}$$

we can read off an expression for $\langle \mathbf{k}_3, \mathbf{k}_4|\, \hat{U}\, |\mathbf{k}_1, \mathbf{k}_2\rangle$ by comparison with eq. (28):

$$\begin{aligned}\langle \mathbf{k}_3, \mathbf{k}_4|\, \hat{U}\, |\mathbf{k}_1, \mathbf{k}_2\rangle = \frac{1}{2}\iint d\mathbf{r}\, d\mathbf{r}'\, U(\mathbf{r}-\mathbf{r}') \\ \times \left[e^{i(\mathbf{k}_1-\mathbf{k}_3)\mathbf{r}}e^{i(\mathbf{k}_2-\mathbf{k}_4)\mathbf{r}'} + e^{i(\mathbf{k}_1-\mathbf{k}_4)\mathbf{r}}e^{i(\mathbf{k}_2-\mathbf{k}_3)\mathbf{r}'} + \{\mathbf{r}\leftrightarrow\mathbf{r}'\}\right]\,,\end{aligned} \tag{277}$$

where $\{\mathbf{r}\leftrightarrow\mathbf{r}'\}$ stands for the two missing but equivalent exponential contributions with interchanged vectors $\mathbf{r}$ and $\mathbf{r}'$.

Transforming (277) to center-of-mass and relative coordinates with

$$\begin{aligned} \mathbf{Q} &= \mathbf{k}_1 + \mathbf{k}_2\,, & \mathbf{S} &= (\mathbf{r}+\mathbf{r}')/2\,, & \mathbf{q} &= (\mathbf{k}_1-\mathbf{k}_2)/2\,, \\ \mathbf{Q}' &= \mathbf{k}_3 + \mathbf{k}_4\,, & \mathbf{s} &= \mathbf{r}-\mathbf{r}'\,, & \mathbf{q}' &= (\mathbf{k}_3-\mathbf{k}_4)/2\,, \end{aligned} \tag{278}$$

we obtain

$$\langle \mathbf{k}_3, \mathbf{k}_4|\, \hat{U}\, |\mathbf{k}_1, \mathbf{k}_2\rangle = \int d\mathbf{S}\, e^{i(\mathbf{Q}-\mathbf{Q}')\mathbf{S}}\int d\mathbf{s}\ \langle \mathbf{k}_{34}|\, \hat{U}^{(1)}\, |\mathbf{k}_{12}\rangle\ . \tag{279}$$

In eq. (279) we introduced

$$\begin{aligned}\langle \mathbf{k}_{34}|\, \hat{U}^{(1)}\, |\mathbf{k}_{12}\rangle = \frac{1}{2}\int d\mathbf{s}\, U(\mathbf{s}) \\ \times \left[e^{i(\mathbf{q}-\mathbf{q}')\mathbf{s}} + e^{-i(\mathbf{q}-\mathbf{q}')\mathbf{s}} + e^{-i(\mathbf{q}+\mathbf{q}')\mathbf{s}} + e^{i(\mathbf{q}+\mathbf{q}')\mathbf{s}}\right]\,,\end{aligned} \tag{280}$$

and the symmetrized single particle states

$$|\mathbf{k}_{12}\rangle = \frac{1}{\sqrt{2}}\left[\,|\mathbf{q}\rangle + |-\mathbf{q}\rangle\,\right]\,, \qquad |\mathbf{k}_{34}\rangle = \frac{1}{\sqrt{2}}\left[\,|\mathbf{q}'\rangle + |-\mathbf{q}'\rangle\,\right]\,. \tag{281}$$

The result (29) is obtained upon integration of (279) over $\mathbf{S}$, leading to conservation of the overall momentum. The properties of the collision process thus depend only on the relative momenta.

As mentioned in Section 2.2, the same separation into center-of-mass and relative coordinates also applies to the T-matrix, see (32):

$$\langle \mathbf{k}_3, \mathbf{k}_4 | \hat{T}_U^{(2)}(E) | \mathbf{k}_1, \mathbf{k}_2 \rangle = (2\pi)^3 \delta(\mathbf{k}_1 + \mathbf{k}_2 - \mathbf{k}_3 - \mathbf{k}_4) \times \langle \mathbf{k}_{34} | \hat{T}_U^{(1)}(E_{12}) | \mathbf{k}_{12} \rangle \, . \tag{282}$$

The energy dependence of the T-matrix arises due to eqs. (32) and (58) (for the vacuum Green's function (33)), and is given by

$$E_{12} = E - E_Q/2 \, . \tag{283}$$

Here, $E_Q/2$ is the energy of the center-of-mass (mass $2m$), and $\hat{T}_U^{(1)}(E_{12})$ is the T-matrix for a single particle scattered by the potential $U(\mathbf{r})$ with energy E_{12} (and mass $m/2$), such that $q = \sqrt{E_{12}/2}$, with $q = |\mathbf{q}|$ if $E = E_1 + E_2$, see (278).

In dependence on the system under consideration, eq. (282) can now be evaluated further. For the case of two-particle interaction in a low-energy dilute system the *contact interaction approximation* amounts to the replacement $U(\mathbf{s}) = g\delta(\mathbf{s})$. The respective diluteness and low-temperature assumption are usually fulfilled in ultracold atom experiments, e. g. involving Bose-Einstein condensates, and can be summarized as $\rho_0^{1/3} a_s \ll 1$ and $a_s \ll \lambda$ [110], where $\lambda = 2\pi/k$ or $\lambda_{dB} = \sqrt{2\pi\hbar^2/mk_BT}$, depending on whether a suitable system temperature T is defined for the de-Broglie wavelength. ρ_0 and a_s determine the initial density of the bosonic cloud and the s-wave scattering length, respectively. The restriction to include only s-wave scattering contributions is identical to the weakly interacting low-temperature limit.

It turns out that for s-wave scattering of identical particles the *Born - approximation* in the zero-momentum limit yields a momentum-independent coupling strength $g = 8\pi a_s$ proportional to the s-wave scattering length [100] (and commonly known from the Gross-Pitaevskii equation.)

However, in order to rigorously justify the contact interaction approximation one has to replace the actual interaction potential by a pseudo-potential for the reduced single-particle problem (we here follow the derivation in [100]),

$$U(\mathbf{s})\psi(\mathbf{s}) = g\delta(\mathbf{s}) \frac{\partial}{\partial s} (s\psi(\mathbf{s})) \, , \tag{284}$$

where $\psi(\mathbf{s})$ is now the quantum mechanical wave function for a single particle at position $\mathbf{s}$. We see now that the operator replacement $U(\mathbf{s}) = g\delta(\mathbf{s})$ mentioned above within the contact interaction approximation is only fulfilled if $\psi(\mathbf{s})$ is regular at $\mathbf{s} = 0$, i. e. if $\lim_{s\to 0} s(\partial/\partial s)\psi(\mathbf{s}) = 0$. In contrast, for a general wave function of the form $\psi(\mathbf{s}) = \phi(\mathbf{s})/s$ (with regular $\phi(\mathbf{s})$), the scattering solution of the Schrödinger equation with potential U as defined in eq. (284) in terms of s-waves turns out as:

$$\psi_{\mathbf{q}}(\mathbf{s}) = e^{i\mathbf{q}\mathbf{s}} - f(q) \frac{e^{iqs}}{s} \, , \tag{285}$$

with the scattering amplitude $f(q)$ defined as:

$$f(q) = \frac{a_s}{1 + iqa_s} \approx a_s(1 - iqa_s) \, . \tag{286}$$

Note that the proportionality to a_s, i. e. $g = 8\pi a_s$, is only obtained in the zero-momentum limit, where q vanishes. For our case of two-particle collisions, where the relative momenta can be different from zero, we must

include the next higher order contribution in (286). The single-particle T-matrix (282) can now be obtained for a particle with the reduced mass $\mu = m/2$ and $q = \sqrt{E_{12}/2}$, from the scattering amplitude (286), via

$$\langle \mathbf{k}| \hat{T}_U^{(1)}(E_{12}) |\mathbf{k}'\rangle = \frac{4\pi\hbar^2}{2\mu} f(q) = 8\pi a_s \left(1 - i a_s \sqrt{\frac{E_{12}}{2}} + \dots\right) . \tag{287}$$

In order to understand the origin of the prefactor, we included $\hbar^2/2m$ in the first and reset it to 1 in the second equality of (287), respectively. If the total energy $E = E_1 + E_2 = k_1^2 + k_2^2$, cf. (283), then $q = |\mathbf{k}_1 - \mathbf{k}_2|/2$, see (278), and (287) reads:

$$\langle \mathbf{k}_{34}| \hat{T}_U^{(1)}(E_{12}) |\mathbf{k}_{12}\rangle = 16\pi a_s \left(1 - \frac{i|\mathbf{k}_1 - \mathbf{k}_2|a_s}{2} + \dots\right) . \tag{288}$$

Note that the additional factor 2 in comparison with (287) arises from eq. (280), due to the symmetry properties of the two-particle subspace.

In another case, relevant in Chapter 4, we find $\mathbf{k}_2 = -\mathbf{k}_1$, such that $E_{12} = E$ and the final result is rather:

$$\langle \mathbf{k}_{34}| \hat{T}_U^{(1)}(E) |\mathbf{k}_{12}\rangle = 16\pi a_s \left(1 - i a_s \sqrt{\frac{E}{2}} + \dots\right) . \tag{289}$$

It can be readily verified that the T-matrix (287) (or equivalently (288) or (289)) with the scattering amplitude (286) fulfills the unitarity of the scattering process, i. e. the *optical theorem*, see (34) and [101].

B.2 FACTORIZATION OF THE N-BODY SCATTERING AMPLITUDES

In this appendix, we show how an arbitrary N-particle scattering diagram can be factorized into single-particle propagators and two-body collisions. We first return to the example diagram shown in Fig. 4a). As shown in Fig. 41, this diagram can be split into four independent subdiagrams. The two subdiagrams connected to the initial state – (i) and (ii) in Fig. 41 – correspond to Møller operators, and the remaining ones – (iii) and (iv) – to Green's operators. This gives rise to the following matrix elements:

$$\Omega_+^{(i)}(E) = \langle \mathbf{p}_9 | \hat{\Omega}_+^{(V)}(E) | \mathbf{k}_1 \rangle , \tag{290}$$

$$\Omega_+^{(ii)}(E) = \frac{1}{2} \iint \frac{d\mathbf{p}_2 d\mathbf{p}_3}{(2\pi)^6} \langle \mathbf{p}_4, \mathbf{p}_7 | \hat{T}_U^{(2)}(E) | \mathbf{p}_2, \mathbf{p}_3 \rangle \langle \mathbf{p}_2, \mathbf{p}_3 | \hat{\Omega}^{(V)}(E) | \mathbf{k}_2, \mathbf{k}_3 \rangle , \tag{291}$$

$$G^{(iii)}(E) = \frac{1}{4} \iiiint \frac{d\mathbf{p}_1 d\mathbf{p}_5 d\mathbf{p}_6 d\mathbf{p}_8}{(2\pi)^{12}} \langle \mathbf{k}_5, \mathbf{k}_6 | \hat{G}_V(E) | \mathbf{p}_5, \mathbf{p}_6 \rangle \times \langle \mathbf{p}_5, \mathbf{p}_6 | \hat{T}_U^{(2)}(E) | \mathbf{p}_1, \mathbf{p}_8 \rangle \langle \mathbf{p}_1, \mathbf{p}_8 | \hat{G}_V(E) | \mathbf{p}_7, \mathbf{p}_9 \rangle , \tag{292}$$

$$G^{(iv)}(E) = \langle \mathbf{k}_4 | \hat{G}_V(E) | \mathbf{p}_4 \rangle . \tag{293}$$

Note that the diagrams (i) and (ii) are not connected to each other in Fig. 41. The corresponding Møller operators can therefore be factorized as in eq. (57). Likewise, the Green's functions corresponding to (iii) and (iv) are factorized according to eq. (58). The respective prefactors 1/2 and 1/4 in eqs. (291) and (292) originate from symmetrization in the two-particle subspace (e. g. the states $|\mathbf{p}_2, \mathbf{p}_3\rangle$ and $|\mathbf{p}_3, \mathbf{p}_2\rangle$ are identical and therefore must not be summed over twice). It turns out, however, that these factors

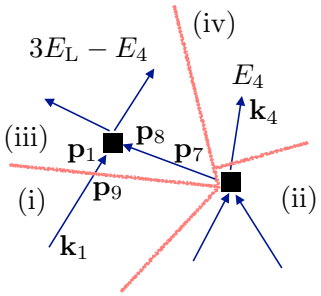

Figure 41: The scratchy red lines split the diagram of Fig. 4a) into 4 subdiagrams (i), (ii), (iii), and (iv). Note that (i) and (ii) – and likewise (iii) and (iv) – are not connected to each other by solid arrows. This allows us to factorize the 3-particle diagram into 1- and 2-particle diagrams. In the following we use the notation based on Fig. 4a).

are compensated by the two possibilities to associate the initial and final singe-particle states with each other in eqs. (57) and (58).

The total transition amplitude results as:

$$\langle \mathbf{k}_4, \mathbf{k}_5, \mathbf{k}_6 | \hat{\Omega}_+(3E_L) | \mathbf{k}_1, \mathbf{k}_2, \mathbf{k}_3 \rangle_{(\text{Fig. 4a})} = \frac{1}{2} \iiint \frac{d\mathbf{p}_4 d\mathbf{p}_7 d\mathbf{p}_9}{(2\pi)^9} \Omega_+^{(i)}(E_L) \Omega_+^{(ii)}(2E_L) \times \int \frac{dE_4}{(-2\pi i)} G^{(iii)}(3E_L - E_4) G^{(iv)}(E_4) \,. \tag{294}$$

Now, we again apply eqs. (57) and (58) to factorize the two-particle Møller and Green's operators on the right-hand side of eqs. (291) and (292), into single-particle operators. In this way, we recover most of the terms in eq. (59). The only ones which appear to differ from eq. (59) are those associated to $\mathbf{k}_1$, $\mathbf{p}_1$, $\mathbf{p}_7$ and $\mathbf{p}_8$, which we reformulate as follows:

$$\begin{aligned} &\frac{1}{2} \int \frac{d\mathbf{p}_9}{(2\pi)^3} \langle \mathbf{p}_1, \mathbf{p}_8 | \hat{G}_V(3E_L - E_4) | \mathbf{p}_7, \mathbf{p}_9 \rangle \langle \mathbf{p}_9 | \hat{\Omega}_+^{(V)}(E_L) | \mathbf{k}_1 \rangle \\ &= \int \frac{dE_1}{(-2\pi i)} \langle \mathbf{p}_1 | \hat{G}_V(E_1) \hat{\Omega}_+^{(V)}(E_L) | \mathbf{k}_1 \rangle G(-E_1) \,. \end{aligned} \tag{295}$$

Again we applied eq. (58), used the completeness relation $\int d\mathbf{p}_9 |\mathbf{p}_9\rangle\langle\mathbf{p}_9| = (2\pi)^3$, and defined:

$$G(-E_1) = \langle \mathbf{p}_8 | \hat{G}_V(3E_L - E_4 - E_1) | \mathbf{p}_7 \rangle \,. \tag{296}$$

Note that $G(-E_1)$ is a complex analytic function of E_1 with poles only in the upper half of the complex plane. This, again, is due to the fact that $\hat{G}_V(E)$ as a function of E exhibits poles only in the lower half, whereas E_1 enters with negative sign on the right-hand side of eq. (296). We now reformulate some terms in (295) as follows:

$$\begin{aligned} \hat{G}_V(E_1) \hat{\Omega}_+^{(V)}(E_L) | \mathbf{k}_1 \rangle &= \left[\mathbb{1} + \hat{G}_V(E_1) \hat{V} \right] \hat{G}_0(E_1) | \mathbf{k}_1 \rangle + \hat{G}_V(E_1) \hat{G}_V(E_L) \hat{V} | \mathbf{k}_1 \rangle \\ &= \frac{1}{E_1 - E_L + i\varepsilon} \left[\mathbb{1} + \left(\hat{G}_V(E_1) + \hat{G}_V(E_L) - \hat{G}_V(E_1) \right) \hat{V} \right] | \mathbf{k}_1 \rangle \\ &= \frac{1}{E_1 - E_L + i\varepsilon} \hat{\Omega}_+^{(V)}(E_L) | \mathbf{k}_1 \rangle \,, \end{aligned} \tag{297}$$

where we used eqs. (53) and (54) and the identity:

$$\hat{G}_V(E_1) \hat{G}_V(E_L) = \frac{1}{E_1 - E_L + i\varepsilon} \left(\hat{G}_V(E_L) - \hat{G}_V(E_1) \right) \tag{298}$$

resulting from $\frac{1}{ab} = \frac{1}{b-a}\left(\frac{1}{a} - \frac{1}{b}\right)$ (where we set the imaginary part in the denominator of $\hat{G}_V(E_1)$, see eq. (55), equal to 2ε instead of ε, and used the fact that $\hat{G}_V(E_1)$ and $\hat{G}_V(E_L)$ have the same set of eigenvectors, i. e. are functions of the same operator $\hat{H}_0 + \hat{V}$). After inserting eq. (297) into eq. (295), we perform the integral over E_1 by closing the integration contour in the lower half of the complex plane. (Remember that $G(-E_1)$ has no poles in the lower half!) Thereby, the energy E_1 is set to E_L, and we finally recover the missing terms in eq. (59):

$$\int \frac{dE_1}{(-2\pi i)} \langle \mathbf{p}_1 | \hat{G}_V(E_1) \hat{\Omega}_+^{(V)}(E_L) | \mathbf{k}_1 \rangle G(-E_1) = \langle \mathbf{p}_1 | \hat{\Omega}_+^{(V)}(E_L) | \mathbf{k}_1 \rangle G(-E_L)\,, \tag{299}$$

The above procedure can be generalized to an arbitrary many-particle scattering diagram: We first divide the whole diagram into independent subdiagrams. Then, some of these subdiagrams turn out to be connected to each other by single-particle propagators. In the above example, Fig. 41, this is the case for the subdiagram (i) and (iii), which are connected by two single-atom propagators from $\mathbf{k}_1$ to $\mathbf{p}_9$ with energy E_L, on the one hand, and from $\mathbf{p}_9$ to $\mathbf{p}_1$ with energy E_1, on the other hand. After connecting these diagrams and integrating over E_1, we obtain a single propagator from $\mathbf{k}_1$ to $\mathbf{p}_1$ with energy E_L. Hence, for the case that one of the propagators is connected to the initial state (and thus corresponds to a Møller operator), the corresponding general identity is given by (299). If both propagators correspond to Green's operators, the required identity is proven as follows:

$$\begin{aligned}
&\int \frac{dE_1 dE_2}{(-2\pi i)^2} \hat{G}_V(E_1) \hat{G}_V(E_2) G_1(-E_1) G_2(-E_2) \\
&\quad = \int \frac{dE_1 dE_2}{(-2\pi i)^2} \frac{1}{E_1 - E_2 + i\varepsilon} \left(\hat{G}_V(E_2) - \hat{G}_V(E_1)\right) G_1(-E_1) G_2(-E_2) \\
&\quad = \int \frac{dE_2}{(-2\pi i)} \hat{G}_V(E_2) G_1(-E_2) G_2(-E_2)\,,
\end{aligned} \tag{300}$$

where we again used eq. (298) and the fact that $G_1(-E_1)$ and $G_2(-E_2)$ (which correspond to arbitrary other subdiagrams where the energy E_1 or E_2 enters with negative sign) exhibit no pole in the lower half of the complex plane. The two propagators $\hat{G}_V(E_1)$ and $\hat{G}_V(E_2)$ merge into a single propagator $\hat{G}_V(E_2)$, according to (298), and due to the fact that the term with $\hat{G}_V(E_1)$ in the second line of eq. (300) vanishes after integrating over E_2, since no pole remains in the lower half.

B.3 COMPLETE DESCRIPTION OF THE EXEMPLARY INELASTIC AND ELASTIC DIAGRAMS FOR TWO PARTICLES

The inelastic diagram shown in Fig. 5a) gives the following contribution to the flux density:

$$\begin{aligned}
\mathbf{J}^{(\text{Fig. 5a})}(\mathbf{r}) &= \frac{2^2}{2^3} \int \frac{d\mathbf{k} d\mathbf{k}_1 d\mathbf{k}_2 d\mathbf{k}_3 d\mathbf{k}_1' d\mathbf{k}_2' d\mathbf{k}_3' d\mathbf{p}_1 d\mathbf{p}_2 d\mathbf{p}_3 d\mathbf{p}_4 d\mathbf{p}_1' d\mathbf{p}_2' d\mathbf{p}_3' d\mathbf{p}_4'}{(2\pi)^{45}} \\
&\times \iint \frac{dE dE'}{|2\pi i|^2} w^*(\mathbf{k}_1') w^*(\mathbf{k}_2') w(\mathbf{k}_1) w(\mathbf{k}_2) \langle \mathbf{k}_1' | \left[\hat{\Omega}^{(V)}(E_L)\right]^\dagger | \mathbf{p}_1' \rangle \langle \mathbf{k}_2' | \left[\hat{\Omega}^{(V)}(E_L)\right]^\dagger | \mathbf{p}_2' \rangle \\
&\times \langle \mathbf{p}_1', \mathbf{p}_2' | \left[\hat{T}_U^{(2)}(2E_L)\right]^\dagger | \mathbf{p}_3', \mathbf{p}_4' \rangle \langle \mathbf{p}_3' | \left[\hat{G}_V(2E_L - E')\right]^\dagger | \mathbf{k}_3' \rangle \langle \mathbf{k}_3' | \hat{\mathbf{J}}(\mathbf{r}) | \mathbf{k}_3 \rangle \\
&\times \langle \mathbf{p}_4' | \left[\hat{G}_V(E')\right]^\dagger | \mathbf{k} \rangle \langle \mathbf{k} | \hat{G}_V(E) | \mathbf{p}_4 \rangle \langle \mathbf{k}_3 | \hat{G}_V(2E_L - E) | \mathbf{p}_3 \rangle \\
&\times \langle \mathbf{p}_3, \mathbf{p}_4 | \hat{T}_U^{(2)}(2E_L) | \mathbf{p}_1, \mathbf{p}_2 \rangle \langle \mathbf{p}_1 | \hat{\Omega}^{(V)}(E_L) | \mathbf{k}_1 \rangle \langle \mathbf{p}_2 | \hat{\Omega}^{(V)}(E_L) | \mathbf{k}_2 \rangle\,.
\end{aligned} \tag{301}$$

The trace formula (63) can now be applied as follows:

1. replace
   $\langle \mathbf{p}_4' | \left[\hat{G}_V(E')\right]^\dagger |\mathbf{k}\rangle\langle\mathbf{k}|\hat{G}_V(E)|\mathbf{p}_4\rangle \to \langle \mathbf{p}_4' | \left(\left[\hat{G}_V(E)\right]^\dagger - \hat{G}_V(E) \right) |\mathbf{p}_4\rangle$
2. delete the integrals $\int d\mathbf{k}/(2\pi)^3$ and $\int dE'/(-2\pi i)$,
3. replace E' by E in $\langle \mathbf{p}_3' | \left[\hat{G}_V(2E_L - E')\right]^\dagger |\mathbf{k}_3'\rangle$.

For the elastic diagram, Fig. 5b), we obtain:

$$\begin{aligned}
\mathbf{J}^{(\text{Fig. 5b})}(\mathbf{r}) = \frac{2^3}{2^3} \int \frac{d\mathbf{k}d\mathbf{k}_1 d\mathbf{k}_2 d\mathbf{k}_3 d\mathbf{k}_1' d\mathbf{k}_2' d\mathbf{k}_3' d\mathbf{p}_1 d\mathbf{p}_2 d\mathbf{p}_3 d\mathbf{p}_4}{(2\pi)^{33}} \\
\times \int \frac{dE}{2\pi i} w^*(\mathbf{k}_1') w^*(\mathbf{k}_2') w(\mathbf{k}_1) w(\mathbf{k}_2) \langle \mathbf{k}_1' | \left[\hat{\Omega}^{(V)}(E_L)\right]^\dagger |\mathbf{k}_3'\rangle\langle\mathbf{k}_3'|\hat{\mathbf{J}}(\mathbf{r})|\mathbf{k}_3\rangle \\
\times \langle \mathbf{k}_2' | \left[\hat{\Omega}^{(V)}(E_L)\right]^\dagger |\mathbf{k}\rangle\langle\mathbf{k}|\hat{G}_V(E)|\mathbf{p}_4\rangle\langle\mathbf{k}_3|\hat{G}_V(2E_L - E)|\mathbf{p}_3\rangle \\
\times \langle \mathbf{p}_3, \mathbf{p}_4 | \hat{T}_U^{(2)}(2E_L)|\mathbf{p}_1, \mathbf{p}_2\rangle\langle\mathbf{p}_1|\hat{\Omega}^{(V)}(E_L)|\mathbf{k}_1\rangle\langle\mathbf{p}_2|\hat{\Omega}^{(V)}(E_L)|\mathbf{k}_2\rangle \,. \qquad (302)
\end{aligned}$$

Here, the trace formula (65) is applied as follows:

1. replace
   $\langle \mathbf{k}_2' | \left[\hat{\Omega}^{(V)}(E_L)\right]^\dagger |\mathbf{k}\rangle\langle\mathbf{k}|\hat{G}_V(E)|\mathbf{p}_4\rangle \to \langle \mathbf{k}_2' | \left[\hat{\Omega}^{(V)}(E_L)\right]^\dagger |\mathbf{p}_4\rangle$,
2. delete the integrals $\int d\mathbf{k}/(2\pi)^3$ and $\int dE/(2\pi i)$,
3. replace E by E_L in $\langle \mathbf{k}_3|\hat{G}_V(2E_L - E)|\mathbf{p}_3\rangle$.

It is also insightful to look at the prefactors: the first factor $1/2$ in (301) results from $(1/\sqrt{2})^2$ in the initial states $|i_2\rangle$ and $\langle i_2|$, see (35). The integration over the final states $|\mathbf{k}_3, \mathbf{k}_4\rangle$ and $\langle \mathbf{k}_3', \mathbf{k}_4'|$ (with $\mathbf{k}_4 = \mathbf{k}_4' = \mathbf{k}$ due to the trace) goes along with two more factors $1/2$ (since both integrations must be performed in the symmetrized subspace). This, however, is counterbalanced by the fact that we may select either one of the two final particles as the detected particle. In (301), we have selected $|\mathbf{k}_3\rangle$ and $\langle \mathbf{k}_3'|$. Therefore, we have to include a factor 2^2 to take into account the other possibilities. In (302), we obtain an additional factor 2 due to the two possibilities in the factorization formula (57) for the dashed amplitudes: $\mathbf{k}_1'$ can be associated with $\mathbf{k}_3'$ and $\mathbf{k}_2'$ with $\mathbf{k}_4' = \mathbf{k}$ – or vice versa.

Finally, the diagrams shown in Fig. 5 can be generalized to $N > 2$ particles. In this case, the remaining $N - 2$ particles are assumed not to interact with the detected particle. Hence, their evolution factorizes from the one of the detected particle and need not be taken into account. The prefactors are then generalized as follows: $1/2 \to N(N-1)/4$ in (301), and $1 \to N(N-1)/2$ in (302).

Let us now compare these prefactors with the ones obtained from the iterative procedure based on the connection of building blocks in Chapter 3 and 4: The factors $N(N-1) \simeq N^2$ (for $N \gg 1$, since $N \to \infty$ in order to obtain a finite density, see eq. (37)) are accounted for by the source term ρ_0 in eqs. (102), (123), and (162), which is proportional to N, see eq. (37), and occurs twice for a two-particle process proportional to the density squared. What remains is a factor $1/2$ for each collision event [twice in Fig. 5a) and once in Fig. 5b)] which is included in the definition of the building blocks in

eqs. (126), (129), (164), (165), and (166). The origin of this factor can be traced back to the indistinguishability of bosonic particles. Indeed, as argued in Section 2.3, all factors related to the indistinguishability finally drop out in the case where all particles are initially in the same state. Since the T-matrix for indistinguishable particles, see eqs. (31) and (287), differs by a factor 2 from the one for distinguishable particles, this must be counterbalanced by the above factor 1/2.

B.4 PROOF OF THE TRACE FORMULAS

We here prove the trace formulas (63) and (65) introduced in Section 2.3 valid for inelastic and elastic collision processes, respectively. In both cases, we apply first the completeness relation

$$\int d\mathbf{k}\, |\mathbf{k}\rangle\langle\mathbf{k}| = (2\pi)^3\,, \tag{303}$$

and then the following identity for the product of two Green's operators:

$$\hat{G}_V^\dagger(E')\hat{G}_V(E) = \frac{1}{E - E' + i\varepsilon}\left(\hat{G}_V^\dagger(E') - \hat{G}_V(E)\right), \tag{304}$$

which is similar to eq. (298). Thereby, (63) is proven as follows:

$$\begin{aligned}
&\iint \frac{dE dE'}{|2\pi i|^2}\int \frac{d\mathbf{k}}{(2\pi)^3}(\dots)_{(-E')}\hat{G}_V^\dagger(E')|\mathbf{k}\rangle\langle\mathbf{k}|\hat{G}_V(E)(\dots)_{(-E)}\\
&\quad= \iint \frac{dE dE'}{|2\pi i|^2}(\dots)_{(-E')}\hat{G}_V^\dagger(E')\hat{G}_V(E)(\dots)_{(-E)}\\
&\quad= \iint \frac{dE dE'}{|2\pi i|^2}\frac{1}{E - E' + i\varepsilon}(\dots)_{(-E')}\left(\hat{G}_V^\dagger(E') - \hat{G}_V(E)\right)(\dots)_{(-E)}\\
&\quad= \int \frac{dE}{2\pi i}(\dots)_{(-E)}\left(\hat{G}_V^\dagger(E) - \hat{G}_V(E)\right)(\dots)_{(-E)}\,.
\end{aligned} \tag{305}$$

In the last step, we have used the fact that $(\dots)_{(-E)}$, as the energy argument appears with a minus sign, is a complex analytic function without poles in the lower half of the complex plane. Similarly, $(\dots)_{(-E')}$ exhibits no poles in the upper half. Thereby, considering the two terms $\hat{G}_V^\dagger(E')$ or $\hat{G}_V(E)$, which only have poles in the upper and lower half of the complex plane, respectively, we can perform the integral either over E or over E', closing the integration contour in the lower or upper half, respectively. In both cases, the term $1/(E - E' + i\varepsilon)$ constitutes the only pole. This fixes $E' = E$, and we arrive at the final result, eq. (305).

Concerning the trace formula for elastic collisions, eq. (65), we proceed in a similar way as in eq. (299). We use the definition (54) of $\hat{\Omega}_+^{(V)}(E_L)$ and the Lippmann-Schwinger equation (53) for $\hat{G}_V(E)$ as follows:

$$\begin{aligned}
&\int \frac{dE}{2\pi i}\int \frac{d\mathbf{k}}{(2\pi)^3}\,\langle\mathbf{k}_L|\left[\hat{\Omega}_+^{(V)}(E_L)\right]^\dagger|\mathbf{k}\rangle\langle\mathbf{k}|\hat{G}_V(E)(\dots)_{(-E)}\\
&\quad= \int \frac{dE}{2\pi i}\,\langle\mathbf{k}_L|\left[\hat{G}_V(E) + \hat{V}\hat{G}_V^\dagger(E_L)\hat{G}_V(E)\right](\dots)_{(-E)}\\
&\quad= \int \frac{dE}{2\pi i}\frac{1}{E - E_L + i\varepsilon}\,\langle\mathbf{k}_L|\left[\mathbb{1} + \hat{V}\left(\hat{G}_V(E) + \hat{G}_V^\dagger(E_L) - \hat{G}_V(E)\right)\right](\dots)_{(-E)}\\
&\quad= \langle\mathbf{k}_L|\left[\mathbb{1} + \hat{V}\hat{G}_V^\dagger(E_L)\right](\dots)_{(-E_L)} = \langle\mathbf{k}_L|\left[\hat{\Omega}_+^{(V)}(E_L)\right]^\dagger(\dots)_{(-E_L)}\,.
\end{aligned} \tag{306}$$

This proves eq. (65).

C

GENERAL PARTICLE AND ENERGY FLUX CONSERVATION

In this appendix, we prove the relations (131) for particle and energy flux conservation irrespective of the particular choice of the two-body collision process.

In order to prove the formula for the conservation of the particle flux, we apply the contact approximation, cf. eq. (121), and conduct the integration over $\mathbf{r}_1$ and $\mathbf{r}_2$ in eq. (111). Since $\mathbf{r}$ only appears as an exponent in (111), the formula $\int d\mathbf{r}\, \exp(i\mathbf{k}\cdot\mathbf{r}) = (2\pi)^3\delta(\mathbf{k})$ yields δ-functions in $\mathbf{k}$-space. From the T-matrix (31), we get another δ-function for momentum conservation of the collision. In total, we obtain:

$$f^{L}_{E_1,E_2,E_3} = 2\left(\frac{4\pi}{\ell_{dis}}\right)^2 \frac{1}{4}\int \frac{d\mathbf{k}_1 d\mathbf{k}_2 d\mathbf{k}_3}{(2\pi)^9} \frac{G^*_{E_1+E_2-E_3}(k_4) - G_{E_1+E_2-E_3}(k_4)}{2\pi i} \times \left|\langle \mathbf{k}_{34}|\hat{T}^{(1)}_U(E_{12})|\mathbf{k}_{12}\rangle\right|^2 \left|G_{E_1}(k_1)\right|^2 \left|G_{E_2}(k_2)\right|^2 \left|G_{E_3}(k_3)\right|^2, \quad (307)$$

where $|\mathbf{k}_{12}\rangle$, $|\mathbf{k}_{34}\rangle$ and $E_{12} = E_1 + E_2 - E_{\mathbf{k}_1+\mathbf{k}_2}/2$ are defined as in eq. (30), with $\mathbf{k}_4 = \mathbf{k}_1 + \mathbf{k}_2 - \mathbf{k}_3$. Now, we can calculate $\int_0^\infty dE_3 \sqrt{E_3} f^{L}_{E_1,E_2,E_3}$. For this purpose, we first note that

$$\begin{aligned}\int_0^\infty dE_3\, \sqrt{E_3} \left(\frac{G^*_{E_1+E_2-E_3}(k_4) - G_{E_1+E_2-E_3}(k_4)}{2\pi i}\right) \left|G_{E_3}(k_3)\right|^2 \\ \simeq \frac{\ell_{dis}}{2i}\left(\frac{1}{E_1+E_2-k_3^2-k_4^2-2i\varepsilon} - \frac{1}{E_1+E_2-k_3^2-k_4^2+2i\varepsilon}\right) \\ \simeq \frac{\ell_{dis}}{2i}\left(\left[G^{(0,m/2)}_{E_{12}}\left(\frac{\mathbf{k}_3-\mathbf{k}_4}{2}\right)\right]^* - G^{(0,m/2)}_{E_{12}}\left(\frac{\mathbf{k}_3-\mathbf{k}_4}{2}\right)\right).\end{aligned} \quad (308)$$

As a first step to obtain (308), we used the identity

$$\sqrt{E_3}\left|G_{E_3}(k_3)\right|^2 = \ell_{dis}\left[G^*_{E_3}(k_3) - G_{E_3}(k_3)\right]/(2i) \quad (309)$$

for the average Green's function, then replaced the average Green's functions by vacuum Green's functions (which is appropriate in the weak disorder limit), and evaluated the integral over E_3 using residual calculus. Second, we replaced $(k_3^2 + k_4^2)/2 \to (\mathbf{k}_1+\mathbf{k}_2)^2/2 - \mathbf{k}_3\mathbf{k}_4 = E_{\mathbf{k}_1+\mathbf{k}_2}/2 - \mathbf{k}_3\mathbf{k}_4$, following from momentum conservation, and set the imaginary part 2ε in the denominator to ε to arrive at eq. (308). We here explicitly indicated with a superscript that the vacuum Green's functions correspond to a particle with mass $m/2$ (and corresponding dispersion relation $E = 2k^2$) , see Appendix B.1 for details.

We can now insert (308) into (307), substitute the variable $\mathbf{k}_3 \to \mathbf{k}_{34} = (\mathbf{k}_3 - \mathbf{k}_4)/2$, and integrate over $\mathbf{k}_{34}$:

$$\begin{aligned} 2\int \frac{d\mathbf{k}_{34}}{(2\pi)^3} \left(\left[G^{(0,m/2)}_{E_{12}}(\mathbf{k}_{34}) \right]^* - G^{(0,m/2)}_{E_{12}}(\mathbf{k}_{34}) \right) \left| \langle \mathbf{k}_{34} | \hat{T}^{(1)}_U(E_{12}) | \mathbf{k}_{12} \rangle \right|^2 \\ = 2\int \frac{d\mathbf{k}_{34}}{(2\pi)^3} \langle \mathbf{k}_{12} | \left[\hat{T}^{(1)}_U(E_{12}) \right]^\dagger \left(\hat{G}^\dagger_{0,m/2}(E_{12}) - \hat{G}_{0,m/2}(E_{12}) \right) | \mathbf{k}_{34} \rangle \\ \times \langle \mathbf{k}_{34} | \hat{T}^{(1)}_U(E_{12}) | \mathbf{k}_{12} \rangle \\ = 2 \langle \mathbf{k}_{12} | \left[\hat{T}^{(1)}_U(E_{12}) \right]^\dagger \left(\hat{G}^\dagger_{0,m/2}(E_{12}) - \hat{G}_{0,m/2}(E_{12}) \right) \hat{T}^{(1)}_U(E_{12}) | \mathbf{k}_{12} \rangle \,. \end{aligned} \tag{310}$$

Application of the optical theorem (34) yields in total:

$$\begin{aligned} \int_0^\infty dE_3 \sqrt{E_3}\, f^L_{E_1,E_2,E_3} = -\frac{(4\pi)^2}{\ell_{dis}} \iint \frac{d\mathbf{k}_1 d\mathbf{k}_2}{(2\pi)^6} \, \mathrm{Im} \left\{ \langle \mathbf{k}_{12} | \hat{T}^{(1)}_U(E_{12}) | \mathbf{k}_{12} \rangle \right\} \\ \times \left| G_{E_1}(k_1) \right|^2 \left| G_{E_2}(k_2) \right|^2 . \end{aligned} \tag{311}$$

On the other hand, taking eq. (110) with the T-matrix (31), under the contact approximation (121), and together with the formula $\sqrt{E_2}\left|G_{E_2}(k_2)\right|^2 = \ell_{dis}[G^*_{E_2}(k_2) - G_{E_2}(k_2)]/(2i)$, the integrals over $\mathbf{r}_1$ and $\mathbf{r}_2$ can be conducted:

$$\begin{aligned} -\sqrt{E_2}\, g^L_{E_1,E_2} = -\frac{(4\pi)^2}{\ell_{dis}} \iint \frac{d\mathbf{k}_1 d\mathbf{k}_2}{(2\pi)^6} \left| G_{E_1}(k_1) \right|^2 \mathrm{Im} \Big\{ \langle \mathbf{k}_{12} | \hat{T}^{(1)}_U(E_{12}) | \mathbf{k}_{12} \rangle \\ \times \left[G^*_{E_2}(k_2) - G_{E_2}(k_2) \right] G_{E_2}(k_2) \Big\} . \end{aligned} \tag{312}$$

Taking only the term $|G_{E_2}(k_2)|^2$ in the second line of (312) exactly reproduces (311). The remaining term $[G_{E_2}(k_2)]^2$ gives a negligible contribution in the limit $\sqrt{E_2}\ell_{dis} \gg 1$. Moreover, one can show that this contribution is cancelled by another diagram where an additional disorder correlation function is inserted just before and after the collision, see the discussion in Section 3.3 and also Figs. 1e) and f) in [186]. This proves the conservation of the particle flux in eq. (131).

The second relation for the conservation of the energy flux, see eq. (131), can be shown in almost the same way. Now, when calculating the expression $\int_0^\infty dE_3\; 2\sqrt{E_3}\, E_3\, f^L_{E_1,E_2,E_3}$, eq. (308) is replaced by:

$$\begin{aligned} \int_0^\infty dE_3\; 2\sqrt{E_3} E_3 \left(\frac{G^*_{E_1+E_2-E_3}(k_4) - G_{E_1+E_2-E_3}(k_4)}{2\pi i} \right) \left| G_{E_3}(k_3) \right|^2 \\ \simeq \frac{\ell_{dis}}{2i} \left(\left[G^{(0,m/2)}_{E_{12}}(\mathbf{k}_{34}) \right]^* - G^{(0,m/2)}_{E_{12}}(\mathbf{k}_{34}) \right) \left(E_1 + E_2 + k_3^2 - k_4^2 \right) . \end{aligned} \tag{313}$$

When integrating over $\mathbf{k}_{34}$ as in eq. (310), the term $(k_3^2 - k_4^2)$ vanishes due to symmetry, but the factor $(E_1 + E_2)$ remains. This proves the conservation of the energy flux in eq. (131).

D

DERIVATION OF TRANSPORT EQUATIONS FOR THE SLAB GEOMETRY

We show in detail how one adapts the general transport equations to the slab geometry considered.

D.1 INCOHERENT TRANSPORT – THE LADDER COMPONENT

D.1.1 *The Linear Ladder Component*

We start out with the general linear transport equation derived up to eq. (100):

$$I(\mathbf{r}) = I_0(z) + \int d\mathbf{r}' \, \frac{e^{-|\mathbf{r}-\mathbf{r}'|/\ell_{dis}}}{4\pi\ell_{dis}|\mathbf{r}-\mathbf{r}'|^2} I(\mathbf{r}') \,, \tag{314}$$

and $I_0(z) = I_0 e^{-z/\ell_{dis}}$ as in eq. (102). Because the slab is infinitely stretched in x and y-direction, the intensity is translationally invariant in these directions and (314) can be separated [230]; the relevant contribution $I(z)$ will dependent on the z-coordinate only. Next, we transform $\mathbf{r}'$ to cylindrical coordinates,

$$\mathbf{r}' = \begin{pmatrix} \rho \cos\phi \\ \rho \sin\phi \\ z' \end{pmatrix} \tag{315}$$

and choose the x and y-coordinates of $\mathbf{r}$ (i. e. $x, y = 0$) such that the integral (314) becomes independent of ϕ (i. e. equal to 2π), and the integral over ρ thus reads

$$\int_0^\infty d\rho \, \rho \, \frac{e^{-\sqrt{(z-z')^2+\rho^2}/\ell_{dis}}}{(z-z')^2+\rho^2} = \int_{|z-z'|}^\infty d\rho' \, \frac{e^{-\rho'/\ell_{dis}}}{\rho'} = \Gamma\left[0, \frac{|z-z'|}{\ell_{dis}}\right] , \tag{316}$$

where we chose $\rho' = \sqrt{(z-z')^2+\rho^2}$ and defined the *upper incomplete Gamma function* [225] as

$$\Gamma(a, x) = \int_x^\infty dt \, t^{a-1} e^{-t} \,. \tag{317}$$

For the sake of completeness, we note that other derivations introduce at this point the *exponential integral function* [225]

$$\mathcal{E}_n(x) = \int_1^\infty dt \, t^{-n} e^{-xt} \,, \tag{318}$$

for which $\Gamma(0, x) = E_1(x)$ holds.

Equation (314) now takes following form

$$I(z) = I_0 e^{-z/\ell_{dis}} + \frac{1}{2\ell_{dis}} \int_0^L dz' \, \Gamma\left[0, \frac{|z-z'|}{\ell_{dis}}\right] I(z') \,. \tag{319}$$

The function (317) exhibits a logarithmic divergence for $|z-z'|=0$ which can be avoided (practical for numerical purposes) if we integrate (319) by parts to finally obtain

$$I(z) = I_0 e^{-z/\ell_{dis}} + \frac{1}{2\ell_{dis}} \left[-\left[I(z')g(z-z')\right]_{z'=0}^{z} + \left[I(z')g(z'-z)\right]_{z'=z}^{L} - \int_0^z dz'\, I'(z')g(z-z') + \int_z^L dz'\, I'(z')g(z'-z) \right], \tag{320}$$

where $I'(z)$ denotes the derivative of I with respect to z, and

$$g(x) = \int_0^x dz\, \Gamma(0, z/\ell_{dis}) = \ell_{dis}\left(x\Gamma(0, x/\ell_{dis})/\ell_{dis} - e^{-x/\ell_{dis}} + 1\right) \tag{321}$$

remains finite for $x \to 0$.
Once one has calculated the intensity as a function of the position in the slab, one obtains the bistatic coefficient $\gamma^L_{(lin)}$ [160] under the emission angle θ, i. e. the normalized incoherent intensity at the point of the detector $\mathbf{R}$ in the far field, as a sum of all scattering paths that leave the slab at position $\mathbf{r}$ and directly propagate to $\mathbf{R}$:

$$\gamma^L_{(lin)}(\theta) = \frac{4\pi R^2}{I_0 A} \int d\mathbf{r}\, I(\mathbf{r}) \frac{e^{-|\mathbf{R}-\mathbf{r}|/\ell_{dis}}}{4\pi\ell_{dis}|\mathbf{R}-\mathbf{r}|^2}\,. \tag{322}$$

The bistatic coefficient is normalized with respect to the source intensity I_0, the illuminated slab surface area A transverse to the incident wave, and the distance to the detector. Since the average intensity can solely be expressed as a function of the slab depth z and the angle of emission θ, see eq. (320) and Fig. 7, and noting that the exponential attenuation of the intensity (Lambert-Beer law) occurs only within the slab (and not within the vacuum), we can use the *Fraunhofer approximation* [156] to derive eq. (322) in the far-field of the slab, i. e. for $|\mathbf{R}| \gg |\mathbf{r}|$, as a function of z only:

$$\gamma^L_{(lin)}(\theta) = \frac{1}{I_0\ell_{dis}} \int_0^L dz\, I(z) e^{-z/(\ell_{dis}\cos\theta)}\,. \tag{323}$$

The integration over the remaining coordinates equals the illuminated surface area $\iint dx\,dy = A$, and thus drops out even in the limit $A \to \infty$. For the derivation we also assumed that the source intensity enters the slab perpendicularly.

D.1.2 *The Nonlinear Ladder Component*

As the final figure of merit for the nonlinear case we rather consider the flux density $\mathbf{J}(\mathbf{R})$, see eq. (119), than the density – a distinction which was not crucial for the elastic case, where single-particle energies remained fixed. Hence, eq. (323) for the nonlinear case must be adjusted and thus reads

$$\gamma^L(\theta) = \int dE\, \gamma^L_E(\theta)\,, \tag{324}$$

with the spectral density of $\gamma^L_E(\theta)$ defined as

$$\gamma^L_E(\theta) = \frac{1}{J_0\ell_{dis}} \int_0^L dz\, J_E(z) e^{-z/(\ell_{dis}\cos\theta)}\,. \tag{325}$$

Here, $J_0 = \sqrt{E_L} I_0$, and the flux density $J_E(z)$ within the slab is defined according to (144). The calculation of $J_E(z)$ was in the focus of Chapter 3 and can be computed with the help of eq. (124). Since the disorder mean free path ℓ_{dis} is independent of the energy for a white noise correlated disorder potential, we can equivalently write (324) according to (144), as

$$\gamma^L(\theta) = \frac{1}{J_0 \ell_{dis}} \int_0^L dz\, J(z) e^{-z/(\ell_{dis}\cos\theta)} . \tag{326}$$

D.2 COHERENT TRANSPORT – THE CROSSED COMPONENT

D.2.1 *The Linear Crossed Component*

The linear crossed component is governed by the transport equation (149), i. e.

$$\begin{aligned} C(\mathbf{r},\mathbf{q}) = {} & C_0 e^{-z/(2\ell_{dis})} e^{-z/(2\ell_{dis}\cos\theta)} e^{i\mathbf{q}\mathbf{r}} \\ & + \int d\mathbf{r}' \, \frac{e^{-|\mathbf{r}-\mathbf{r}'|/\ell_{dis}}}{4\pi\ell_{dis}|\mathbf{r}-\mathbf{r}'|^2} C(\mathbf{r}',\mathbf{q}) , \end{aligned} \tag{327}$$

which we now also adapt to the slab geometry. In (327), we used

$$\mathbf{k}_{in} = \begin{pmatrix} 0 \\ 0 \\ k_L \end{pmatrix} , \quad \mathbf{k}_{out} = \begin{pmatrix} k_D \sin\theta' \\ 0 \\ k_D \cos\theta' \end{pmatrix} , \quad \mathbf{q} = \mathbf{k}_{in} + \mathbf{k}_{out} = \begin{pmatrix} k_D \sin\theta \\ 0 \\ k_L - k_D \cos\theta \end{pmatrix} , \tag{328}$$

with the backscattering angle $\theta = \pi - \theta'$ in the spherical representation of $\mathbf{k}_{out}$.

As in the derivation of the corresponding ladder component, we want to obtain an expression for the crossed intensity which only depends on the z-component. Since (327) depends on x and y due to the term $e^{i\mathbf{q}\mathbf{r}}$, we define the transverse Fourier transform

$$\widetilde{C}(z,\mathbf{q}) = e^{-i(q_x x + q_y y)} C(\mathbf{r},\mathbf{q}) , \tag{329}$$

which turns out to be independent of x and y. Eq. (327) thus transforms to the following expression:

$$\begin{aligned} \widetilde{C}(z,\mathbf{q}) = {} & C_0 e^{-z/(2\ell_{dis})} e^{-z/(2\ell_{dis}\cos\theta)} e^{iq_z z} \\ & + \int_0^L dz' \iint d\bar{x}\, d\bar{y} \, \frac{e^{-\sqrt{(z-z')^2+\bar{x}^2+\bar{y}^2}/\ell_{dis}}}{4\pi\ell_{dis}((z-z')^2+\bar{x}^2+\bar{y}^2)} e^{-i(q_x\bar{x}+q_y\bar{y})} \widetilde{C}(z',\mathbf{q}) , \end{aligned} \tag{330}$$

where $\bar{x} = x - x'$ and $\bar{y} = y - y'$.
We again perform the transformation to cylindrical coordinates, see (315), to evaluate the integrals over $\bar{x}$ and $\bar{y}$, and note that

$$\int_0^{2\pi} d\phi \, e^{iq_\perp \rho \cos\phi} = 2\pi J_0(\rho|q_\perp|) , \tag{331}$$

where $q_\perp = \sqrt{q_x^2 + q_y^2}$, and J_0 is the *Bessel function of the first kind* [225]. We now have to integrate the following expression:

$$\frac{1}{2\ell_{dis}} \int_0^L dz' \int_0^\infty d\rho\, \rho \, \frac{e^{-\sqrt{(z-z')^2+\rho^2}/\ell_{dis}}}{(z-z')^2+\rho^2} J_0(\rho|q_\perp|) \widetilde{C}(z',\mathbf{q}) . \tag{332}$$

Even more, we would like to generalize the expression (332), for later convenience, to include also inelastic contributions, i. e. contributions where the single particle wave numbers of counter-propagating scattering amplitudes k and k' are different from each other and different from k_L, and replace $1/\ell_{dis} \to \tilde{q} = 1/\ell_{dis} - i(k - k')$ in the exponent. This gives rise to the crossed component where the solid amplitude propagates with the single-particle energy E (and it is implicitly assumed that the conjugated amplitude has the single-particle energy $\overline{E} = E_L + E_D - E$, see eq. (152)), i. e. $\widetilde{C}(z', \mathbf{q}) \to \widetilde{C}_E(z', \mathbf{q})$. We will show later how to separate the elastic and inelastic component again.
Using eq. (28c) in [231], we replace (332) with

$$\frac{1}{2\ell_{dis}} \int_0^L dz'\, f_E(|z - z'|, q_\perp) \widetilde{C}_E(z', \mathbf{q}) \,, \tag{333}$$

where

$$\begin{aligned} f_E(|z - z'|, q_\perp) &= \int_0^\infty d\rho\, \rho\, \frac{e^{-\tilde{q}\sqrt{(z-z')^2+\rho^2}}}{(z - z')^2 + \rho^2} J_0(\rho |q_\perp|) \\ &= \int_1^\infty dt\, \frac{e^{-\tilde{q}|z-z'|\sqrt{t^2+(q_\perp/\tilde{q})^2}}}{\sqrt{t^2 + (q_\perp/\tilde{q})^2}} \,. \end{aligned} \tag{334}$$

For numerical convenience it is again in order to perform the integral over z' in (333) by parts, for which we introduce the general integral of (334)

$$\begin{aligned} F_E(z - z', q_\perp) &= \int_z^{z'} dz''\, f_E(|z - z''|, q_\perp) \\ &= -\int_1^\infty dt\, \frac{1 - e^{-\tilde{q}(z-z')\sqrt{t^2+(q_\perp/\tilde{q})^2}}}{\tilde{q}(t^2 + (q_\perp/\tilde{q})^2)} \,, \end{aligned} \tag{335}$$

for $z' \leqslant z$, and

$$F_E(z - z', q_\perp) = -F_E(-(z - z'), q_\perp) \,, \tag{336}$$

for $z' > z$. (333) can thus be written as

$$\begin{aligned} &\Big[F_E(z - z')\widetilde{C}_E(z', \mathbf{q})\Big]_{z'=0}^{z'=z} - \Big[F_E(z' - z)\widetilde{C}_E(z', \mathbf{q})\Big]_{z'=z}^{z'=L} \\ &- \int_0^z dz'\, F_E(z - z')\widetilde{C}'_E(z', \mathbf{q}) + \int_z^L dz'\, F_E(z' - z)\widetilde{C}'_E(z', \mathbf{q}) \,, \end{aligned} \tag{337}$$

where $\widetilde{C}'_E(z', \mathbf{q})$ defines the derivative of $\widetilde{C}_E(z', \mathbf{q})$ with respect to z'. Using (336) and $F_E(0) = 0$, we can simplify (337) to

$$\begin{aligned} &- F_E(z)\widetilde{C}_E(0, \mathbf{q}) - F_E(L - z)\widetilde{C}_E(L, \mathbf{q}) \\ &- \int_0^z dz'\, F_E(z - z')\widetilde{C}'_E(z', \mathbf{q}) + \int_z^L dz'\, F_E(z' - z)\widetilde{C}'_E(z', \mathbf{q}) \,. \end{aligned} \tag{338}$$

Replacing the integral (333) by expression (338) and substituting this result in (330), we obtain a general equation for the crossed component within the medium:

$$\begin{aligned} \widetilde{C}_E(z, \mathbf{q}) &= C_0 e^{-z/(2\ell_{dis})} e^{-z/(2\ell_{dis}\cos\theta)} e^{iq_z z} \\ &+ \frac{1}{2\ell_{dis}} \Big[- F_E(z, q_\perp)\widetilde{C}_E(0, \mathbf{q}) - F_E(L - z, q_\perp)\widetilde{C}_E(L, \mathbf{q}) \\ &- \int_0^z dz'\, F_E(z - z', q_\perp)\widetilde{C}_E(z', \mathbf{q}) + \int_z^L dz'\, F_E(z' - z, q_\perp)\widetilde{C}_E(z', \mathbf{q}) \Big] \,. \end{aligned} \tag{339}$$

Note that the elastic contribution $\widetilde{C}(z,\mathbf{q})$ is obtained from (339) for $E = (E_L + E_D)/2 \Leftrightarrow E = \overline{E}$, i.e. $\widetilde{q} = 1/\ell_{dis}$, see e.g. (334). If additionally $\theta = 0$, i.e. in exact backscattering direction, also $q_\perp = 0$ and (334) and (335) become, respectively (see (317) and (321)):

$$\begin{aligned} f_{\frac{E_L+E_D}{2}}(|z-z'|, q_\perp = 0) &= \int_1^\infty dt\, \frac{e^{-\widetilde{q}|z-z'|t}}{t} = \Gamma\left[0, \frac{|z-z'|}{\ell_{dis}}\right], \\ F_{\frac{E_L+E_D}{2}}(z-z', q_\perp = 0) &= -g(z-z') \quad \text{for} \quad z \geqslant z'. \end{aligned} \tag{340}$$

This limit also corresponds to $q_z = 0$, and the linear elastic crossed contribution in backscattering direction becomes indistinguishable from the corresponding ladder contribution (cf. eq. (320)):

$$\begin{aligned} \widetilde{C}(z,0) = C(z,0) &= C_0 e^{-z/\ell_{dis}} \\ &+ \frac{1}{2\ell_{dis}}\left[g(z)C(0,0) + g(L-z)C(L,0)\right. \\ &\left. + \int_0^z dz'\, g(z-z')C'(z',0) - \int_z^L dz'\, g(z'-z)C'(z',0)\right]. \end{aligned} \tag{341}$$

Therefore, as expected for the case of linear transport theory, the backscattered intensity will be enhanced by a factor of two (after subtracting the single-scattering contribution) [232].

The linear crossed bistatic coefficient as a function of the backscattering angle is derived just as eq. (323), with the only difference that now one scattering amplitude exits the slab under an angle of θ, and the other perpendicularly:

$$\begin{aligned} \gamma^C_{(lin)}(\theta) = \frac{1}{C_0\ell_{dis}} \int_0^L dz \Big[&\widetilde{C}(z,\mathbf{q}) e^{-z(1+1/\cos\theta)/(2\ell_{dis})} e^{-iq_z z} \\ &- \widetilde{C}_0(z,\mathbf{q}) e^{-z(1+1/\cos\theta)/(2\ell_{dis})} e^{-iq_z z}\Big]. \end{aligned} \tag{342}$$

with $\widetilde{C}_0(z,\mathbf{q}) = e^{-z(1+1/\cos\theta)/(2\ell_{dis})} e^{iq_z z}$. We again stress that, in exact backscattering direction, and except for the subtracted single scattering contribution (second line in the integral above), one cannot differentiate whether the elastic scattering contribution results from an incoherent or a coherent process, respectively (323) and (342), since the source intensities $I_0 = C_0 = \rho_0$, as well as the intensities within the medium, $\widetilde{C}(z,0) = C(z,0) = I(z)$, see eq. (341), are equal.

D.2.2 *The Nonlinear Crossed Component*

In eq. (339) of the previous section we already stated the linear equation responsible for the transport of counter-propagating amplitudes with different energies, as a result of inelastic scattering. Hence, in order to transform eqs. (162) and (163) in Chapter 4 to a form such they depend on z and θ only, we first have to replace the linear crossed propagation in the first lines of eqs. (162) and (163) by eq. (339), under consideration of $\widetilde{C}^{(1,2)}_E(z,\mathbf{q}) = C^{(1,2)}_E(\mathbf{r},\mathbf{q}) e^{-i(q_x x + q_y y)}$, respectively. The collision terms, i.e. the second and third lines of eqs. (162) and (163), are unaffected by this transformation as the phase factors cancel each other due to the con-

tact interaction approximation, cf. eq. (161). Thus, eqs. (162) and (163) read, respectively:

$$\begin{aligned}\widetilde{C}_E^{(1)}(z,\mathbf{q}) &= C_0 e^{-z/(2\ell_{\text{dis}})} e^{-z/(2\ell_{\text{dis}}\cos\theta)} e^{iq_z z}\,\delta(E-E_L)\\ &+\frac{1}{2\ell_{\text{dis}}}\Bigg[-F_E(z,q_\perp)\widetilde{C}_E^{(1)}(0,\mathbf{q})-F_E(L-z,q_\perp)\widetilde{C}_E^{(1)}(L,\mathbf{q})\\ &-\int_0^z dz'\,F_E(z-z',q_\perp)\widetilde{C}_E^{(1)}(z',\mathbf{q})+\int_z^L dz'\,F_E(z'-z,q_\perp)\widetilde{C}_E^{(1)}(z',\mathbf{q})\Bigg]\\ &+\int_0^\infty dE'\left[\left(g^C_{E',E}+\left[g^C_{E',\overline{E}}\right]^*\right)\widetilde{C}_E^{(1)}(z,\mathbf{q})+\int_0^{E_q} dE''\,f^C_{E',E'',E}\widetilde{C}_{E''}^{(1)}(z,\mathbf{q})\right] I_{E'}(z)\\ &+\int_0^{E_q} dE'\left[h^C_{\overline{E},\overline{E'}}\right]^*\widetilde{C}_{E'}^{(1)}(z,\mathbf{q})I_E(z)\,,\end{aligned}\tag{343}$$

$$\begin{aligned}\widetilde{C}_E^{(2)}(z,\mathbf{q}) &= \frac{1}{2\ell_{\text{dis}}}\Bigg[-F_E(z,q_\perp)\widetilde{C}_E^{(2)}(0,\mathbf{q})-F_E(L-z,q_\perp)\widetilde{C}_E^{(2)}(L,\mathbf{q})\\ &-\int_0^z dz'\,F_E(z-z',q_\perp)\widetilde{C}_E^{(2)}(z',\mathbf{q})+\int_z^L dz'\,F_E(z'-z,q_\perp)\widetilde{C}_E^{(2)}(z',\mathbf{q})\Bigg]\\ &+\int_0^\infty dE'\left[\left(g^C_{E',E}+\left[g^C_{E',\overline{E}}\right]^*\right)\widetilde{C}_E^{(2)}(z,\mathbf{q})+\int_0^{E_q} dE''f^C_{E',E'',E}\widetilde{C}_{E''}^{(2)}(z,\mathbf{q})\right] I_{E'}(z)\\ &+\int_0^{E_q} dE' h^C_{E',E}\left(\widetilde{C}_{E'}^{(1)}(z,\mathbf{q})+\widetilde{C}_{E'}^{(2)}(z,\mathbf{q})\right) I_{\overline{E'}}(z)\,.\end{aligned}\tag{344}$$

As for the nonlinear bistatic coefficient of the crossed component, the final figure of merit is determined by the flux density, see eq. (171). Upon normalization of this quantity with respect to the incoming flux and the distance to the detector, we obtain

$$\gamma^C(\theta)=\int dE_D\,\gamma^C_{E_D}(\theta)\,,\tag{345}$$

where the spectrum of $\gamma^C_{E_D}(\theta)$ with detected energy E_D is defined as

$$\begin{aligned}\gamma^C_{E_D}(\theta) &= \frac{1}{J_0^C\,\ell_{\text{dis}}}\int_0^L dz\; e^{-z(1+1/\cos\theta)/(2\ell_{\text{dis}})}e^{-iq_z z}\\ &\times\left[\sqrt{E_D}\,\widetilde{C}_{E_D}^{(1)}(z,\mathbf{q})+\sqrt{E_D}\,\widetilde{C}_{E_D}^{(2)}(z,\mathbf{q})-\sqrt{E_L}\widetilde{C}_0(z,\mathbf{q})\right]\,,\end{aligned}\tag{346}$$

with $J_0^C=\sqrt{E_L}C_0$.

E

COMPUTATION OF USEFUL INTEGRALS

We summarize the rigorous calculation of the integrals referred to in Fig. 15 in Chapter 3. For the case of Fig. 15, all Green's functions are evaluated at the same single-particle energy $E = k^2$. We therefore suppress the explicit energy dependence of the Green's functions in this appendix.

- First we treat the integral over an intermediate point where two average Green's functions (93) are connected:

$$\begin{aligned}
&\int d\mathbf{r}_3\, G(\mathbf{r}_1-\mathbf{r}_3)G(\mathbf{r}_3-\mathbf{r}_2) = \int d\mathbf{r}_3\, G(\mathbf{r}_{13})G(\mathbf{r}_{32}) \\
&= \int d\mathbf{r}_{13}\, G(\mathbf{r}_{13})G(\mathbf{r}_{32}) \\
&= \frac{1}{(4\pi)^2}\int d\mathbf{r}_{13}\, \frac{e^{i\widetilde{k}(r_{13}+|\mathbf{r}_{12}-\mathbf{r}_{13}|)}}{r_{13}|\mathbf{r}_{12}-\mathbf{r}_{13}|} \\
&= \frac{1}{8\pi}\int dr_{13}\, r_{13}\int d\cos(\theta)\, \frac{e^{i\widetilde{k}(r_{13}+|\mathbf{r}_{12}-\mathbf{r}_{13}|)}}{|\mathbf{r}_{12}-\mathbf{r}_{13}|} \\
&= \frac{-1}{8\pi r_{12}}\int dr_{13}\, e^{i\widetilde{k}r_{13}}\int_{r_{12}+r_{13}}^{|r_{12}-r_{13}|} dy\, e^{i\widetilde{k}y}\,,
\end{aligned}$$

  with $\widetilde{k} = k + i/(2\ell_{\text{dis}})$ as in eq. (83). Furthermore, we introduced spherical coordinates, defined $y = |\mathbf{r}_{12}-\mathbf{r}_{13}|$, and $d\cos(\theta) = -y dy/(r_{12}r_{13})$, such that the integration over y can be performed immediately:

$$\begin{aligned}
&= \frac{i}{8\pi\widetilde{k}r_{12}}\int_0^\infty dr_{13}\, e^{i\widetilde{k}r_{13}}\left[e^{i\widetilde{k}(r_{12}+r_{13})} - e^{i\widetilde{k}|r_{12}-r_{13}|}\right] \\
&= \frac{-i}{8\pi\widetilde{k}}e^{i\widetilde{k}r_{12}} = \frac{ir_{12}}{2\widetilde{k}}G(\mathbf{r}_{12}) = \frac{ir_{12}}{2\widetilde{k}}G(\mathbf{r}_1-\mathbf{r}_2)\,, \qquad (347)
\end{aligned}$$

  For the integration over r_{13} we used that $\mathrm{Im}[\widetilde{k}] > 0$, to ensure convergence of the integral at infinity.

- The same result holds for the vacuum Green's functions (73) under the replacement $k \to k + i\varepsilon$ and subsequent limit $\varepsilon \to 0$:

$$\begin{aligned}
&\int d\mathbf{r}_3\, G_0(\mathbf{r}_1-\mathbf{r}_3)G_0(\mathbf{r}_3-\mathbf{r}_2) \\
&= \frac{1}{(4\pi)^2}\lim_{\varepsilon\to 0}\int d\mathbf{r}_{13}\, \frac{e^{i(k+i\epsilon)(r_{13}+|\mathbf{r}_{12}-\mathbf{r}_{13}|)}}{r_{13}|\mathbf{r}_{12}-\mathbf{r}_{13}|} \\
&= \frac{ir_{12}}{2k}G_0(\mathbf{r}_1-\mathbf{r}_2)\,. \qquad (348)
\end{aligned}$$

- The integration procedure remains the same if one replaces one of the Green's functions by its complex conjugate:

$$\begin{aligned}
&\int d\mathbf{r}_3\, G^*(\mathbf{r}_1-\mathbf{r}_3)G(\mathbf{r}_3-\mathbf{r}_2)\\
&= \frac{1}{(4\pi)^2}\int d\mathbf{r}_{13}\,\frac{e^{i\widetilde{k}r_{13}-i\widetilde{k}^*|\mathbf{r}_{12}-\mathbf{r}_{13}|}}{r_{13}|\mathbf{r}_{12}-\mathbf{r}_{13}|}\\
&= \frac{i\ell_{dis}}{2k}\left(G^*(\mathbf{r}_{12})-G(\mathbf{r}_{12})\right) = \frac{\ell_{dis}}{4\pi k}\frac{\sin(kr_{12})}{r_{12}}\,,
\end{aligned} \tag{349}$$

  where $\widetilde{k}^* = k - i/(2\ell_{dis})$.

- Integration over common points of origin always appears when the two Green's functions originate from the same correlated disorder event. We hence multiply by the correlation factor $4\pi/\ell_{dis}$ and obtain

$$\frac{4\pi}{\ell_{dis}}\int d\mathbf{r}\, G(\mathbf{r})G(\mathbf{r}) = \frac{4\pi}{1-2ik\ell_{dis}}\,, \tag{350}$$

  and

$$\frac{4\pi}{\ell_{dis}}\int d\mathbf{r}\, G^*(\mathbf{r})G(\mathbf{r}) = \int d\mathbf{r}\, P(\mathbf{r}) = 1\,. \tag{351}$$

BIBLIOGRAPHY

[1] S. Chandrasekhar. *Radiative Transfer*. Dover Publications, New York, 1960.

[2] P. A. Lee and T. V. Ramakrishnan. Disordered electronic systems. *Rev. Mod. Phys.*, 57:287–337, 1985.

[3] J. Nelson. *The physics of solar cells*. Imperial College Press, London, 2003.

[4] G. D. Scholes, T. Mirkovic, D. B. Turner, F. Fassioli, and A. Buchleitner. Solar light harvesting by energy transfer: from ecology to coherence. *Energy Environ. Sci.*, 5:9374–9393, 2012.

[5] L. Erdös. Lecture notes on quantum Brownian motion. In J. Fröhlich, M. Salmhofer, V. Mastropietro, W. de Roeck, and L. F. Cugliandolo, editors, *Quantum Theory from Small to Large Scales*, Oxford University Press, Oxford. 2012.

[6] G. S. Ohm. *Die galvanische Kette, mathematisch bearbeitet*. Rieman, Berlin, 1827.

[7] P. Drude. Zur Elektronentheorie der Metalle. *Ann. d. Physik*, 306:566–613, 1900.

[8] P. Drude. Zur Elektronentheorie der Metalle; II. Teil. Galvanomagnetische und thermomagnetische Effecte. *Ann. d. Physik*, 308:369–402, 1900.

[9] R. Brown. A brief account of microscopical observations made in the months of June, July and August, 1827, on the particles contained in the pollen of plants; and on the general existence of active molecules in organic and inorganic bodies. *Edinburgh new Philosophical Journal*, 358-371, 1928.

[10] A. Einstein. Über die von der molekularkinetischen Theorie der Wärme geforderte Bewegung von in ruhenden Flüssigkeiten suspendierten Teilchen. *Ann. d. Physik*, 322:549, 1905.

[11] M. von Smoluchowski. Zur kinetischen Theorie der Brownschen Molekularbewegung und der Suspensionen. *Ann. d. Physik*, 326:756–780, 1906.

[12] J. Perrin. Mouvement brownien et réalité moléculaire. *Annales de Chimie et de Physique*, 18:5–104, 1909.

[13] K. Huang. *Statistical Mechanics*. John Wiley and Sons, New York, 2nd edition, 1987.

[14] M. Lewenstein, A. Sanpera, V. Ahufinger, B. Damski, A. Sen(De), and U. Sen. Ultracold atomic gases in optical lattices: mimicking condensed matter physics and beyond. *Adv. Phys.*, 56:243–379, 2007.

[15] C. D'Errico, M. Moratti, E. Lucioni, L. Tanzi, B. Deissler, M. Inguscio, G. Modugno, M. B. Plenio, and F. Caruso. Quantum diffusion with disorder, noise and interaction. *New. J. Phys.*, 15:045007, 2013.

[16] A. Polkovnikov, K. Sengupta, A. Silva, and M. Vengalattore. *Colloquium* : Nonequilibrium dynamics of closed interacting quantum systems. *Rev. Mod. Phys.*, 83:863–883, 2011.

[17] P. W. Anderson. Absence of Diffusion in Certain Random Lattices. *Phys. Rev.*, 109:1492, 1958.

[18] E. Abrahams, P .W. Anderson, D. C. Licciardello, and T. V. Ramakrishnan. Scaling Theory of Localization: Absence of Quantum Diffusion in Two Dimensions. *Phys. Rev. Lett.*, 42:673, 1979.

[19] A. F. Ioffe and A. R. Regel. Non-crystalline, amorphous and liquid electronic semiconductors. *Prog. Semicond.*, 4:237, 1960.

[20] D. S. Wiersma, P. Bartolini, A. Lagendijk, and R. Righini. Localization of light in a disordered medium. *Nature*, 390:671, 1997.

[21] H. Hu, A. Strybulevych, J. H. Page, S. E. Skipetrov, and B. A. van Tiggelen. Localization of ultrasound in a three-dimensional elastic network. *Nat. Phys.*, 4:945, 2008.

[22] J. Billy, V. Josse, Z. Zuo, A. Bernard, B. Hambrecht, P. Lugan, D. Clement, L. Sanchez-Palencia, P. Bouyer, and A. Aspect. Direct observation of Anderson localization of matter waves in a controlled disorder. *Nature*, 453:881, 2008.

[23] G. Roati, C. D'Errico, L. Fallani, M. Fattori, C. Fort, M. Zaccanti, G. Modugno, M. Modugno, and M. Inguscio. Anderson localization of a non-interacting Bose-Einstein condensate. *Nature*, 453:895, 2008.

[24] F. Jendrzejewski, A. Bernard, K. Müller, P. Cheinet, V. Josse, M. Piraud, L. Pezze, L. Sanchez-Palencia, A. Aspect, and P. Bouyer. Three-dimensional localization of ultracold atoms in an optical disordered potential. *Nat. Phys.*, 8:398–403, 2012.

[25] S. S. Kondov, W. R. McGehee, J. J. Zirbel, and B. DeMarco. Three-Dimensional Anderson Localization of Ultracold Matter. *Science*, 334:66–68, 2011.

[26] J. E. Bayfield, G. Casati, I. Guarneri, and D. W. Sokol. Localization of classically chaotic diffusion for hydrogen atoms in microwave fields. *Phys. Rev. Lett.*, 63:364–367, 1989.

[27] M. Arndt, A. Buchleitner, R. N. Mantegna, and H. Walther. Experimental study of quantum and classical limits in microwave ionization of rubidium Rydberg atoms. *Phys. Rev. Lett.*, 67:2435–2438, 1991.

[28] D. L. Shepelyansky. Coherent propagation of two interacting particles in a random potential. *Phys. Rev. Lett.*, 73:2607–2610, 1994.

[29] A. S. Pikovsky and D. L. Shepelyansky. Destruction of Anderson Localization by a Weak Nonlinearity. *Phys. Rev. Lett.*, 100:094101, 2008.

[30] M. V. Ivanchenko, T. V. Laptyeva, and S. Flach. Anderson localization or nonlinear waves: A matter of probability. *Phys. Rev. Lett.*, 107:240602, 2011.

[31] E. Lucioni, B. Deissler, L. Tanzi, G. Roati, M. Zaccanti, M. Modugno, M. Larcher, F. Dalfovo, M. Inguscio, and G. Modugno. Observation of subdiffusion in a disordered interacting system. *Phys. Rev. Lett.*, 106:230403, 2011.

[32] D. M. Basko, I. L. Aleiner, and B. L. Altshuler. Metal–insulator transition in a weakly interacting many-electron system with localized single-particle states. *Annals of Physics*, 321:1126 – 1205, 2006.

[33] A. Aspect and M. Inguscio. Anderson localization of ultracold atoms. *Physics Today*, 62:30–35, 2009.

[34] Ad Lagendijk, B. van Tiggelen, and D. S. Wiersma. Fifty years of Anderson localization. *Physics Today*, 62:24–29, 2009.

[35] L. Pezzé, M. Robert de Saint-Vincent, T. Bourdel, J.-P. Brantut, B. Allard, T. Plisson, A. Aspect, P. Bouyer, and L. Sanchez-Palencia. Regimes of classical transport of cold gases in a two-dimensional anisotropic disorder. *New J. Phys.*, 13:095015, 2011.

[36] J.-P. Brantut, J. Meineke, D. Stadler, S. Krinner, and T. Esslinger. Conduction of ultracold fermions through a mesoscopic channel. *Science*, 337:1069–1071, 2012.

[37] S. Flach, D. O. Krimer, and Ch. Skokos. Universal spreading of wave packets in disordered nonlinear systems. *Phys. Rev. Lett.*, 102:024101, 2009.

[38] K. Huang and H. Meng. Hard-sphere Bose gas in random external potentials. *Phys. Rev. Lett.*, 69:644–647, 1992.

[39] A. V. Lopatin and V. M. Vinokur. Thermodynamics of the Superfluid Dilute Bose Gas with Disorder. *Phys. Rev. Lett.*, 88:235503, 2002.

[40] P. Lugan, D. Clément, P. Bouyer, A. Aspect, M. Lewenstein, and L. Sanchez-Palencia. Ultracold Bose Gases in 1D Disorder: From Lifshits Glass to Bose-Einstein Condensate. *Phys. Rev. Lett.*, 98:170403, 2007.

[41] P. Lugan and L. Sanchez-Palencia. Localization of Bogoliubov quasiparticles in interacting Bose gases with correlated disorder. *Phys. Rev. A*, 84:013612, 2011.

[42] T. Paul, P. Leboeuf, N. Pavloff, K. Richter, and P. Schlagheck. Nonlinear transport of Bose-Einstein condensates through waveguides with disorder. *Phys. Rev. A*, 72:063621, 2005.

[43] T. Paul, M. Hartung, K. Richter, and P. Schlagheck. Nonlinear transport of Bose-Einstein condensates through mesoscopic waveguides. *Phys. Rev. A*, 76:063605, 2007.

[44] M. Hartung, T. Wellens, C. A. Müller, K. Richter, and P. Schlagheck. Coherent Backscattering of Bose-Einstein Condensates in Two-Dimensional Disorder Potentials. *Phys. Rev. Lett.*, 101:020603, 2008.

[45] C. Weiss and Y. Castin. Elastic scattering of a quantum matter-wave bright soliton on a barrier. *Phys. A*, 45:455306, 2012.

[46] R. G. Scott and D. A. W. Hutchinson. Incoherence of Bose-Einstein condensates at supersonic speeds due to quantum noise. *Phys. Rev. A*, 78:063614, 2008.

[47] T. Ernst, T. Paul, and P. Schlagheck. Transport of ultracold Bose gases beyond the Gross-Pitaevskii description. *Phys. Rev. A*, 81:013631, 2010.

[48] E. Akkermans and G. Montambaux. *Mesoscopic Physics of Electrons and Photons*. Cambridge University Press, Cambridge, UK, 2007.

[49] G. Bergmann. Proximity Effect in Weak Localization. *Phys. Rev. Lett.*, 53:1100, 1984.

[50] D. U. Sharvin and Y. U. V. Sharvin. Magnetic Flux Quantization in a Cylindrical Film of a Normal Metal. *J. Exp. Theor. Phys. Lett.*, 34:272, 1981.

[51] G. Müller. Helligkeitsbestimmungen der großen Planeten und einiger Asteroiden. *Public. d. Astrophysikalischen Observatoriums zu Potsdam*, 30:198, 1893.

[52] A. Tourin, A. Derode, P. Roux, B. A. van Tiggelen, and M. Fink. Time-Dependent Coherent Backscattering of Acoustic Waves. *Phys. Rev. Lett.*, 79:3637, 1997.

[53] P.-E. Wolf and G. Maret. Weak Localization and Coherent Backscattering of Photons in Disordered Media. *Phys. Rev. Lett.*, 55:2696, 1985.

[54] G. Labeyrie, F. de Tomasi, J.-C. Bernard, C. A. Müller, C. Miniatura, and R. Kaiser. Coherent Backscattering of light by cold atoms. *Phys. Rev. Lett.*, 83:5266, 1999.

[55] F. Jendrzejewski, K. Müller, J. Richard, A. Date, T. Plisson, P. Bouyer, A. Aspect, and V. Josse. Coherent backscattering of ultracold atoms. *Phys. Rev. Lett.*, 109:195302, 2012.

[56] G. Labeyrie, T. Karpiuk, J.-F. Schaff, B. Grémaud, C. Miniatura, and D. Delande. Enhanced backscattering of a dilute Bose-Einstein condensate. *Europhys. Lett.*, 100:66001, 2012.

[57] A. A. Golubentsev. The suppression of interference effects in the multiple scattering of light. *J. Exp. Theor. Phys.*, 86:47, 1984.

[58] C. A. Müller and C. Miniatura. Multiple scattering of light by atoms with internal degeneracy. *Phys A*, 35:10163, 2002.

[59] T. Chanelière, D. Wilkowski, Y. Bidel, R. Kaiser, and C. Miniatura. Saturation induced coherence loss in coherent backscattering of light. *Phys. Rev. E*, 70:036602, 2004.

[60] V. Shatokhin, C. A. Müller, and A. Buchleitner. Elastic versus inelastic coherent backscattering of laser light by cold atoms: A master equation treatment. *Phys. Rev. A*, 73:063813, 2006.

[61] T. Wellens, B. Grémaud, D. Delande, and C. Miniatura. Coherent backscattering of light with nonlinear atomic scatterers. *Phys. Rev. A*, 73:013802, 2006.

[62] T. Wellens. Nonlinear coherent backscattering. *Appl. Phys. B*, 95:189, 2009.

[63] N. Cherroret, T. Karpiuk, C. A. Müller, B. Grémaud, and C. Miniatura. Coherent backscattering of ultracold matter waves: Momentum space signatures. *Phys. Rev. A*, 85:011604, 2012.

[64] F. Dalfovo, S. Giorgini, L. P. Pitaevskii, and S. Stringari. Theory of Bose-Einstein condensation in trapped gases. *Rev. Mod. Phys.*, 71:463–512, 1999.

[65] H. Spohn. *Large scale dynamics of interacting particles*. Springer-Verlag, Berlin, 1991.

[66] P. Gaspard. *Chaos, Scattering and Statistical Mechanics*. Cambridge University Press, New York, 1998.

[67] J. M. Deutsch. Quantum statistical mechanics in a closed system. *Phys. Rev. A*, 43:2046–2049, 1991.

[68] M. Srednicki. Chaos and quantum thermalization. *Phys. Rev. E*, 50:888–901, 1994.

[69] T. Kinoshita, T. Wenger, and D. S. Weiss. A quantum Newton's cradle. *Nature*, 440:900–903, 2006.

[70] G. P. Berman, F. Borgonovi, F. M. Izrailev, and A. Smerzi. Irregular Dynamics in a One-Dimensional Bose System. *Phys. Rev. Lett.*, 92:030404, 2004.

[71] M. Rigol, V. Dunjko, and M. Olshanii. Thermalization and its mechanism for generic isolated quantum systems. *Nature*, 452:854–858, 2008.

[72] C. Gogolin, M. P. Müller, and J. Eisert. Absence of thermalization in nonintegrable systems. *Phys. Rev. Lett.*, 106:040401, 2011.

[73] J. Hämmerling, B. Gutkin, and T. Guhr. Collective vs. single-particle motion in quantum many-body systems: Spreading and its semiclassical interpretation in the perturbative regime. *Europhys. Lett.*, 96:20007, 2011.

[74] R. Dorner, J. Goold, C. Cormick, M. Paternostro, and V. Vedral. Emergent thermodynamics in a quenched quantum many-body system. *Phys. Rev. Lett.*, 109:160601, 2012.

[75] B. Shapiro. Cold atoms in the presence of disorder. *Phys A*, 45:143001, 2012.

[76] S. N. Bose. Plancks Gesetz und Lichtquantenhypothese. *Zeitschrift für Physik*, 26:178–181, 1924.

[77] A. Einstein. Quantentheorie des einatomigen idealen Gases. *Sitzungsberichte der Preussischen Akademie der Wissenschaften*, 1:261, 1924.

[78] M. H. Anderson, J. R. Ensher, M. R. Matthews, C. E. Wieman, and E. A. Cornell. Observation of Bose-Einstein Condensation in a Dilute Atomic Vapor. *Science*, 269:198–201, 1995.

[79] K. B. Davis, M. O. Mewes, M. R. Andrews, N. J. van Druten, D. S. Durfee, D. M. Kurn, and W. Ketterle. Bose-Einstein Condensation in a Gas of Sodium Atoms. *Phys. Rev. Lett.*, 75:3969–3973, 1995.

[80] R. P. Feynman. Simulating physics with computers. *International Journal of Theoretical Physics*, 21:467–488, 1982.

[81] W. J. Mullin and A. R. Sakhel. Generalized Bose-Einstein Condensation. *J. Low Temp. Phys.*, 166:125–150, 2012.

[82] O. Penrose and L. Onsager. Bose-Einstein Condensation and Liquid Helium. *Phys. Rev.*, 104:576–584, 1956.

[83] E. H. Lieb, R. Seiringer, J. P. Solovej, and J. Yngvason. *The mathematics of the Bose gas and its condensation*. Birkhäuser, Basel, 2005.

[84] J. R. Taylor. *Scattering Theory: The Quantum Theory on Nonrelativistic Collisions*. John Wiley and Sons, New York, 1972.

[85] S. Flach, K. Kladko, and R. S. MacKay. Energy Thresholds for Discrete Breathers in One-, Two-, and Three-Dimensional Lattices. *Phys. Rev. Lett.*, 78:1207–1210, 1997.

[86] M. Inguscio, S. Stringari, and C. E. Wieman, editors. *Bose-Einstein Condensation in Atomic Gases*. Proc. Int. School of Physics Enrico Fermi. Italian Physical Society, 1999.

[87] L. Pitaevskii and S. Stringari. *Bose-Einstein Condensation*. Oxford University Press, Oxford, 2003.

[88] M. R. Andrews, C. G. Townsend, H.-J. Miesner, D. S. Durfee, D. M. Kurn, and W. Ketterle. Observation of interference between two Bose condensates. *Science*, 275:637–641, 1997.

[89] M.-O. Mewes, M. R. Andrews, D. M. Kurn, D. S. Durfee, C. G. Townsend, and W. Ketterle. Output Coupler for Bose-Einstein Condensed Atoms. *Phys. Rev. Lett.*, 78:582–585, 1997.

[90] I. Bloch, T. W. Hänsch, and T. Esslinger. Atom laser with a cw output coupler. *Phys. Rev. Lett.*, 82:3008–3011, 1999.

[91] Max-Planck Institute for Quantum Optics. `http://www.quantum-munich.de/fileadmin/media/media/atomlaser/alas3d_3.jpg`, accessed at 12.02.2013.

[92] W. Guerin, J.-F. Riou, J. P. Gaebler, V. Josse, P. Bouyer, and A. Aspect. Guided quasicontinuous atom laser. *Phys. Rev. Lett.*, 97:200402, 2006.

[93] A. Couvert, M. Jeppesen, T. Kawalec, G. Reinaudi, R. Mathevet, and D. Guéry-Odelin. A quasi-monomode guided atom laser from an all-optical Bose-Einstein condensate. *Europhys. Lett.*, 83:50001, 2008.

[94] G. L. Gattobigio, A. Couvert, M. Jeppesen, R. Mathevet, and D. Guéry-Odelin. Multimode-to-monomode guided-atom lasers: An entropic analysis. *Phys. Rev. A*, 80:041605, 2009.

[95] G. Kleine Büning, J. Will, W. Ertmer, C. Klempt, and J. Arlt. A slow gravity compensated atom laser. *Appl. Phys. B*, 100:117–123, 2010.

[96] R. G. Dall, S. S. Hodgman, M. T. Johnsson, K. G. H. Baldwin, and A. G. Truscott. Transverse mode imaging of guided matter waves. *Phys. Rev. A*, 81:011602, 2010.

[97] F. Vermersch, C. M. Fabre, P. Cheiney, G. L. Gattobogio, R. Mahevet, and D. Guéry-Odelin. Guided-atom laser: Transverse mode quality and longitudinal momentum distribution. *Phys. Rev. A*, 84:043618, 2011.

[98] G. L. Gattobigio, A. Couvert, B. Georgeot, and D. Guéry-Odelin. Exploring classically chaotic potentials with a matter wave quantum probe. *Phys. Rev. Lett.*, 107:254104, 2011.

[99] J. Fortágh and C. Zimmermann. Magnetic microtraps for ultracold atoms. *Rev. Mod. Phys.*, 79:235–289, 2007.

[100] J. Dalibard. Collisional dynamics of ultra-cold atomic gases. In M. Inguscio, S. Stringari, and C. E. Wieman, editors, *Bose-Einstein Condensation in Atomic Gases*, Proc. Int. School of Physics Enrico Fermi, IOS Press, Amsterdam. 1999.

[101] B. A. Lippmann and J. Schwinger. Variational principles for scattering processes. *Phys. Rev.*, 79:469–480, 1950.

[102] E. Tiesinga, B. J. Verhaar, and H. T. C. Stoof. Threshold and resonance phenomena in ultracold ground-state collisions. *Phys. Rev. A*, 47:4114–4122, 1993.

[103] S. Inouye, M. R. Andrews, J. Stenger, H.-J. Miesner, D. M. Stamper-Kurn, and W. Ketterle. Observation of Feshbach resonances in a Bose-Einstein condensate. *Nature*, 392:151–154, 1998.

[104] E. Timmermans, P. Tommasini, M. Hussein, and A. Kerman. Feshbach resonances in atomic Bose-Einstein condensates. *Phys. Reports*, 315:199 – 230, 1999.

[105] T. Köhler, K. Góral, and P. S. Julienne. Production of cold molecules via magnetically tunable Feshbach resonances. *Rev. Mod. Phys.*, 78:1311–1361, 2006.

[106] J. E. Lye, L. Fallani, C. Fort, V. Guarrera, M. Modugno, D. S. Wiersma, and M. Inguscio. Effect of interactions on the localization of a Bose-Einstein condensate in a quasiperiodic lattice. *Phys. Rev. A*, 75:061603, 2007.

[107] G. Roati, M. Zaccanti, C. D'Errico, J. Catani, M. Modugno, A. Simoni, M. Inguscio, and G. Modugno. ^{39}K Bose-Einstein Condensate with Tunable Interactions. *Phys. Rev. Lett.*, 99:010403, 2007.

[108] M. Inguscio, W. Ketterle, and C. Salomon, editors. *Ultra-cold Fermi Gases*. Proc. Int. School of Physics Enrico Fermi. IOS Press, 2008.

[109] J. Bardeen, L. N. Cooper, and J. R. Schrieffer. Theory of Superconductivity. *Phys. Rev.*, 108:1175–1204, 1957.

[110] C. J. Pethick and H. Smith. *Bose-Einstein condensation in dilute gases*. Cambridge University Press, 2nd edition, 2008.

[111] L. Fallani, C. Fort, and M. Inguscio. Bose–Einstein Condensates in Disordered Potentials. In E. Arimondo et al., editor, *Advances in Atomic, Molecular, and Optical Physics*, volume 56, pages 119 – 160. Academic Press, 2008.

[112] L. Sanchez-Palencia and M. Lewenstein. Disordered quantum gases under control. *Nat. Phys.*, 6:87–95, 2010.

[113] U. Gavish and Y. Castin. Matter-wave localization in disordered cold atom lattices. *Phys. Rev. Lett.*, 95:020401, 2005.

[114] B. Gadway, D. Pertot, J. Reeves, M. Vogt, and D. Schneble. Glassy behavior in a binary atomic mixture. *Phys. Rev. Lett.*, 107:145306, 2011.

[115] M. Giglio, M. Carpineti, and A. Vailati. Space intensity correlations in the near field of the scattered light: A direct measurement of the density correlation function $g(r)$. *Phys. Rev. Lett.*, 85:1416–1419, 2000.

[116] A. Gatti, D. Magatti, and F. Ferri. Three-dimensional coherence of light speckles: Theory. *Phys. Rev. A*, 78:063806, 2008.

[117] R. C. Kuhn, O. Sigwarth, C. Miniatura, D. Delande, and C. A. Müller. Coherent matter wave transport in speckle potentials. *New J. Phys.*, 9:161, 2007.

[118] D. Clément, A. F. Varón, J. A. Retter, L. Sanchez-Palencia, A. Aspect, and P. Bouyer. Experimental study of the transport of coherent interacting matter-waves in a 1d random potential induced by laser speckle. *New J. Phys.*, 8:165, 2006.

[119] N. P. Proukakis and B. Jackson. Finite-temperature models of Bose–Einstein condensation. *J. Phys. B*, 41:203002, 2008.

[120] C. Gaul and C. A. Müller. Bogoliubov excitations of disordered Bose-Einstein condensates. *Phys. Rev. A*, 83:063629, 2011.

[121] D. S. Jin, J. R. Ensher, M. R. Matthews, C. E. Wieman, and E. A. Cornell. Collective Excitations of a Bose-Einstein Condensate in a Dilute Gas. *Phys. Rev. Lett.*, 77:420–423, 1996.

[122] M.-O. Mewes, M. R. Andrews, N. J. van Druten, D. M. Kurn, D. S. Durfee, C. G. Townsend, and W. Ketterle. Collective Excitations of a Bose-Einstein Condensate in a Magnetic Trap. *Phys. Rev. Lett.*, 77:988–991, 1996.

[123] E. A. Uehling and G. E. Uhlenbeck. Transport Phenomena in Einstein-Bose and Fermi-Dirac Gases. *Phys. Rev.*, 43:552–561, 1933.

[124] O. Lanford. On the derivation of the Boltzmann equation. *Astérisque*, 40:117–137, 1976.

[125] H. Spohn. *Kinetic equations for quantum many-particle systems*. Springer, in press, preprint arXiv:0706.0807.

[126] D. Benedetto, F. Castella, R. Esposito, and M. Pulvirenti. From the N-body Schrödinger Equation to the Quantum Boltzmann Equation: a Term-by-Term Convergence Result in the Weak Coupling Regime. *Commun. Math. Phys.*, 277:1–44, 2008.

[127] J. Lukkarinen and H. Spohn. Weakly nonlinear Schrödinger equation with random initial data. *Inventiones mathematicae*, 183:79–188, 2011.

[128] E. Zaremba, T. Nikuni, and A. Griffin. Dynamics of Trapped Bose Gases at Finite Temperatures. *J. Low Temp. Phys.*, 116:277–345, 1999.

[129] D. Benedetto, F. Castella, R. Esposito, and M. Pulvirenti. Some Considerations on the Derivation of the Nonlinear Quantum Boltzmann Equation II: The Low Density Regime. *J. Stat. Phys.*, 124:951–996, 2006.

[130] T. R. Kirkpatrick and J. R. Dorfman. Transport theory for a weakly interacting condensed Bose gas. *Phys. Rev. A*, 28:2576–2579, 1983.

[131] T. R. Kirkpatrick and J. R. Dorfman. Transport in a dilute but condensed nonideal Bose gas: Kinetic equations. *J. Low Temp. Phys.*, 58:301–331, 1985.

[132] C. W. Gardiner and P. Zoller. Quantum kinetic theory: A quantum kinetic master equation for condensation of a weakly interacting Bose gas without a trapping potential. *Phys. Rev. A*, 55:2902–2921, 1997.

[133] D. Jaksch, C. W. Gardiner, and P. Zoller. Quantum kinetic theory. II. Simulation of the quantum Boltzmann master equation. *Phys. Rev. A*, 56:575–586, 1997.

[134] C. W. Gardiner and P. Zoller. Quantum kinetic theory. III. Quantum kinetic master equation for strongly condensed trapped systems. *Phys. Rev. A*, 58:536–556, 1998.

[135] D. Jaksch, C. W. Gardiner, K. M. Gheri, and P. Zoller. Quantum kinetic theory. IV. Intensity and amplitude fluctuations of a Bose-Einstein condensate at finite temperature including trap loss. *Phys. Rev. A*, 58:1450–1464, 1998.

[136] C. W. Gardiner and P. Zoller. Quantum kinetic theory. V. Quantum kinetic master equation for mutual interaction of condensate and noncondensate. *Phys. Rev. A*, 61:033601, 2000.

[137] M. D. Lee and C. W. Gardiner. Quantum kinetic theory. VI. The growth of a Bose-Einstein condensate. *Phys. Rev. A*, 62:033606, 2000.

[138] M. J. Davis, C. W. Gardiner, and R. J. Ballagh. Quantum kinetic theory. VII. The influence of vapor dynamics on condensate growth. *Phys. Rev. A*, 62:063608, 2000.

[139] C. W. Gardiner and P. Zoller. *Quantum Noise*. Springer Berlin / Heidelberg, 3rd edition, 2004.

[140] R. Walser, J. Williams, J. Cooper, and M. Holland. Quantum kinetic theory for a condensed bosonic gas. *Phys. Rev. A*, 59:3878–3889, 1999.

[141] R. Walser, J. Cooper, and M. Holland. Reversible and irreversible evolution of a condensed bosonic gas. *Phys. Rev. A*, 63:013607, 2000.

[142] A. Schelle, T. Wellens, D. Delande, and A. Buchleitner. Number-conserving master equation theory for a dilute Bose-Einstein condensate. *Phys. Rev. A*, 83:013615, 2011.

[143] N. P. Proukakis. Self-consistent quantum kinetics of condensate and non-condensate via a coupled equation of motion formalism. *J. Phys. B*, 34:4737, 2001.

[144] J. Wachter, R. Walser, J. Cooper, and M. Holland. Equivalence of kinetic theories of Bose-Einstein condensation. *Phys. Rev. A*, 64:053612, 2001.

[145] M. Imanovic-Tomasovic and A. Griffin. *Progress in Nonequilibrium Green's Functions*, chapter Generalized Boltzmann Equation for a Trapped Bose-Condensed Gas Using the Kadanoff-Baym Formalism. World Scientific, Singapore, 2000.

[146] M. Imamovic-Tomasovic and A. Griffin. Quasiparticle Kinetic Equation in a Trapped Bose Gas at Low Temperatures. *J. Low Temp. Phys.*, 122:617–655, 2001.

[147] L. P. Kadanoff and G. Baym. *Quantum Statistical Mechanics*. W. A. Benjamin Inc., New York, 1962.

[148] J. W. Kane and L. P. Kadanoff. Green's functions and superfluid hydrodynamics. *J. Math. Phys.*, 6:1902–1912, 1965.

[149] H. T. C. Stoof. Coherent Versus Incoherent Dynamics During Bose-Einstein Condensation in Atomic Gases. *J. Low Temp. Phys.*, 114:11–108, 1999.

[150] G. Grawert. *Quantenmechanik*. AULA-Publishing House, Wiesbaden, 4th edition, 1985.

[151] M. C. Tichy, M. Tiersch, F. de Melo, F. Mintert, and A. Buchleitner. Zero-transmission law for multiport beam splitters. *Phys. Rev. Lett.*, 104:220405, 2010.

[152] F. Eckert. Transport in non-linear disordered media. Master's thesis, University of Freiburg, `http://www.freidok.uni-freiburg.de/volltexte/7696/`, 2010.

[153] M. C. W. van Rossum and Th. M. Nieuwenhuizen. Multiple scattering of classical waves: microscopy, mesoscopy, and diffusion. *Rev. Mod. Phys.*, 71:313–371, 1999.

[154] P. M. Morse and H. Feshbach. *Methods of Theoretical Physics*. McGraw-Hill Book Company, New York, 1953.

[155] I am grateful for free graphics. `www.vecteezy.com`.

[156] L. Mandel and E. Wolf. *Optical Coherence and Quantum Optics*. Cambridge University Press, New York, 1995.

[157] F. Eckert, A. Buchleitner, and T. Wellens. Weak disorder corrections of the scattering and transport mean free path. *J. Phys. A*, 45:395101, 2012.

[158] D. Vollhardt and P. Wölfle. Anderson localization in $d \leqslant 2$ dimensions: A self-consistent diagrammatic theory. *Phys. Rev. Lett.*, 45:842–846, 1980.

[159] D. Vollhardt and P. Wölfle. Diagrammatic, self-consistent treatment of the Anderson localization problem in $d \leqslant 2$ dimensions. *Phys. Rev. B*, 22:4666–4679, 1980.

[160] A. Ishimaru. *Wave Propagation and Scattering in Random Media*. Academic Press, New York, 1978.

[161] E. A. Milne. Radiative equilibrium in the outer layers of a star. *Monthly Notices of the Royal Astronomical Society*, 81:361–375, 1921.

[162] G. Pólya. Über eine Aufgabe der Wahrscheinlichkeitsrechnung betreffend die Irrfahrt im Straßennetz. *Mathematische Annalen*, 84:149–160, 1921.

[163] T. Wellens and B. Grémaud. Coherent propagation of waves in dilute random media with weak nonlinearity. *Phys. Rev. A*, 80:063827, 2009.

[164] T. Geiger, T. Wellens, and A. Buchleitner. Inelastic multiple scattering of interacting bosons in weak random potentials. *Phys. Rev. Lett.*, 109:030601, 2012.

[165] J. J. Sakurai. *Advanced Quantum Mechanics*. Pearson Education, 2006.

[166] T. Wellens. *private communication*. 2012.

[167] M. Srednicki. The approach to thermal equilibrium in quantized chaotic systems. *J. Phys. A*, 32:1163, 1999.

[168] M. Berry. Semi-classical mechanics of regular and irregular motion. In G. Iooss, R. H. G. Helleman, and R. Stora, editors, *Chaotic Behavior of Deterministic Systems*, Amsterdam, 1983. North-Holland.

[169] T. Binninger. Multiple scattering of intense laser light in a cloud of cold atoms. Master's thesis, University of Freiburg, `http://www.freidok.uni-freiburg.de/volltexte/8812/`, 2012.

[170] Y. P. Chen, J. Hitchcock, D. Dries, M. Junker, C. Welford, and R. G. Hulet. Phase coherence and superfluid-insulator transition in a disordered Bose-Einstein condensate. *Phys. Rev. A*, 77:033632, 2008.

[171] H.-J. Miesner, D. M. Stamper-Kurn, M. R. Andrews, D. S. Durfee, S. Inouye, and W. Ketterle. Bosonic Stimulation in the Formation of a Bose-Einstein Condensate. *Science*, 279:1005–1007, 1998.

[172] L. Fallani, J. E. Lye, V. Guarrera, C. Fort, and M. Inguscio. Ultracold Atoms in a Disordered Crystal of Light: Towards a Bose Glass. *Phys. Rev. Lett.*, 98:130404, 2007.

[173] R. Seiringer, J. Yngvason, and V. A. Zagrebnov. Disordered Bose Einstein Condensates with Interaction. *ArXiv e-prints*, 2012.

[174] J. W. Goodman. *Statistical Optics*. Wiley, New York, 1985.

[175] S. Fiebig, C. M. Aegerter, W. Bührer, M. Störzer, E. Akkermans, G. Montambaux, and G. Maret. Conservation of energy in coherent backscattering of light. *Europhys. Lett.*, 81:64004, 2008.

[176] A. Knothe. Conservation of Energy in Coherent Backscattering of Light. Bachelor thesis, University of Freiburg, `http://www.freidok.uni-freiburg.de/volltexte/8724/`, 2012.

[177] T. Jonckheere, C. A. Müller, R. Kaiser, C. Miniature, and D. Delande. Multiple scattering of Light by Atoms in the Weak Localization Regime. *Phys. Rev. Lett.*, 85:4269, 2000.

[178] G. Labeyrie, D. Delande, R. Kaiser, and C. Miniatura. Light transport in cold atoms and thermal decoherence. *Phys. Rev. Lett.*, 97:013004, 2006.

[179] V. Shatokhin, C. A. Müller, and A. Buchleitner. Coherent Inelastic Backscattering of Intense Laser Light by Cold Atoms. *Phys. Rev. Lett.*, 94:43603, 2005.

[180] T. Geiger. New approach to multiple scattering of intense laser light by cold atoms. Master's thesis, University of Freiburg, `http://www.freidok.uni-freiburg.de/volltexte/6986/`, 2009.

[181] T. Geiger, T. Wellens, V. Shatokhin, and A. Buchleitner. The pump-probe approach to coherent backscattering of intense laser light from cold atoms. *Photonics and Nanostructures*, 8:244 – 253, 2010.

[182] T. Wellens, T. Geiger, V. Shatokhin, and A. Buchleitner. Scattering laser light on cold atoms: Toward multiple scattering signals from single-atom responses. *Phys. Rev. A*, 82:013832, 2010.

[183] T. Wellens and B. Grémaud. Observation of coherent backscattering 'factor of three' in a numerical experiment. *J. Phys. B*, 39:4719, 2006.

[184] C. D'Errico, M. Moratti, E. Lucioni, L. Tanzi, B. Deissler, M. Inguscio, G. Modugno, M. B. Plenio, and F. Caruso. Quantum diffusion with disorder, noise and interaction. *ArXiv e-prints*, 2012.

[185] C. Chin, R. Grimm, P. Julienne, and E. Tiesinga. Feshbach resonances in ultracold gases. *Rev. Mod. Phys.*, 82:1225–1286, 2010.

[186] N. Cherroret and T. Wellens. Fokker-Planck equation for transport of wave packets in nonlinear disordered media. *Phys. Rev. E*, 84:021114, 2011.

[187] G. Schwiete and A. M. Finkel'stein. Kinetics of the disordered Bose gas with collisions. *ArXiv e-prints*, 2013.

[188] T. F. Gallagher. *Rydberg Atoms*. Cambridge University Press, Cambridge, UK, 1994.

[189] D. Kleppner, M. G. Littman, and M. L. Zimmerman. Highly excited atoms. *Scientific American*, 244:130–149, 1981.

[190] D. Jaksch, J. I. Cirac, P. Zoller, S. L. Rolston, R. Côté, and M. D. Lukin. Fast quantum gates for neutral atoms. *Phys. Rev. Lett.*, 85:2208–2211, 2000.

[191] M. D. Lukin, M. Fleischhauer, R. Cote, L. M. Duan, D. Jaksch, J. I. Cirac, and P. Zoller. Dipole blockade and quantum information processing in mesoscopic atomic ensembles. *Phys. Rev. Lett.*, 87:037901, 2001.

[192] H. Schempp, G. Günter, C. S. Hofmann, C. Giese, S. D. Saliba, B. D. DePaola, T. Amthor, M. Weidemüller, S. Sevinçli, and T. Pohl. Coherent Population Trapping with Controlled Interparticle Interactions. *Phys. Rev. Lett.*, 104:173602, 2010.

[193] M. Viteau, P. Huillery, M. G. Bason, N. Malossi, D. Ciampini, O. Morsch, E. Arimondo, D. Comparat, and P. Pillet. Cooperative Excitation and Many-Body Interactions in a Cold Rydberg Gas. *Phys. Rev. Lett.*, 109:053002, 2012.

[194] A. Buchleitner, D. Delande, and J. Zakrzewski. Non-dispersive wave packets in periodically driven quantum systems. *Phys. Rep.*, 368:409 – 547, 2002.

[195] F. B. Dunning, J. C. Lancaster, C. O. Reinhold, S. Yoshida, and J. Burgdörfer. The Kicked Rydberg Atom. *Adv. At. Mol. Opt. Phys.*, 52:49 – 103, 2005.

[196] M. Saffman, T. G. Walker, and K. Mølmer. Quantum information with Rydberg atoms. *Rev. Mod. Phys.*, 82:2313–2363, 2010.

[197] R. Heidemann, U. Raitzsch, V. Bendkowsky, B. Butscher, R. Löw, L. Santos, and T. Pfau. Evidence for Coherent Collective Rydberg Excitation in the Strong Blockade Regime. *Phys. Rev. Lett.*, 99:163601, 2007.

[198] U. Raitzsch, V. Bendkowsky, R. Heidemann, B. Butscher, R. Löw, and T. Pfau. Echo Experiments in a Strongly Interacting Rydberg Gas. *Phys. Rev. Lett.*, 100:013002, 2008.

[199] K. Singer, J. Stanojevic, M. Weidemüller, and R. Côté. Long-range interactions between alkali Rydberg atom pairs correlated to the ns-ns, np–np and nd–nd asymptotes. *J. Phys. B*, 38:S295, 2005.

[200] Y. O. Dudin and A. Kuzmich. Strongly Interacting Rydberg Excitations of a Cold Atomic Gas. *Science*, 336:887–889, 2012.

[201] Y. O. Dudin, L. Li, F. Bariani, and A. Kuzmich. Observation of coherent many-body Rabi oscillations. *Nat. Phys.*, 8:790–794, 2012.

[202] C. Ates and I. Lesanovsky. Entropic enhancement of spatial correlations in a laser-driven Rydberg gas. *Phys. Rev. A*, 86:013408, 2012.

[203] H. Weimer, R. Löw, T. Pfau, and H. P. Büchler. Quantum Critical Behavior in Strongly Interacting Rydberg Gases. *Phys. Rev. Lett.*, 101:250601, 2008.

[204] F. Robicheaux and J. V. Hernández. Many-body wave function in a dipole blockade configuration. *Phys. Rev. A*, 72:063403, 2005.

[205] E. Urban, T. A. Johnson, T. Henage, L. Isenhower, D. D. Yavuz, T. G. Walker, and M. Saffman. Observation of Rydberg blockade between two atoms. *Nat. Phys.*, 5:110–114, 2009.

[206] A. Gaetan, Y. Miroshnychenko, T. Wilk, A. Chotia, M. Viteau, D. Comparat, P. Pillet, A. Browaeys, and P. Grangier. Observation of collective excitation of two individual atoms in the Rydberg blockade regime. *Nat. Phys.*, 5:115–118, 2009.

[207] F. Robicheaux. Ionization due to the interaction between two Rydberg atoms. *J. Phys. B*, 38:S333, 2005.

[208] M. Viteau, M. G. Bason, J. Radogostowicz, N. Malossi, D. Ciampini, O. Morsch, and E. Arimondo. Rydberg Excitations in Bose-Einstein Condensates in Quasi-One-Dimensional Potentials and Optical Lattices. *Phys. Rev. Lett.*, 107:060402, 2011.

[209] S. K. Dutta, J. R. Guest, D. Feldbaum, A. Walz-Flannigan, and G. Raithel. Ponderomotive Optical Lattice for Rydberg Atoms. *Phys. Rev. Lett.*, 85:5551–5554, 2000.

[210] H. Pichler, A. J. Daley, and P. Zoller. Nonequilibrium dynamics of bosonic atoms in optical lattices: Decoherence of many-body states due to spontaneous emission. *Phys. Rev. A*, 82:063605, 2010.

[211] I. B. Mekhov and H. Ritsch. Quantum optics with ultracold quantum gases: towards the full quantum regime of the light–matter interaction. *J. Phys. B*, 45:102001, 2012.

[212] F. Gerbier and Y. Castin. Heating rates for an atom in a far-detuned optical lattice. *Phys. Rev. A*, 82:013615, 2010.

[213] I. Lesanovsky. Many-Body Spin Interactions and the Ground State of a Dense Rydberg Lattice Gas. *Phys. Rev. Lett.*, 106:025301, 2011.

[214] C. Cohen-Tannoudji, J. Dupont-Roc, and G. Grynberg. *Atom-Photon Interactions*. Wiley-VCH Verlag, Weinheim, 2004.

[215] C. W. Gardiner. *Handbook of Stochastic Methods*. Springer Verlag, Berlin, 1985.

[216] G. H. Wannier. Wave Functions and Effective Hamiltonian for Bloch Electrons in an Electric Field. *Phys. Rev.*, 117:432–439, 1960.

[217] E. J. Heller. Time-dependent approach to semiclassical dynamics. *The Journal of Chemical Physics*, 62:1544–1555, 1975.

[218] A. Buchleitner and D. Delande. Secular motion of three-dimensional Rydberg states in a microwave field. *Phys. Rev. A*, 55:R1585–R1588, 1997.

[219] A. S. Sørensen and K. Mølmer. Entangling atoms in bad cavities. *Phys. Rev. A*, 66:022314, 2002.

[220] D. F. James and J. Jerke. Effective Hamiltonian theory and its applications in quantum information. *Canadian Journal of Physics*, 85:625–632, 2007.

[221] O. Gamel and D. F. V. James. Time-averaged quantum dynamics and the validity of the effective Hamiltonian model. *Phys. Rev. A*, 82:052106, 2010.

[222] R. H. Lehmberg. Radiation from an N-Atom System. 1. General Formalism. *Phys. Rev. A*, 2:883, 1970.

[223] M. O. Scully and M. Suhail Zubairy. *Quantum Optics*. Cambridge University Press, Cambridge, UK, 1997.

[224] H. P. Breuer and F. Petruccione. *The Theory of Open Quantum Systems*. Oxford University Press, Oxford, 2007.

[225] M. Abramowitz and I. A. Stegun, editors. *Handbook of Mathematical Functions with Formulas, Graphs, and Mathematical Tables*. Dover Publications, New York, Dover, 9 edition, 1972.

[226] M. Lax. Formal Theory of Quantum Fluctuations from a Driven State. *Phys. Rev.*, 129:2342, 1963.

[227] S. Swain. Master equation derivation of quantum regression theorem. *J. Phys. A*, Math. Gen. 14:2577, 1981.

[228] B. Olmos, R. González-Férez, and I. Lesanovsky. Creating collective many-body states with highly excited atoms. *Phys. Rev. A*, 81:023604, 2010.

[229] T. Laycock, B. Olmos, and I. Lesanovsky. Creation of collective many-body states and single photons from two-dimensional Rydberg lattice gases. *J. Phys. B*, 44:184017, 2011.

[230] E. Akkermans, G. Montambaux, J.-L. Pichard, and J. Zinn-Justin. *Mesoscopic Quantum Physics*. Elsevier, Amsterdam, 1994.

[231] M. B. van der Mark, M. P. van Albada, and A. Lagendijk. Light scattering in strongly scattering media: Multiple scattering and weak localization. *Phys. Rev. B*, 37:3575–3592, 1988.

[232] E. Akkermans, P. E. Wolf, and R. Maynard. Coherent Backscattering of Light by Disordered Media: Analysis of Peak Line Shape. *Phys. Rev. Lett.*, 56:1471, 1986.